UNIVERSITY OF
BIRMINGHAM

Advanced HVDC Systems for Renewable Energy Integration and Power Transmission: Modelling and Control for Power System Transient Stability

Mr. Dechao Kong

Thesis submitted in accordance with the requirements for

University of Birmingham for the degree of

The Doctor of Philosophy (PhD)

School of Electronic, Electrical and Computer Engineering

June 2013

Abstract

This PhD thesis is focused on modelling and control of advanced HVDC Systems for integration renewable energy and power delivery for power system transient stability:

The first part of the thesis is concerned with the dynamic aggregated modelling of the large-scale offshore wind farms including the two mainstream variable-speed wind turbines, the WT-DFIGs and WT-PMSGs and their integration into the electricity transmission systems via the point-to-point VSC-HVDC links. The dynamic aggregated modelling method of the large-scale offshore wind farms are firstly proposed to achieve the effective representations of these wind turbines for the balance between the computational time and requirement of simulation accuracy for transient stability analysis. The dynamic modelling of the point-to-point VSC-HVDC systems and their control strategies for grid integration of offshore wind farms are investigated. And the comparisons of two control schemes of rectifier-side converter in VSC-HVDC link are carried out to evaluate their dynamic performance for grid integration of the large-scale offshore wind farms consisting of the WT-DFIGs and WT-PMSGs in terms of transient stability.

The second part of the PhD thesis is to address the advanced power transmission systems with innovative HVDC configurations. Based on the characteristics of CSC-HVDC systems, the feasibility studies of the upgrade schemes of the existing monoplolar CSC-HVDC link with the support of the neighbouring monopolar VSC-HVDC link operating in parallel as the hybrid bipolar CSC/HVDC system is carried out via simulation to validated the effectiveness

of support from VSC-HVDC link to dealing with two key issues of the CSC-HVDC. Furthermore, the small-signal modelling of the emerging multi-terminal VSC-based HVDC grids is investigated and the parameter optimisation of the PI controller of the converters in the multi-terminal HVDC (MTDC) grids is carried out using the particle-swarm optimisation method for the small-signal models of the whole system at multiple operating points to obtain a set of optimised parameters of PI controllers to improve the dynamic performance of the MTDC grids at multiple operating points.

Acknowledge

Firstly, I would like to express my deepest appreciation and gratitude to my PhD supervisor Prof. Xiao-Ping Zhang for his generous support and worthwhile guidance during my studies for the PhD degree.

Secondly, I would extend my appreciation to Prof. Ping Ju and Prof Feng Wu, Hohai University, China, for their valuable advice on my PhD education in the UK.

Thirdly, I am also expressing my thanks for the kind support from my colleagues in the Institute for Energy Research and Policy, the colleagues from the Science City Energy Efficiency & Demand project, the staff at the University of Birmingham.

Fourthly, I gratefully acknowledge the financial support from Advantages West Midlands Science City Energy Efficiency & Demand Project for my PhD studies.

Finally, I would like to extend my deepest appreciation and gratitude to my parents, my wife Mrs. Yuanyuan Cui, my other family members and friends for their long-term support, encouragement, tolerance and understanding throughout my self-development.

Table of Contents

List of Figures

List of Tables

List of Abbreviations

CC	Constant Current
CEA	Constant Extinction Angle
CFA	Constant Firing Angle
CV	Constant Voltage
CSC	Current-Sourced Converter
EC	Evolutionary Computation
FACTS	Flexible AC Transmission System
FRT	Fault Ride Through
GA	Genetic Algorithm
HFF	High-frequency Filter
HVAC	High Voltage Alternating Current
HVDC	High Voltage Direct Current
IGBT	Insulated-Gate Bipolar Transistor
LFF	Low-frequency Filter
LVRT	Low-voltage Ride-Through
MMC	Multi-level Modular Converter
MTDC	Multi-terminal VSC-based HVDC
NSSS	North Sea Supergrid Scheme
OLTC	On-Load Tap Changer
PCC	Point of Common Coupling
PI	Proportional-Integral
PLL	Phase-Locked Loop

PSO	Particle Swarm Optimisation
PSS	Power System Stabiliser
PWM	Pulse-Width Modulation
RTDS	Real Time Digital Simulator
SCR	Short-circuit Ratio
SMIB	Single Machine Infinite Bus
SSTI	Sub-synchronous Torsional Interaction
STATCOM	Static Synchronous Compensator
SVC	Static Var Compensator
TCSC	Thyristor-controlled Series Compensator
TSO	Transmission System Operator
VDCOL	Voltage-Dependent Current-Order Limit
VSC	Voltage-Sourced Converter
WT-DFIG	Wind Turbine with Doubly-Fed Induction Generator
WT-FSIG	Wind Turbine with Fixed-Speed Induction Generator
WT-PMSG	Wind Turbine with Permanent Magnetic Synchronous Generator

Chapter 1

Introduction

1.1 Motivation

1.1.1 Importance of Power System Transient Stability

If a power system in initial operating condition is subjected to a physical disturbance and is able to return to the initial operating condition or regaining equilibrium after dynamic motions of system variables, the ability of this system can be referred to the power system stability based on the definition in [1].

For the modern large-scale power systems in most countries around the world, their main infrastructures are established based on the alternating-current (AC) technology. On the one hand, the system frequency and voltage-levels are two of the most important factors in the AC power systems. One the other hand, most of electric power in the power systems is generated from three-phase AC synchronous generators (mostly thermal and hydro). During the normal operation of a power system, the mechanical and electromagnetic torques acting on each generator should keep balance and all the synchronous generators rotate at the same electrical speed in synchronisation with the system frequency (so-called synchronism).

As a result, these three factors are of great importance to the power system security. And the classification of power system stability has been specified in Fig-1.1 [1] based on different impacts of disturbances on these three factors.

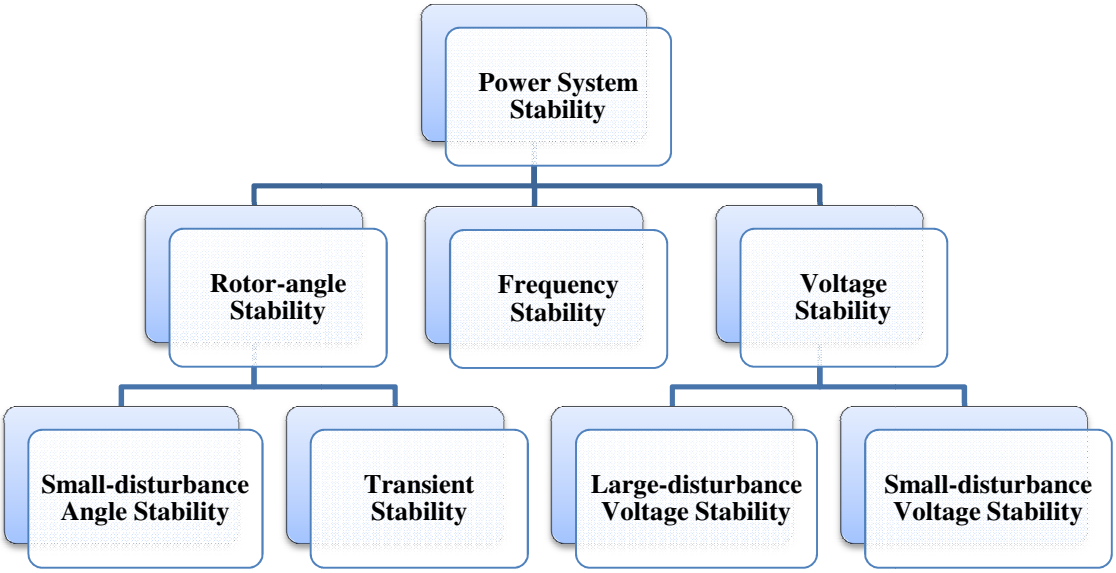

Fig-1.1 The Classification of Power System Stability

For the high voltage transmission systems, they are directly connected to generation units via step-up transformers and usually widely distributed for long-distance bulk power delivery from generator-side to demanding-side. So the disturbances especially the large ones in a high voltage transmission system could bring big impacts not only on itself but also the generators in adjacent to the disturbance. Short-circuit faults especially the temporary ones within the transmission lines caused by lightning and tree fallings are the most common and severe faults in the transmission systems and they usually cause the imbalance between the mechanical and electromagnetic torques acting on the generators in vicinity of the short-circuit faults which brings big changes of generators' rotor-angle and triggers the power oscillations [2]. If the power system under large disturbances such as short-circuit faults within the transmission lines is able to maintain the synchronism of generators. This ability can be referred to the transient stability defined by [1]. Otherwise, lack of transient stability could cause the changes of rotor-angle continuously and the self-exciting power oscillations to further bring severe damages to the power system components such as generators and

transmission lines or even cause the blackout of the power system. Due to the short-circuit faults with tree fallings on the 345 kV transmission lines in USA, the lack of transient stability played an important role in the biggest blackout event in Northern American History– the Northern Blackout of 2003 which caused power losses for about 50 million people in USA and Canada for nearly two days and estimated economical losses of 6 billion dollars [3]. As a result, the physical nature, methodology for transient stability should be carefully investigated to guarantee power system security, especially when new technologies are integrated into the power systems such as high voltage direct current (HVDC) and renewable energy which have their own dynamic characteristics for transient stability. As a result, dynamic impacts of the systems with such emerging technologies on power system transient stability should be carefully investigated for power system security.

1.1.2 Grid Integration of Large-scale Energy Systems with HVDC Transmission Technology

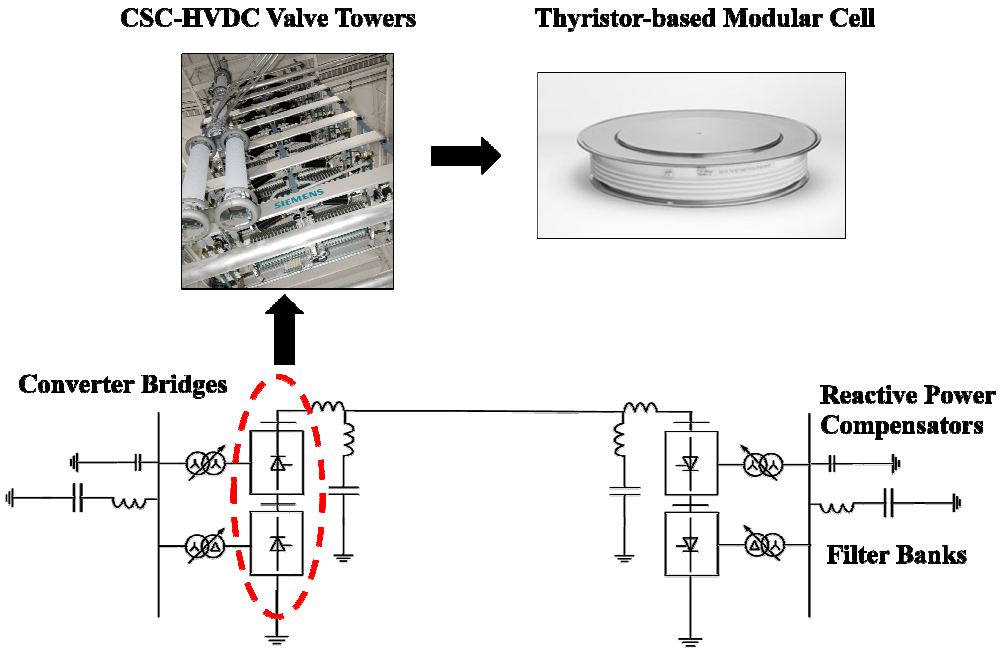

Fig-1.2 The General Layout of CSC-HVDC Systems using Thyristor Cells

In the so-called “War of Currents” in the late 1880s [4], the power transmission technology based on AC prevailed over that based on DC to become the preferred standard for the global power industry with overwhelming advantages over DC techniques especially in terms of achieving high-voltage levels for reduction of power losses in long-distance power transmission at that time. With the rapid development of semiconductor-based power electronics from 1947 [4], the HVDC technology has overcome the technical bottlenecks to realise the high voltage-levels for long-distance power transmission. Furthermore, HVDC technology has gradually reflected its unique benefits as follows [5, 6]:

1) Real-time controllable power flows;
2) Improvement of dynamic stability with converter controllers;
3) No need for reactive power compensation to the transmission lines;
4) Capability of interconnection of asynchronous systems with different system frequencies.

For the HVDC technology, there are two possibilities [5]: the classic technology based on the current-sourced converters (CSC) and the emerging one based on the voltage-sourced converters (VSC). For the CSC-HVDC technology, the basic modules in the AC/DC converters are the thyristor-based modular cells shown in Fig-1.2 [2, 4, 7, 8]. Due to long-term development, this technology has become so mature and well-proven that it is widely used in the long-distance point-to-point power delivery and interconnection of asynchronous systems around the world [4, 7, 8]. In the GB transmission system in the UK, there have been three CSC-HVDC interconnectors in commercial operation with a total power capacity of 3500 MW [4, 7, 8]. For the first integral HVDC link in the GB transmission systems—the 2000 MW Western-Link HVDC Project [9], the CSC-HVDC technology has been chosen

for this project in terms of development requirements of electricity infrastructure for grid integration of large-scale renewable energy systems especially the wind and hydro-power in Scotland to meet the increasing energy demands in England and Wales.

The other possibility is the emerging next-generation VSC-HVDC technology, of which the basic modules in the AC/DC converters are the IGBT-based modular cells shown in Fig-1.3 [5]. Since the first commercial application in undersea power transmission project in 1999 [10], the VSC-HVDC technology has gradually shown its key advantages over HVAC and CSC-HVDC technology listed as follows [5, 6]:

1) Independent active and reactive power control;
2) No needs for extra reactive power support during operation;
3) Grid access to weak AC networks such as islands and offshore wind farms;
4) The capability of black-start;
5) Power reversal without changing DC polarities;
6) Compact layout and scalability for lower space requirements.

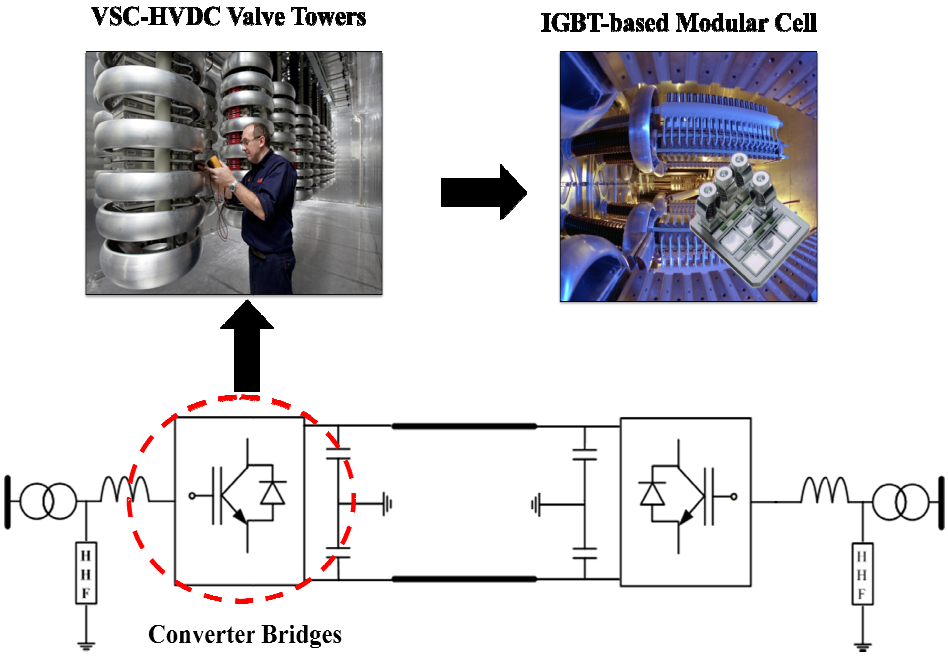

Fig-1.3 The General Layout of VSC-HVDC System using IGBT Cells

As a result, the VSC-HVDC technology is commonly regarded as the optimal solution to grid integration of large-scale offshore wind farms and has challenged the market dominance of original HVAC technology with new projects listed in the Table-1.1 [11, 12].

Table-1.1 The List of Offshore Wind Farms Using VSC-HVDC Systems by 2015

Project Name	Power Rating	Total Distances	Commission Year
BorWin Alpha	400 MW	200 km	2012
BorWin Beta	800 MW	200 km	2013
DolWin Alpha	800 MW	165 km	2013
HelWin Alpha	576 MW	130 km	2013
SylWin Alpha	864 MW	205 km	2014
DolWin Beta	900 MW	135 km	2015
HelWin Beta	690 MW	130 km	2015

As a result, the VSC-HVDC technology will play an active role in the future development of the power system and the studies of modelling and control of VSC-HVDC systems are of great importance to understand their dynamic characteristics so that the technology risk can be identified as soon as possible to move towards the wide application of the VSC-HVDC technology for collection of offshore renewable energy and long-distance bulk power delivery.

1.1.3 Dynamic Aggregated Modelling of Large-scale Offshore Wind Farms for Transient Stability Analysis

In Europe, the European Union (EU) has published its renewable energy proposals in January 2008 with the core targets of achieving a reduction of greenhouse gas emissions by 20% and increasing the share of renewable energy in the EU's total energy generation to 20% both in 2020 [13]. For the EU countries around the North Sea, offshore wind energy resources are rich and widely distributed. To achieve the EU's renewable energy targets, an increasing number of offshore wind farms have

been commissioned, constructed or proposed by those countries such as UK and Germany who have been playing the pioneering roles in the development of offshore wind industries in the world [9, 11, 12].

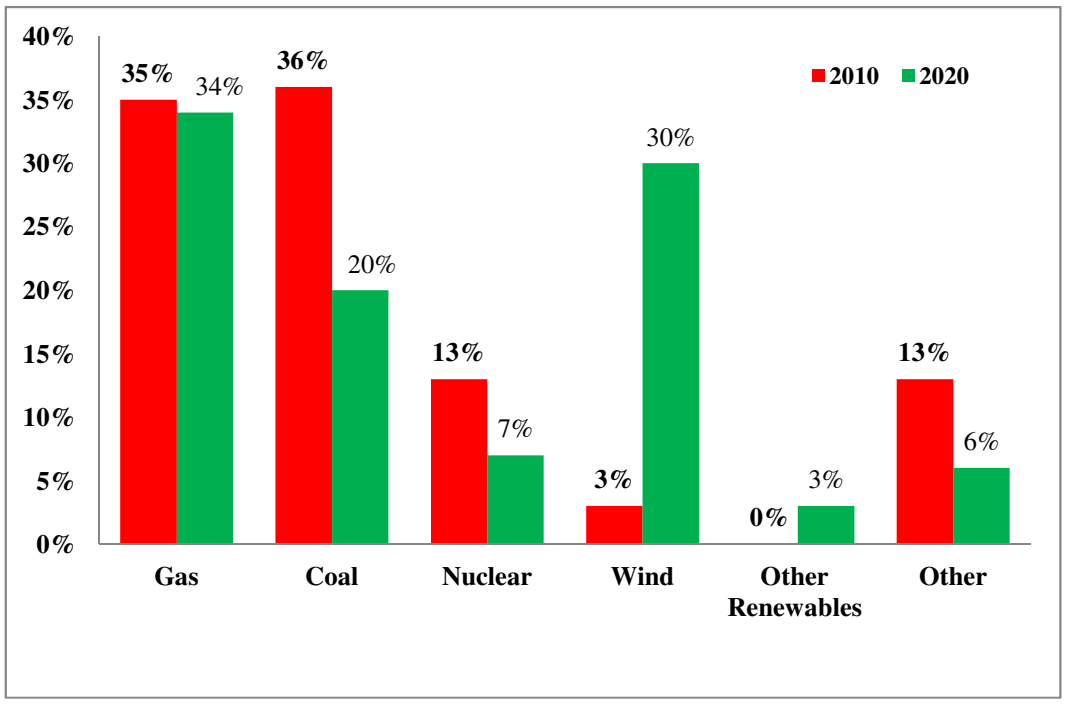

Fig-1.4 The UK's Gone Green Scenario: Generation Mix in 2010 and 2020

Taking the UK as an example, it has potentially the richest offshore wind resources in Europe. To move towards a low-carbon economy in the UK, wind energy has been playing a key role in the renewable energy development with increasing integration of offshore wind energy into the UK's electricity transmission networks. From the generation mix in Gone Green scenario endorsed by UK's government shown in Fig-1.4 [9, 14, 15], the share of wind energy will increase significantly from just 3% in 2010 to 30% with 32 GW of new wind energy (20 GW offshore and 12 GW onshore) integrated into UK's electricity transmission networks by 2020.

According to the UK's development plans for offshore wind energy, the London Array project [16], the expected largest offshore wind farms in the world with the total installation capacity of 1,000 MW has been under construction and other eight

proposed offshore wind areas for the UK's Crown Estate Round 2 and 3 Plans by 2020 shown in Table-1.2 are expected to be ranked in the top-10 list of proposed offshore wind resources areas in the world with a potentially accumulative installation capacity of 31.9 GW [9, 17, 18].

Table-1.2 The Proposed Offshore Wind Farm Areas in the UK by 2030

Project Name	Total (MW)
Dogger Bank	9,000
Norfolk Bank	7,200
Irish Sea	4,200
Hornsea	4,000
Firth of Forth	3,500
Bristol Channel	1,500
Moray Firth	1,300
Triton Knoll	1,200

In order to explore the maximum potentials of offshore wind resources, not only the per-unit power ratings of wind turbines will be increased [19], but also the number of wind turbines installed in the offshore wind farms will be increased greatly in the future. For the largest offshore wind farm project under construction, the Phase-1 of London Array project will be completed at the end of 2012 with the total capacity of 630.0 MW. And the number of wind turbines in this project has reached 175. For the Phase-2 project, another 166 units of wind turbines with the total installation capacity of 370 MW will be installed and the overall number of wind turbines can reach 341 [16, 17].

With increasing integration of the large-scale offshore wind farms, their dynamic impacts on the electricity transmission networks are of vital importance for the operation security and stability. In order to build the transmission systems to meet the requirements of these large-scale offshore wind farms in terms of security and

stability, the dynamic characteristics of the large-scale offshore wind farms should be carefully investigated. However, due to a large number of wind turbines in the offshore wind farms, huge amount of computational efforts should be needed for transient stability analysis. In this way, the effective representations of the large-scale offshore wind farms are necessary to identified for achieving the balance between the computational time and requirement of simulation accuracy in the transient stability analysis.

1.1.4 Optimised Control of Multi-terminal VSC-based HVDC Grids

Fig-1.5 The North Sea Supergrid Scheme

For the EU countries around the North Sea, they are facing the increasing challenges for how to integrate their rich renewable energy resources into the electricity transmission networks to meet the countries' increasing energy demands and boost a low-carbon economy. To deal with these issues, the North Sea Supergrid Scheme (NSSS) [20-22] shown in Fig-1.5 [23] have been proposed by the EU countries around the North Sea to build the new electricity transmission infrastructure for facilitating the collection, delivery and trade of large-scale renewable energy such as the offshore wind energy in North Sea areas and hydro power in Nordic countries.

The NSSS has received great support from governments, industrial and academic organisations in these EU countries.

For the NSSS, the electricity transmission infrastructure is of great importance. With the advantages over HVAC and CSC-HVDC technology mentioned in Section 1.1.2, the multi-terminal VSC-based HVDC grids (MTDC) have been proposed as the preferred solutions to building the backbone of the new electricity transmission infrastructure around the North Sea in terms of the higher requirements for system reliability, stability and flexibility [5, 20, 22]. However, due to the absence of MTDC system in the world, the operation experiences for such systems are so limited [20, 21]. As a result, the investigation of the operating characteristics of the MTDC systems for feasibility studies and establishment of operational specification such as the grid code are of great necessity to move towards the reality of multi-terminal VSC-HVDC grids like North Sea Supergrid.

1.2 Contributions

1) Proposing the dynamic aggregated modelling method to simplify the detailed representation of the large-scale offshore wind farms to some extent by using several equivalent machines representing the mainstream variable-speed wind turbines─ WT-DFIGs and WT-PMSGs respectively in the offshore wind farms with the purpose of achieving the balance between the computational time and requirement of simulation accuracy for the transient stability analysis which is hard to achieve simultaneously by conventional methods using either detailed models over-simplified single equivalent machine.
2) Comparing the classical and emerging control schemes for the rectifier-side converter of point-to-point VSC-HVDC link for grid integration of large-scale

offshore wind farms including WT-DFIGs and WT-PMSGs. After comparisons of simulation results for these two control schemes, the preferred control scheme is validated by simulation for grid integration of large-scale offshore wind farms including WT-DFIGs and WT-PMSGs in terms of transient stability.

3) Investigating a feasibility of the upgrade scheme of monopolar CSC-HVDC link with the operating of a neighbouring monopolar VSC-HVDC link in parallel as the proposed hybrid bipolar CSC/VSC-HVDC system. With the design of the control schemes of the VSC-HVDC link, the performance of extra support from VSC-HVDC link is validated for helping conventional CSC-HVDC link to deal with the reactive power support and mitigation of potential risks of inverter-side commutation failure.

4) Proposing the PSO-based parameter optimisation method for PI controllers of voltage-sourced converters in the emerging multi-terminal HVDC (MTDC) grid with multiple system operation points based on the small-signal models of the whole system. Compared with conventional PSO-based parameter optimisation methods for single operating point, the set of parameters of PI controllers optimised by the proposed method is validated for improving the dynamic performance of the MTDC grid at multiple operating points in terms of transient stability.

1.3 Outline

The PhD thesis is organised as follow:

Chapter 2: The literatures are reviewed.

Chapter 3: The dynamic models and control strategies of two mainstream wind turbines — WT-DFIG and WT-PMSG are investigated. Then the dynamic aggregated modelling method for large-scale offshore wind

farms consisting of WT-DFIGs and WT-PMSGs is proposed for transient stability analysis. The simulation systems with different representations of aggregated models in the offshore wind farms are tested in the DIgSILENT/PowerFactory to evaluate their dynamic performance for identification of the effective representation of the system with the balance between the computational time and requirement of simulation accuracy in terms of transient stability .

Chapter 4: The dynamic models and control strategies for the rectifier- and inverter-side converters in the point-to-point bipolar VSC-HVDC systems are investigated. The dynamic performance of two control schemes for grid integration of large-scale offshore farms of WT-DFIGs and WT-PMSGs are evaluated via the simulation systems in the DIgSILENT/PowerFactory to identify the preferred control scheme of rectifier-side converter for grid integration of the large-scale offshore wind farms in terms of transient stability.

Chapter 5: The mathematical models and control strategies for rectifier- and inverter-side converters in the bipolar CSC-HVDC systems are investigated. The layout out hybrid bipolar CSC/VSC HVDC system is proposed and the control strategies of monopolar VSC-HVDC link are designed to give extra support to the neighbouring monopolar CSC-HVDC link in parallel in terms of its two issues: reactive power support and inverter-side commutation failure. The simulation systems for bipolar CSC-HVDC and hybrid HVDC systems in the DIgSILENT/PowerFactory are tested to evaluate the dynamic characteristics of CSC-HVDC systems and the feasibilities of the extra

support from neighbouring VSC-HVDC systems to deal with these two key issues of the conventional CSC-HVDC systems.

Chapter 6: The small-signal models for the three-terminal VSC-based HVDC grid with radial topology are derived. Based on the small-signal models if the whole system at multiple operating points, the PSO method is applied for the parameter optimisation of the PI controllers of VSCs in the three-terminal HVDC grid. The comparisons of the simulation systems with original and optimised parameters are carried out in MATLAB/SIMULINK for the whole system at two different operating points to evaluate their dynamic performance in terms of transient stability.

Chapter 7: Conclusions of the work in the PhD thesis are drawn and research work plans in the future are described.

Chapter 2

Literature Review

2.1 Grid Code for Power System Transient Stability

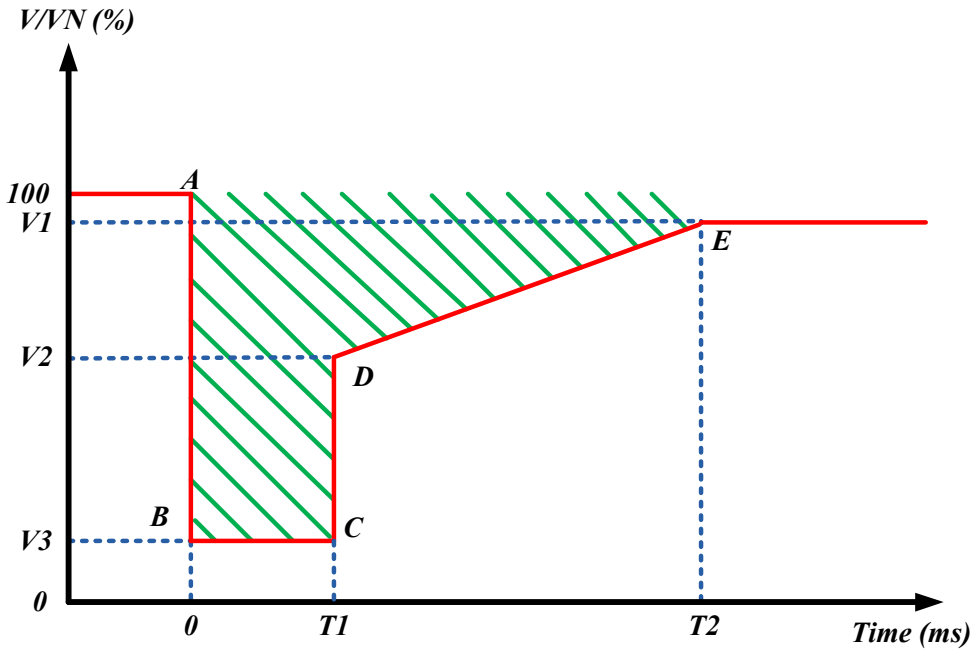

Fig-2.1 The Fault Ride-Through Requirements in Grid Code

In [1], the classification, definition of three types of power system stability including rotor-angle stability, frequency stability and voltage stability are described based on their physical nature. As the large-disturbance rotor angle stability or so-called transient stability, it refers to the ability of power system under large disturbances such as the short-circuit faults within the transmission lines to maintain the synchronism of generators. Transient stability of a power system is mainly influenced by the initial operating condition (or called operating point) and severity of the disturbances. The initial operating condition usually is determined by the steady-state power flow and the severity of disturbances depends mainly on the time duration and strength of disturbances. As described in [2] [24], the short-circuit faults especially on the transmission lines are the most common large-disturbances in the high voltage

transmission systems. For the strength of short-circuit faults, it depends mainly on the types of short-circuit faults, grounded impedance, and the short-circuit ratio (SCR) of power system.

For the transmission system operators (TSOs), so-called grid code has been developed as the operational specifications to keep the reliable, economical and efficient system operation. In terms of transient stability, so-called fault ride-through (FRT) requirements have been specified in the grid code [25, 26]. The general concepts of the FRT requirements are illustrated in Fig-2.1 and the red-colour curve is drawn according to the events described below as the boundary for FRT requirements: The voltage dropped from **Point A** at 1.0 p.u. to **Point B** at *V3* when the fault was applied at 0+ s. At T_1, the fault was removed and the voltage increased suddenly from **Point C** at *V3* to **Point D** at *V2*. From T_1 to *T2*, the voltage recovered from **Point D** at *V2* to **Point E** at *V1*. For all the primary-side components in a transmission system such as transmission lines or transformers, their voltage changes during the time between 0+ s to T_2 should be located within the shadow zone with the colour of dark green around the boundary in which they are not permitted to be isolated from the system (so-called FRT requirements). For the operational specifications of grid code, T_1 is usually specified as 140 ms or 150 ms and T_2 is specified as 500 ms in [25, 26].

Otherwise, if the severity of the fault is large enough to make voltage changes of some component outside the shadow zone just like strength of a fault exceeds the *V1* or time duration of a fault is longer than *T1*, such component should be isolated as soon as possible by protective devices such as circuit breakers according to [25, 26].

2.2 Challenges for Grid Integration of Large-scale Offshore Wind Farms

With increasing concerns about the significant impacts of global climate changes and exhaustion of fossil-fuels on the sustainable development of human beings, the renewable energy resources with zero greenhouse gas emissions such as wind, hydro and solar energy have obtained worldwide attention in the recent years. Due to the wide distribution of potential large-scale wind resources in the world, wind energy has been well considered as one of the key alternatives to replace conventional thermal power plants fuelled by fossil fuels for large-scale power generation. And with the strong support from governments, industrial and academic organisations all around the world, the global wind industries have developed very quickly with steady increases in past ten years: the global total installation capacity of wind energy has increased sharply from 24,322 MW in 2001 to 239,900 MW in 2011 with a significant growth-rate of 886.34% [27]. For the EU countries around the North Sea, offshore wind energy resources are rich and widely distributed. To achieve the EU's renewable energy targets [13], an increasing number of offshore wind farms have been commissioned, constructed or proposed by those countries such as UK, Germany and Demark who have been playing the pioneering roles in the development of offshore wind energy in the world [11, 12, 16-18, 28]. The world's first offshore wind farm is the Danish Vindeby Project which was put into operation in 1991 for DONG Energy and it consists of 11 units of wind turbines with a rated per-unit capacity of 0.45 MW [28]. Since the first offshore wind farm put into operation 21 years ago, great changes have taken place in the offshore wind industries especially in EU countries to not only act as the key alternatives to fossil fuels for large-scale power generation but also meet these countries' increasing energy demands. Taking the UK as an example,

according to the UK's development plans for offshore wind energy, the London Array Project, the expected largest offshore wind farms in the world with a total installation capacity of 1,000 MW has been under construction [9, 16] and other eight proposed offshore wind areas for the UK's Crown Estate Round 2 and 3 Plans by 2020 [18] are expected to be ranked in the top-10 list of proposed offshore wind farm areas in the world with a potentially accumulative installation capacity of 31.9 GW [9, 17, 18].

To meet the technical specifications of increasing integration of offshore wind power, the science and technology related to the offshore wind industries has developed very quickly and there are three key features for the future development of offshore wind energy systems:

1) Development of offshore wind turbine technology. At the initial stage, the wind turbine with the fixed-speed induction generators (WT-FSIGs) are widely installed in the offshore wind farms just like Vindeby project [28, 29]. Due to operation in constant wind speed, the energy efficiency of this kind of machines is not so high without system adjustment for wind speed changes [29]. And the per-unit power ratings of the WT-FSIGs are usually in the range of kW-level.

   With the development of aerodynamic techniques [19], the mechanical components of the wind turbine have been improved greatly to meet the requirements of variable-speed operation, for instance, equipping with blade pitch-angle control systems to achieve dynamic adjustment of the wind turbine in responses to wind speed changes [29]. Furthermore, due to the fast development of power electronics, the back-to-back power converters are applied in the next-generation wind turbine, the so-called WT-DFIGs (wind turbines with doubly-fed

induction generator), to achieve partial power controls of the generator in response to the wind speed changes. For the WT-DFIGs, the energy efficiency and operation reliability have been improved obviously and the power ratings of the WF-DFIGs can usually reach in the range of 1-5 MW [29]. And the WT-DFIGs have become the mainstream wind turbines for market dominance.

With the reduced costs in power converters, the full-scale power converters have been gradually applied in the emerging so-called WT-PMSGs (Wind turbine with permanent magnetic synchronous generators) and the power of the generator can be fully controlled to enhance the operation reliability, flexibility and energy-efficiency. Furthermore, for the design of multi-pole direct-driven structure of the generator, the wind turbine can operate in the low rotational speed especially suitable for circumstances of low wind speed so that operating and maintenance costs can be reduced due to the absence of slip-ring and gearbox [29]. With the benefits mentioned above, the WT-PMSGs have gradually seized the market shares and become the favourite options for manufacturing the wind turbines mainly in the range of 4.5-7.0 MW [30, 31].

2) Development of foundation installation technology for offshore wind turbines. With the development of foundation installation technology, the wind turbines can be installed in deeper sea areas to explore the potentials of offshore wind areas far from the seashore. The gravity-based foundations are commonly used for most of the current offshore wind farms with the water depth of 30-50 m [32]. For the current the most remote offshore wind farm using the gravity-based foundations, the maximum water depth is 41 m and the distance of the subsea cables is 125 km [33]. For the water depth more than 50 m, the floating

foundation [19, 32, 34] can be applied for such deep sea areas and offshore wind farms can be potentially in the sea areas more than 125 km to maximize the exploration of offshore wind energy.

3) Increasing total installation capacity of offshore wind farms. In order to explore the maximum potentials of offshore wind energy resources, not only the per-unit power ratings of wind turbines will be increased, but also the number of wind turbines installed in the offshore wind farms will be increased greatly in the future. For the current world's largest offshore wind farm —Walney project in the UK, the total installation capacity can reach 367.2 MW with 102 units of wind turbines [17]. Furthermore, for the largest offshore wind farm projects under construction, the Phase-1 of London Array project will be completed at the end of 2012 to surpass the Walney project to be ranked as the first largest offshore wind farms with the total capacity of 630.0 MW. And the number of wind turbines in this project has reached 175. For the Phase-2 project, another 166 units of wind turbines with the total installation capacity of 370 MW will be installed and the overall number of wind turbines can reach 341 [16, 17]. So the total installation capacity of the offshore wind farms will increase greatly with hundreds of wind turbines

Considering the three key features for the development of the large-scale offshore wind farms, there are three key challenges for grid integration of large-scale offshore wind farm in terms of operation security and stability listed as follows:

1) With increasing integration of large-scale offshore wind farms, the dynamic impacts of such wind farms on the external power systems interconnected should be carefully investigated for maintaining the operation security and stability of

the whole systems. As a result, the mainstream wind turbines in the offshore wind farms should be studied firstly for representation of their dynamic characteristics reasonably for transient stability analysis. Based on their dynamic characteristics, control strategies for different types of wind turbines should be further investigated to maintain the operation stability of the wind turbines in the offshore wind farms under large disturbances.

2) In the future, the large-scale offshore wind farms will consist of a large amount of wind turbines. In the transient stability analysis, if all the wind turbines are represented in detail, huge amount of computational efforts should be required. If the overall dynamic performance of an offshore wind farms are concerned only, then alternative modelling methods can be investigated to simplify the whole offshore wind farm to some extent to compromise between computational time and the requirement of simulation accuracy and for transient stability analysis.

3) For the offshore wind farms, not only the total installation capacity has increased greatly but also the transmission distances between the offshore wind farms and the onshore stations will become much longer than ever before. In this situation, it has brought great challenges for the transmission technology with high technical specifications in terms of operation security, stability.

2.3 Modelling and Control of Variable-speed Wind turbines in the Offshore Wind Farms

With the increasing integration of large-scale offshore wind farms, their dynamic impacts on the external power systems interconnected should be considered of great importance for the operation security and stability of the whole systems. In this way, the dynamic characteristics of the wind turbines, especially the mainstream WT-DFIGs and WT-PMSGs should be carefully investigated and some work has been

carried out to investigate their unique characteristics. In [35-47], the dynamic modelling methods of WT-DFIG systems have been investigated for transient stability analysis. In [45, 46, 48-52], some work has been carried out focusing on the effective control of WT-DFIG systems to enhance their performance against large disturbances such as the capacity of FRT or so-called low-voltage ride-through (LVRT). In [53, 54], the support for reactive power and system frequency regulations of the WT-DFIG systems have been investigated. In [55], the characteristics of short-circuit currents in the WT-DFIG systems have been investigated.

For the emerging WT-PMSG systems, the dynamic modelling methods for small-signal modelling have been described in [56, 57]. The dynamic modelling methods for transient stability analysis have been described in [58-63]. The general control strategies for integration into the power systems have been described in [64-68]. In [57, 69, 70], the optimal control strategies of the WT-PMSGs have been investigated. In [71, 72], the robust control strategies have been investigated for the WT-PMSG systems during fault condition. In [73], the control scheme have been proposed to enhance the LVRT capabilities of the WT-PMSG systems. Furthermore, the dynamic performance of the WT-PMSG systems during the short-circuit fault condition have been investigated in [74]. In [75], the support capabilities of WT-PMSG systems for the external power systems during faults condition have been studied. In [76-79], The LVRT capabilities of the WT-PMSG systems for the severe voltage dips have been tested.

2.4 Dynamic Equivalent Modelling Methods for Power System Transient Stability Analysis

For the power system transient stability analysis, a large number of generators with detailed representations can take a huge number of computational efforts. To solve such issues, the studies of dynamic equivalent modelling of large-scale power systems have been carried out to investigate the balance between the computational time and requirement of simulation accuracy. In [24], three equivalent modelling methods have been described. The first one is the dynamic aggregated modelling method based on the identification of the generators with the similar dynamic responses which are selected into a so-called coherency group and aggregated into an equivalent machine. The studies in [80, 81] are based on this principle. The second one is the modal dynamic equivalent modelling method based the modal analysis of the small-signal models of the power systems to identify the generators with the similar modes of oscillation in the coherency group [82, 83]. The third one is based on the parametric identification of the equivalent machine to make the dynamic responses of equivalent machine similar to those of the generators in the coherency group [84, 85]. Evaluating all the three methods, the modal analysis method is too complex with needs for deriving the small-signal models of the large-scale power systems which usually contain a large number of generators and their supplementary elements. For the third method, the equivalent models are usually represented using the single-machine. Due to such over-simplifications, some important dynamic characteristics of the generators could be neglected. For the first-method, the identification of the coherency groups is based on their dynamic responses in the transient simulation and it is much easier to carry out than the second method. And for the first method, the large-scale power systems are divided into several coherency groups which are represented by their own

equivalent machines in order to avoid the issues of over-simplifications similar to the third method. So the first method has been considered as the most effective method and commonly used in the dynamic equivalent modelling of large-scale power systems for transient stability analysis.

2.5 Dynamic Equivalent Modelling Methods for Offshore Wind Farms in Transient Stability Analysis

For the large-scale offshore wind farms, they usually consist of a large number of wind turbine and the issues of computational time is similar to those for large-scale power systems. In [86], the dynamic aggregated method has been proposed for the WT-FSIG systems based on the first method and the slip speeds of eight FSIGs as the dynamic responses are identified as the criteria for coherency groups [24]. In [87-93] the wind farm with WT-DFIGs has been represented with an equivalent single machine with the equivalent impedance for the wind farms' AC networks. Although the simulation results are acceptable with different improvements, this method is only tested in a small system. In the large-scale offshore wind farms, such over-simplifications will bring problems for the requirement of simulation accuracy. In [94], although the first-method has been applied in the identification of the coherency groups of WT-DFIG systems, but the parameter aggregation of the equivalent model for each elements of the WT-DFIG systems are not mentioned. In [95], the third method is used for parametric identification of the single equivalent machine with online measurement of key states of the wind farm. But the simulation system with this method is only tested for a wind farm with six units of WT-DFIGs. This method should be further tested in the large-scale wind farm for validating the simulation accuracy. In [96], dynamic aggregated modelling of the wind farm with twelve units WT-PMSGs are proposed. The four units of WT-PMSGs connected in the same chain

were aggregated into a group without any criteria for identification of coherency group. And for such kind of WT-PMSG systems, the uncontrollable diode-based converter has been equipped on the rectifier-side of the power converter. Furthermore, for the rapid development of power converters in the WT-PMSG systems, the controllable VSC-based converters have been equipped to both-side of the power converter in the WT-PMSG systems [29].

2.6 Modelling and Control of the Point-to-point VSC-HVDC Systems for Grid Integration of Offshore Wind Farms

With the advantages over HVAC and conventional CSC-HVDC transmission technology mentioned in Section 1.1.2 [5, 6], the VSC-HVDC technology has been widely considered as the preferred solution to connecting the large-scale offshore wind farm in future. So the dynamic characteristics of the VSC-HVDC systems and their control strategies for rectifier- and inverter-side converters should be investigated for transient stability analysis. The dynamic modelling of the VSC-HVDC systems has been described in [97-103] with the same principles. For the VSC-HVDC systems, the controllers are usually designed for two-stage controller structure: for the inner control loop, the feed-forward method has been applied for the decoupled current control [104, 105]. The controlled modulation index is sent to generate fire signals for the IGBTs for AC/DC transformation. For the outer control loop, different system variables can be supervised and controlled independently using the commonly-used PI controllers. With different combination of control variables, different control targets can be achieved. The decoupled power control has been usually designed for rectified-side voltage-sourced converter for supervisory of input

AC power flow [104-106], and additional damping controller has been added to the active power controller as the frequency controllers for the small-signal stability [101]. Input active power and AC voltage at the rectifier-side point of common coupling (PCC) are supervised and controlled with the similar control structures for grid integration of weak-grids [98, 107]. The decoupled voltage control is usually designed for inverter-side VSC for supervisory of DC-side voltage of converter on the inverter-side for normal DC power delivery as well as the AC voltage at the inverter-side PCC to keep synchronous with the external power system interconnected [108, 109]. Some alternative controllers have been also studied: DC voltages of the inverter-side converter and output reactive power at inverter-side PCC are supervised and controlled for inverter-side converters [105, 110, 111]. In [112], grid integration of the WT-DFIG based offshore wind farm using VSC-HVDC system has been described and the different control scheme for the rectifier-side VSC controller with aim of only controlling the AC voltage at the PCC has been proposed. In [113], the improved control strategies similar to those in [112] have been proposed in order to enhance the LVRT capabilities of the WT-DFIG based offshore wind farm.

2.7 Modelling and Control of the Hybrid HVDC Systems

With the development of VSC-based technology, it has provided great potentials for enhancing the capabilities of the original CSC-HVDC systems for power transmission. In [114], the so-called hybrid HVDC system has been proposed for power transmission to island networks which was only consisting of passive elements. In this hybrid HVDC system, the VSC-based static synchronous compensator (STATCOM) and the inverter-side of CSC-HVDC system were connected with the same AC bus. Due to the operating characteristics of thyristor-based AC/DC converters, they are not able to commutate without AC voltage sources [4]. So the STATCOM played the role

as the voltage source to provide the commutation voltage for the inverter-side converters. In [115, 116], another concept of hybrid HVDC system has been proposed for grid integration of the WT-DFIGs based wind farms. The STATCOM and the rectifier-side converter were connected with the same AC bus. During the operation of CSC-HVDC systems, it should absorb extra reactive power [4] and the STATCOM can provide flexible reactive power compensation. With the coordination between the STATCOM and the CSC-HVDC system during normal and fault condition, the dynamic performance of whole transmission system has been improved. In [117], the third hybrid concept is proposed: Due to operating without reactive power support [5, 6], the VSC on the rectifier-side is connected directly with the wind farm without extra devices for reactive power compensation and the CSC on the inverter-side was connected with the AC active network. The feasibility of the hybrid system has been validated with dynamic simulation in the transient stability analysis. Besides that, the obvious advantages of this hybrid system over pure VSC-HVDC are the lower investment costs and power losses. In [118], the fourth concept of hybrid HVDC system has been proposed: a monopolar VSC-HVDC system worked in parallel with the monopolar CSC-HVDC system as the bipolar hybrid HVDC system. For the fourth concept, not only acting as the transmission system, the VSCs on the rectifier- and inverter-side have the same characteristics as the STATCOM for independent reactive power control and voltage support which have been proposed in the first and second concepts [5, 6, 67, 112, 113, 119, 120]. Considering the power reversal, the DC polarities of the CSCs should be reversed but not necessary for VSCs. Considering the third concept for connecting these two kinds of converters in series, such systems only tested for connecting with wind farms which the direction of power flows are mostly from wind farm to the external power systems. For two AC systems

with frequent power exchange, the feasible schemes for coordinating these two kinds of converters should be further investigated. For the fourth concept, the detailed switching scheme of the switches has been described to realise the changes the DC voltage polarities of the VSCs in response to the power directions for symmetrical operation with CSC-HVDC system in [118].

Evaluating these four concepts of hybrid HVDC systems, the fourth one is the most effective and practical way. As a result, with the fourth concept, the upgrade scheme has been approval for the existing Skagerrak 3 CSC-HVDC Link which was established in 1993 between Denmark and Norway. The Skagerrak 4 VSC-HVDC project is expected to be commissioned in 2014 and work in parallel with the Skagerrak 3 CSC-HVDC Link to increase the power transmission capability from 440 MW to 1140 MW.

2.8 Small-signal Modelling of Multi-terminal VSC-based HVDC Grids

Although the North Sea Supergrid based on the MTDC are considered having promising future, there is still a long road to make it a reality. Nowadays, there is no such HVDC grid existing in world and the experiences are so limited for the operation and control of such systems. To move towards the development of MTDC grids, the feasibility studies of the different design plans and establishments of technical specifications such as the grid code should be needed to meet the higher requirements in terms of security, stability for such complex AC/DC systems.

As described in [2], the small-signal modelling and analysis of the power systems are effective ways to understand the dynamic characteristics of the power systems using

classic control theories and methodologies. In [102], the small-signal modelling and analysis of the four-terminal HVDC grid with meshed structure have been carried out to investigate the dynamic characteristics of the HVDC grid which was connecting with two offshore wind farms including the WT-FSIG systems and a synchronous generator. During the analysis processes, with changing of the parameters of PI controllers, different eigen-values in the state matrix for different operating points can be calculated which can reflect the systems' dynamic characteristics directly. In [103], the small-signal modelling and analysis of the HVDC grid triangle structure was carried out to investigate the dynamic characteristics of the HVDC grid which was connecting with two external grids and a wind farm. Using the other small-signal analysis method with root-locus plotting, the dynamic characteristics of this HVDC grid can be identified directly.

2.9 Optimised Control of Multi-terminal VSC-based HVDC Grid at Multiple Operating Points

As the preferred solution to building the backbone of the North Sea Supergrid [23, 121], it will bring higher requirements for the MTDC grids involved in the pan-European electricity market [20, 21]. As driven by the market benefits, the power exchange among the TSOs at the cross-borders will be changed frequently in a relatively short periods. As a result, the MTDC grids will be operating at the different operating points on the frequent basis and it will bring great challenges for such MTDC grids in terms of system security and stability. In [102], the small-signal analysis of the four-terminal HVDC grid has been carried to investigate the dynamic performance of the HVDC grid for grid integration of offshore wind farms. During the analysis processes, the parameters of the PI controllers in the converters have big influences on the eigen-values in the state matrix of the small-signal models of the

HVDC grid which can reflect the dynamic characteristics of the whole system. In this way, the parameters of the PI controllers in the MTDC grids can be tuned to some extent to improve dynamic performance of the systems at multiple operating points.

For tuning the parameters of controllers in the power systems, the optimisation methods just like the evolutionary computation (EC) techniques are regarded as the preferred solution. Currently, the genetic algorithm (GA), one of the most popular EC methods at early stage, has been widely applied for the parameter optimisation of the controllers in the power systems [122-131]. With the rapid development of EC techniques, the so-called particle-swarm optimisation (PSO) methods were proposed and developed by Dr. Russell Eberhart and Dr. James Kennedy, who learnt from the studies of social behaviours in the flocks of birds during their research [132, 133]. The PSO methods have been well-proven for good performance in parameter optimisation and advantages over GA: In [134], the PSO method has been applied in the design of power system stabiliser (PSS) to improve its capabilities to mitigate the low-frequency oscillation in the power systems. Comparing the dynamic simulation results for the synchronous generators equipped with gradient-, GA- and PSO-based PSSs, the effects of the proposed PSO-based PSS were better than those with the other two methods. In [135], the parameter optimisations of the controllers of thyristor-controllable series compensators (TCSCs) based on the GA and PSO have been carried out. After evaluating the dynamic performance of the power systems equipped with GA- and PSO-based TCSCs, the PSO was validated to be better than GA for parameter optimisation of the controllers of the TCSCs. Furthermore, in [57, 136], the PSO method has been applied in the parameter optimisation of the PI controllers which are equipped to the two mainstream variable-speed wind turbines—WT-DFIG

and WT-PMSG to improve their dynamic performance under small and large disturbances. In [137], the improved adaptive PSO method has been applied in the parameter optimisation of the PI controllers of the CSC-HVDC system and the proposed APSO method was tested in the CIGRE HVDC Benchmark model to validate its feasibility.

In [138, 139], the so-called Simplex algorithm, a nonlinear optimisation method based on geometric considerations, has been applied in the parameter optimisation of the PI controllers in the VSC- and CSC-HVDC systems respectively. For such algorithm, it has not become as well-proven as the PSO for the applications in the power systems. As a result, the PSO methods are still considered as a preferred solution to the parameter optimisation of PI controllers in the VSC-based HVDC grids.

Chapter 3

Dynamic Aggregated Modelling of Large-scale Offshore Wind Farms for Transient Stability Analysis

3.1 Introduction

In the power system transient stability analysis, it is mainly concern about the overall dynamic impacts of a wind farm on the external power systems interconnected. In this way, only their overall dynamic impacts on the external power systems are considered rather than the detailed dynamic behaviours of each wind turbine. So these wind farms can be simplified to some extent that they are represented using few equivalent machines to reflect their key characteristics so that the computational time for the simulation in transient stability analysis can be reduced to some extent. With these principles, the dynamic aggregated modelling method is proposed. In this method, the wind turbines with similar dynamic responses are selected into a coherency group and they are aggregated into an equivalent machine. As a result, the wind farm can be represented with several simplified aggregated machines to compromise between the computational time and requirement of simulation accuracy for transient stability analysis.

3.2 Modelling of WT-DFIG Systems

The general configuration of the WT-DFIG system is shown in Fig-3.1 [35]. The prime mover consisting of wind turbine with blade pitch-angle controller, shafts and gearbox, extracts kinetic energy from air flow through the turbine blades and then converts it into rotational mechanical torque of shafts to drive the induction generator to generate electricity. For the electrical components of WT-DFIG system, the three-phase stator winding of the induction generator is connected to the external power system directly, and the three-phase

rotor winding is indirectly connected with the grid by the back-to-back VSC-based power converter between them. The so-called rotor-side converter connected with the slip-ring of rotor and the grid-side converter connected with the external power system. A DC capacitor connected to both DC sides of the two converters acts as the DC voltage resource for AC/DC power transformation.

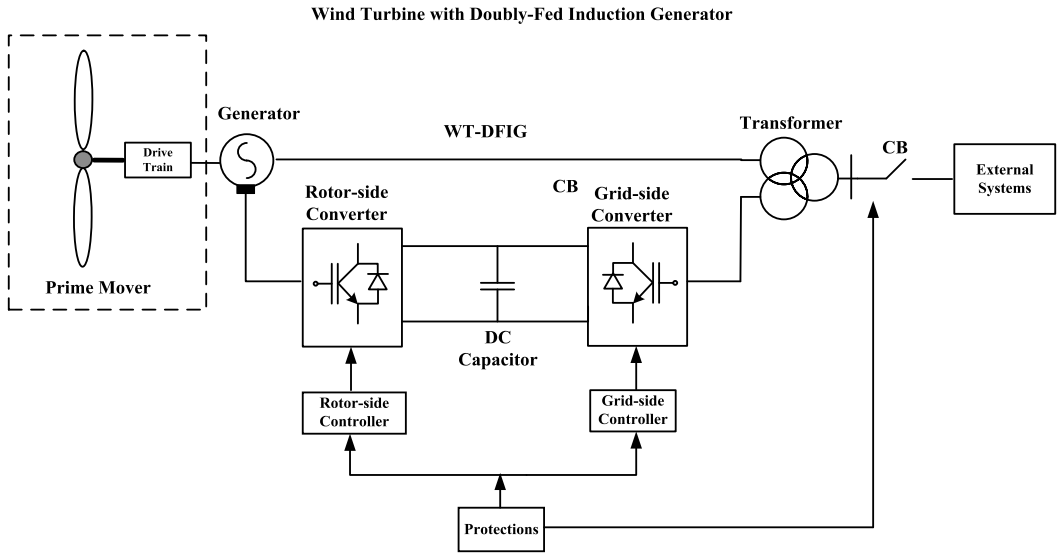

Fig-3.1 The General Configuration of WT-DFIG System

3.2.1 Modelling of Wind Turbine

The kinetic energy extracted from air flow via wind turbine blades is given by [136]:

$$P_m = \frac{1}{2}\rho\pi R^2 V_w{}^3 C_p \tag{3.1}$$

where P_m is the mechanical power from wind turbine; ρ is the air density; R is the blade radius of wind turbine; V_w is the wind speed; C_p is the power coefficient and is a function of tip speed ratio λ and blade pitch-angle β given by (3.2):

$$\begin{cases} C_p(\lambda,\beta) = \frac{1}{2}\left(\frac{RC_f}{\lambda} - 0.022\beta - 2\right)e^{-0.255\frac{RC_f}{\lambda}} \\ \lambda = \frac{R\omega_t}{V_w} \end{cases} \tag{3.3}$$

where C_f is the blade design constant coefficient and ω_t is the rotational speed of wind turbine.

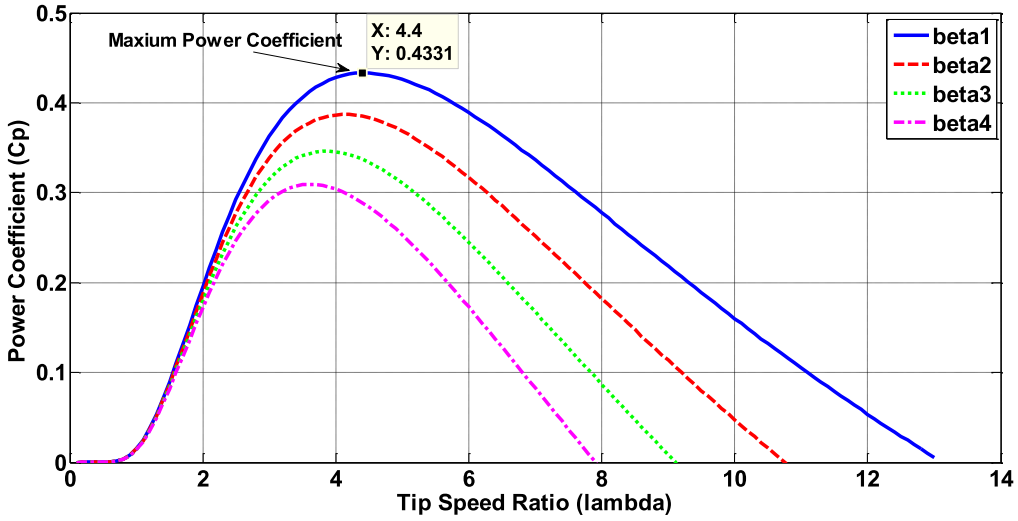

Fig-3.2 The Power Coefficient Curves with Different Pre-setting Pitch-angle

When V_w is under the rated speed, β is kept at the minimum limit β_1 and ω_t can be continuously adjusted to keep λ constant at specific level which the maximum C_p can be achieved as shown in Fig-3.2 and the generator speed can be adjusted to increase.

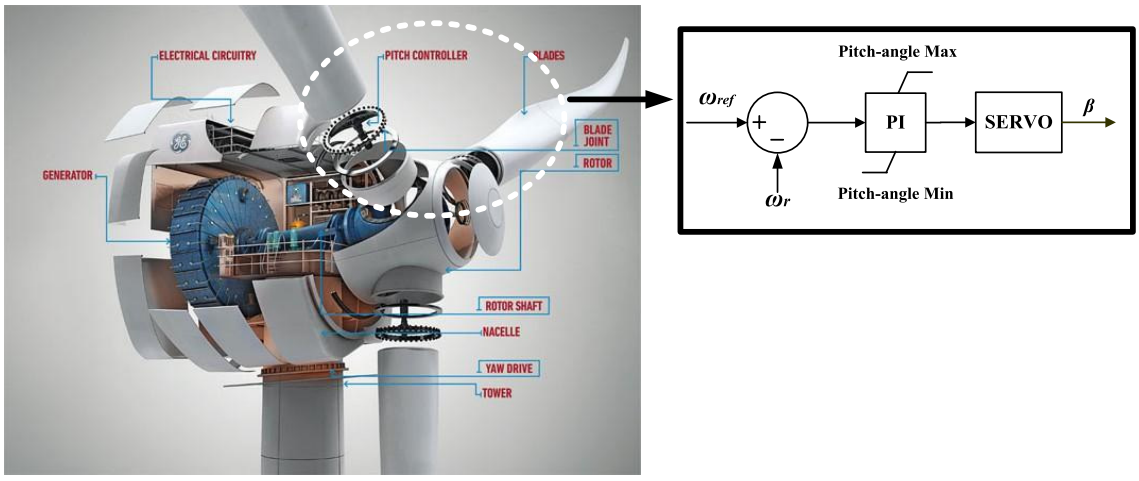

Fig-3.3 The Control Diagram of Blade Pitch-angle Controller

When the wind speed increases above the rated speed, a blade pitch-angle controller is usually applied in a variable-speed wind turbine shown in Fig-3.3 [140]. The blade pitch-angle controller usually consists of a PI controller and servomechanism. There is a feedback of the generator rotational speed ω_r in this controller. Beyond the rated wind speed, the speed deviation can be regulated by this pitch-angle controller to increase β until it reaches the maximum limit β_4 [35].

3.2.2 Modelling of Two-mass Drive-Train

The drive train are usually represented by a two-mass models for the combination of the turbine's low speed shaft and generator' high speed shaft coupled by the gearbox. The drive-train's two-mass models are given by [136]:

$$\begin{cases} 2H_t \dfrac{d\omega_t}{dt} = T_m - T_{sh} \\ 2H_g \dfrac{d\omega_r}{dt} = T_{sh} - T_{em} \\ \dfrac{d\theta_{tw}}{dt} = \omega_t - \omega_r \\ T_{sh} = K_{sh} \times \theta_{tw} + D_{sh} \times \dfrac{d\theta_{tw}}{dt} \end{cases} \tag{3.4}$$

$$\begin{cases} T_m = \dfrac{P_m}{\omega_t} \\ T_{em} = \dfrac{P_s}{\omega_r} \end{cases} \tag{3.5}$$

where H_t is the inertia constant of wind turbine; H_g is the inertia constant of generator; T_m is the mechanical torque of wind turbine; T_{em} is the electromagnetic torque of generator; T_{sh} is the shaft torque; θ_{tw} is the shaft twist angle; K_{sh} is the shaft stiffness coefficient; D_{sh} is the damping coefficient; P_s is the active power of generator's stator winding.

3.2.3 Modelling of DFIG

The 2nd-order dynamic models for the rotor-side of DFIG can be expressed [38, 47, 136]:

$$\begin{cases} \dfrac{dE'_d}{dt} = s\omega_s E'_q - \dfrac{\omega_s L_m}{L_r} V_{rq} - \dfrac{1}{T'_0}[E'_d + (X_s - X'_s) I_{sq}] \\ \dfrac{dE'_q}{dt} = -s\omega_s E'_d + \dfrac{\omega_s L_m}{L_r} V_{rd} - \dfrac{1}{T'_0}[E'_q - (X_s - X'_s) I_{sd}] \end{cases} \tag{3.6}$$

where E'_d is the d-axis voltage behind the transient reactance; E'_q is the q-axis voltage behind the transient reactance; V_{rd} is the d-axis voltage on rotor-side of DFIG; V_{rq} the q-axis voltage on rotor-side of DFIG; I_{sd} is the d-axis current on stator-side of DFIG; I_{sq} is the q-axis

current on stator-side of DFIG; s is the rotor slip of DFIG; ω_s is the synchronous rotational speed; L_s is the self-inductance on the stator-side of DFIG; L_m is the mutual inductance on the stator-side of DFIG; T_0' is the circuit time constant on the rotor-side of DFIG; X_s is the reactance on the stator-side of DFIG; X_s' is the transient reactance on the stator-side of DFIG. The modelling in detail is described in Appendix A.

And the 2nd-order dynamic models for the stator-side of DFIG are expressed [38, 47, 136]:

$$\begin{cases} \dfrac{X_s'}{\omega_s}\dfrac{dI_{sd}}{dt} = V_{sd} - [R_s + \dfrac{1}{\omega_s T_0'}(X_s - X_s')]I_{sd} - (1-s)E_d' + \dfrac{L_m}{L_r}V_{rq} + \dfrac{1}{\omega_s T_0'}E_q' + X_s' I_{sq} \\ \dfrac{X_s'}{\omega_s}\dfrac{dI_{sq}}{dt} = V_{sq} - [R_s + \dfrac{1}{\omega_s T_0'}(X_s - X_s')]I_{sq} - (1-s)E_q' + \dfrac{L_m}{L_r}V_{rd} - \dfrac{1}{\omega_s T_0'}E_d' - X_s' I_{sd} \end{cases} \tag{3.7}$$

where V_{sd} is the d-axis voltage on the stator-side of DFIG; V_{sq} is the q-axis voltage on the stator-side of DFIG; R_s is the resistance on the stator-side of DFIG. So the detailed dynamic models of the DFIG can be represented by the 4th-order differential equations of E_d', E_q', I_{sd} and I_{sq}. The modelling in detail is described in Appendix A.

3.2.4 Modelling of DC Link

Assuming the power losses in the rotor- and grid-side converters can be neglected, so the active power can keep balance through the two converters expressed by [47]:

$$P_{rc} = P_{gc} + P_{cap} \tag{3.8}$$

where P_{rc} is the active power in the rotor-side converter; P_{gc} is the active power in the grid-side converter; P_{cap} is the active power in the DC capacitor. They are given by [47]:

$$\begin{cases} P_{rc} = V_{rd} I_{rd} + V_{rq} I_{rq} \\ P_{gc} = V_{sd} I_{gd} + V_{sq} I_{gq} \end{cases} \tag{3.9}$$

$$P_{cap} = V_{dc} I_{dc} = C_{dc} V_{dc} \frac{dV_{dc}}{dt} \tag{3.10}$$

where I_{rd} is the *d*-axis current on rotor-side of DFIG; I_{rq} is the *q*-axis current on rotor-side of DFIG; I_{gd} is the *d*-axis current of grid-side converter; I_{gq} is the *q*-axis current of grid-side converter; V_{dc} is the DC voltage of DC capacitor; I_{dc} is the DC current of DC capacitor; C_{dc} is the capacitance of DC capacitor. So the dynamic model of the DC link is expressed by:

$$\frac{dV_{dc}}{dt} = \frac{1}{C_{dc}V_{dc}}(V_{rd}I_{rd} + V_{rq}I_{rq} - V_{sd}I_{gd} - V_{sq}I_{gq}) \tag{3.11}$$

3.3 Control Strategies for the WT-DFIG Systems

3.3.1 The Rotor-side VSC Controller

As described with detail in Appendix A, the voltage equations for the rotor-side induction generator is given by (3.12):

$$\begin{cases} V_{rd} = \dfrac{d\psi_{rd}}{dt} - s\omega_s \times \psi_{rq} \\ V_{rq} = \dfrac{d\psi_{rq}}{dt} + s\omega_s \times \psi_{rd} \end{cases} \tag{3.12}$$

where ψ_{rd} and ψ_{rq} are the rotor-side *d*- and *q*-axis flux linkage which are expressed in (3.13):

$$\begin{cases} \psi_{rd} = L_r \times I_{rd} + L_m \times I_{sd} \\ \psi_{rq} = L_r \times I_{rq} + L_m \times I_{sq} \end{cases} \tag{3.13}$$

And substituting (3.13) into (3.12):

$$\begin{cases} V_{rd} = \dfrac{d\psi_{rd}}{dt} - (\omega_s - \omega_r)L_r \times I_{rq} - (\omega_s - \omega_r)L_m \times I_{sq} \\ V_{rq} = \dfrac{d\psi_{rq}}{dt} + (\omega_s - \omega_r)L_r \times I_{rd} + (\omega_s - \omega_r)L_m \times I_{sd} \end{cases} \tag{3.14}$$

In (3.14), $\frac{d\psi_{rd}}{dt}$ and $\frac{d\psi_{rq}}{dt}$ are replaced from V_{rd}^* and V_{rq}^* using the PI controllers expressed by (3.15):

$$\begin{cases} V_{rd}^* = \dfrac{d\psi_{rd}}{dt} = K_{rd}(I_{rd}^{ref} - I_{rd}) + K_{ird}\int (I_{rd}^{ref} - I_{rd})dt \\ V_{rq}^* = \dfrac{d\psi_{rq}}{dt} = K_{rq}(I_{rq}^{ref} - I_{rq}) + K_{irq}\int (I_{rq}^{ref} - I_{rq})dt \end{cases} \tag{3.15}$$

where K_{rd} and K_{ird} are the proportional and integral gains of d-axis PI controller; K_{rq} and K_{irq} are the proportional and integral gains of q-axis PI controller. For the PI controllers, time constant T_i of integrator is also used for (3.16) and the relationship between time constant T_i and integral gain K_i is expressed by:

$$K_i = \frac{1}{T_i} \tag{3.17}$$

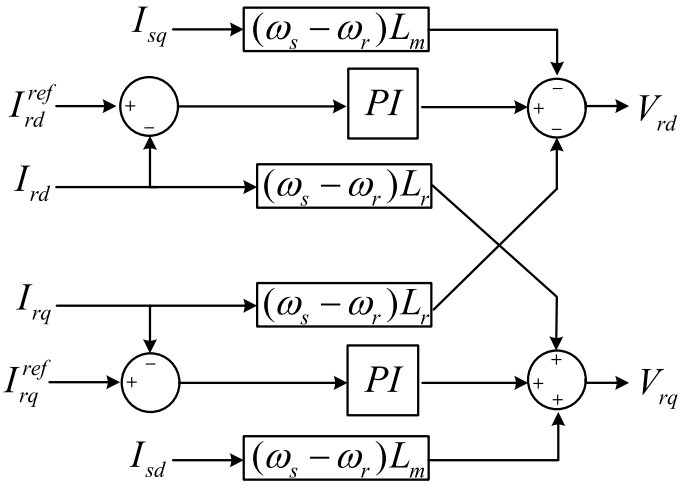

Fig-3.4 The Second-Stage Current Controller for Rotor-side VSC

Based on (3.14) and (3.15), the decoupled current controller is shown in Fig-3.4. V_{rd} and V_{rq} are regulated as the modulation index for generating the firing-signal for the rotor-side converter [141].

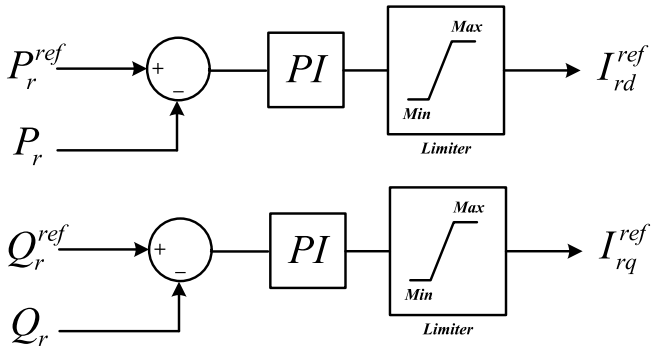

Fig-3.5 The First-stage Power Controller for Rotor-side VSC

The WT-DFIG's output active and reactive power P_r and Q_r at the PCC are compared with their reference values P_r^{ref} and Q_r^{ref}. Then their deviations are sent to the two PI controllers

respectively for being specified as the reference values I_{rd}^{ref} and I_{rq}^{ref} for the current controller in Fig-3.5:

$$\begin{cases} I_{rd}^{ref} = K_P(P_r^{ref} - P_r) + K_{iP}\int(P_r^{ref} - P_r)dt \\ I_{rq}^{ref} = K_Q(Q_r^{ref} - Q_r) + K_{iQ}\int(Q_r^{ref} - Q_r)dt \end{cases} \tag{3.18}$$

where K_P and K_{iP} are the proportional and integral gains d-axis PI controller; K_Q and K_{iQ} are the proportional and integral gains of q-axis PI controller. As the result, the two-stage PI controllers are used for the rotor-side VSC controller [35, 47].

3.3.2 The Grid-side VSC Controller

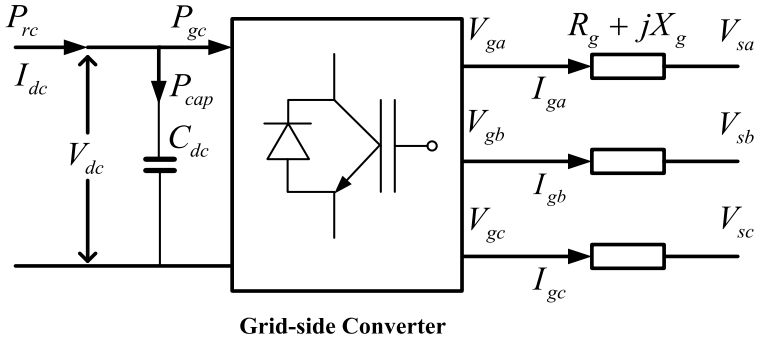

Fig-3.6 The Diagram of Grid-side Converter

According to the derivation of grid-side converter models in detail in Appendix A, the d- and q-axis voltage V_{gd} and V_{gq} of the grid-side converter from the original three-phase V_{ga} ,V_{gb} and V_{gc} shown in Fig-3.6 are expressed by:

$$\begin{cases} V_{gd} = V_{sd} + R_g I_{gd} + L_g \dfrac{dI_{gd}}{dt} - \omega_s L_g I_{gq} \\ V_{gq} = V_{sq} + R_g I_{gq} + L_g \dfrac{dI_{gq}}{dt} + \omega_s L_g I_{gd} \end{cases} \tag{3.19}$$

where I_{gd} and I_{gq} are the d and q-axis current of grid-side converter; R_g is the grid-side converter resistance; L_g is the grid-side converter reactance; ω_g is the rotational speed of the grid-side converter. In (3.19), $L_g \dfrac{dI_{gd}}{dt}$ and $L_g \dfrac{dI_{gq}}{dt}$ are replaced from V_{gd}^* and V_{gq}^* using the PI controllers expressed by (3.20):

$$\begin{cases} V_{gd}^{*} = L_g \dfrac{dI_{gd}}{dt} = K_{gd}(I_{gd}^{ref} - I_{gd}) + K_{igd}\int (I_{gd}^{ref} - I_{gd})dt \\ V_{gq}^{*} = L_g \dfrac{dI_{gq}}{dt} = K_{gq}(I_{gq}^{ref} - I_{gq}) + K_{igq}\int (I_{gq}^{ref} - I_{gq})dt \end{cases} \tag{3.20}$$

where K_{gd} and K_{igd} are the proportional and integral gains d-axis PI controller; K_{gq} and K_{igq} are the proportional and integral gains of q-axis PI controller. Based on (3.19) and (3.20), the decoupled current controller is shown in Fig-3.7. V_{gd} and V_{rq} are regulated as the modulation index for generating the firing-signal for the grid-side converter [141].

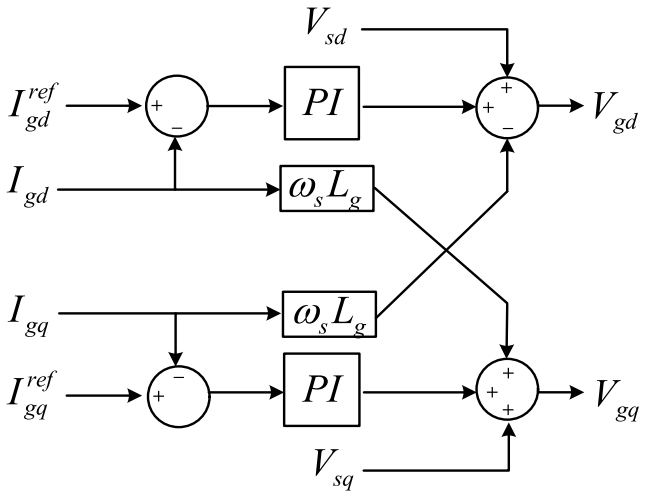

Fig-3.7 The Second Stage Current Controller for Grid-side VSC

The deviations of DC voltage of DC link and its reference value are sent to the d-axis PI controller to be specified as the I_{gd}^{ref} which is express by (3.21) in Fig-3.8 [35, 47]:

$$I_{gd}^{ref} = K_{dc}(V_{dc}^{ref} - V_{dc}) + K_{idc}\int (V_{dc}^{ref} - V_{dc})dt \tag{3.21}$$

where K_{dc} and K_{idc} are the proportional and integral gains of d-axis PI controller.

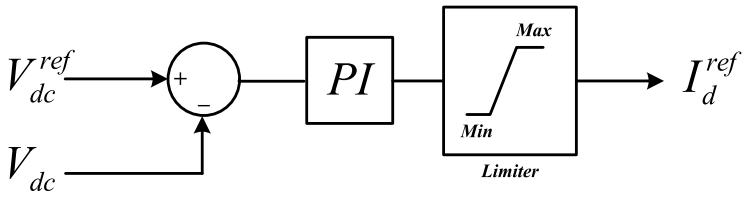

Fig-3.8 The First-stage DC Voltage Controller for Grid-side VSC

The q-axis current reference I_{gq}^{ref} is usually predefined as zero. In this way, the grid-side VSC controller can be used to control the DC voltage of DC link to maintain it at the normal level for AC/DC power transformation during normal operation and disturbances.

3.4 Modelling of WT-PMSG Systems

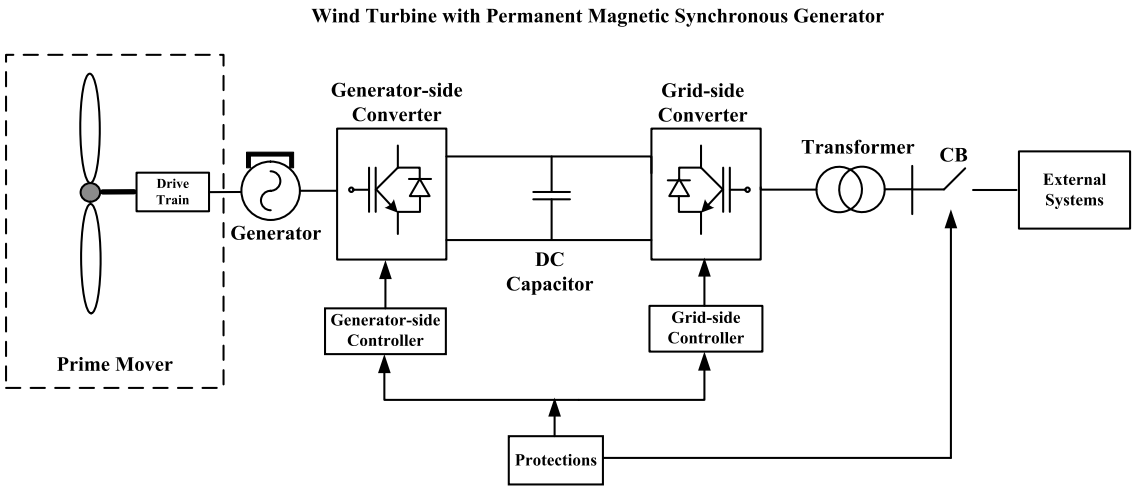

Fig-3.9 The Configuration of WT-PMSG System

The typical configuration of the WT-PMSG system is shown in Fig-3.9 [47, 57]. For the prime mover, the multi-pole generator is directly driven by the shafts without the gearbox. And the wind turbine and blade pitch-angle controller are similar to those in the WT-DFIG system. For the electrical components, the three-phase stator winding of the generator is indirectly connected to the external power system by the full-scale back-to-back VSC-based power converter between them. The so-called generator-side converter is connected with the stator of the PMSG and the grid-side converter is connected with the external power system. A DC capacitor connected to both DC sides of the two converters acts as the DC voltage resource for AC/DC power transformation.

3.4.1 Modelling of Drive-Train

The drive train is usually represented by the one-mass model for the combination of shafts of wind turbine and generator. The differential equation of the one-mass model is given by [57]:

$$2(H_t + H_g)\frac{d\omega_t}{dt} = T_m - T_g \tag{3.22}$$

$$\begin{cases} T_m = \dfrac{P_m}{\omega_t} \\ T_g = \dfrac{P_s}{\omega_g} \\ \omega_t = \dfrac{\omega_g}{p} \end{cases} \tag{3.23}$$

where P_m is the mechanical power of wind turbine; P_s is the active power of generator's stator; H_t is the inertia constant of wind turbine; H_g is the inertia constant of generator; ω_t is the rotational angular speed of generator; ω_t is the rotational angular speed of wind turbine and ω_g is the rotational angular speed of generator; T_m is the mechanical torque of wind turbine; T_g is the electromagnetic torque of generator; p is the pole-number of generator.

3.4.2 Modelling of PMSG

The 2nd-order dynamic models of the PMSG are given by [47, 57]:

$$\begin{cases} V_{sd} = R_s I_{sd} + L_s \dfrac{dI_{sd}}{dt} - \omega_p L_s I_{sq} \\ V_{sq} = R_s I_{sq} + L_s \dfrac{dI_{sq}}{dt} + \omega_p L_s I_{sd} + \omega_p \psi \end{cases} \tag{3.24}$$

where V_{sd} is the d-axis voltage on the stator-side of PMSG; V_{sq} is the q-axis voltage on the stator-side of PMSG; I_{sd} is the d-axis current on the stator-side of PMSG; I_{sq} is the q-axis current on the stator-side of PMSG; R_s is the resistance on the stator-side of PMSG; L_s is the self-inductance on the stator-side of PMSG, ψ is the constant flux linkage of PMSG. The modelling in detail is described in Appendix B.

3.4.3 Model of DC Link

$$\frac{dV_{dc}}{dt} = \frac{1}{C_{dc}V_{dc}}(V_{sd}I_{sd} + V_{sq}I_{sq} - V_{gd}I_{gd} - V_{gq}I_{gq}) \tag{3.25}$$

With some principles described in Section 3.2.4, the dynamic model of the DC link inserted into the two converters is given in (3.25). Where V_{gd} is the *d*-axis voltage of grid-side converter; V_{gq} is the *q*-axis voltage of grid-side converter; I_{gd} is the *d*-axis current of grid-side converter; I_{gq} is the *q*-axis current of grid-side converter; V_{dc} is the DC voltage of the DC capacitor; I_{dc} is the DC current of the DC capacitor; C_{dc} is DC the capacitance of DC capacitor.

3.5 Control Strategies for the WT-PMSG Systems

3.5.1 The Generator-side VSC Controller

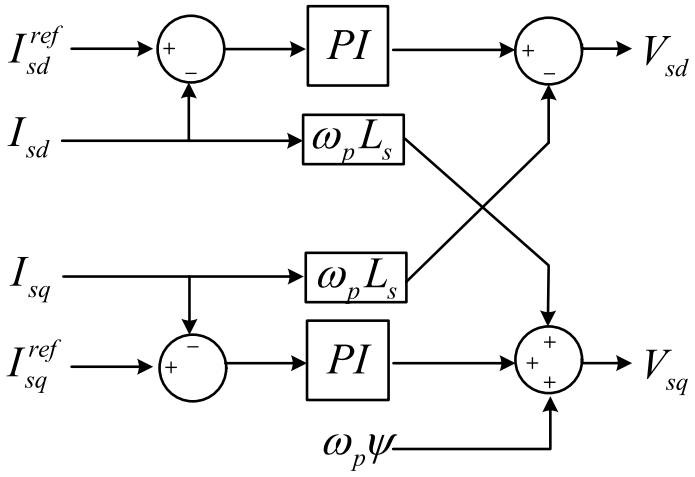

Fig-3.10 The Second-stage Current Controller for Generator-side Converter

As described in Section 3.4.2 and Appendix B, the dynamic models of PMSG are expressed in (3.24). And $L_s \frac{dI_{sd}}{dt}$ and $L_s \frac{dI_{sq}}{dt}$ are replaced from V_{sd}^* and V_{sq}^* using the PI controllers expressed by (3.26):

$$\begin{cases} V_{sd}^* = L_s \dfrac{dI_{sd}}{dt} = K_{sd}(I_{sd}^{ref} - I_{sd}) + K_{isd}\int (I_{sd}^{ref} - I_{sd})dt \\ V_{sq}^* = L_s \dfrac{dI_{sq}}{dt} = K_{sq}(I_{sq}^{ref} - I_{sq}) + K_{isq}\int (I_{sq}^{ref} - I_{sq})dt \end{cases} \tag{3.26}$$

where K_{sd} and K_{isd} are the proportional and integral gains of *d*-axis PI controller; K_{sq} and K_{isq} are the proportional and integral gains of *q*-axis PI controller. Based on (3.24) and (3.26), the decoupled current controller is shown in Fig-3.10.

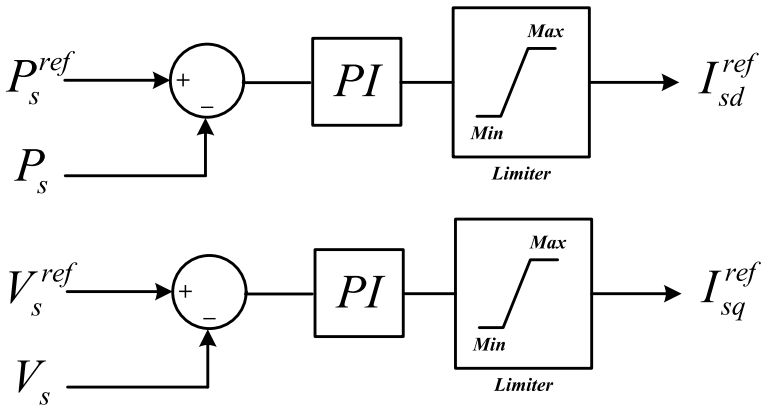

Fig-3.11 The First-stage Controller for Generator-side Converter

For the generator-side VSC controller, similar to those for WT-DFIG system, two-stage PI controllers are commonly used. For the first-stage controller illustrated in Fig-3.11, the output active power of the PMSG P_s is set as the control target to be supervised and controlled in *d*-axis and the derivation of P_s and its reference P_s^{ref} is sent to the PI regulator for being specified as the reference values I_{sd}^{ref} for the second-stage *d-axis* current controller. In the *q*-axis, the PMSG AC voltage V_s is set as the control target to maintain it stable for system operation, the derivation of V_s and its reference V_s^{ref} is sent to the PI regulator for being specified as the reference values I_{sq}^{ref} for the second-stage *q-axis* current controller.

$$\begin{cases} I_{sd}^{ref} = K_P(P_r^{ref} - P_r) + K_{iP}\int (P_r^{ref} - P_r)dt \\ I_{sq}^{ref} = K_s(V_s^{ref} - V_s) + K_{is}\int (V_s^{ref} - V_s)dt \end{cases} \tag{3.27}$$

where K_P and K_{iP} are the proportional and integral gains of *d*-axis PI controller; K_s and K_{is} are the proportional and integral gains of *q*-axis PI controller.

3.5.2 The Grid-side VSC Controller

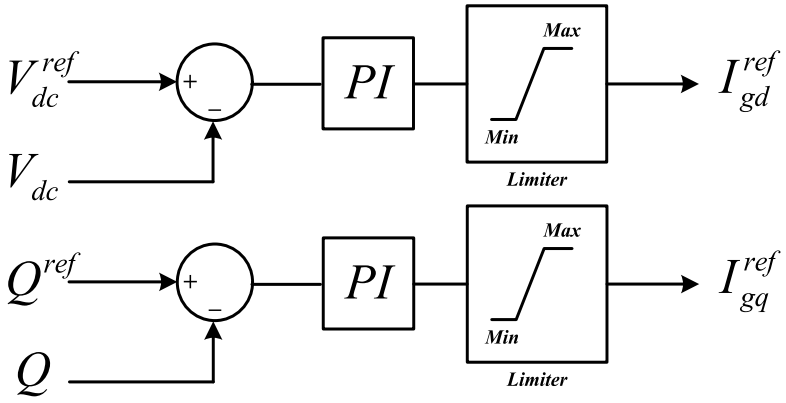

Fig-3.12 The First-stage Controller for Grid-side Converter

The grid-side converter for WT-PMSG system is identical to that for WT-DFIG system described in Section 3.3.2 and Appendix A. So the second-stage current controller is as same as that for WT-DFIG system in Fig-3.7. However, for the first-stage VSC controller of WT-PMSG system shown in Fig-3.12, the *d*-axis first-stage controller is supervising the voltage of DC link V_{dc} and regulating it to its reference value V_{dc}^{ref} for keeping the balance of AC/DC power transformation between the generator- and grid-converters. The *q*-axis first-stage controller is supervising and controlling the reactive power Q_g and regulating it to its reference value Q_g^{ref} for maintain the AC voltage level at the PCC. Their deviations are sent to the two PI controllers respectively for being specified as the reference values I_{gd}^{ref} and I_{gq}^{ref} which are expressed by:

$$\begin{cases} I_{gd}^{ref} = K_{dc}(V_{dc}^{ref} - V_{dc}) + K_{idc}\int (V_{dc}^{ref} - V_{dc})dt \\ I_{gq}^{ref} = K_{Q}(Q_{g}^{ref} - Q_{g}) + K_{iQ}\int (Q_{g}^{ref} - Q_{g})dt \end{cases} \tag{3.28}$$

where K_{dc} and K_{idc} are the proportional and integral gains of *d*-axis PI controller; K_Q and K_{iQ} are the proportional and integral gains of *q*-axis PI controller.

3.6 Dynamic Aggregated Modelling for Offshore Wind Farms

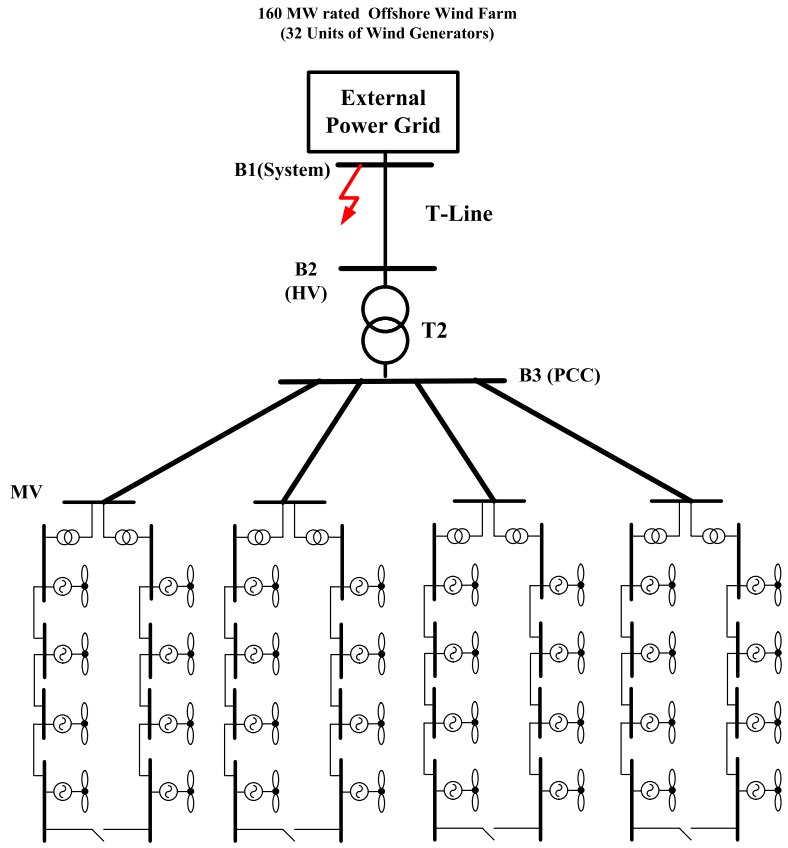

Fig-3.13 The Layout of an Offshore Wind Farm Interconnected with External power system

In general, there are two main objectives for the dynamic aggregated modelling method: 1) The computational efforts for the simplified system models can be obviously reduced compared with models in detail; 2) The simulation accuracy of the simplified models can be obtained at the acceptable levels which the key characteristics of the systems can be kept for steady- and transient-state analysis.

For a large offshore wind farm shown in Fig-3.13 , it usually consists of a large amount of wind turbines which are represented by a set of dynamic models and the passive network including the collector cables, step-up transformers. If the dynamic characteristics of some wind turbines are similar, they can be selected in a group called coherency group [24] and be represented by an equivalent machine to reduce the computational efforts. For the equivalent

machine, the passive network connected to the wind turbines in the coherency group should be reduced as equivalent impedance which is connected to the equivalent machine to keep the output power flow at the PCC equal to that for original system in detail. Furthermore, a set of aggregated parameters should be specified for the equivalent machine to keep the key dynamic characteristics of the original system in detail. With these principles for achieving the objectives above, the dynamic aggregated modelling method can be divided into three steps as follows [24]:

1) Identification of coherency groups
2) Network reduction
3) Parameters aggregation

3.6.1 Assumptions and Simplifications

Considering the typical characteristics of offshore wind farms, some assumptions and simplifications are considered as follows:

1) The wind turbines connected in the same chain are configured with identical system parameters;
2) The time range of the transient processes of wind turbines is very short in the transient stability analysis. So during of transient stability analysis, the wind speed is consumed to be constant in a wind farm for all the wind turbines at the same normal operating points during the whole process of the simulation.
3) In the simulation, the disturbances are incurred outside the wind farm.
4) The protection systems for each wind turbine in the wind farms are not considered during the disturbances.

3.6.2 Identification of Coherency groups

During the large disturbances in the power system such as the short-circuit faults, some generators in the same areas can reflect some dynamic responses similar to each other. In this

way, those generators are selected into a group which is usually acted as the coherency group and these generators are represented using an aggregated equivalent single-machine to not only reflect their common dynamic responses but also simplify the power systems for transient stability analysis.

The methods for coherency group identification of the synchronous generators for transient stability analysis have been described in [24, 80, 81]. For these methods, the rotor-angle swing responses of the generators can be chosen as the key characteristic to act as the criterion for coherency group identification which is given by [24, 80, 81]:

$$\underset{t\in[0,T]}{Max}\left|\Delta\delta_i(t)-\Delta\delta_j(t)\right|\le\varepsilon \tag{3.29}$$

For the criterion that, if the relative rotor angle deviations of two generators are not greater than a specified threshold value at any time during the simulation time $t\in[0,T]$, the two generators can be selected into a coherency group. The simulation time duration T=3~5s and ε=5°~10°.

Furthermore the relationship between the deviations of rotor angle δ and rotational angular speed ω_r is given:

$$\frac{d\delta}{dt}=\omega_r-1 \tag{3.30}$$

From (3.30), the coherency groups also can be identified from the wind turbines' rotor angular speed characteristics. As shown in Fig-3.13, four units of wind turbines are connected to the same row in the offshore wind farm. From their rotor angular speed swing curves shown in Fig-3.14, the same rotor angular speed swing responses are reflected from the wind turbines during a short-circuit fault. So they can be selected into a coherency group and can be further divided into more coherency groups for higher simulation accuracy.

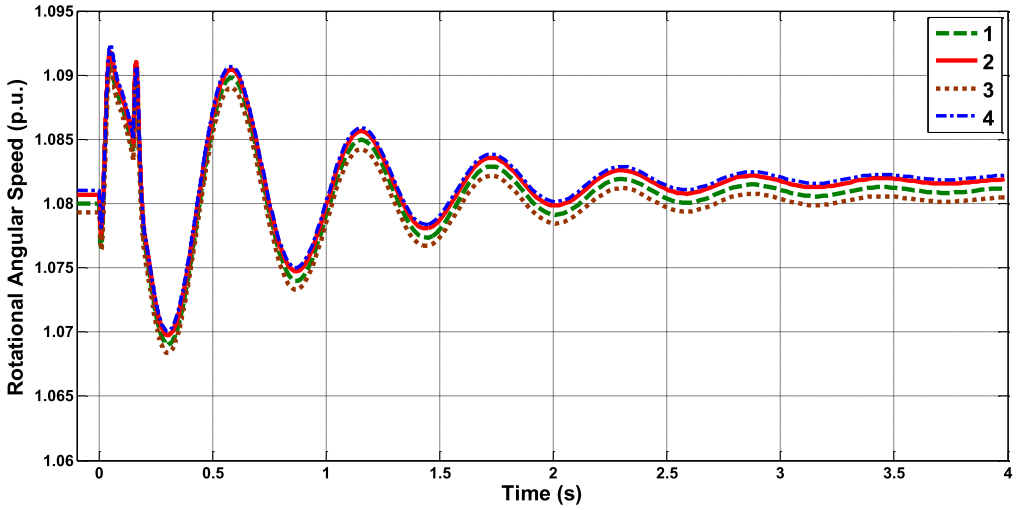

Fig-3.14 The Rotational Angular Speed from Wind turbines in the Same Chain

3.6.3 Network Reduction

When a set of generators are selected into a coherency group, the buses, transformers and transmission lines connected to them are aggregated into the equivalent bus and impedance. Compared with the layout of conventional large-scale power systems, the topology of the typical offshore wind farms shown is much simpler with radiant network structure shown in Fig-3.15 [142]. In this way, the network reduction method can refer to the methods in [143].

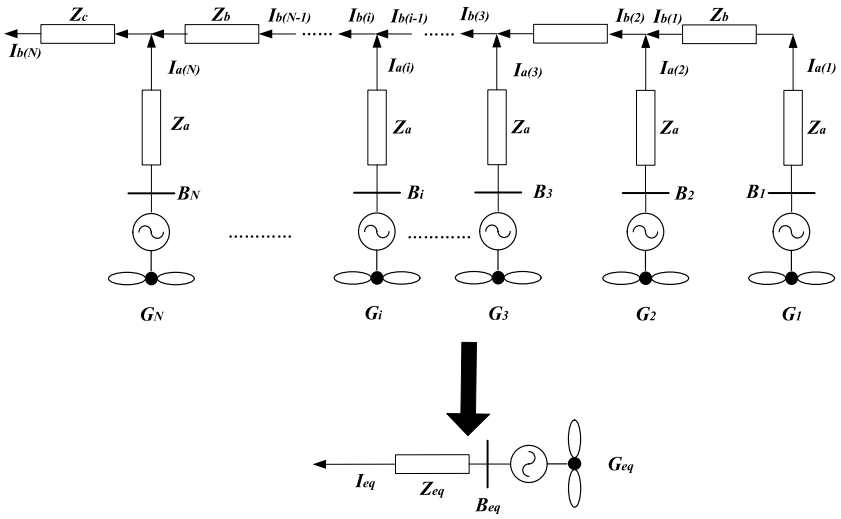

Fig-3.15 The Network Reduction of One Chain in the Offshore Wind Farm

$$Z_{eq} = \frac{\Delta S_a + \Delta S_b + \Delta S_c}{N^2 \times I^2} = \frac{NZ_a + \sum_1^{N-1} i^2 Z_b + N^2 Z_c}{N^2} \tag{3.31}$$

where Z_{eq} is the equivalent impedance; Z_a is the impedance for each branch of the wind turbine, Z_b.is the impedance of each transmission cable between two wind turbines; Z_c is the impedance of transmission cable connected to the external power systems; N is the total number of machine units in a coherency group and $i \in [1, N]$.

3.6.4 Parameter Aggregation of WT-DFIG Systems

3.6.4.1 Parameter Aggregation of the Shaft Models

There are ***N*** units of WT-DFIGs in a coherency group and the shaft models of the ***i***th machine are given [43, 136]:

$$\begin{cases} 2H_{t(i)} \dfrac{d\omega_{t(i)}}{dt} = T_{m(i)} - T_{sh(i)} \\ 2H_{g(i)} \dfrac{d\omega_{r(i)}}{dt} = T_{sh(i)} - T_{em(i)} \\ \dfrac{d\theta_{tw(i)}}{dt} = \omega_{t(i)} - \omega_{r(i)} \\ T_{sh(i)} = K_{sh(i)} \times \theta_{tw(i)} + D_{sh(i)} \times \dfrac{d\theta_{tw(i)}}{dt} \end{cases} \tag{3.32}$$

where all the parameters are transformed to per unit values based on their own rated apparent power. Both sides of the equations are multiplied by the ratio of $\boldsymbol{S_i}$ and $\boldsymbol{S_G}$:

$$\begin{cases} \dfrac{S_i}{S_G} \times 2H_{t(i)} \dfrac{d\omega_{t(i)}}{dt} = \dfrac{S_i}{S_G} \times (T_{m(i)} - T_{sh(i)}) \\ \dfrac{S_i}{S_G} \times 2H_{g(i)} \dfrac{d\omega_{r(i)}}{dt} = \dfrac{S_i}{S_G} \times (T_{sh(i)} - T_{em(i)}) \\ \dfrac{S_i}{S_G} \times \dfrac{d\theta_{tw(i)}}{dt} = \dfrac{S_i}{S_G} \times (\omega_{t(i)} - \omega_{r(i)}) \\ \dfrac{S_i}{S_G} \times T_{sh(i)} = \dfrac{S_i}{S_G} \times (K_{sh(i)} \times \theta_{tw(i)} + D_{sh(i)} \times \dfrac{d\theta_{tw(i)}}{dt}) \end{cases} \tag{3.33}$$

And the sum of the model equations of ***N*** units of machines is given:

$$\begin{cases} \sum_{\forall i \in G} \frac{S_i}{S_G} \times 2H_{t(i)} \frac{d\omega_{t(i)}}{dt} = \sum_{\forall i \in G} \frac{S_i}{S_G} \times (T_{m(i)} - T_{sh(i)}) \\ \sum_{\forall i \in G} \frac{S_i}{S_G} \times 2H_{g(i)} \frac{d\omega_{r(i)}}{dt} = \sum_{\forall i \in G} \frac{S_i}{S_G} \times (T_{sh(i)} - T_{em(i)}) \\ \sum_{\forall i \in G} \frac{S_i}{S_G} \times \frac{d\theta_{tw(i)}}{dt} = \sum_{\forall i \in G} \frac{S_i}{S_G} \times (\omega_{t(i)} - \omega_{r(i)}) \\ \sum_{\forall i \in G} \frac{S_i}{S_G} \times T_{sh(i)} = \sum_{\forall i \in G} \frac{S_i}{S_G} \times (K_{sh(i)} \times \theta_{tw(i)} + D_{sh(i)} \times \frac{d\theta_{tw(i)}}{dt}) \end{cases} \tag{3.34}$$

Considering all the WT-DFIGs in the coherency group have the similar dynamic characteristics, so it assumes:

$$\omega_{r(1)} = \cdots = \omega_{r(i)} \cdots = \omega_{r(N)} = \omega_r \tag{3.35}$$

$$\omega_{t(1)} = \cdots = \omega_{t(i)} \cdots = \omega_{t(N)} = \omega_t \tag{3.36}$$

In this way, the equivalent equations of the aggregated shaft models are given:

$$\begin{cases} 2H_{t\_G} \frac{d\omega_t}{dt} = T_{m\_G} - T_{sh\_G} \\ 2H_{g\_G} \frac{d\omega_r}{dt} = T_{sh\_G} - T_{em\_G} \\ \frac{d\theta_{tw}}{dt} = \omega_t - \omega_r \\ T_{sh\_G} = K_{sh\_G} \times \theta_{tw} + D_{sh\_G} \times \frac{d\theta_{tw}}{dt} \end{cases} \tag{3.37}$$

where H_{t_G} and H_{g_G} are the aggregated inertia constant respectively; K_{sh_G} is the aggregated shaft stiffness coefficient; D_{sh_G} is the aggregated damping coefficient; T_{sh_G} is the aggregated shaft torque; T_{m_G} is the aggregated mechanical torque of equivalent wind turbine; T_{em_G} is the electromagnetic torque of equivalent generator. Each aggregated parameter is the weighted average value of the corresponding parameters of N units of WT-DFIGs in the coherency group G ($G \in [0, N]$). And the derivations of these aggregated parameters for the WT-DFIG's shaft models are given:

$$H_{t\_G} = \frac{\sum_{\forall i \in G} S_i \times H_{t(i)}}{S_G} \tag{3.38}$$

$$H_{g\_G} = \frac{\sum_{\forall i \in G} S_i \times H_{g(i)}}{S_G} \tag{3.39}$$

$$K_{sh\_G} = \frac{\sum_{\forall i \in G} S_i \times K_{sh(i)}}{S_G} \tag{3.40}$$

$$D_{sh\_G} = \frac{\sum_{\forall i \in G} S_i \times D_{sh(i)}}{S_G} \tag{3.41}$$

where all the aggregated parameters are transformed to per unit values based on apparent power of the aggregated machine $\boldsymbol{S_G}$.

3.6.4.2 Parameter Aggregation of DFIG

With the similar principles, the aggregated parameters for the equivalent generator equal to the weighted average value of the corresponding parameters of *N* units of WT-DFIGs in the coherency group *G*.

$$L_{s\_G} = \frac{\sum_{\forall i \in G} S_i \times L_{ss(i)}}{S_G} \tag{3.42}$$

$$L_{r\_G} = \frac{\sum_{\forall i \in G} S_i \times L_{rr(i)}}{S_G} \tag{3.43}$$

$$L_{m\_G} = \frac{\sum_{\forall i \in G} S_i \times L_{m(i)}}{S_G} \tag{3.44}$$

$$R_{s\_G} = \frac{\sum_{\forall i \in G} S_i \times R_{s(i)}}{S_G} \tag{3.45}$$

$$X'_{s\_G} = \frac{\sum_{\forall i \in G} S_i \times X'_{s(i)}}{S_G} \tag{3.46}$$

$$T'_{0\_G} = \frac{\sum_{\forall i \in G} S_i \times T'_{0(i)}}{S_G} \tag{3.47}$$

where L_{s_G} is the aggregated stator self-inductance; L_{r_G} is the aggregated rotor self-inductance; L_{m_G} is the aggregated mutual inductance; R_{s_G} is the aggregated resistance of the stator; X'_{s_G} is the aggregated stator transient reactance; T'_{0_G} is the aggregated rotor circuit time constant.

3.6.4.3 Parameter Aggregation of DC Link

The aggregated parameters for the equivalent DC link are given with similar principles:

$$C_{dc\_G} = \frac{\sum_{\forall i \in G} S_i \times C_{dc(i)}}{S_G} \tag{3.48}$$

where $\boldsymbol{C_{dc\_G}}$ is the aggregated DC capacitance.

3.6.4.4 Parameter Aggregation of Control System

A set of aggregated parameters for the equivalent control systems are given with similar aggregation principles:

$$C_G = \frac{\sum_{\forall i \in G} S_i \times C_i}{S_G} \tag{3.49}$$

where C_G is the set of aggregated parameters for controllers in the WT-DFIG systems.

3.6.5 Parameter Aggregation of WT-PMSG Systems

3.6.5.1 Parameter Aggregation of the Shaft Model of WT-PMSG Systems

There are N units of WT-PMSGs in a coherency group and the shaft models of the ith machine are given:

$$2(H_{t(i)} + H_{g(i)}) \frac{d\omega_{t(i)}}{dt} = T_{m(i)} - T_{em(i)} \tag{3.50}$$

The aggregated shaft model is given by:

$$2(H_{t\_G} + H_{g\_G}) \frac{d\omega_t}{dt} = T_{m\_G} - T_{em\_G} \tag{3.51}$$

$$H_{t\_G} = \frac{\sum_{\forall i \in G} S_i \times H_{t(i)}}{S_G} \tag{3.52}$$

$$H_{g\_G} = \frac{\sum_{\forall i \in G} S_i \times H_{g(i)}}{S_G} \tag{3.53}$$

where H_{t_G} and H_{g_G} are the aggregated inertia constant respectively for the WT-PMSGs.

3.6.5.2 Parameter Aggregation of PMSGs

The aggregated parameters for the equivalent generator equal the weighted average value of the corresponding parameters of ***N*** units of WT-PMSGs in the coherency group ***G***.

$$R_{s\_G} = \frac{\sum_{\forall i \in G} S_i \times R_{s(i)}}{S_G} \tag{3.54}$$

$$L_{s\_G} = \frac{\sum_{\forall i \in G} S_i \times L_{s(i)}}{S_G} \tag{3.55}$$

where L_{s_G} is the aggregated stator self-inductance; R_{s_G} is the aggregated stator resistance.

3.6.5.3 Parameter Aggregation of DC Link and Control System

The aggregated parameters for the DC link and control system are derived with the same principles described in Section 3.6.4.3 and 3.6.4.4.

3.7 Case Studies for WT-DFIG based Offshore Wind Farms

3.7.1 Simulation Systems

In the simulation cases, an offshore wind farm consisting of 32 units of 5 MW rated WT-DFIG systems are interconnected with the Single-Machine Infinite Bus (SMIB). The layout of the wind farm is illustrated in Fig-3.13, each four units of machines are connected line by line in a chain and the power of all the machines in these eight rows is collected at the collector bus and then the power is sent to the external system via the step-up transformer and a 150 km transmission line, a three-phase short-circuit fault was incurred in 0+ s at Bus ***B1*** and after 150 ms the fault was removed based on the time suggested by Grid Code. The offshore wind farm systems with point-to-point connections are usually weak systems

without any interconnections with other power systems. So the SCRs of the offshore wind farms are usually less than 2 and they are highly sensitive to the grounded resistances of the faults. In order to avoid final instability, the ground resistance was set as 15 ohm. The simulation time was 4 s. All the simulation cases were carried out with DIgSILENT/PowerFactory and the details are described in Appendix E.

3.7.2 Case 1: Sixteen Equivalent Machines

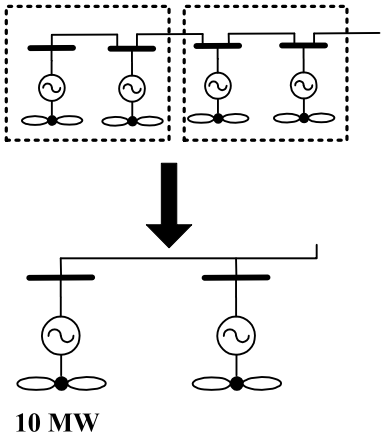

Fig-3.16 A Coherency Group Including Two WT-DFIGs

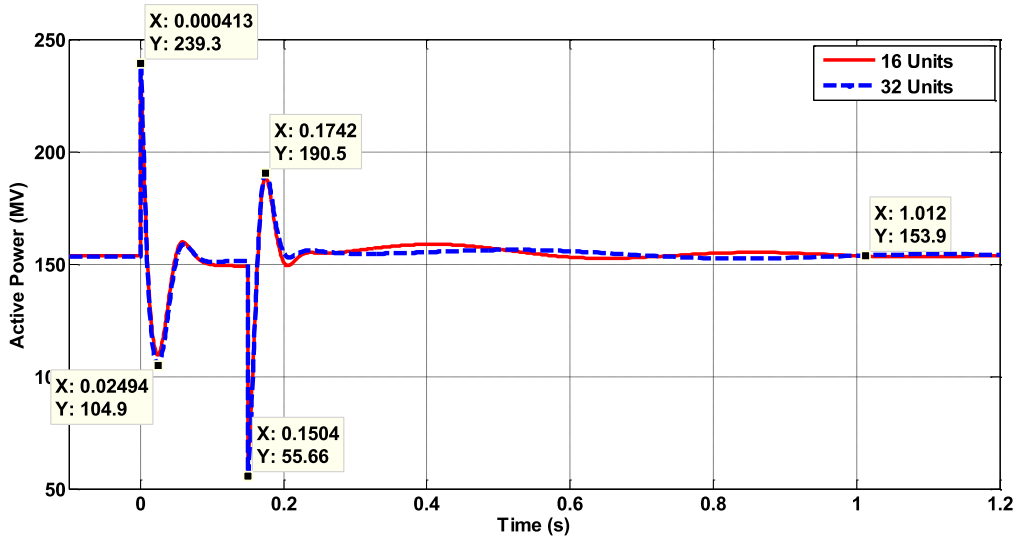

Fig-3.17 The Output Active Power for Detailed and Sixteen Equivalent Machines Models

In **Case 1**, each two machines in a chain were selected into a coherency group shown in Fig-3.16 and this system was divided into sixteen coherency groups. In this way, this system can be simplified using sixteen units of aggregated machine. The simulation results including the

output power and terminal AC voltage at the PCC compared with those with detailed models are illustrated from Fig-3.17 to Fig-3.19.

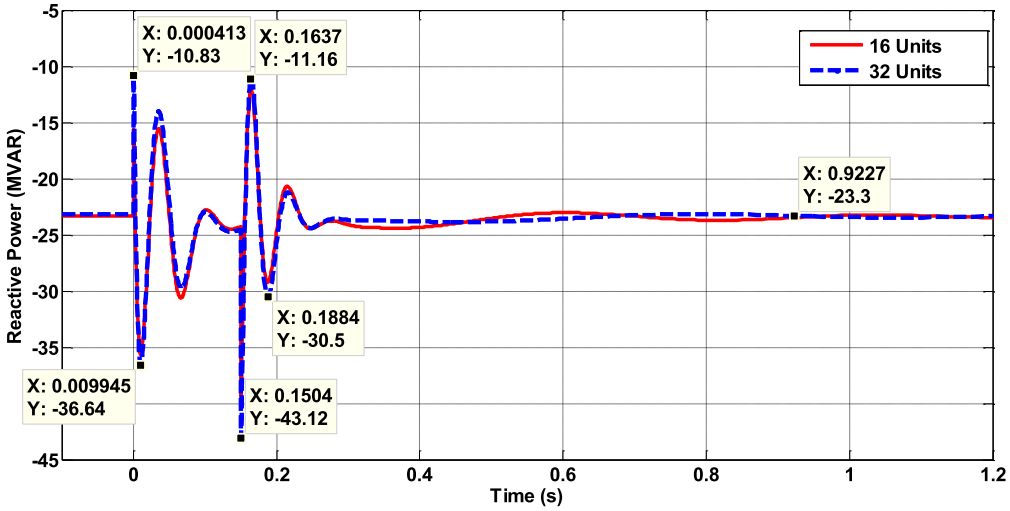

Fig-3.18 The Output Reactive Power for Detailed and Sixteen Equivalent Machines Models

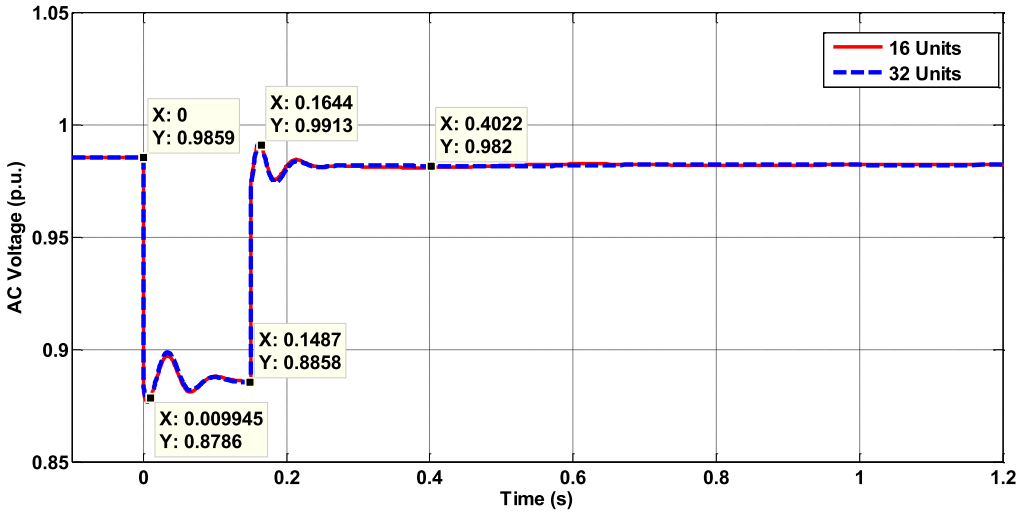

Fig-3.19 The AC Voltage at PCC for Detailed and Sixteen Equivalent Machines Models

3.7.3 Case 2: Eight Equivalent Machines

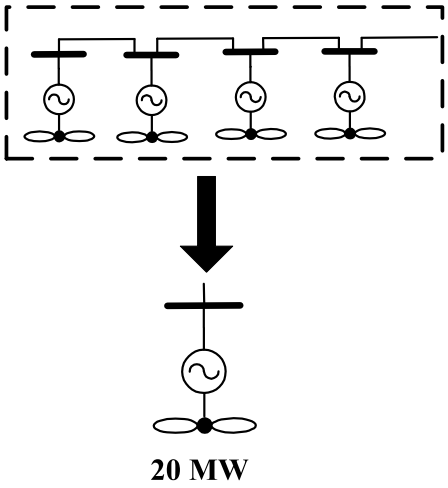

Fig-3.20 A Coherency Group Including Four WT-DFIGs

In **Case 2**, each four machines in a chain were selected into a coherency group shown in Fig-3.20 and this system was divided into eight coherency groups. Then each coherency group was represented using an aggregated machine. So this system can be simplified using eight units of aggregated machine. The simulation results including the output power and AC voltage at the PCC compared with those with detailed models are illustrated from Fig-3.21 to Fig-3.23.

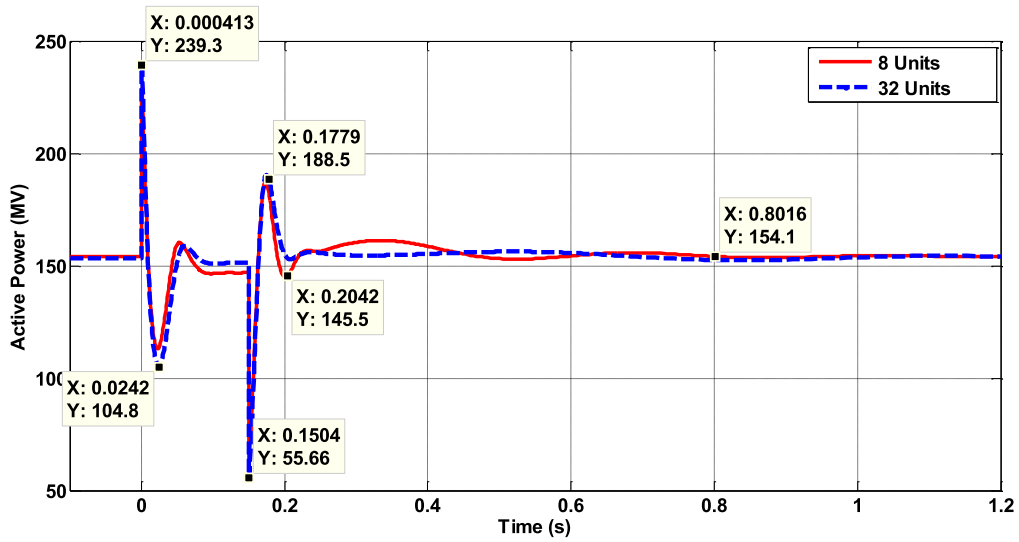

Fig-3.21 The Output Active Power for Detailed and Eight Equivalent Machines Models

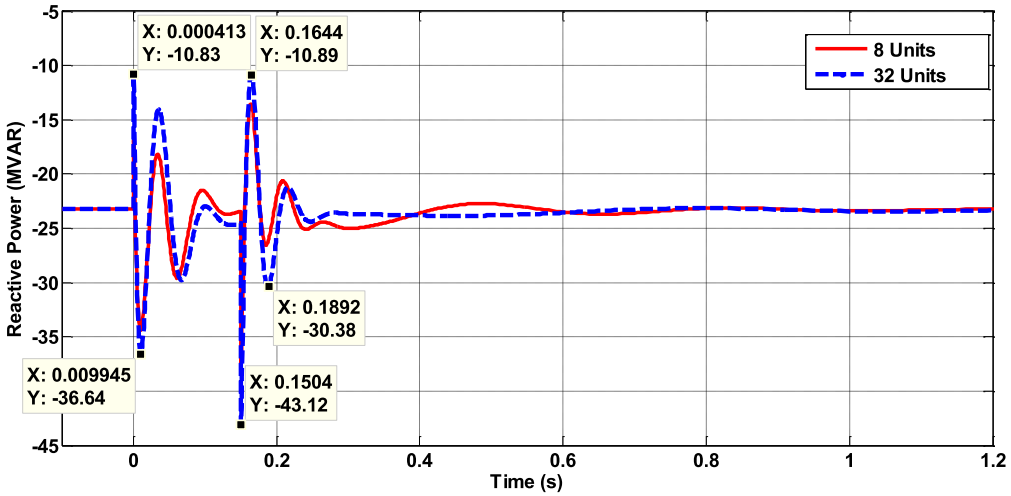

Fig-3.22 The Output Reactive Power for Detailed and Eight Equivalent Machines Models

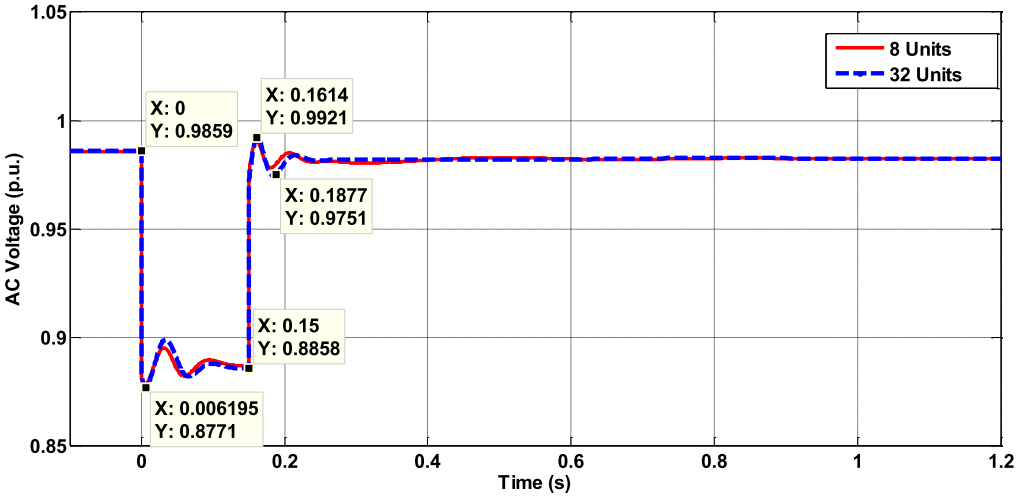

Fig-3.23 The AC Voltage at PCC for Detailed and Eight Equivalent Machines Models

3.7.4 Case 3: Four Equivalent Machines

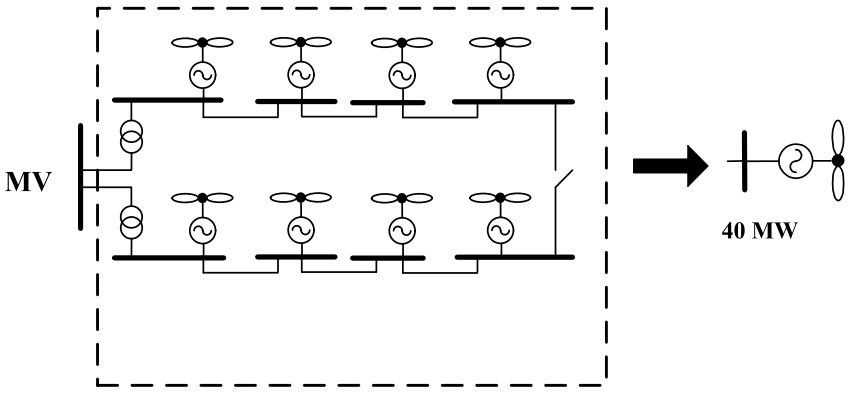

Fig-3.24 A Coherency Group Including Eight WT-DFIGs

In **Case 3**, each eight machines in the neighbouring two chains were selected into a group shown in Fig-3.24 and the system was represented using four units of aggregated machines. The simulation results are shown from Fig-3.25 to Fig-3.27.

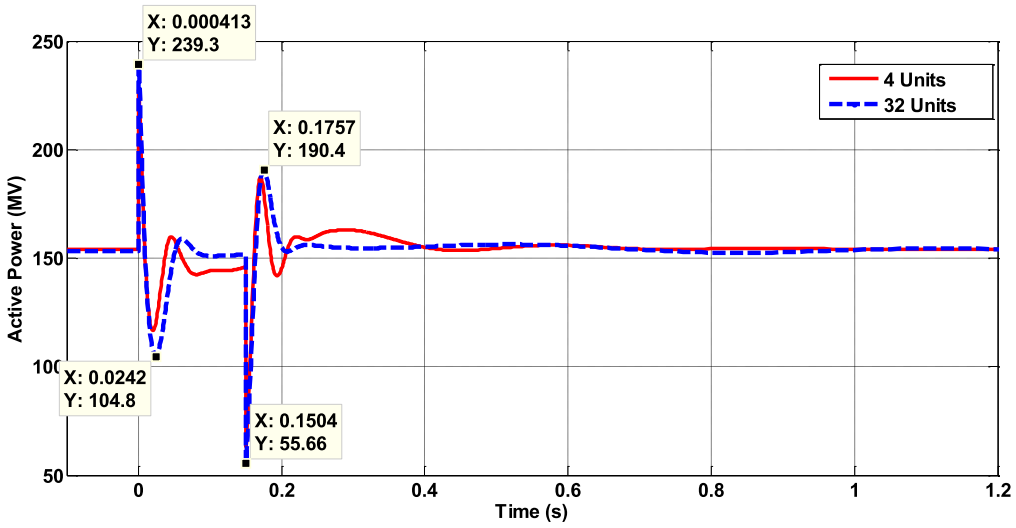

Fig-3.25 The Output Active Power for Detailed and Four Equivalent Machines Models

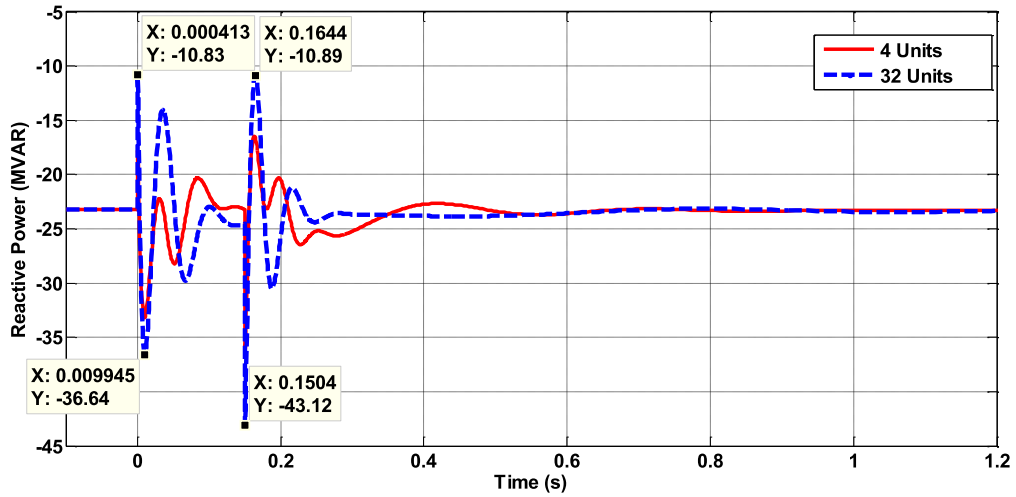

Fig-3.26 The Output Reactive Power for Detailed and Four Equivalent Machines Models

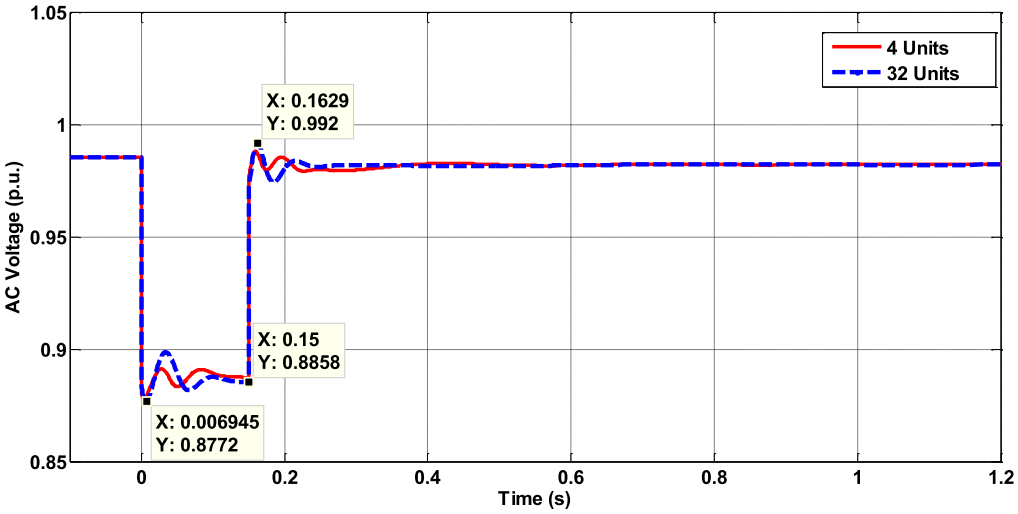

Fig-3.27 The AC Voltage at PCC for Detailed and Four Equivalent Machines Models

3.7.5 Case 4: Two Equivalent Machines

In **Case 4**, each sixteen machines in the neighbouring four chains were selected into a group and the system was represented using two units of aggregated machines shown in Fig-3.28. The simulation results are shown from Fig-3.29 to Fig-3.31.

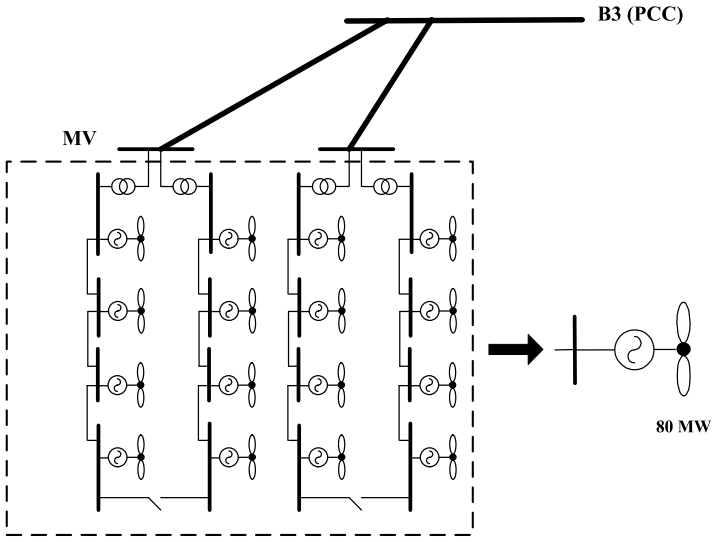

Fig-3.28 A Coherency Group Including Sixteen WT-DFIGs

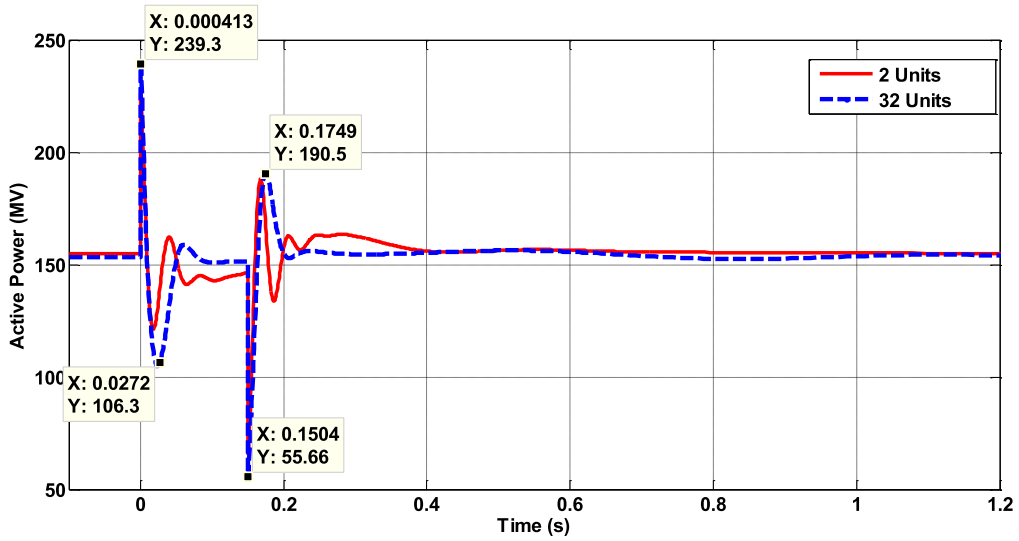

Fig-3.29 The Output Active Power for Detailed and Two Equivalent Machines Models

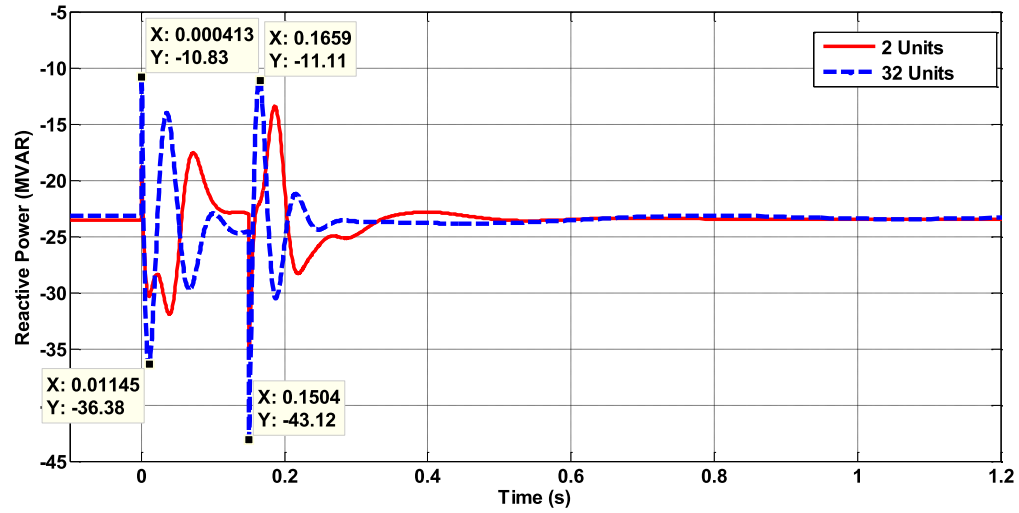

Fig-3.30 The Output Reactive Power for Detailed and Two Equivalent Machines Models

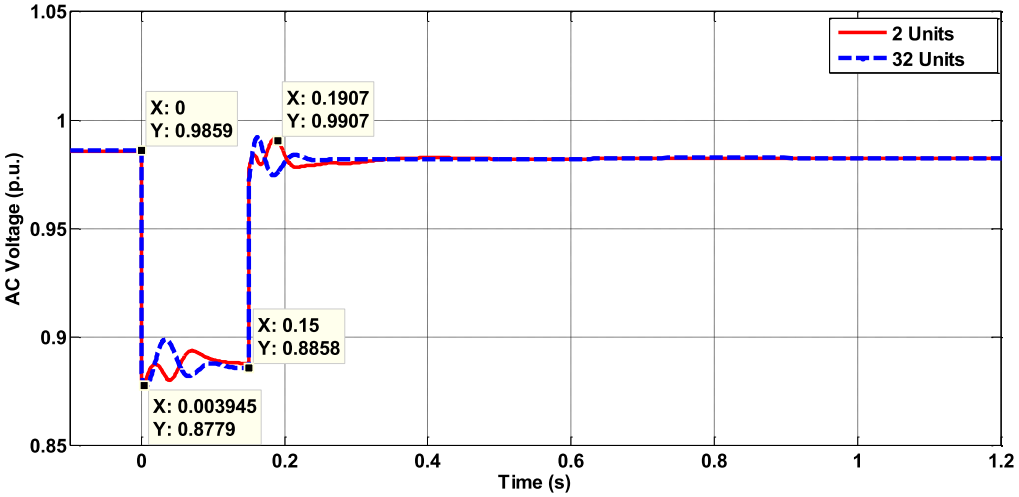

Fig-3.31 The AC Voltage at PCC for Detailed and Two Equivalent Machines Models

3.7.6 Case 5: Single Equivalent Machine

In **Case 5**, all the machines in the wind farm were aggregated into single aggregated machine and the simulation results are shown from Fig-3.32 to Fig-3.34.

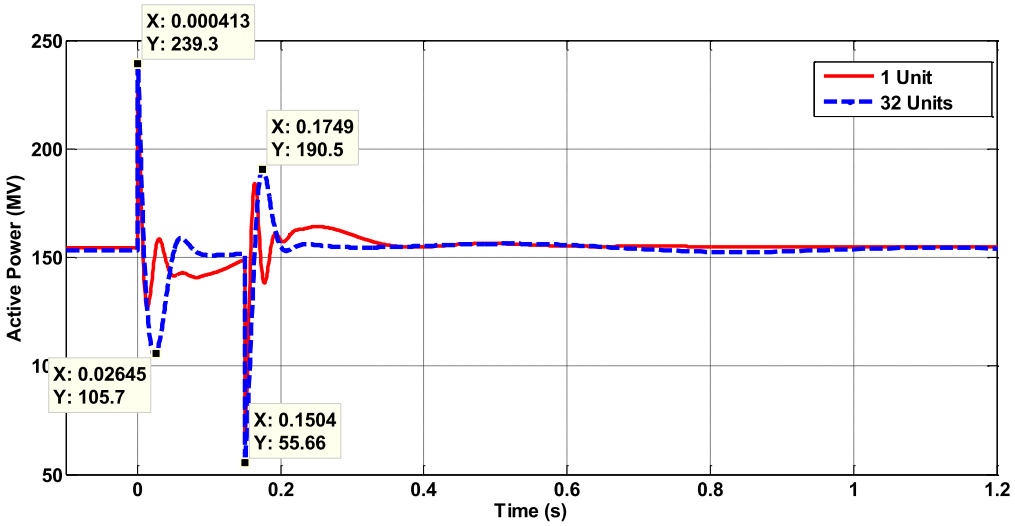

Fig-3.32 The Output Active Power for Detailed and One Equivalent Machine Models

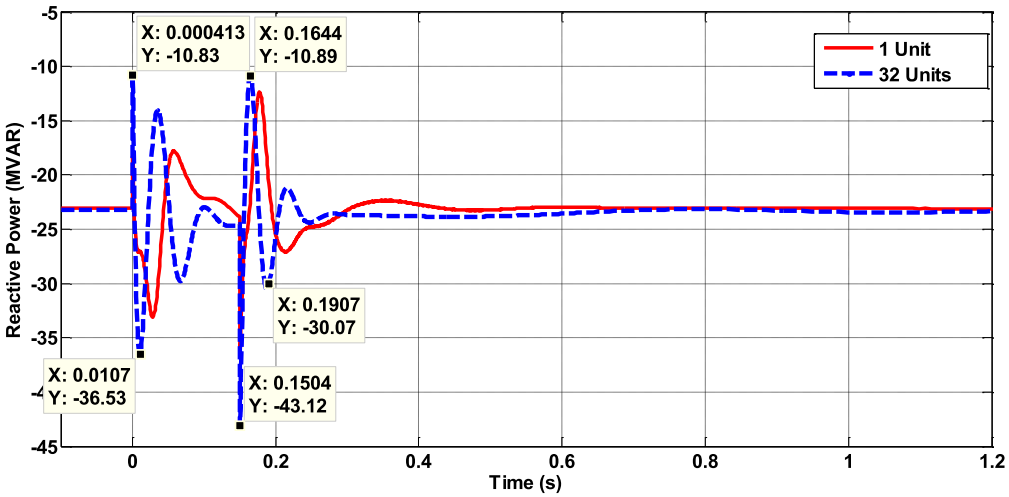

Fig-3.33 The Output Reactive Power for Detailed and One Equivalent Machine Models

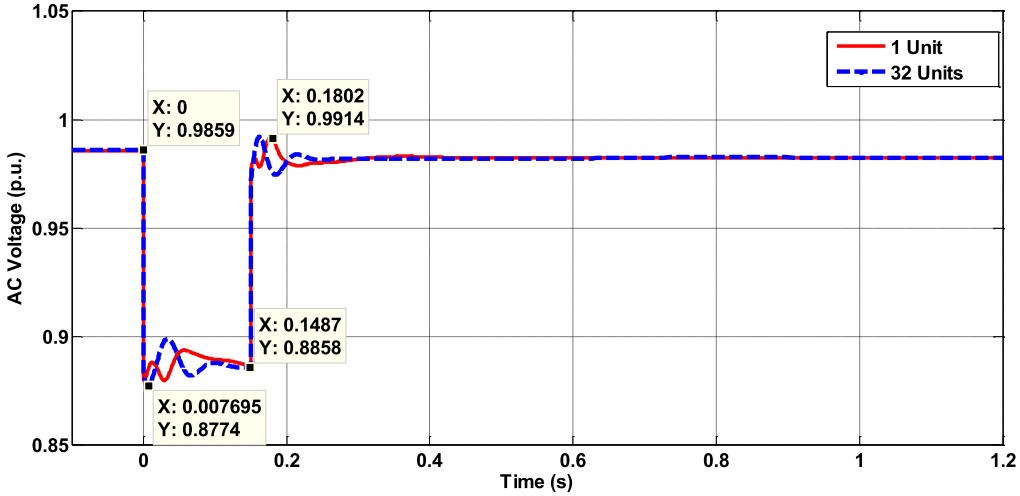

Fig-3.34 Terminal Voltage at PCC for Detailed and One Equivalent Machine Models

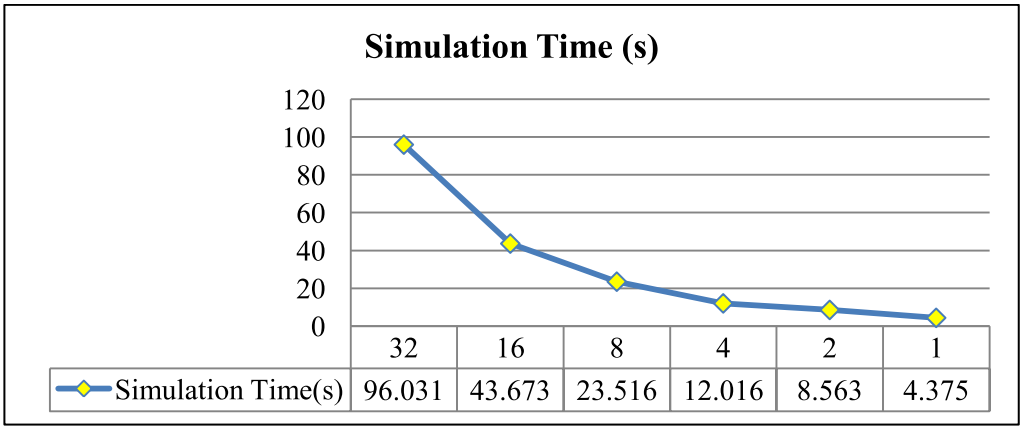

Fig-3.35 The Simulation Time versus Group Number in SMIB System

From the simulation results for the models in detail shown in Fig-3.17 to Fig-3.19, The AC voltage at PCC suddenly dropped from 0.9859 p.u. to 0.8786 p.u. at 0+ s in Fig-3.19. Through the strength of voltage dip is not so big, it brought obvious impacts on the output power at PCC. At same time, the active power suddenly increased from 153.9 MW to 239.3 MW by 55.49% in Fig-3.17 and the reactive power suddenly increased from -23.3 MVar to -10.83 MVar by 53.51% in Fig-3.18. Due to the control of power converters in the WT-DFIG systems, the active power was suppressed from 239.3 MW to 104.9 MW at 0.0249 s and returned to stable condition after the first-swing. The reactive power was suppressed from -10.83 MVar to -36.64 MVar at 0.0099 s and returned to stable condition after the second-

swing. At the 150 ms, the fault was removed and the AC voltage from 0.8858 p.u. to the stable condition at 0.982 p.u. after the first-swing. The active power suddenly dropped to 55.66 MW at 0.1504 s and it returned to the stable condition at 153.9 MW after the first-swing. For the reactive power, it suddenly dropped to -43.12 MW at 0.1504 s and it returned to the stable condition at -23.3 MVar after the second-swing. With the control of power converters, this offshore wind farm with detailed representation of 32 units of WT-DFIGs can maintain the transient stability in this fault event. And the simulation results at the PCC for the 32 units of WT-DFIGs are regarded as the benchmarks for comparing with those for different simplified models in **Case 1-5**.

Comparing the simulations results in **Case 1**, the two curves for AC voltage have nearly overlapped with each others in Fig-3.19. For the simulation results in Fig-3.17 and Fig-3.18, the two curves in each diagram are very similar with several small differences. Comparing the simulations results in **Case 2**, two curves for active power in Fig-3.21 as well as two curves for AC voltage in Fig-3.23 are very similar to each other with several small differences. For the reactive power in Fig-3.22, the difference of the two curves during the swings are nearly between 2-3 MVar, but the overall changes of reactive are similar in this two curves. Comparing the simulation results in **Case 3-5**, the differences between the two curves in each diagram are much more obvious than those in **Case 1-2** due to over-simplification. So the simplified models in **Case 3-5** are not considered. Furthermore, with comparison of simulation time for different cases illustrated in the Fig-3.35, the simulation time for **Case 1** and **Case 2** are only 45.48% and 24.49% of that for simulation system with models in detail. For the balance between computational time and the requirement of simulation accuracy and, the difference of 2-3 MVar between the two curves during the swings in Fig-3.22 are usually acceptable so that the simplified system with eight aggregated

machines in **Case 2** is highly proposed for representing this offshore wind farm instead of system in detail for transient stability analysis.

3.8 Case Studies for WT-PMSG based Offshore Wind Farms

The cases studies are similar to those for the rated 160 MW offshore wind farm consisting of 32 units of WT-PMSGs connecting with the SMIB system shown in Fig-3.13. The detailed information of the simulation system is described in Appendix E.

3.8.1 Case 6: Sixteen Equivalent Machines

For **Case 6** including sixteen coherency groups, the simulation results are illustrated in Fig-3.36 to Fig-3.38.

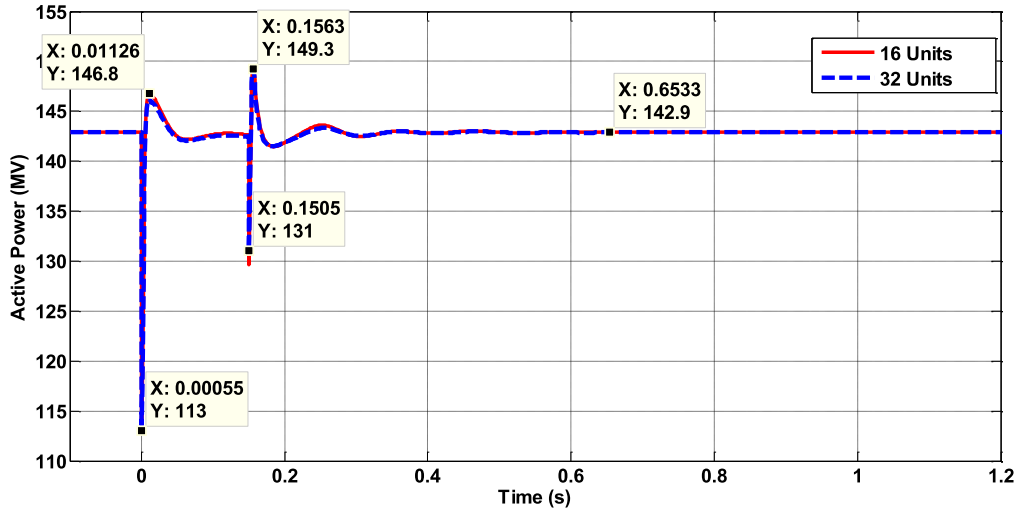

Fig-3.36 The Output Active Power for Detailed and Sixteen Equivalent Machines Models

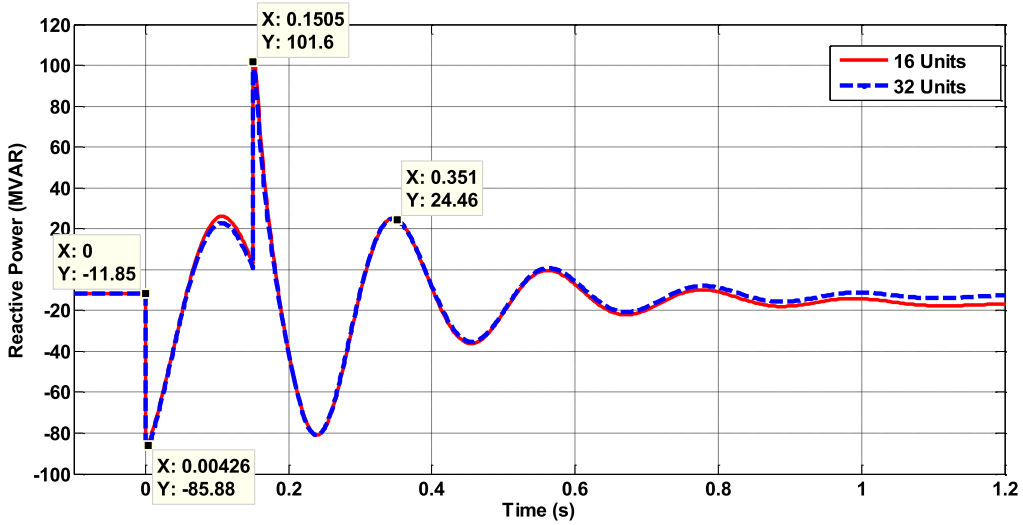

Fig-3.37 The Output Reactive Power for Detailed and Sixteen Equivalent Machines Models

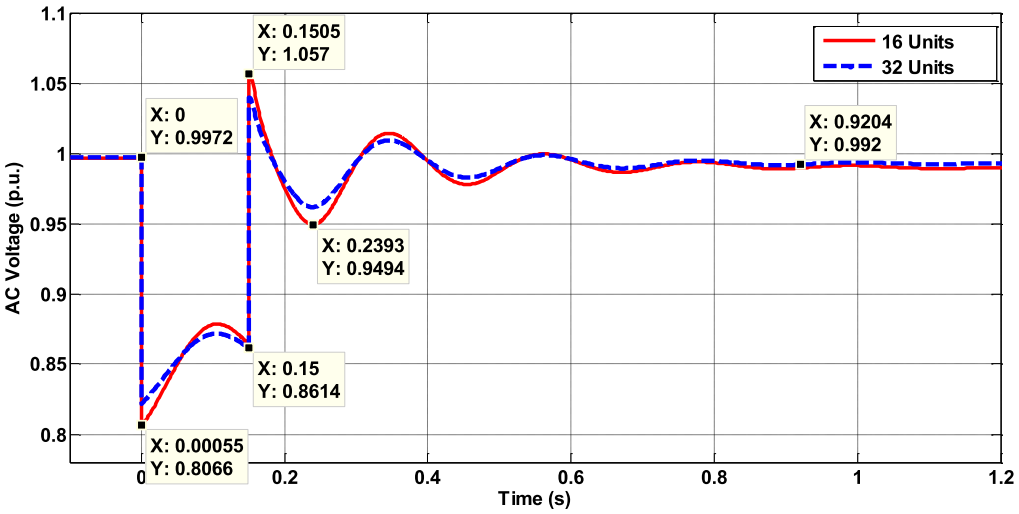

Fig-3.38 The AC Voltage at PCC for Detailed and Sixteen Equivalent Machines Models

3.8.2 Case 7: Eight Equivalent Machines

For **Case 7** including eight coherency groups, the simulation results are shown in Fig-3.39 to Fig-3.41.

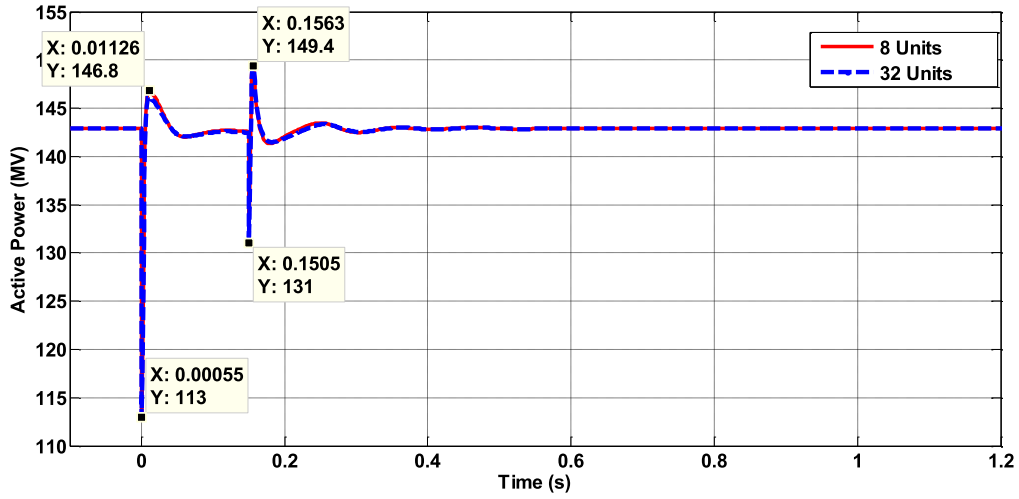

Fig-3.39 The Output Active Power for Detailed and Eight Equivalent Machines Models

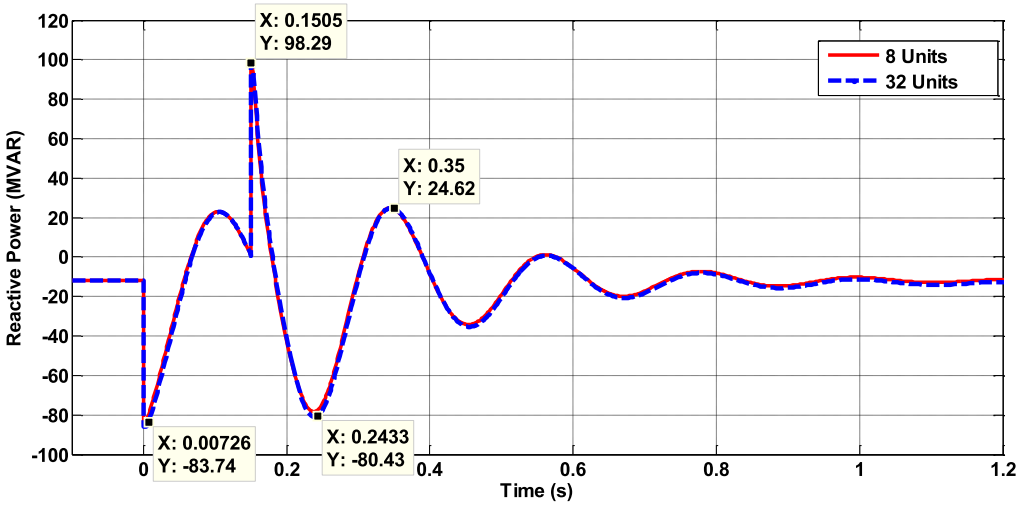

Fig-3.40 The Output Reactive Power for Detailed and Eight Equivalent Machines Models

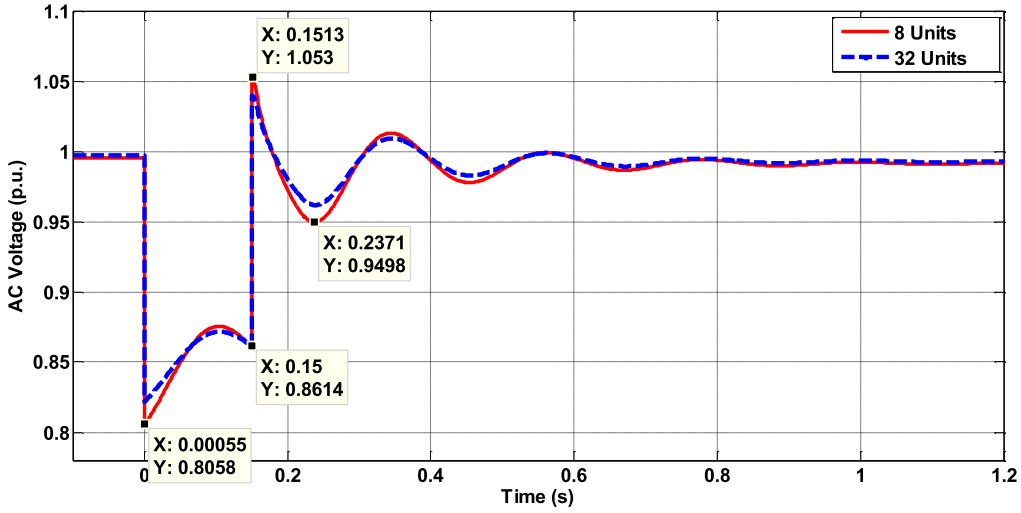

Fig-3.41 The AC Voltage at PCC for Detailed and Eight Equivalent Machines Models

3.8.3 Case 8: Four Equivalent Machines

For **Case 8** including four equivalent machines, the simulation results are illustrated in Fig-3.42 to Fig-3.44.

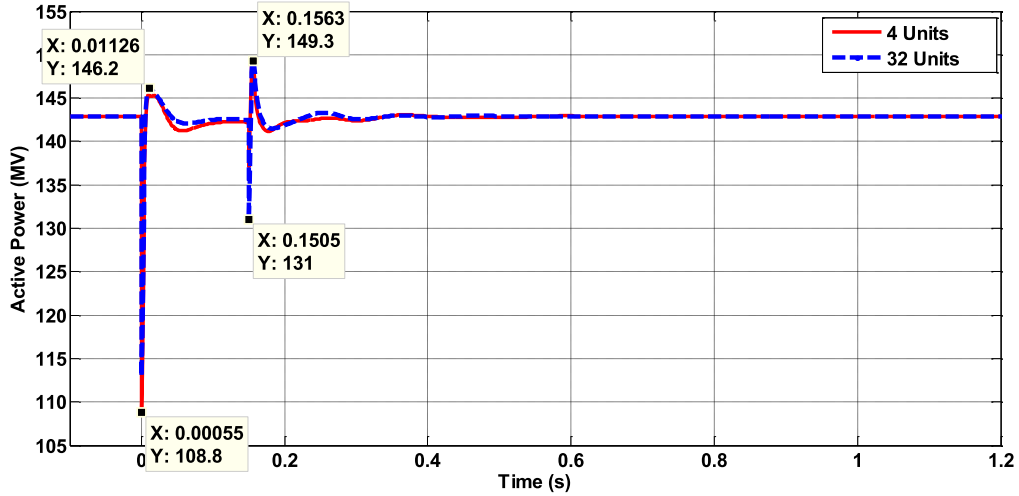

Fig-3.42 The Output Active Power for Detailed and Four Equivalent Machines Models

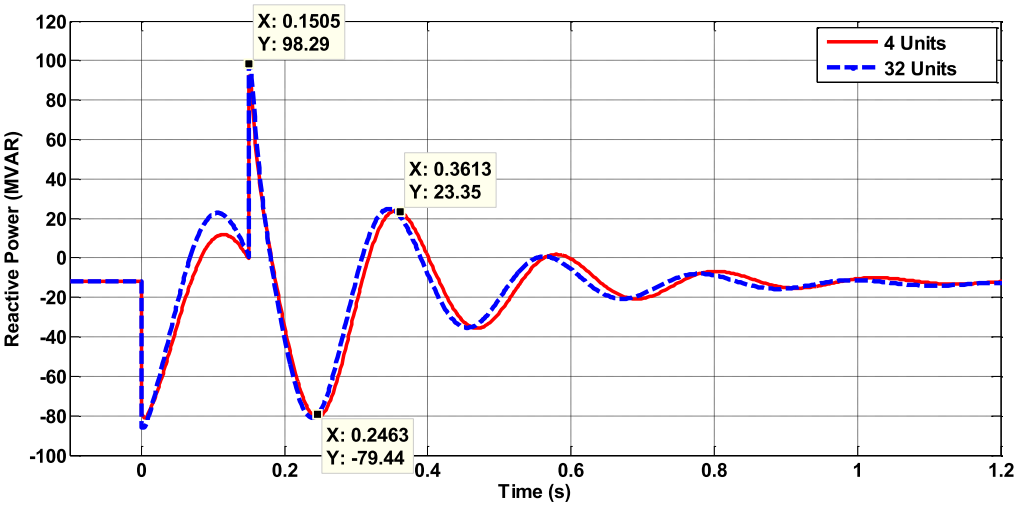

Fig-3.43 The Output Reactive Power for Detailed and Four Equivalent Machines Models

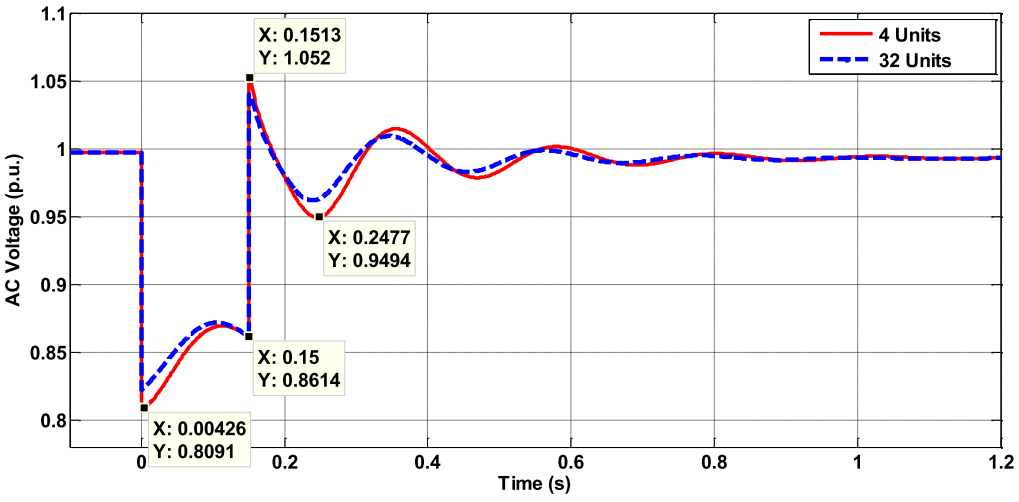

Fig-3.44 The AC Voltage at PCC for Detailed and Four Equivalent Machines Models

3.8.4 Case 9: Two Equivalent Machines

For **Case 9** including two equivalent machines, the simulation results are illustrated in Fig-3.45 to Fig-3.47.

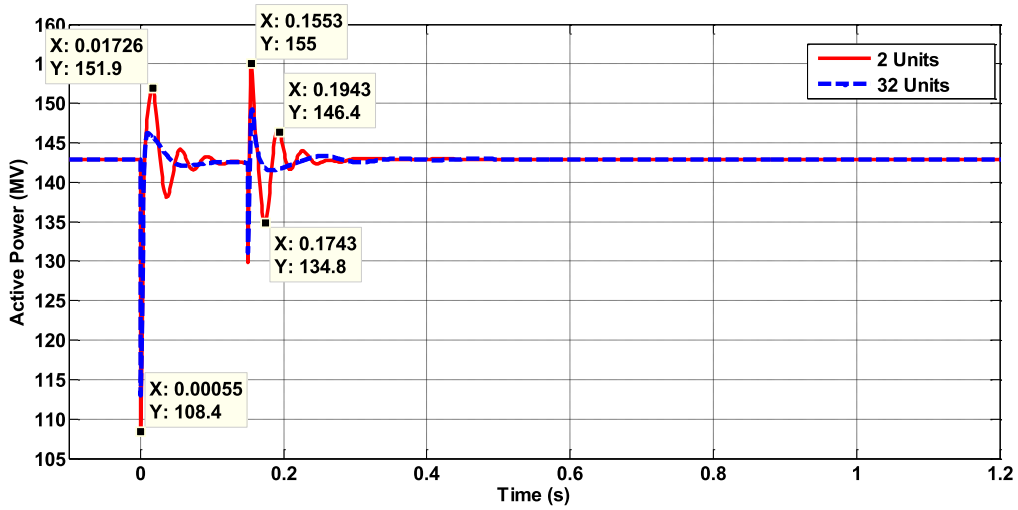

Fig-3.45 The Output Active Power for Detailed and Two Equivalent Machines Models

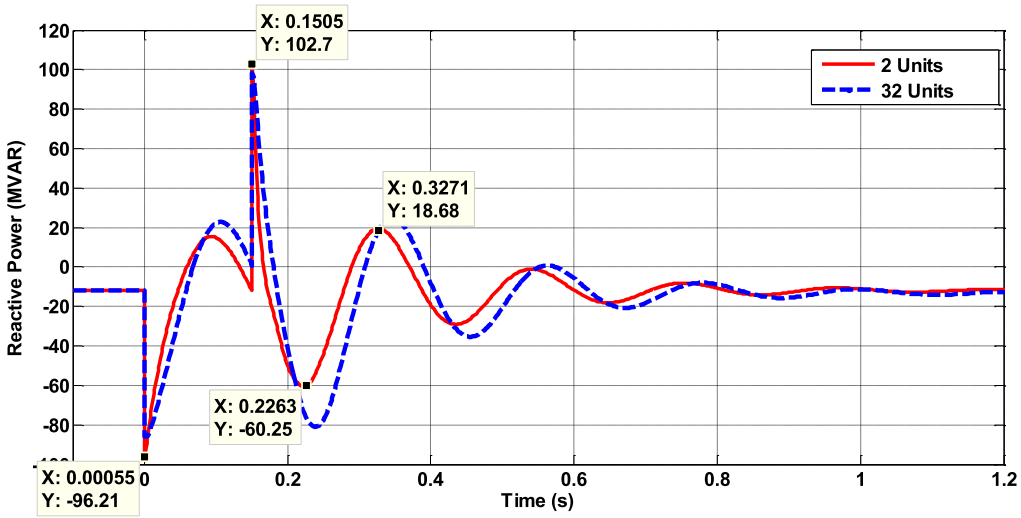

Fig-3.46 The Output Reactive Power for Detailed and Two Equivalent Machines Models

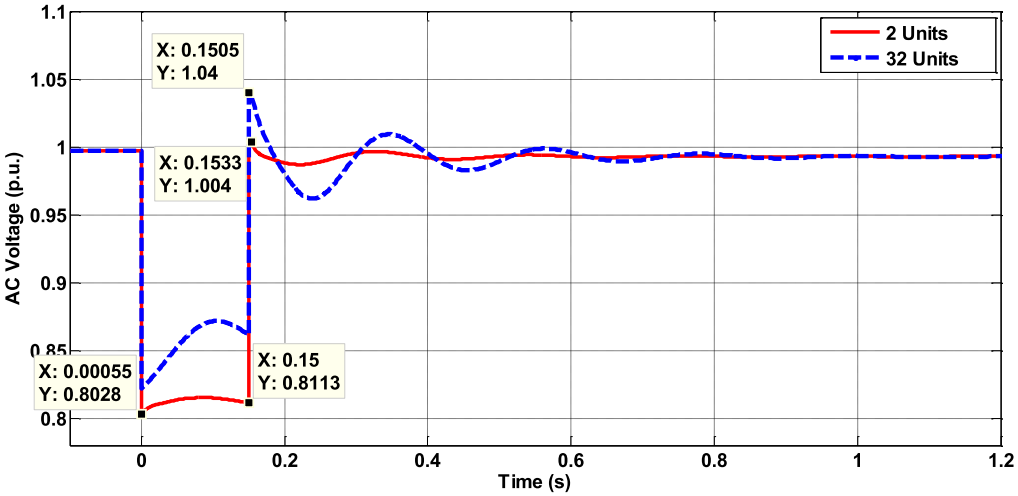

Fig-3.47 The AC Voltage at PCC for Detailed and Two Equivalent Machines Models

3.8.5 Case 10: Single Equivalent Machine

For **Case 10** including single equivalent machine, the simulation results are shown in Fig-3.48 to Fig-3.50.

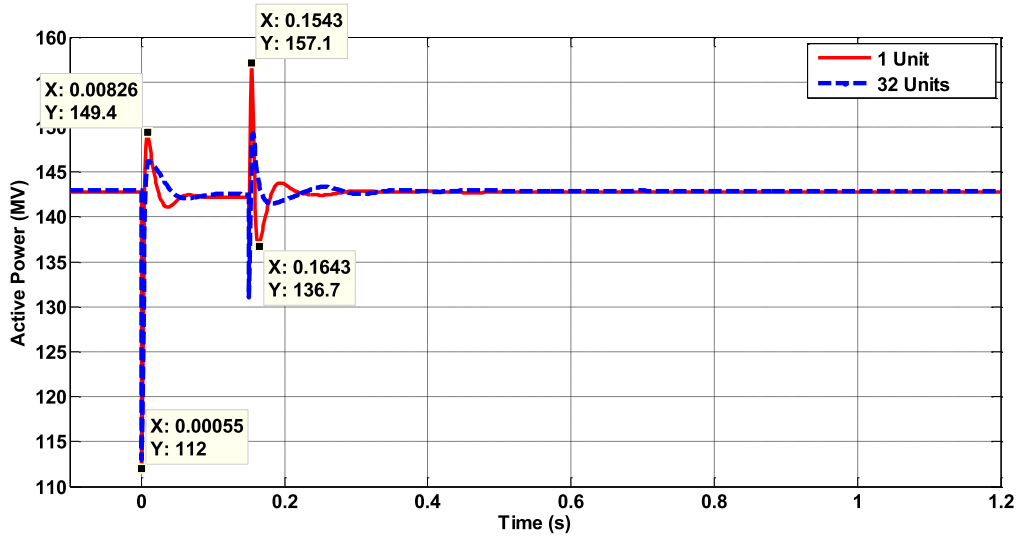

Fig-3.48 The Output Active Power for Detailed and Single Equivalent Machine Models

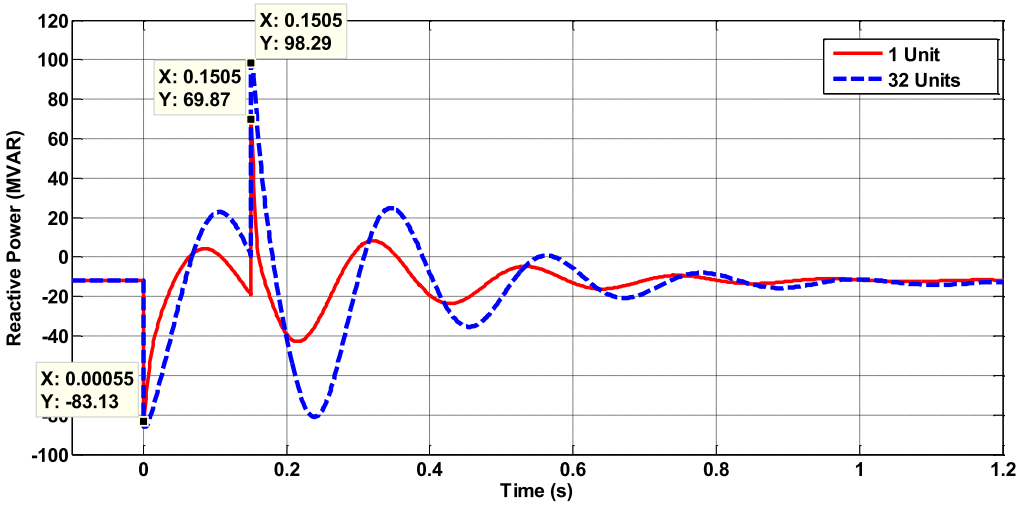

Fig-3.49 The Output Reactive Power for Detailed and Single Equivalent Machine Models

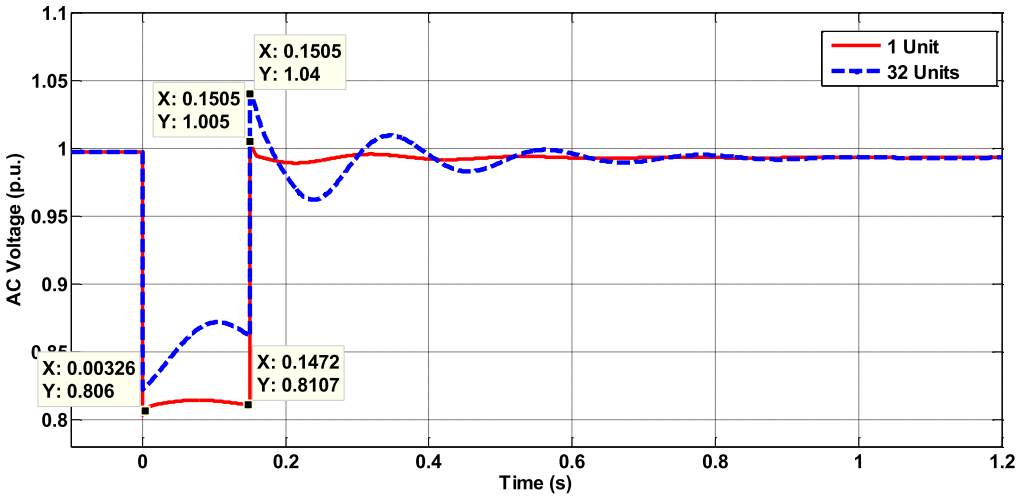

Fig-3.50 The AC Voltage at PCC for Detailed and Single Equivalent Machine Models

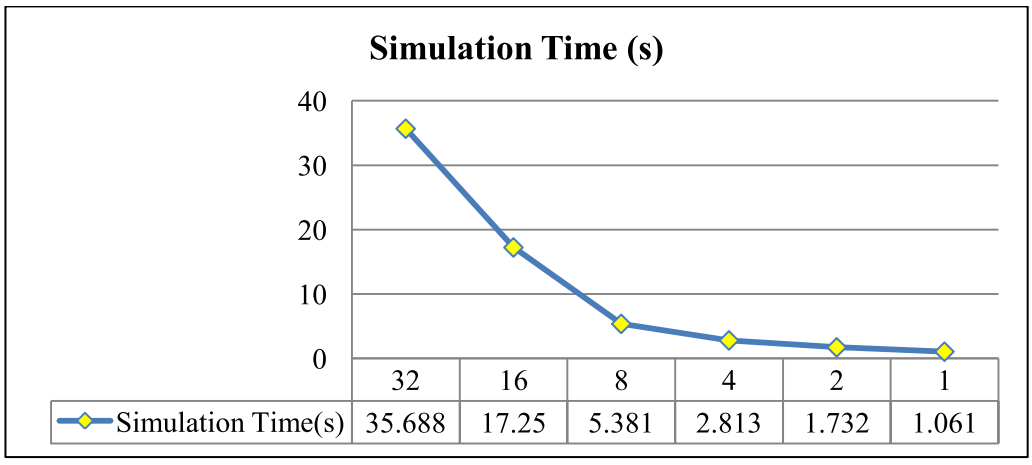

Fig-3.51 The Simulation Time versus Group Number in SMIB System

From the simulation results for the models in detail shown in Fig-3.36 to Fig-3.38, The AC voltage at PCC suddenly dropped from 0.9972 p.u. to 0.8066 p.u. at 0+ s in Fig-3.38. At same time, the active power suddenly decreased from 142.9 MW to 113 MW by 20.92% in Fig-3.17 and the reactive power suddenly decreased greatly from -11.85 MVar to -85.88 MVar by 624.73% in Fig-3.37. Due to the control of power converters in the WT-PMSG systems, the active power was recovered to 146.8 MW at 0.0112 s and returned to stable condition after the first-swing. At the 150 ms, the fault was removed and the active power suddenly dropped to 131 MW at 0.1505 s and increased to 149.3 MW at 0.1563 s and then it returned to the original condition after the second swing. For the reactive power, it suddenly jumped to 101.6 MVar at 0.1505s when the fault was removed at 0.15 s and it returned to the normal condition after several swings. For the AC voltage, it recovered from 0.8614 p.u. at 0.15s to 1.057 p.u. at 0.1505 s and returned to the 0.992 for normal operation after several swings. With the control of power converters, this offshore wind farm with detailed representation of 32 units of WT-PMSGs can maintain the transient stability in this fault event. And the simulation results at the PCC for the 32 units of WT-PMSGs are regarded as the benchmarks for comparing with those for different simplified models in **Case 6-10**.

Comparing the simulations results in **Case 6-7**, the two curves for active power in Fig-3.36 and Fig-3.39, the two curves for reactive power in Fig-3.37 and Fig-3.40 are nearly overlapped with each other. For the AC voltage in Fig-3.38 and Fig-3.41, the two curves in each diagram are similar with several small differences. Comparing the simulations results in **Case 8**, the two curves for active power in Fig-3.42 and are the two curves for AC voltage in Fig-3.44 are very similar with several small differences. For the reactive power in Fig-3.43, the difference of the two curves during the swings are nearly between 2-3 MVar, but the overall changes of reactive are similar in this two curves. Comparing the simulation results in

Case 9-10, the differences between the two curves in each diagram are much more obvious than those in **Case 6-8** due to over-simplification. So the simplified models in **Case 9-10** are not considered.

Furthermore, with comparison of simulation time for different cases illustrated in the Fig-3.35, the simulation time for **Case 6-8** are only 45.48%, 24.49% and 7.88% of that for simulation system with models in detail. For the balance between the computational time and requirement of simulation accuracy, the difference of 2-3 MVar between the two curves during the swings in Fig-3.43 are usually acceptable so that the simplified system with four aggregated machines in **Case 8** is highly proposed for representing this offshore wind farm instead of system in detail for transient stability analysis.

3.9 Summary and Conclusions

In this chapter, the dynamic aggregated modelling method has been proposed to find the effective representations of the large-scale offshore wind farms including WT-DFIGs and WT-PMSGs in terms of the computational time and simulation accuracy for transient stability analysis By separating these wind turbines with similar dynamic characteristics into few coherency groups and representing each group with equivalent aggregated models, the fully-represented models of the wind farm have been simplified to some extent to achieve the balance between computational time and requirement of simulation accuracy and. The proposed aggregated models have been validated in the simulation systems to validate that the computation speed has been obviously improved and the simulation accuracy is acceptable for the requirements of transient stability analysis.

.

Chapter 4

Dynamic Modelling and Control of VSC-HVDC Systems for Grid Integration of Large-scale Offshore Wind Farms

Since the application of connecting the first offshore wind farm in Denmark in 1991 [28], the HVAC transmission technology has dominated the market for 20 years. Considering the future development of large-scale offshore wind farms with great increases in total installation capacity and connection length [11, 12, 16-18, 28], the HVAC transmission technology will show its limits in terms of operation reliability, stability and cost-efficiency [4]. As a result, alternative solution should be needed for connecting these large-scale offshore wind farms in the future. With the advantages over HVDC and conventional CSC-HVDC transmission technology [5, 6], the VSC-HVDC technology has been widely regarded as the optimal solution to connecting the large-scale offshore wind farm in future. From the offshore wind farms listed in the Table-1.1, the VSC-HVDC technology has gradually seized the market shares for grid integration of large-scale offshore wind farms.

For this state-of-the-art technology, the operation experiences are still limited especially for the coordinated operation between offshore wind farms and the VSC-HVDC systems. In this way, the dynamic characteristics of the VSC-HVDC systems should be investigated to understand their whole performance for connecting the offshore wind farms. Furthermore, for the offshore wind farms including the mainstream variable-speed WT-DFIGs and -PMSGs, these wind turbines are equipped with IGBT-based power converters and operate in their control modes for different control targets which have big influences on the whole dynamic characteristics of the offshore wind farms. In this way, the control strategies of VSC-HVDC

transmission systems should be coordinated with the offshore wind farm to maintain the operation stability of the whole system.

In this chapter, the dynamic modelling of rectifier- and inverter-side converters is firstly represented to know the key factors for the dynamic performance of the point-to-point VSC-HVDC systems. Then control strategies for the rectifier- and inverter-side converters of the VSC-HVDC systems are studied to achieve the decoupled controls for different control targets. Finally, the VSC-HVDC system is built for connecting with two offshore wind farms consisting of the WT-DFIG and WT-PMSG systems respectively in the DIgSILENT/-PowerFactory. The comparisons of two different control schemes for the rectifier-side converter are carried out to investigate their performance for maintaining the operation stability during fault condition and to validate the preferred control scheme for the rectifier-side converters in VSC-HVDC systems for grid integration of offshore wind farms in terms of operation stability.

4.1 Modelling of VSC-HVDC Systems

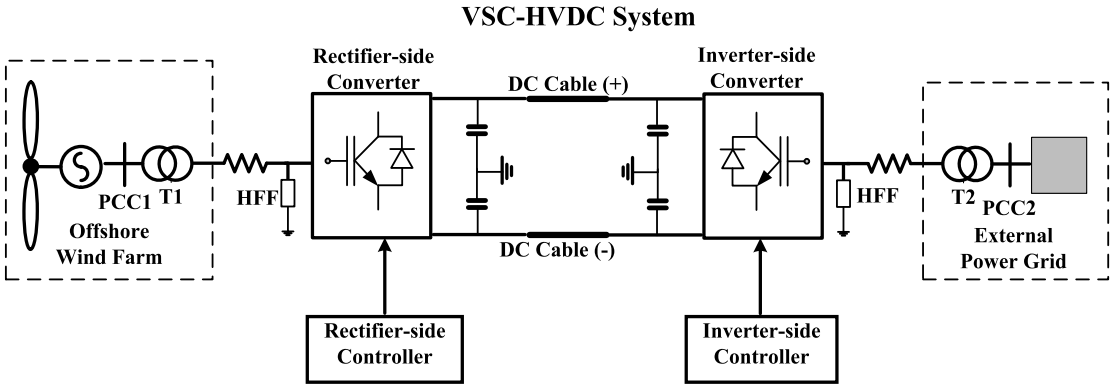

Fig-4.1 The General Configuration of Point-to-point VSC-HVDC System

The typical layout of point-to-point VSC-HVDC systems for grid integration of offshore wind farms is shown in Fig-4.1. The VSCs on the rectifier- and inverter-side are consisting of self-commutated IGBTs to realise the AC/DC power transformation. The DC capacitors on

both sides maintain the balance between the AC and DC power as the DC voltage sources. And the AC transformers and series reactors are connected to the AC buss on both sides of VSC-HVDC system. And the high-frequency filters (HHFs) are needed to eliminate the high frequency components of AC harmonics generated by module cells [5].

4.1.1 Modelling of Rectifier-side Converter

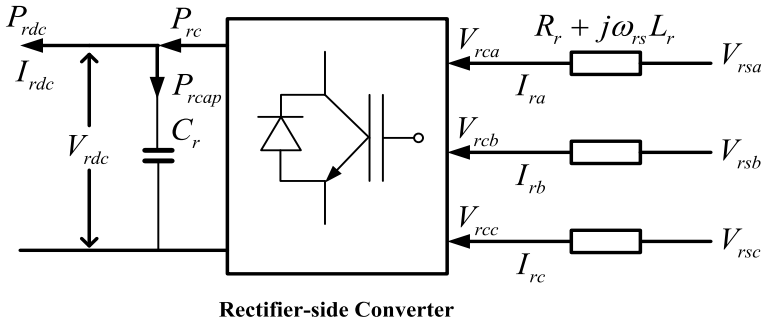

Fig-4.2 The Diagram of Rectifier-side Circuit

For the AC circuit on the rectifier-side shown in Fig-4.2, the relationship of three-phase voltages on the system- and converter-side can be expressed by the (4.1):

$$\begin{cases} V_{rsa} = V_{rca} + R_r I_{ra} + L_r \dfrac{dI_{ra}}{dt} \\ V_{rsb} = V_{rcb} + R_r I_{rb} + L_r \dfrac{dI_{rb}}{dt} \\ V_{rsc} = V_{rcc} + R_r I_{rc} + L_r \dfrac{dI_{rc}}{dt} \end{cases} \tag{4.1}$$

where V_{rsa}, V_{rsb} and V_{rsc} are the three-phase AC voltages at the PCC for external power system; V_{rca}, V_{rcb} and V_{rcc} are the three-phase AC voltages on the AC-side of rectifier; I_{ra}, I_{rb} and I_{rc} are the three-phase AC currents on the rectifier-side; L_r and R_r are the total inductance and resistance of the AC transformer and series AC reactor on the rectifier-side.

The (4.1) is converted from *a-b-c* to *d-q* coordinate system expressed in the (4.2) with the Park transformation [2]:

$$\begin{cases} V_{rcd} = V_{rsd} - R_r I_{rd} - L_r \dfrac{dI_{rd}}{dt} + \omega_{rs} L_r I_{rq} \\ V_{rcq} = V_{rsq} - R_r I_{rq} - L_r \dfrac{dI_{rq}}{dt} - \omega_{rs} L_r I_{rd} \end{cases} \tag{4.2}$$

V_{rsd} and V_{rsq} are the d- and q-axis voltage on system-side of rectifier-side converter; V_{rcd} and V_{rcq} are the d- and q-axis voltage on converter-side of rectifier-side converter; I_{rd} and I_{rq} are the d- and q-axis current of rectifier-side converter; ω_{rs} is the rotational angular speed of AC system on the rectifier-side and $\omega_{rs} = 2\pi f_{rs}$ (f_{rs} is the system frequency on rectifier-side). The derivation of the dynamic models for rectifier-side converter in detail is described in Appendix C.

So the dynamic models on the AC-side of the rectifier-side converter are given by [102, 112]:

$$\begin{cases} \dfrac{dI_{rd}}{dt} = -\dfrac{R_r}{L_r} I_{rd} + \omega_{rs} I_{rq} + \dfrac{V_{rsd} - V_{rcd}}{L_r} \\ \dfrac{dI_{rq}}{dt} = -\dfrac{R_r}{L_r} I_{rq} - \omega_{rs} I_{rd} + \dfrac{V_{rsq} - V_{rcq}}{L_r} \end{cases} \tag{4.3}$$

The AC-side active power of the rectifier is given by:

$$P_{rc} = V_{rcd} I_{rd} + V_{rcq} I_{rq} \tag{4.4}$$

Assuming the active power losses inside the rectifier are neglected, there is the balance between the AC active power and DC power of the rectifier given by [102, 112]:

$$P_{rc} = P_{rdc} + P_{rcap} \tag{4.5}$$

$$V_{rcd} I_{rd} + V_{rcq} I_{rq} = V_{rdc} I_{rdc} + V_{rdc} C_r \frac{dV_{rdc}}{dt} \tag{4.6}$$

where P_{rc} and Q_{rc} are the active and reactive power on the rectifier-side; P_{rdc} is the DC power on the rectifier-side of DC cables; P_{rcap} is the power in the DC capacitor on rectifier-side and C_r is the capacitance of DC capacitor; V_{rdc} and I_{rdc} are the voltage and current of the DC-side of converter on the rectifier-side.

So the dynamic equation for the DC voltage on rectifier-side is given by:

$$\frac{dV_{rdc}}{dt} = \frac{(V_{rcd}I_{rd} + V_{rcq}I_{rq})}{V_{rdc}C_r} - \frac{I_{rdc}}{C_r} \tag{4.7}$$

4.1.2 Modelling of Inverter-side Converter

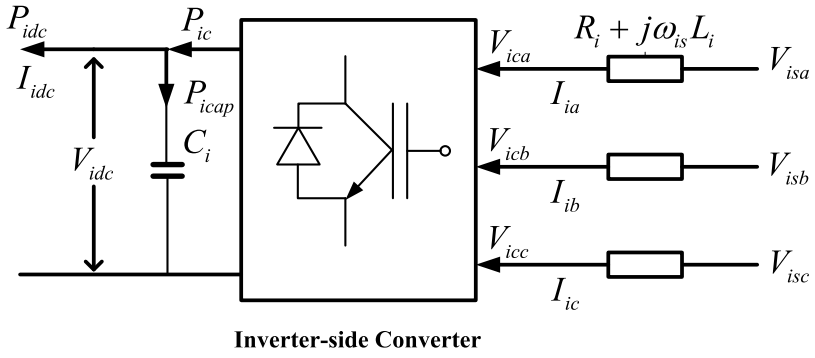

Fig-4.3 The Diagram of Inverter-side Circuit

For the AC circuit on the inverter-side shown in Fig-4.3, the relationship of three-phase voltages on the system-side and inverter-side are defined as same as those on the rectifier-side.

$$\begin{cases} V_{isa} = V_{ica} + R_i I_{ia} + L_i \dfrac{dI_{ia}}{dt} \\ V_{isb} = V_{icb} + R_i I_{ib} + L_i \dfrac{dI_{ib}}{dt} \\ V_{isc} = V_{icc} + R_i I_{ic} + L_i \dfrac{dI_{ic}}{dt} \end{cases} \tag{4.8}$$

where V_{isa}, V_{isb} and V_{isc} are the three-phase AC voltages at the PCC for external power system on the inverter-side; V_{ica}, V_{icb} and V_{icc} are the three-phase AC voltages on the AC-side of inverter; I_{ia}, I_{ib} and I_{ic} are the three-phase AC currents; L_i and R_i and are the total resistance and inductance of AC transformer and series AC reactor on the inverter-side. (4.8) is converted from *a-b-c* to *d-q* coordinate system expressed in (4.9) with the Park transformation:

$$\begin{cases} V_{icd} = V_{isd} - R_i I_{id} - L_i \dfrac{dI_{id}}{dt} + \omega_{is} L_i I_{iq} \\ V_{icq} = V_{icq} - R_i I_{iq} - L_i \dfrac{dI_{iq}}{dt} - \omega_{is} L_i I_{id} \end{cases} \tag{4.9}$$

V_{isd} and V_{isq} are the d- and q-axis voltage on system-side of inverter-side converter; V_{icd} and V_{icq} are the d- and q-axis voltage on converter-side of inverter-side converter; I_{id} and I_{iq} are the d- and q-axis current of inverter-side converter; ω_{is} is the rotational angular speed of AC system on the inverter-side and $\omega_{is} = 2\pi f_{is}$ (f_{is} is the system frequency on inverter-side). The derivation of the dynamic models for invert-side converter in detail is described in Appendix C.

So the dynamic models on the AC-side of the inverter-side converter are given by [102, 112]:

$$\begin{cases} \dfrac{dI_{id}}{dt} = -\dfrac{R_i}{L_i} I_{id} + \omega_{is} I_{iq} + \dfrac{V_{isd} - V_{icd}}{L_i} \\ \dfrac{dI_{iq}}{dt} = -\dfrac{R_i}{L_i} I_{iq} - \omega_{is} I_{id} + \dfrac{V_{isq} - V_{icq}}{L_i} \end{cases} \tag{4.10}$$

Assuming the active power losses inside the inverter are neglected, there is the balance between the AC active power and DC power of the inverter given by [102, 112]:

$$P_{ic} = P_{idc} + P_{icap} \tag{4.11}$$

$$V_{icd} I_{id} + V_{icq} I_{iq} = V_{idc} I_{idc} + V_{idc} C_i \frac{dV_{idc}}{dt} \tag{4.12}$$

where P_{ic} is the active power on the inverter-side; P_{idc} is the DC power on inverter-side of DC cables; P_{icap} is the power losses of DC capacitors on inverter-side and C_i is the capacitance of DC capacitor; V_{idc} and I_{idc} are the voltage and current of the DC-side of inverter. So the dynamic equation for the DC voltage is given:

$$\frac{dV_{idc}}{dt} = \frac{(V_{icd} I_{id} + V_{icq} I_{iq})}{V_{idc} C_i} - \frac{I_{idc}}{C_i} \tag{4.13}$$

4.2 Control Strategies of Point-to-point VSC-HVDC Systems

4.2.1 The Rectifier-side VSC Controller

As described in Section 4.1.1 and Appendix C, the models of rectifier-side converter can be expressed by (4.2). So $L_r \frac{dI_{rd}}{dt}$ and $L_r \frac{dI_{rq}}{dt}$ are replaced from V_{rd}^* and V_{rq}^* using the PI controllers expressed by (4.14):

$$\begin{cases} V_{rd}^* = L_r \dfrac{dI_{rd}}{dt} = K_{rp}(I_{rd}^{ref} - I_{rd}) + K_{ri}\int (I_{rd}^{ref} - I_{rd}) \\ V_{rq}^* = L_r \dfrac{dI_{rq}}{dt} = K_{rp}(I_{rq}^{ref} - I_{rq}) + K_{ri}\int (I_{rq}^{ref} - I_{rq}) \end{cases} \tag{4.14}$$

where I_{rd} and I_{rd}^{ref} are the d-axis current and its reference on the rectifier-side; I_{rq} and I_{rq}^{ref} are the q-axis current and its reference on the rectifier-side; K_{rp} and K_{ri} are the proportional and integral gain of PI controllers on the rectifier-side. Assuming the ratio between the L_r and R_r is large enough, the R_r can be neglected and the (4.2) is expressed by (4.15) [102, 112]:

$$\begin{cases} V_{rcd} = V_{rsd} - V_{rd}^* + \omega_{rs} L_r I_{rq} \\ V_{rcq} = V_{rsq} - V_{rq}^* - \omega_{rs} L_r I_{rd} \end{cases} \tag{4.15}$$

According to (4.15), the diagram for the rectifier-side Inner Current Controller is illustrated in the Fig-4.4.

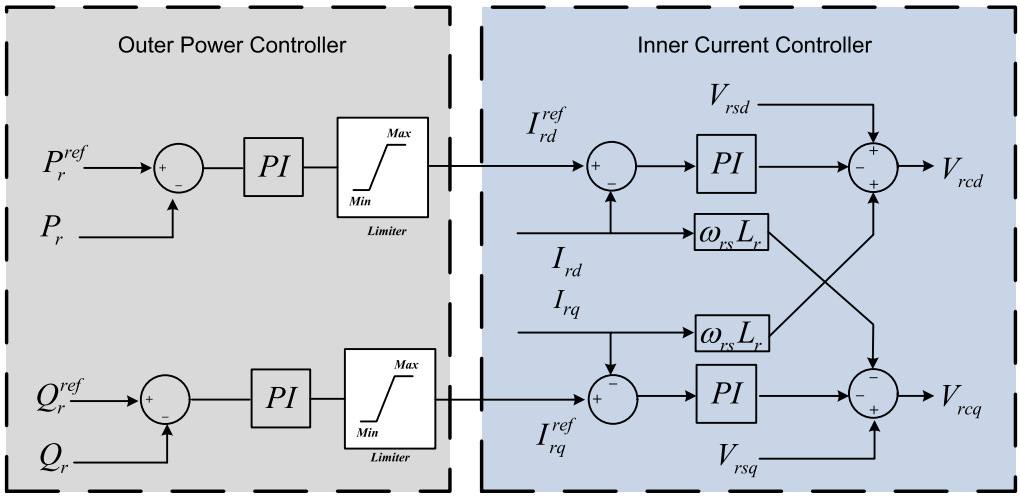

Fig-4.4 The Diagram of Rectifier-side VSC Controller (Scheme 1)

As similar to those controllers for power converters in wind turbines such as WT-DFIGs and PMSGs, The two-stage controllers are usually applied for power converters in the VSC-HVDC systems. For the outer controller on rectifier-side, the classic Scheme 1 is usually used: the ***P*** Mode is usually applied to control the input active power at the PCC via the *d*-axis PI controller on the rectifier-side. For the *q*-axis, the ***Q*** Mode controlling the input reactive power at the PCC is usually used on the rectifier-side to maintain the voltage-levels at PCC for grid integration of external power sources. So the equations for outer power controller on the rectifier-side are expressed by:

$$\begin{cases} I_{rd}^{ref} = K_{Pr}(P_r^{ref} - P_r) + K_{iPr}\int (P_r^{ref} - P_r) \\ I_{rq}^{ref} = K_{Qr}(Q_r^{ref} - Q_r) + K_{iQr}\int (Q_r^{ref} - Q_r) \end{cases} \tag{4.16}$$

where P_r and P_r^{ref} are the output active power and its reference on the rectifier-side PCC; Q_r and Q_r^{ref} are the output reactive power and its reference on the rectifier-side PCC; K_{Pr} and K_{iPr} are the proportional and integral gain of *d*-axis PI controller; K_{Qr} and K_{iQr} are the proportional and integral gain of *q*-axis PI controller.

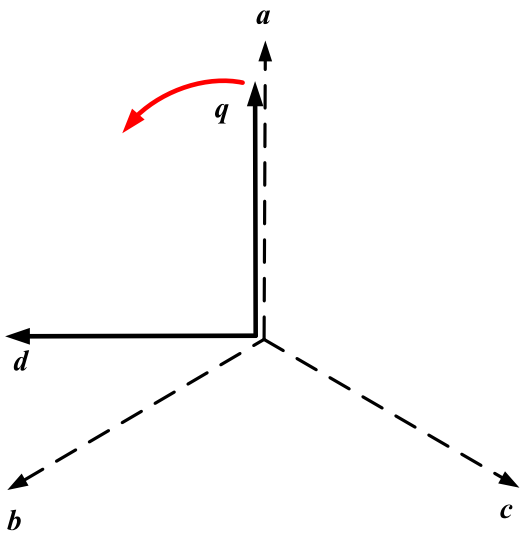

Fig-4.5 The Voltage-oriented *d-q* Coordinate System

However, for the mainstream wind turbines such as WT-DFIGs and WT-PMSGs, they have equipped with the IGBT-based power converters and their output power can ben controlled

by their VSC controllers. So for the design of rectifier-side VSC controller, the Scheme 2 can be applied for VSC controller which could just operate in the q-axis V_{ac} Mode to provide the voltage reference at the PCC of rectifier-side for grid integration of the offshore wind farms in synchronous operation. For the rotational d-q coordinate system on the rectifier-side, the q-axis in the rotational d-q coordinate system rotates in synchronous with the one phase of the AC three-phase voltages at the synchronous speed ω_s (ω_s=2πf_s) shown in Fig-4.5. And the d- and q-axis components of the AC voltages of the rectifier are given by:

$$\begin{cases} V_{rcd} = 0 \\ V_{rcq} = V_{rc} \end{cases} \tag{4.17}$$

So (4.15) can be re-expressed by (4.18):

$$V_{rc} = V_{rsq} - V_{rq}^{*} - \omega_{rs} L_r I_{rd} \tag{4.18}$$

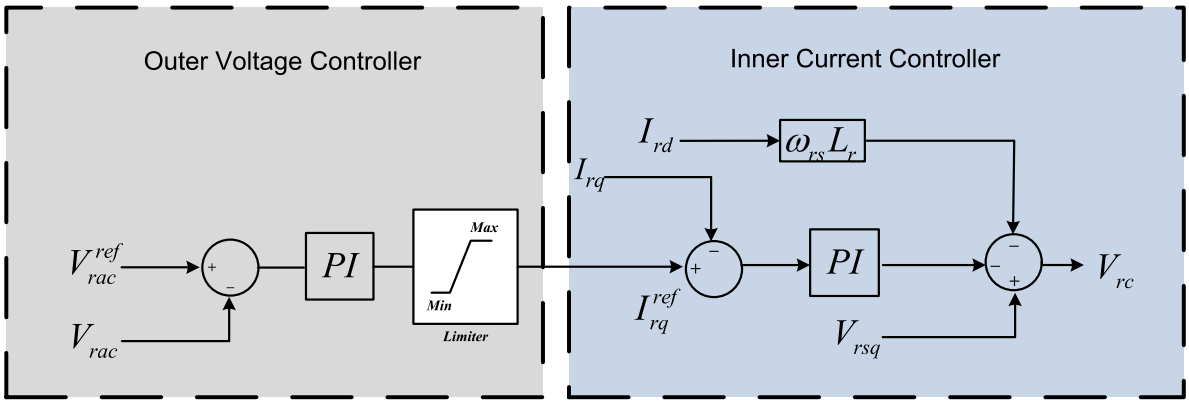

Fig-4.6 The Diagram of Rectifier-side VSC Controller (Scheme 2)

According to (4.18), the diagram for the rectifier-side Inner Current Controller in Scheme 2 is illustrated in the Fig-4.6. And the equation for outer q-axis V_{ac} controller on the rectifier-side is expressed by:

$$I_{rq}^{ref} = K_V (V_{rac}^{ref} - V_{rac}) + K_{iV} \int (V_{rac}^{ref} - V_{rac}) \tag{4.19}$$

where V_{rac} and V_{rac}^{ref} are the terminal AC voltage and its reference at PCC; K_V and K_{iV} are the proportional and integral gain of q-axis PI controller.

4.2.2 The Inverter-side VSC Controller

In the (4.9), the $L_i \frac{dI_{id}}{dt}$ and $L_i \frac{dI_{iq}}{dt}$ are replaced from V_{rd}^* and V_{iq}^* using the PI controllers expressed by (4.20):

$$\begin{cases} V_{id}^* = L_i \frac{dI_{id}}{dt} = K_{ip}(I_{id}^{ref} - I_{id}) + K_{ii}\int (I_{id}^{ref} - I_{id}) \\ V_{iq}^* = L_i \frac{dI_{iq}}{dt} = K_{ip}(I_{iq}^{ref} - I_{iq}) + K_{ii}\int (I_{iq}^{ref} - I_{iq}) \end{cases} \tag{4.20}$$

where I_{id} and I_{id}^{ref} are the d-axis current and its reference on the inverter-side; I_{iq} and I_{iq}^{ref} are the q-axis current and its reference on the inverter-side; K_{ip} and K_{ii} are the parameters for the proportional gain and integrator of PI controllers of the current controller on the inverter-side. Assuming the ratio between the L_i and R_i is large enough, the R_i can be neglected and the (4.2) is expressed by (4.21) [102, 112]:

$$\begin{cases} V_{icd} = V_{isd} - V_{id}^* + \omega_{is} L_i I_{iq} \\ V_{icq} = V_{isq} - V_{iq}^* - \omega_{is} L_i I_{id} \end{cases} \tag{4.21}$$

According to (4.21), the diagram for the inverter-side VSC controller is illustrated in the Fig-4.7.

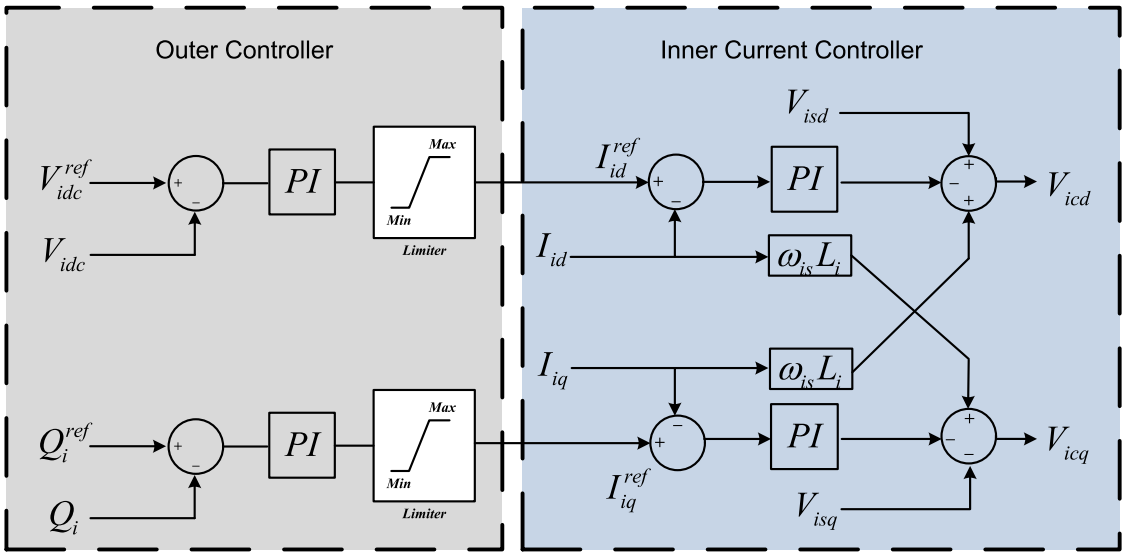

Fig-4.7 The Diagram of Inverter-side VSC Controller

For the first-stage PI regulator in *d*-axis, the $\boldsymbol{V_{dc}}$ Mode is applied for maintaining the DC voltage for AC/DC power transformation. For the *q*-axis PI regulator, the $\boldsymbol{Q}$ Mode is applied to control the output reactive power into the external power system [105, 110, 111]. So the equations for outer controller on the inverter-side are expressed by:

$$\begin{cases} I_{id}^{ref} = K_{dc}(V_{idc}^{ref} - V_{idc}) + K_{idc}\int(V_{idc}^{ref} - V_{idc}) \\ I_{iq}^{ref} = K_{Qi}(Q_i^{ref} - Q_i) + K_{iQi}\int(Q_i^{ref} - Q_i) \end{cases} \tag{4.22}$$

where V_{idc} and V_{idc}^{ref} are the DC voltage of inverter-side converter; Q_i and Q_i^{ref} are the output reactive power and its reference on the rectifier-side PCC; K_{dc} and K_{idc} are the proportional and integral gain of *d*-axis PI controller; K_{Qi} and K_{iQi} are the proportional and integral gain of *q*-axis PI controller.

4.3 Case Studies

4.3.1 Case Studies for VSC-HVDC System Connecting with WT-DFIGs

In this simulation system in DIgSILENT/PowerFactory, the offshore wind farms with total rated 200 MW rated WT-DFIGs was connected with the ±150 kV 300 MW rated bipolar VSC-HVDC system. The details of the simulation system are described in Appendix F.

4.3.1.1 Case 1: The Short-circuit Grounded Fault at Rectifier-side

In **Case 1**, a three-phase short-circuit grounded fault was applied at the PCC1 on the rectifier-side of the VSC-HVDC system shown in Fig-4.1 at 0.1 s and the time duration was 150 ms. Because the fault was closed to the wind farm whose SCR was smaller compared with external power system on inverter-side which was usually set more than 3. The system is sensitive to the grounded resistance of the fault. In order to avoid final instability, the grounded resistance was set as 15 ohm. In this condition, the AC voltage at PCC1 dropped from 0.9959 p.u. to 0.8647 p.u. shown in Fig-4.8 when the fault was applied at the 0.1s.

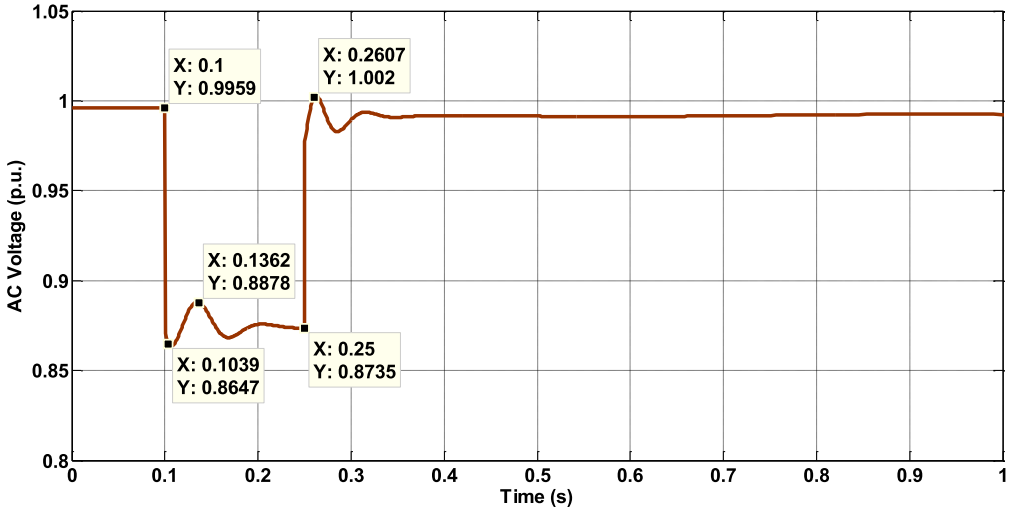

Fig-4.8 The AC Voltage at PCC1 on the Rectifier-side

The comparisons of simulation results for the dynamic impacts on the inverters-side of the VSC-HVDC system with two different control schemes for the rectifier-side VSC are shown from Fig-4.9 to Fig-4.12. For the output active power at PCC2 in Fig-4.9, the overall changes of the two curves are similar with nearly the same oscillation periods and changing trends. However, the strength of the oscillation for Scheme 1 is bigger than that for Scheme 2 during the fault. As seen from Fig-4.9, the undershoot for Scheme 1 is 137.6 MW at 0.1141 s and that for Scheme 2 is 146.3 at 0.1146 s. After the fault, the power oscillations for Scheme 1 and 2 are similar with small differences. For the reactive power at PCC2 in Fig-4.10, the two curves for Scheme 1 and 2 are nearly similar with small differences before and during the faults. However, the overshoot for Scheme 1 is 3.54 MVar at 0.2626 s and it is bigger than that for Scheme 2 which is 2.681 at 0.2596 s. For the DC voltage of inverter-side converter in Fig-4.11, the strength of the oscillation for Scheme 1 is obvious than that for Scheme 2. For the AC voltage at the PCC2 in Fig-4.12, these two curves are similar with small differences.

After review of these diagrams, there are two key features for this case event: Firstly, the dynamic impacts of this large disturbance on the inverter-side of the VSC-HVDC system were not so obvious due to the control systems of the VSC-HVDC system as the buffer

between the rectifier-side fault and the external system on the inverter-side and the whole system recovered to normal operation after the quick transient processes. Secondly, with the Scheme 1 and 2 for the rectifier-side VSC controller, the dynamic performance on the inverter-side of the VSC-HVDC system is nearly similar with acceptable differences. So for different control schemes on the rectifier-side, the dynamic performance on the inverter-side is mainly controlled by the inverter-side VSC controller. So for the large-disturbances on the rectifier-side, both of these control schemes are acceptable but Scheme 2 are a little bit better.

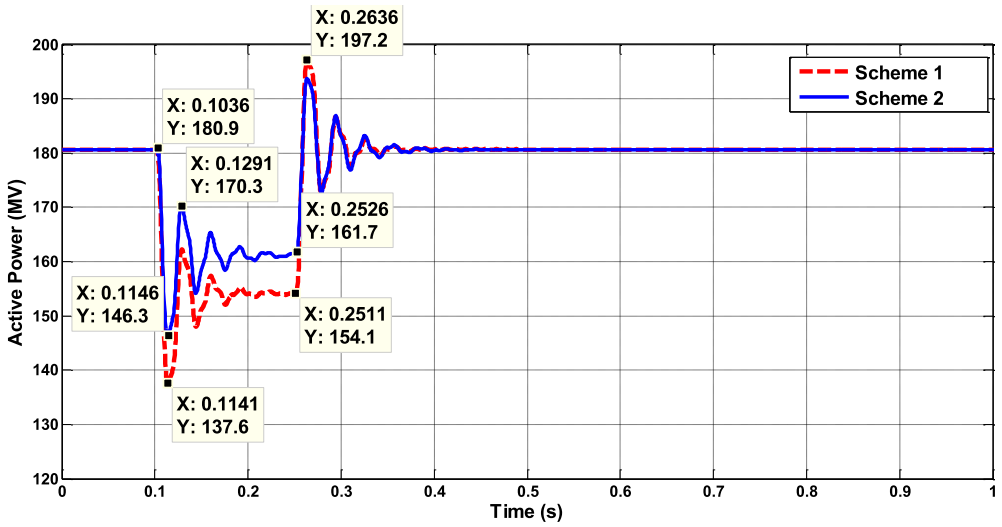

Fig-4.9 The Output Active Power at PCC2 on the Inverter-side (Scheme 1 & 2)

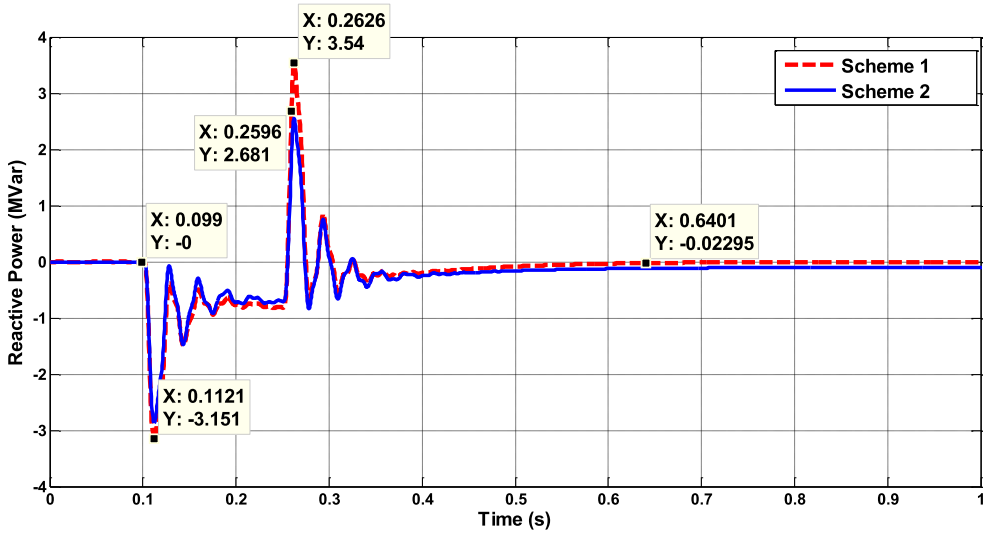

Fig-4.10 The Output Reactive Power at PCC2 on the Inverter-side (Scheme 1 & 2)

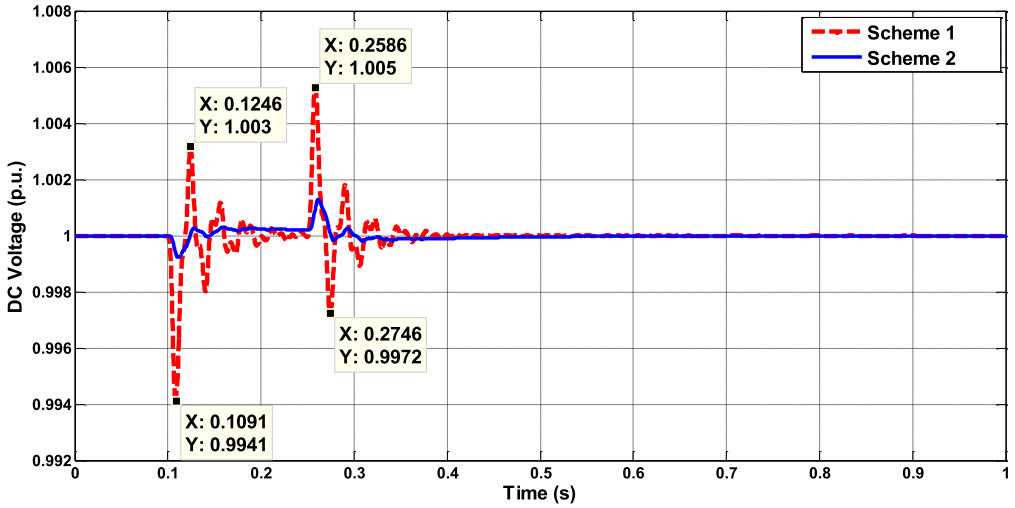

Fig-4.11 The DC Terminal Voltage on the Inverter-side (Scheme 1 & 2)

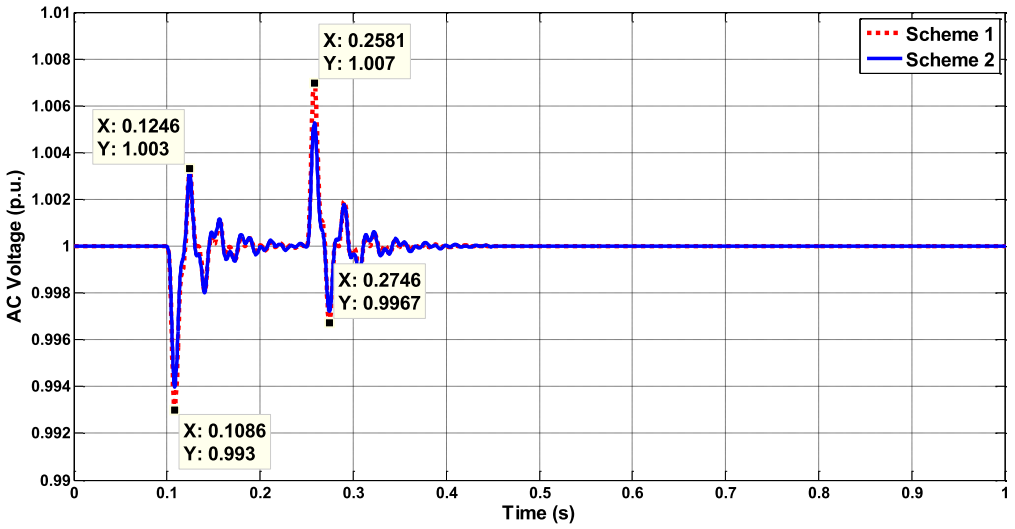

Fig-4.12 The AC Voltage at the PCC2 on Inverter-side (Scheme 1 & 2)

4.3.1.2 Case 2: The Short-circuit Grounded Fault at Inverter-side

In **Case 2**, a three-phase short-circuit grounded fault was applied at the PCC2 on the inverter-side of the VSC-HVDC system at 0.1 s and the time duration is 150 ms. Because the fault was closed to the inverter-side external system whose SCR is set as 3. The system on the inverter-side is less sensitive to the grounded resistance of the faults than that with small SCR such as offshore wind farms. So the grounded resistance was set as 5 ohm. In this condition, the AC voltage at PCC2 dropped sharply from 1.0 p.u. to 0.5137 p.u. illustrated in Fig-4.13.

The comparisons of simulation results on the rectifier-side of the VSC-HVDC system with two different control schemes for the rectifier-side VSC are shown from Fig-4.14 to Fig-4.16.

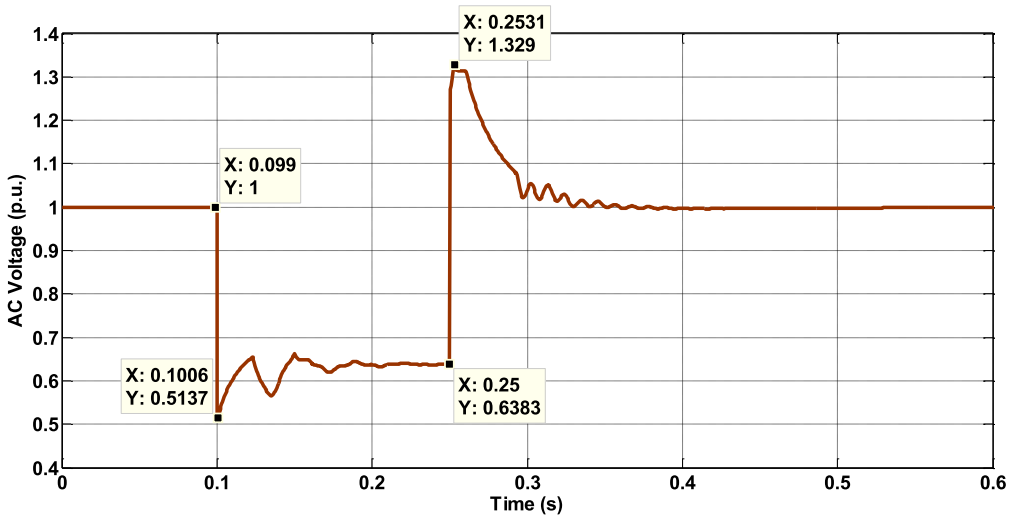

Fig-4.13 The AC Voltage at PCC2 at Inverter-side

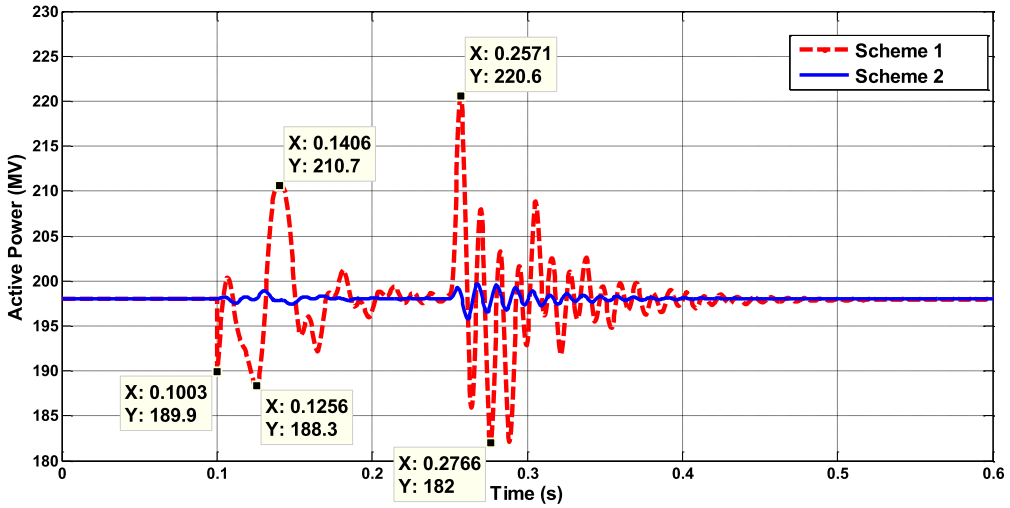

Fig-4.14 The Input Active Power at PCC1 on the Rectifier-side (Scheme 1 & 2)

For the output active power at PCC1 in Fig-4.14, the strength of the power oscillation for Scheme 1 is obvious much stronger than that for Scheme 2 with maximum overshoot of 220.6 MW at 0.2571 s and the minimum undershoot of 182 MW at 0.2766 s. The power oscillation for Scheme 2 is in the range of 195 to 200 MW. For the output reactive power at PCC1 in Fig-4.15, the strength of the power oscillation for Scheme 1 is obvious much stronger than that for Scheme 2 with maximum overshoot of 30.77 MVar at 0.2756 s and the minimum undershoot of -93.15 MVar at 0.2571 s. The power oscillation for Scheme 2 is in

the range of -30 to -10 MVar. For the AC voltage at PCC1 in Fig-4.16, the strength of the voltage oscillation for Scheme 1 is obvious much stronger than that for Scheme 2 with maximum overshoot of 1.16 p.u. at 0.2581 s and the minimum undershoot of 0.9082 p.u. at 0.1286 s. The voltage oscillation for Scheme 2 is in the range of 0.98 p.u. to 1.01 p.u..

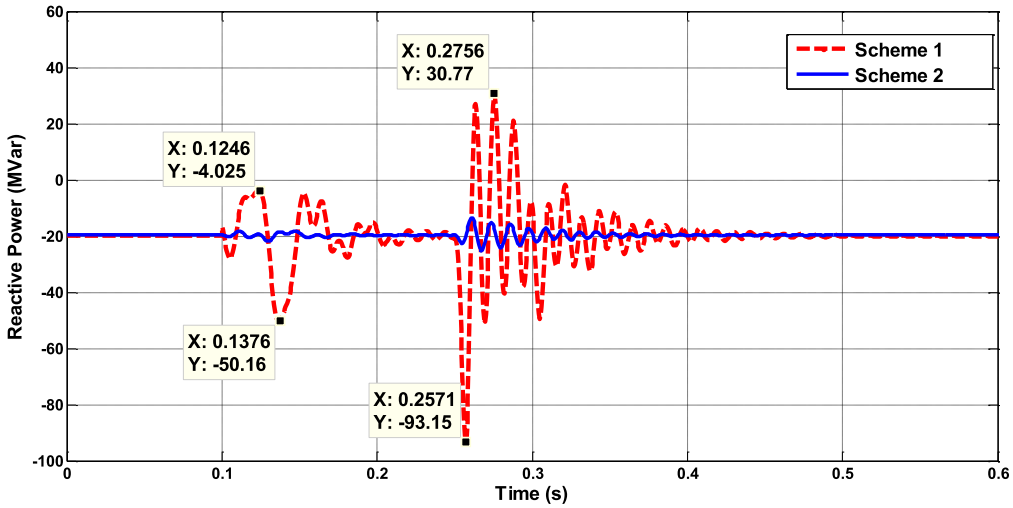

Fig-4.15 The Input Reactive Power at PCC1 on the Rectifier-side (Scheme 1 & 2)

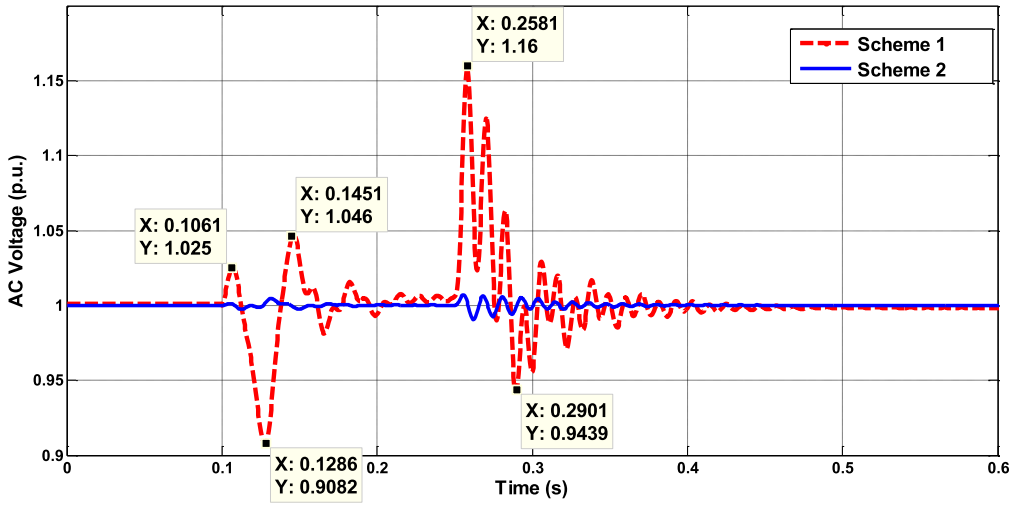

Fig-4.16 The AC Voltage at PCC1 on the Rectifier-side (Scheme 1 & 2)

Compared the dynamic performance on the rectifier-side converter with these two control schemes from Fig-4.14 to Fig-4.16, there are three key features for the simulation results: For such large disturbances on the inverter-side, the dynamic impacts on the offshore wind farms are obvious due to the small SCR of the offshore wind farm. However, with the control

systems of the VSC-HVDC system, the offshore wind farm returned to stable operation condition even with several oscillation swings. Secondly, the dynamic impacts with Scheme 1 are more obvious than those with Scheme 2. Duo to control of the AC voltage at PCC1 of the offshore wind farm, the changes of power exchange between the offshore wind farm and the VSC-HVDC system maintained at acceptable levels. However, with great changes of AC voltage at PCC1 shown in Fig-4.16, the reactive power changed significantly from initial -20 MVar suddenly dropped to nearly -93.15 Mvar in Scheme 1. So Scheme 2 is more suitable for the rectifier-side converter.

Considering the overall dynamic performance with the two control schemes on the rectifier-side converter of the VSC-HVDC system, the Scheme 2 for controlling the terminal voltage of rectifier-side PCC is more suitable for connecting the offshore wind farms consisting of the WT-DFIGs in terms of transient stability.

4.3.2 Case Studies for VSC-HVDC System Connecting with WT-PMSGs

In this simulation system in DIgSILENT/PowerFactory, the offshore wind farms with total rated 144 MW rated WT-PMSGs was connected with the ±150 kV 300 MW rated bipolar VSC-HVDC system. The details of the simulation system are described in Appendix F.

4.3.2.1 Case 3: The Short-circuit Grounded Fault at Rectifier-side

In **Case 3**, with the same case event in **Case 1**, the AC voltage at PCC1 dropped from 1.0 p.u. to 0.8582 p.u. shown in Fig-4.17 when fault was applied at 0.1 s. After 150 ms, the fault was removed and the voltage returned to normal condition of 0.9924 p.u. after several oscillation swings. So the simulation results for the dynamic impacts on the inverters-side of the VSC-HVDC system with two different control schemes for the rectifier-side VSC are shown from Fig-4.18 to Fig-4.21.

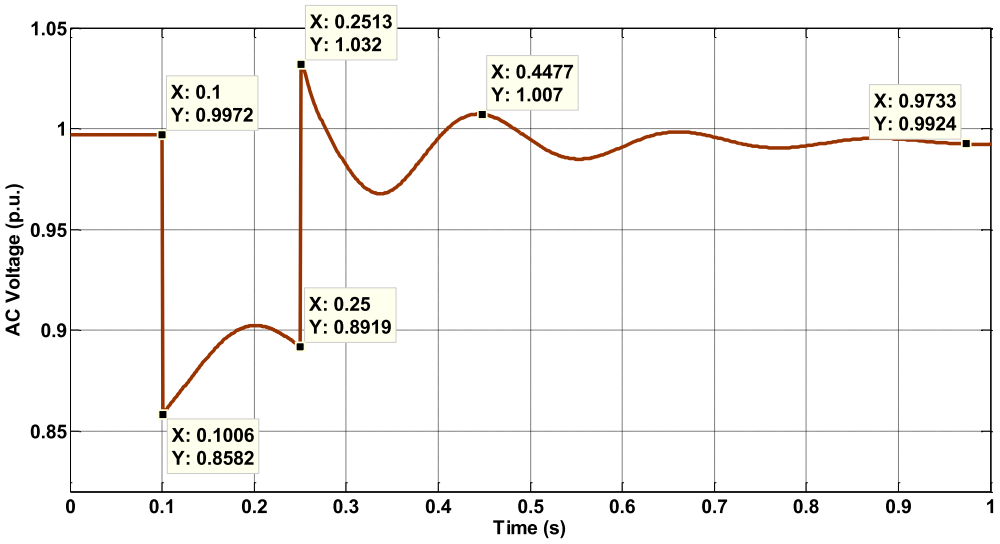

Fig-4.17 The AC Voltage at PCC1 on the Rectifier-side

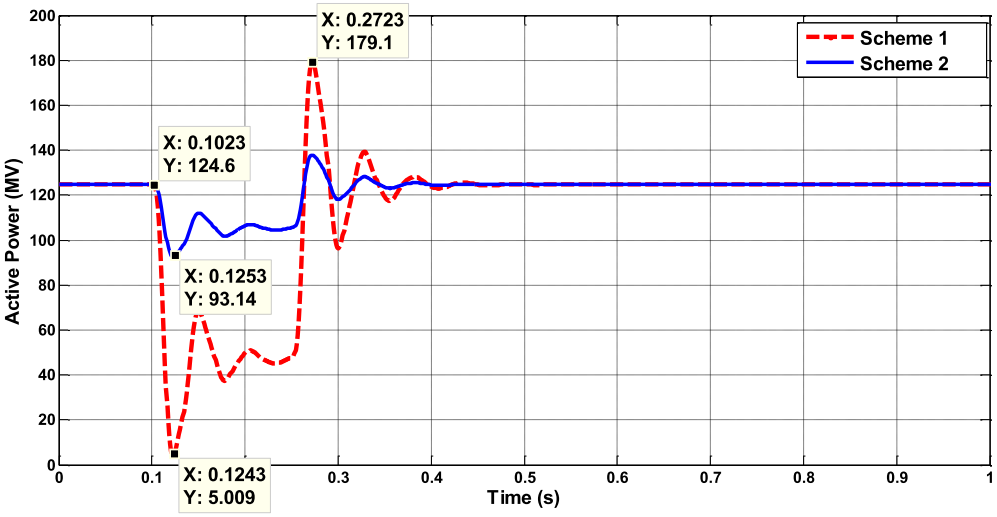

Fig-4.18 The Output Active Power at PCC2 on the Inverter-side (Scheme 1 & 2)

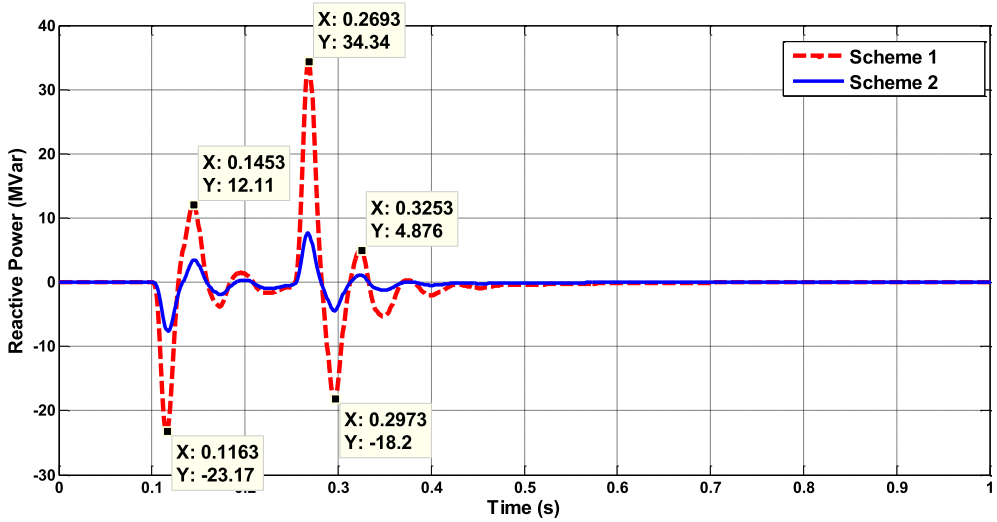

Fig-4.19 The Output Reactive Power at PCC2 on the Inverter-side (Scheme 1& 2)

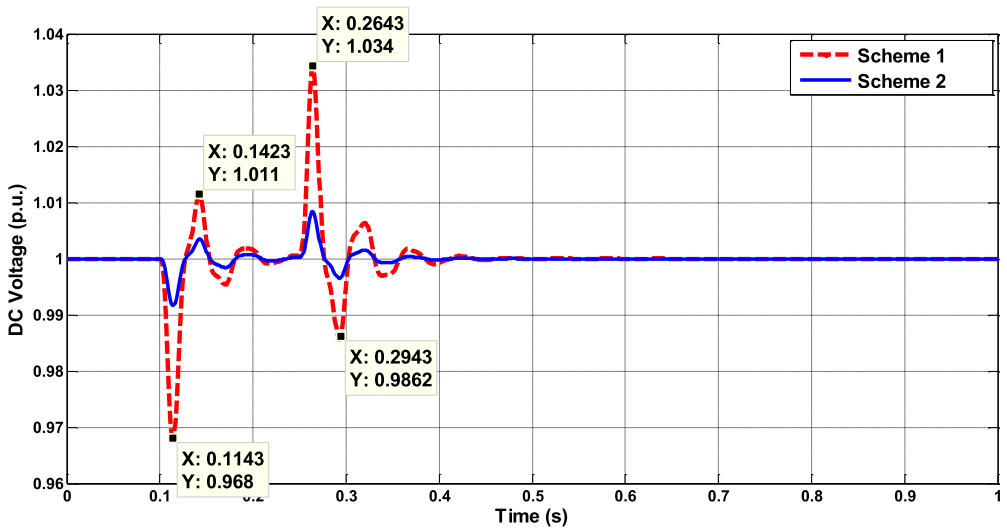

Fig-4.20 The DC Terminal Voltage on the Inverter-side (Scheme 2)

For the output active power at PCC2 in Fig-4.18, the strength of the power oscillation for Scheme 1 is obvious much stronger than that for Scheme 2 with maximum overshoot of 179.1 MW at 0.2723 s and the minimum undershoot of 5.009 MW at 0.1243 s. The power oscillation for Scheme 2 is in the range of 90 to 140 MW. For the output reactive power at PCC2 in Fig-4.15, the strength of the power oscillation for Scheme 1 is obvious much stronger than that for Scheme 2 with maximum overshoot of 34.34 MVar at 0.2693 s and the minimum undershoot of -23.17 MVar at 0.1163 s. The power oscillation for Scheme 2 is in the range of -10 to 10 MVar. For the DC voltage on the inverter-side in Fig-4.20, the strength of the voltage oscillation for Scheme 1 is obvious much stronger than that for Scheme 2 with maximum overshoot of 1.034 p.u. at 0.2643 s and the minimum undershoot of 0.968 p.u. at 0.1143 s. The voltage oscillation for Scheme 2 is in the range of 0.99 p.u. to 1.01 p.u..

For the AC voltage at PCC2 in Fig-4.21, the strength of the voltage oscillation for Scheme 1 is obvious much stronger than that for Scheme 2 with maximum overshoot of 1.015 p.u. at 0.2673 s and the minimum undershoot of 0.9886 p.u. at 0.1153 s. The voltage oscillation for Scheme 2 is in the range of 0.995 p.u. to 1.005 p.u..

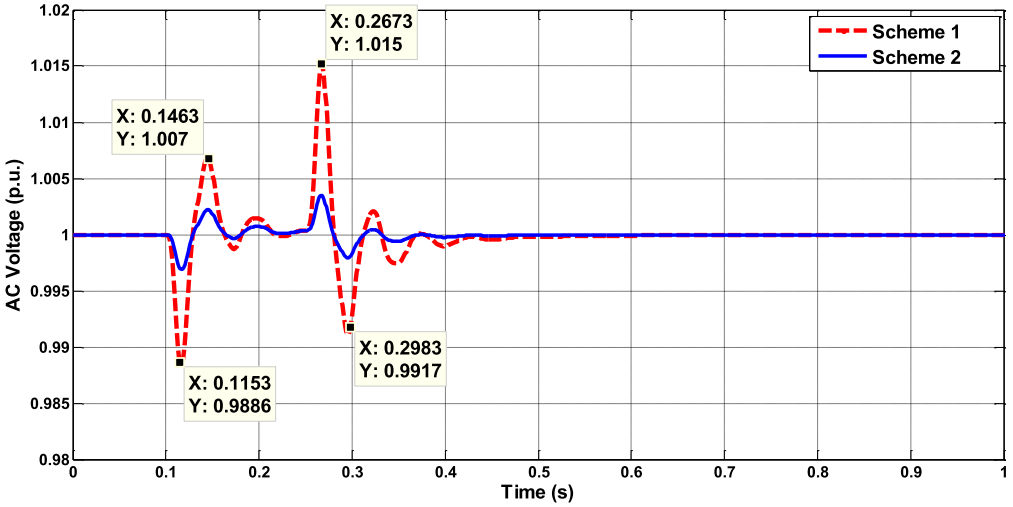

Fig-4.21 The AC Voltage at the PCC2 on Inverter-side (Scheme 1 & 2)

Compared these diagrams in Fig-4.18 to Fig-4.21., there are two key features for this case event: Firstly, the whole system returned to normal operation condition after the transient oscillations under this disturbance with these two control schemes. Secondly, strengths of the oscillations with Scheme 1 are greater than those with Scheme 2. In general, Scheme 2 is more suitable than Scheme 1 for this case event.

4.3.2.2 Case 4: The Short-circuit Grounded Fault at Inverter-side

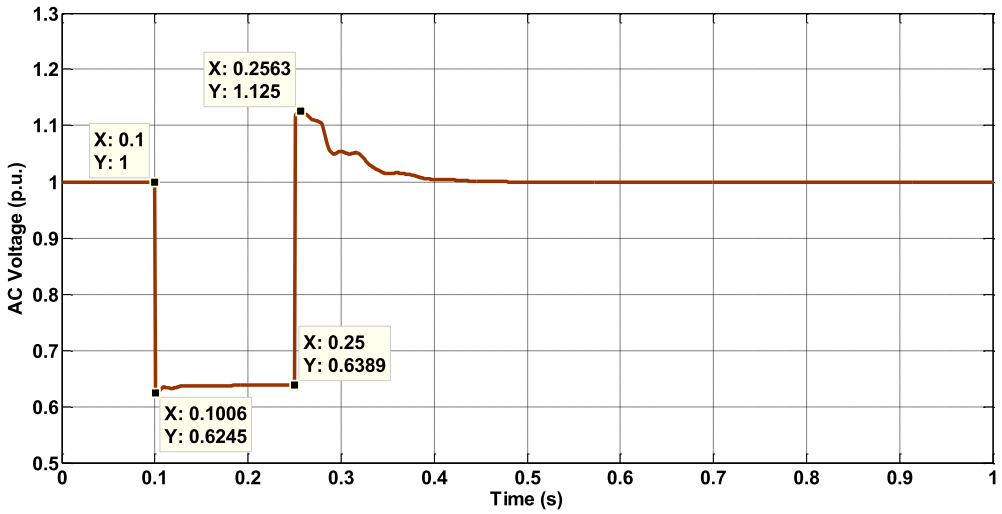

Fig-4.22 The AC Voltage at PCC2 at Inverter-side

In the **Case 4**, the same fault was applied similar to that in **Case 2**. In this condition, the AC voltage at PCC2 in Fig-4.22 dropped sharply from 1.0 p.u. to 0.6245 p.u. at 0.1 s. After 150

ms, the fault was removed and AC voltage at PCC2 recovered to normal operation after the transient process.

For the output active power at PCC1 in Fig-4.23, the strength of the power oscillation for Scheme 1 is obvious much stronger than that for Scheme 2 with maximum overshoot of 143.9 MW at 0.2593 s and 0.3013 s, the minimum undershoot of 141.1 MW at 0.2723 s. The power oscillation for Scheme 2 is in the range of 142.5 to 143 MW. For the output reactive power at PCC2 in Fig-4.24, the strength of the power oscillation for Scheme 1 is obvious much stronger than that for Scheme 2 with maximum overshoot of -7.719 MVar at 0.2763 s and the minimum undershoot of -16.4 MVar at 0.3073 s. The power oscillation for Scheme 2 is in the range of -12 to -11 MVar. For the AC voltage at PCC2 in Fig-4.25, the strength of the voltage oscillation for Scheme 1 is obvious much stronger than that for Scheme 2 with maximum overshoot of 1.04 p.u. at 0.2633 s and the minimum undershoot of 0.9444 p.u. at 0.2783 s. The voltage oscillation for Scheme 2 is in the range of 0.99 p.u. to 1.0 p.u..

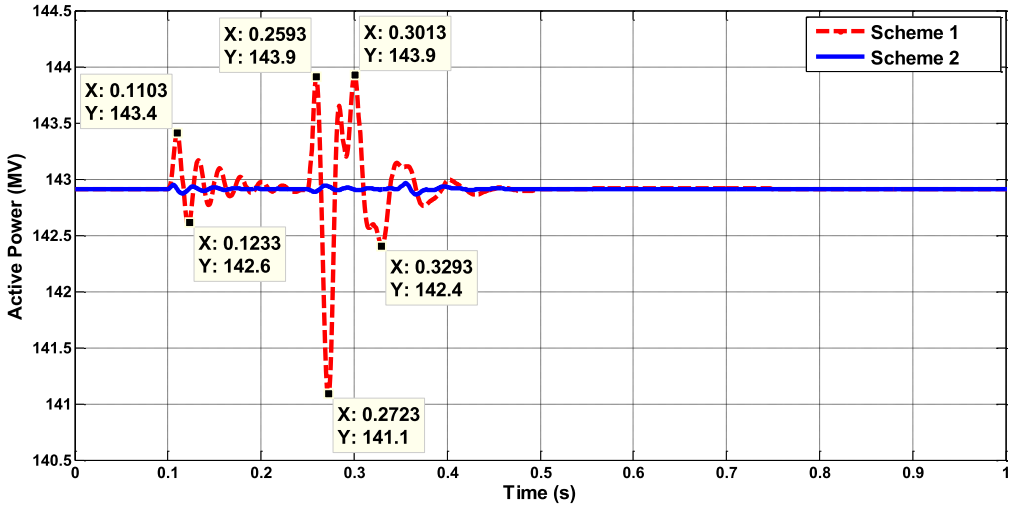

Fig-4.23 The Input Active Power at PCC1 on the Rectifier-side (Scheme 1 & 2)

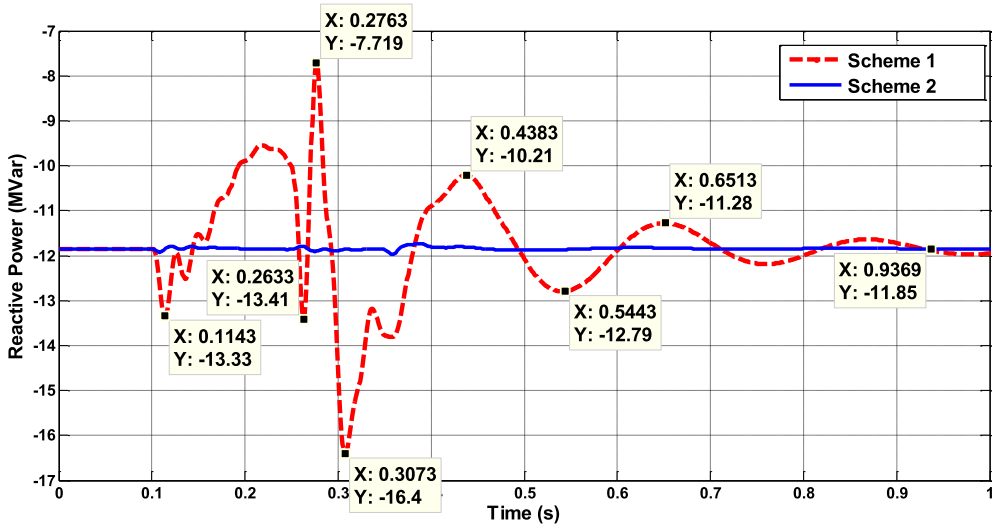

Fig-4.24 The Input Reactive Power at PCC1 on the Rectifier-side (Scheme 1 & 2)

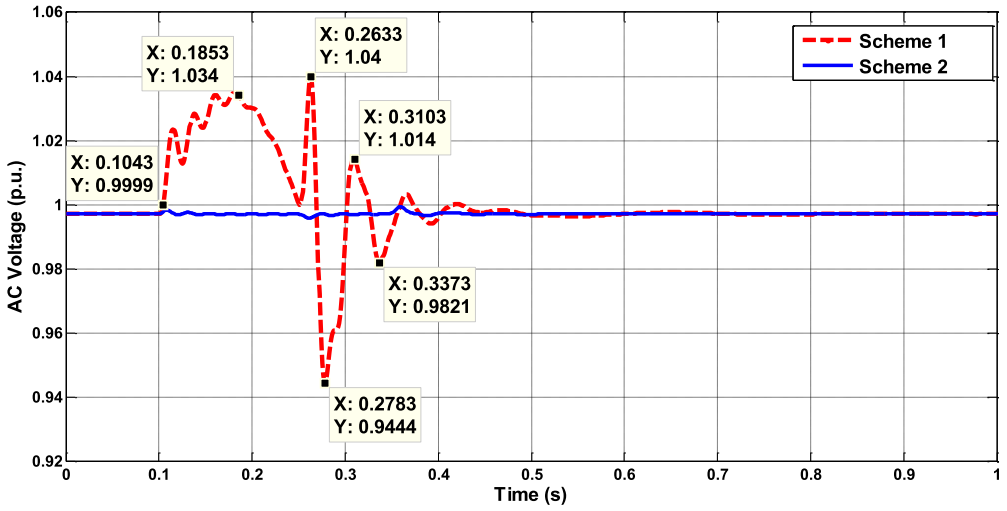

Fig-4.25 The AC Voltage at PCC1 on the Rectifier-side (Scheme 1 & 2)

Compared these diagrams in Fig-4.23 to Fig-4.25, there are two key features for this case event: Firstly, the whole system returned to normal operation condition after the transient oscillations under this disturbance with these two control schemes. Secondly, strengths of the oscillations with Scheme 1 are greater than those with Scheme 2.

In general, Scheme 2 is more suitable than Scheme 1 for this case event. In general, comparing the overall performance of VSC-HVDC system with these two control schemes for the rectifier-side VSC controller during the large disturbances on both sides, Scheme 2

with the aim to control the AC voltage of the rectifier-side PCC is preferred to grid integration of the offshore wind farms with WT-DFIGs and WT-PMSGs in terms of transient stability.

4.4 Summary and Conclusions

In this chapter, the dynamic modelling of rectifier- and inverter-side converters has been firstly represented for transient stability analysis. Then two different control schemes for the rectifier-side converter of the VSC-HVDC systems have been proposed for grid integration of offshore wind farms for transient stability analysis. Finally, the simulation systems for VSC-HVDC systems connecting with two offshore wind farms consisting of WT-DFIGs and WT-PMSGs are tested in DIgSILENT/PowerFactory to evaluate the dynamic performance of the whole system with these two control schemes on rectifier-side of VSC-HVDC system. With the comparisons of the simulation results, the control scheme with the aim of control of the AC voltage at the rectifier-side PCC been validated as the preferred control scheme for rectifier-side converter in the point-to-point VSC-HVDC system to connect with the large-scale offshore wind farms consisting of WT-DFIGs and WT-PMSGs in terms of transient stability.

Chapter 5

Modelling and Control of Bipolar Hybrid CSC/VSC HVDC Systems

5.1 Introduction

Although the CSC-HVDC technology is still dominating the markets for GW-level long-distance power transmission, the VSC-HVDC has great potentials to achieve the higher technical specifications for voltage-levels and power ratings and it can provide new solution to upgrade of current CSC-HVDC systems especially for long-distance power transmission. Taking the BritNed CSC-HVDC project between the GB and Netherlands as an example, the 1000 MW project has been put into commercial operation in 2011 to strengthen UK's role in the EU's electricity market [9]. In the future, with further development of pan-European electricity market, the current CSC-HVDC system should be upgraded such as enhancing the power capacity to meet the further requirements of cross-border power transmission between GB and continental Europe. In this way, there are three possibilities for the upgrade schemes:

1) Upgrades of current components of CSC-HVDC systems to enhance the DC voltage levels and power ratings;
2) Building of new CSC-HVDC systems to operate in parallel with current systems;
3) Building of new VSC-HVDC systems to operate in parallel with current CSC-HVDC systems as the bipolar hybrid CSC/VSC HVDC systems.

Evaluating these schemes, the third is a preferred solution with the reasons as follows:

1) For the Scheme 1 and 2, the extra costs for AC filter banks and reactive power support devices are needed. And such costs can be obviously reduced for scheme 3 due to the characteristics of VSC-HVDC system that no needs for reactive power support [5];

2) The VSC-HVDC systems can even provide reactive power support to the paralleled CSC-HVDC systems due to independent power control of VSC-HVDC systems [5]. Furthermore, during the maintenance of one converter station in the VSC-HVDC system, the other converter station can operate as the STATCOM [114, 115, 144] to provide the reactive power support to the CSC-HVDC system. So it will enhance the reliability, flexibility and cost-efficiency of the upgraded systems;
3) For the power reversal, the voltage polarities of the CSC-HVDC systems should be changed according to the changes of power flow directions. But the voltage polarities of VSC-HVDC systems do not needed to change which is suitable for frequent power reversals in the cross-border interconnectors [5, 6];
4) For the CSC-HVDC system, it has the potential risks of sub-synchronous torsional interaction (SSTI) to damage the shafts of turbine-generators due to the CSC-HVDC converters. With the support from VSC-HVDC systems, the risks of SSTI can be improved [145].

Considering the benefits mentioned above, the scheme 3 of hybrid CSC/VSC HVDC systems is an effective solution to the upgrade of the current CSC-HVDC systems to maximise their potentials with improved operation reliability, flexibility and cost-efficiency to meet the further requirements for long-distance power transmission. And such upgrade scheme has been approval for the upgrade of the existing monopolar Skagerrak 3 CSC-HVDC Link which was established in 1993 between Denmark and Norway. The new Skagerrak 4 monopolar VSC-HVDC project is expected to be commissioned in 2014 and work in parallel with the Skagerrak 3 CSC-HVDC Link as the bipolar hybrid CSC/VSC system to increase the power transmission capability from 440 MW to 1140 MW.

In this chapter, the modelling of the CSC-HVDC system is investigated at first to determine the key factors for the dynamic performance of the whole system in the transient stability analysis. Secondly, the control strategies for the rectifier- and inverter-side converters are designed to achieve the coordination between each other to maintain the operation stability under small and large disturbances. Thirdly, the updating schemes for the existing CSC-HVDC are described to improve two key issues of CSC-HVDC systems with the support from the parallel VSC-HVDC systems. Finally, the bipolar CSC- and hybrid CSC/VSC HVDC systems are built in DIgSILENT/PowerFactory for transient stability analysis to evaluate the whole performance of the CSC-HVDC systems and feasibilities of the proposed upgrade scheme for the CSC-HVDC systems with the support of the VSC-HVDC systems in parallel for power transmission.

5.2 Configuration of CSC-HVDC Systems

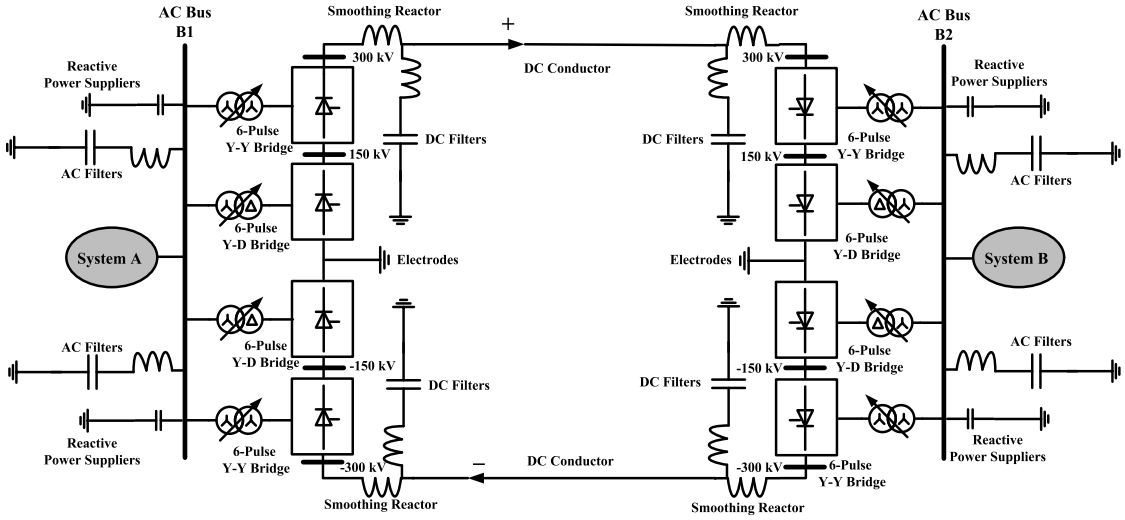

Fig-5.1 The General Configuration of 24-Pulse Bipolar CSC-HVDC Systems

The CSC-HVDC systems are commonly classified into three types according to their configurations: monopolar, bipolar and homopolar layouts. For the real industrial applications, the bipolar links are mostly built due to their advantages over other two types such as independent operation of valve groups in two polarities and no ground current [2]. The

general configuration of the bipolar CSC-HVDC systems is shown in Fig-5.1 above and they usually contain two groups of basic monopolar links in the positive- and negative-polarity. For the homopolar links, the configuration is very similar to Fig-5.1. However, the same polarity, usually the negative polarity, is used for all the valves groups. The detailed configurations of monopolar and homopolar CSC-HVDC systems are described in [2]. The key components in the one polarity of the 24-pulse bipolar links are listed as follows:

1) **Converters**: Two 6-pulse valve bridges on each side to perform the AC-DC power transformations and they are connected in series to obtain required DC voltages for HVDC systems.
2) **Converter Transformer**: two converter transformers with Y/Y and Y/Δ connections are connected between the AC buses and two valves bridges respectively to not only adjust the AC voltages of HVDC converters with tap-changers [2, 4] but also effectively eliminated the 5th and 7th harmonics on the AC-side to reduce the costs for such harmonic filters [2].
3) **AC Filter Banks**: for the 12-pulse valve bridges, the 11th, 13th and 23th harmonics are the main components of AC harmonics so the filter banks consisting of three branches are designed to eliminate the effects of the harmonics with such orders [2].
4) **Reactive Power Suppliers**: for the normal operation of CSC-HVDC system, it should absorb large amount of reactive power. So reactive power support devices should be needed for maintaining the AC-side voltages of valve bridges at rated levels. In this way, reactive power suppliers such as shunt capacitor banks or FACTS devices such as SVCs (Static Var Compensators) and STATCOMs can be connected to the AC buses in shunt to realise the adjustable reactive power compensation [114, 115, 144].
5) **Smoothing Reactors**: On the DC-side, smoothing reactors with large inductance are connected to the DC-sides of converter with the main purposes described in [2]:

5.3 Modelling of CSC-HVDC System

5.3.1 The Characteristics of Thyristor Valves

The thyristor valves shown in Fig-5.2 can be acted as the controllable diode. It only can be conducted when two requirements are both met:

1) The relative voltage between the Anode polarity and Cathode polarity is positive;
2) The ignition signal is sent to the Gate polarity to make the thyristor switch-on.

When the two requirements are met, the current goes from the Anode polarity to Cathode polarity. When the relative voltage between these two polarities is negative, the thyristor is blocked and the current through the thyristor is zero.

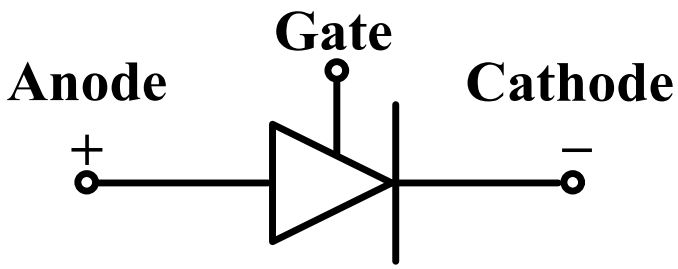

Fig-5.2 The Diagram of Thyristor Valve

5.3.2 Modelling of Rectifier-side CSC

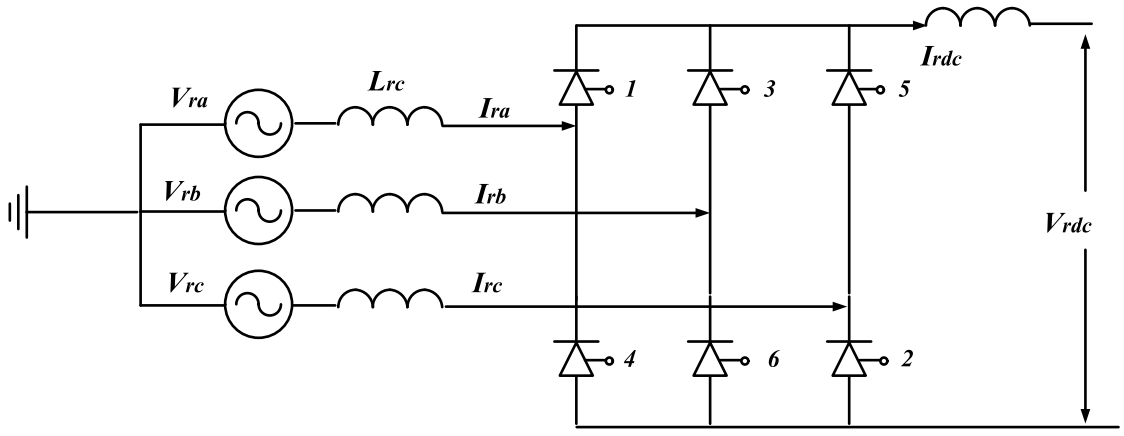

Fig-5.3 The Diagram of 6-Pulse Bridge for Thyristor-based AC/DC Converter

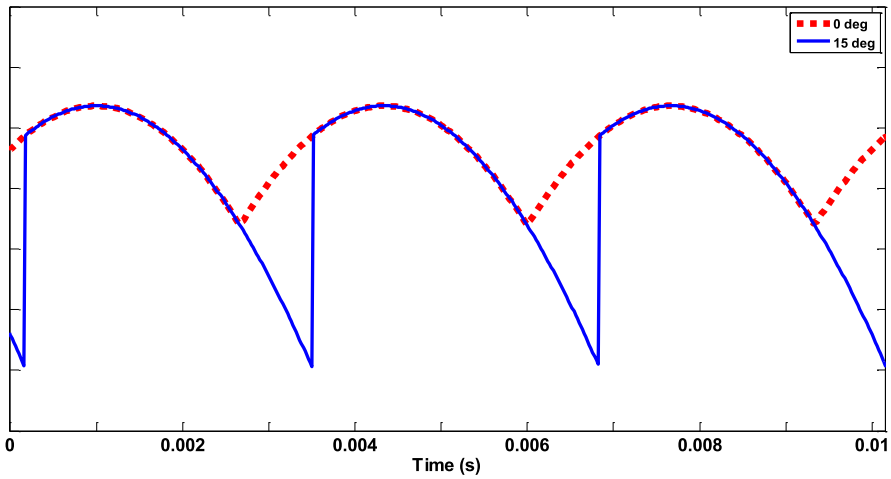

Fig-5.4 The Comparisons between DC Voltages for *α=0*º and *15*º at Rectifier-side Converter

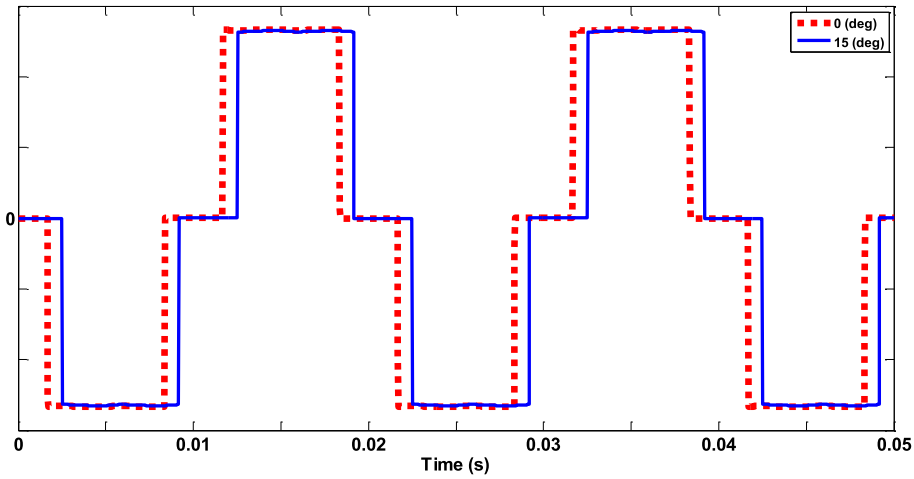

Fig-5.5 The Comparisons between DC Currents for *α=0*º and *15*º at Rectifier-side Converter

The equivalent circuit of the thyristor-based AC/DC converter on the rectifier-side is shown in Fig-5.3 [2]. In this diagram, the DC voltage on the rectifier-side can be expressed by:

$$V_{rdc0} = \frac{3\sqrt{2}}{\pi} V_{rac} \tag{5.1}$$

where V_{rdc0} is the DC voltage without ignition and overlap delays and V_{rac} is the RMS value of AC-side voltage of valve bridges. The thyristor can be controlled to conduct by the delayed ignition signal, the so called "delay angle" α, so the DC voltage with ignition delay but no overlap delay is given [2]:

$$V_{rdc} = V_{rdc0} \cos\alpha \tag{5.2}$$

So DC voltages and currents on the rectifier-side converter with α=0º and 15º are shown in Fig-5.4 and Fig-5.5. Due to the effects of AC inductance, the specific time delay exists for the transfer of phase currents and this specific time is called "overlap time" μ. So the commutation from one-phase current to another starts at the time α and finishes at the time $\alpha+\mu$, δ is defined as the so-called "extinction angle" which equals the sum of α and μ. So the DC voltage on the rectifier-side with the effects of ignition and overlap delays is given by [2]:

$$V_{rdc} = \frac{V_{rdc0}}{2}(\cos\alpha + \cos\delta) \tag{5.3}$$

And the DC voltage can be also represented by:

$$V_{rdc} = V_{rdc0} \cos\alpha - \Delta V_{rdc} = V_{rdc0} \cos\alpha - R_{rc} I_{dc} \tag{5.4}$$

$$R_{rc} = \frac{3}{\pi} \omega L_{rc} = \frac{3}{\pi} X_{rc} \tag{5.5}$$

where R_c is the so-called equivalent commutating resistance [2] to express the effects of overlap delay of AC inductances for the DC voltage drop on the rectifier-side. So DC voltage and current on the rectifier-side converter with and without overlap delay at $\boldsymbol{\alpha}$=0º are shown in Fig-5.6 and Fig-5.7.

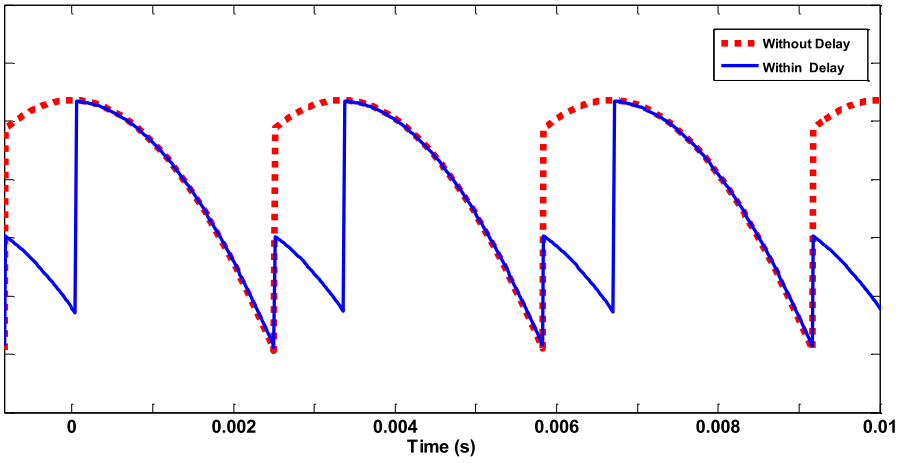

Fig-5.6 The Comparisons between DC Voltage with and without Overlap Delay

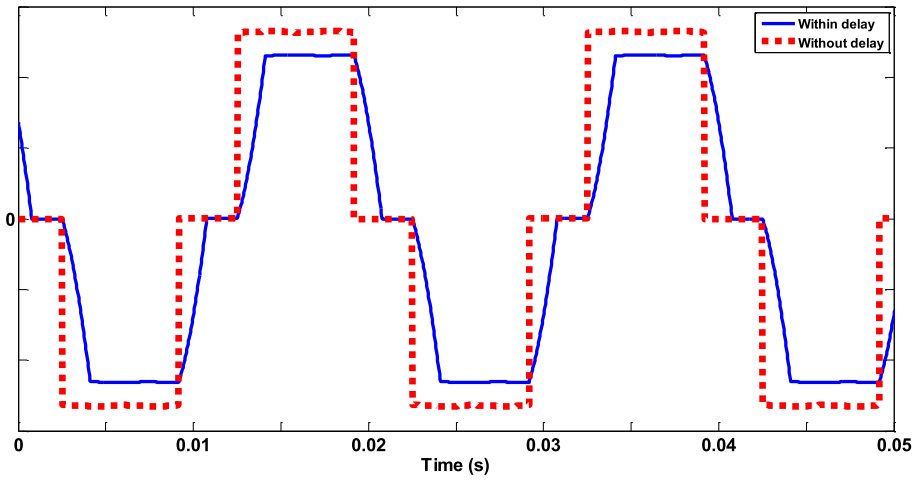

Fig-5.7 The Comparisons between DC Current with and without Overlap Delay

5.3.3 Modelling of Inverter-side CSC

For the modelling of the inverter-side converter, the principles are similar to those for rectifier-side converter. Because the values for α and μ are in the range between 90º and 180º, the two other variables are usually defined for the inverter given by:

$$\beta = \pi - \alpha \tag{5.6}$$

$$\gamma = \pi - \delta \tag{5.7}$$

where β is the ignition advance angle, γ is the extinction advanced angle. And the DC voltage on the inverter-side is given by [2]:

$$V_{idc} = \frac{V_{idc0}}{2}(\cos\beta + \cos\gamma) \tag{5.8}$$

or given by [2]:

$$V_{idc} = V_{idc0}\cos\gamma - R_{ic}I_{dc} \tag{5.9}$$

5.4 Control Strategies for CSC-HVDC Systems

5.4.1 The Normal Operation Characteristics of CSC-HVDC System

With the expressions of DC voltages on the rectifier- and inverter-side in (5.4) and (5.9), the DC current cross the CSC-HVDC system is given [2]:

$$I_{dc} = \frac{3\sqrt{2}(V_{rac}\cos\alpha - V_{idc}\cos\gamma)}{\pi(R_{rc} + R_L - R_{ic})} \tag{5.10}$$

As seen from the (5.10), the CSC-HVDC systems are controlled by the fast-response α and γ in milliseconds primarily and AC voltages of the converters regulated by the supplementary on-load tap-changers (OLTC) of the converter transformers in seconds. Furthermore, in order to achieve the high power factor of the CSC-HVDC systems, the α and γ should be kept as low as possible [2, 4]. As a result, the α and γ are the key control objectives for the controllers of the rectifier- and inverter-side converters. For the practical operation characteristics of CSC-HVDC systems, the operation curves of DC voltages versus DC current are shown in Fig-5.8 for the rectifier- and inverter-side converters.

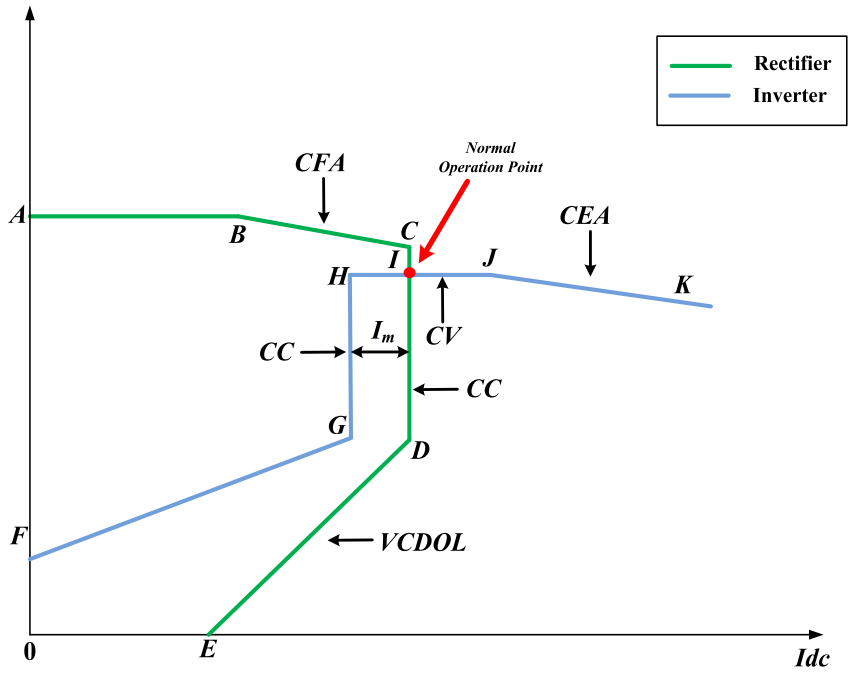

Fig-5.8 The Relationship of V_{dc} and I_{dc} in the CSC-HVDC Systems

Normally, the constant DC current mode (**CC**) [2, 4] is chosen for the rectifier-side controller in its operating points from the ***C*** to ***D*** in Fig-5.8 by changing the α in responses to the derivations between the I_{dc} and its current order I_{ord}. For the inverter-side, the constant DC voltage mode (**CV**) from ***H*** to ***J*** is applied for the practical operation of CSC-HVDC systems, And the constant extinction angle mode (**CEA**) from ***J*** to ***K*** is proposed as well in [2, 4]. So

these two modes are applied together for different operation condition. And the cross-point ***I*** of the two operation curves is the normal operation point for the CSC-HVDC system.

5.4.2 The VDCOL Characteristics of CSC-HVDC System

In the operation curves shown in Fig-5.8, the operating points from ***D*** to ***E*** and from ***F*** to ***G*** for the rectifier- and inverter-side converters reflect the characteristics of voltage-dependent current-order limit (VDCOL) for reducing the current orders in responses to the condition of low-voltage dynamically to solve the problems caused by low voltages during abnormal operation condition [2].

5.4.3 The Rectifier-side CSC Controller

According to the operating curves of CSC-HVDC system, the rectifier-side CSC controller is shown in Fig-5.9 for the CC mode by regulating α in response to the derivations between the I_{dc} and its current order I_{ord} in (5.11) via the PI controller.

$$I_{ord} = \frac{P_{ord}}{V_{rdc}} \tag{5.11}$$

where P_{ord} is the per-unit input power order for the normal operation of the system.

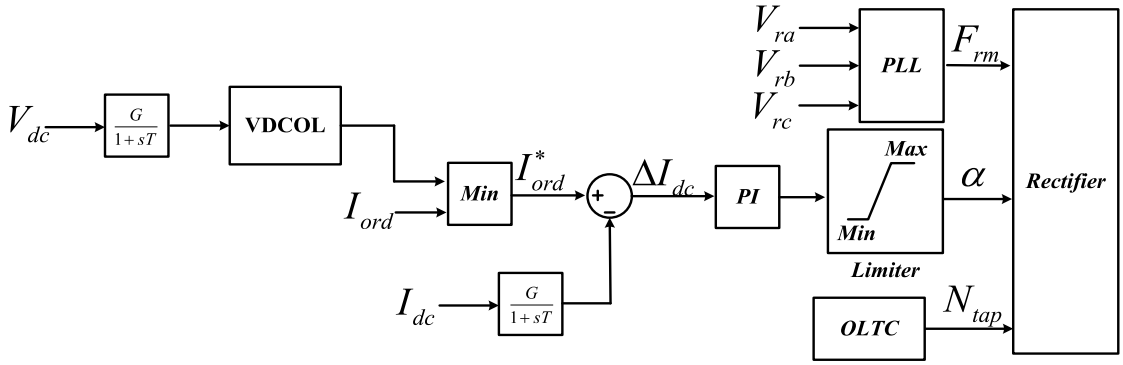

Fig-5.9 The Rectifier-side CSC Controller

If the DC voltage on the rectifier-side drops below the point ***D***, the function of VDCOL will be applied to reduce the I_{ord} dynamically in response to voltage drops. And the slow-response OLTC controller is applied as the supplementary controller to increase the AC voltages by changing the tap-positions of the tap-changers in the rectifier-side converter transformers to

help support the fast-response $\boldsymbol{\alpha}$ controller for maintain the stability operation when the $\boldsymbol{\alpha}$ reaches its minimum limit [4].

5.4.4 The Inverter-side CSC Controller

According to the operating curves of CSC-HVDC system, the inverter-side CSC controller is shown in

Fig-5.10 for the CV and CEA modes: the inverter-side DC voltage V_{idc} and γ are compared with their reference values respectively. And the minimum-selector is applied to send the minimum derivations to the PI controllers for regulating the specified γ for the inverter-side converter.

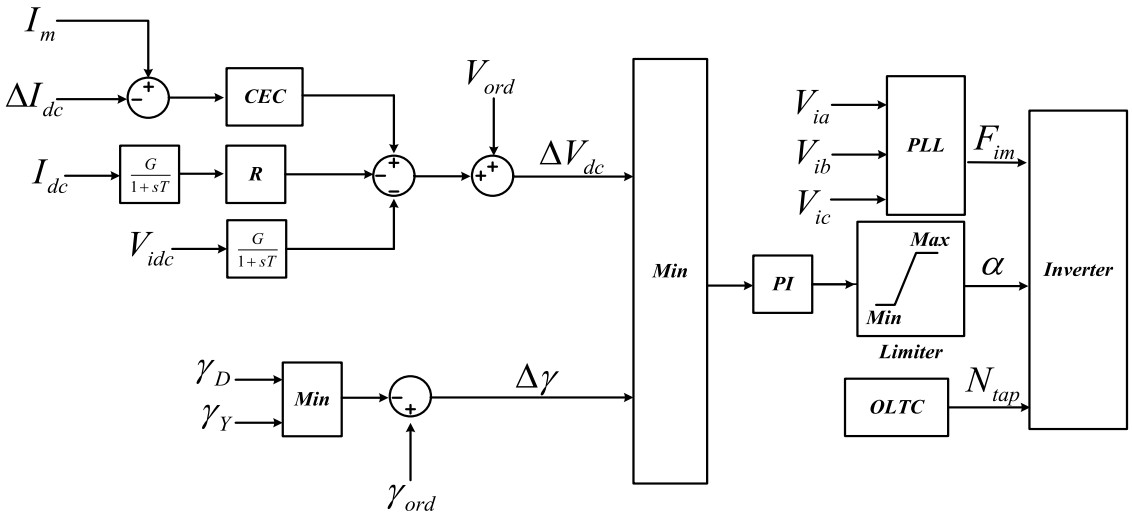

Fig-5.10 The Inverter-side CSC Controller

5.5 Support of VSC-HVDC Systems for CSC-HVDC Systems

5.5.1 Two Key Issues of CSC-HVDC Systems

5.5.1.1 Reactive Power Support

For the normal operation of the CSC-HVDC systems, the reactive power compensations are needed. According to the power flow analysis of the CSC-HVDC systems, the relationship between the converter's active power P_c and reactive power Q_c can be approximately

represented by the linear curve shown in Fig-5.11. The reactive power is changing dynamically in responses to the different power ratings of the CSC-HVDC systems.

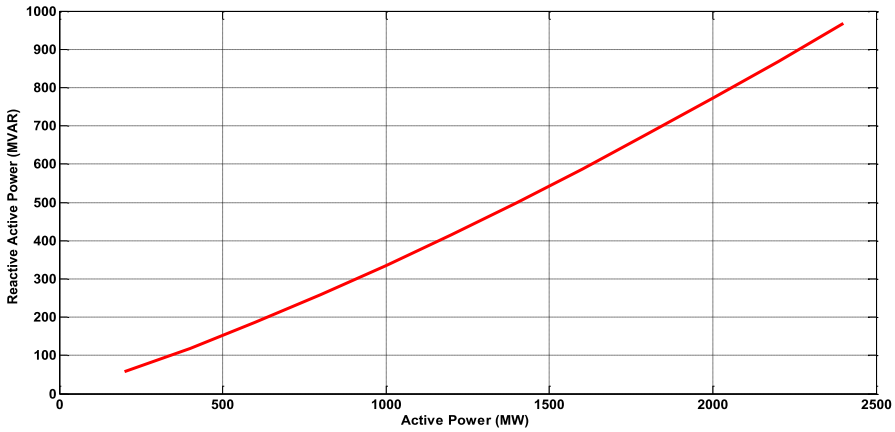

Fig-5.11 The Relationship of Active- and Reactive Power in CSCs

Currently, there are three possibilities: the shunt capacitors, the AC filter banks and the FACTS-based devices such as SVCs and STATCOMs. Besides the function as the harmonic filters, the AC filter banks can play the roles as the shunt capacitors for reactive compensations [2, 4]. So the AC filter banks are regarded as the economic solution to reactive power compensation for the CSC-HVDC systems. However, due to the characteristics of capacitors for charging and discharging, the response-time for the AC filter banks is very slow (Average 5-6 s to switch-on or –off). Furthermore, the power capacity of each capacitor branch is fixed and the reactive power is not able to change dynamically according to the changes of power rating of CSC-HVDC systems. For the FACTS-based devices such as SVC and STATCOMs, they can provide the reactive power dynamically according to the changes of power rating. However, the costs for such devices are much higher comparing with the costs for AC filter banks. The VSC-HVDC systems have the functions similar to the VSC-based STATCOMs to provide the reactive power support according to the characteristics of VSC-HVDC systems for dynamic control of reactive power in response to the changes of the power rating [5, 6]. In this way, the VSC-HVDC systems can not only increase the transmission capacity but also provide the extra reactive

power support to the neighbouring CSC-HVDC systems in parallel dynamically and the costs for extra reactive power compensators can be largely reduced.

5.5.1.2 Inverter-side Commutation Failure

The failure of the commutation before the transfer of the phase voltages is called the commutation failure [2]. Such abnormal condition will bring great damages to the valve bridges and the converters should be blocked when such abnormal condition exist. The commutation failures are mainly caused by low AC voltages due to the short-circuit faults [2, 4] and they are more common on the inverter-side than the rectifier-side. And the VSC-HVDC Systems can provide the fast AC voltage support for the CSC-HVDC Systems to mitigate the potential risks of commutation failures mentioned in [118].

5.5.2 Configuration of Bipolar Hybrid CSC/VSC HVDC Systems

The bipolar hybrid CSC/VSC HVDC systems are suitable for upgrade of the monopolar CSC-HVDC systems mentioned in Section 5.1, operating in parallel with neighbouring monopolar VSC-HVDC system as the bipolar hybrid HVDC system shown in Fig-5.12. The strategies of the power reversal for the bipolar hybrid HVDC systems are proposed in [118] with the coordination of circuit breakers in the converter stations.

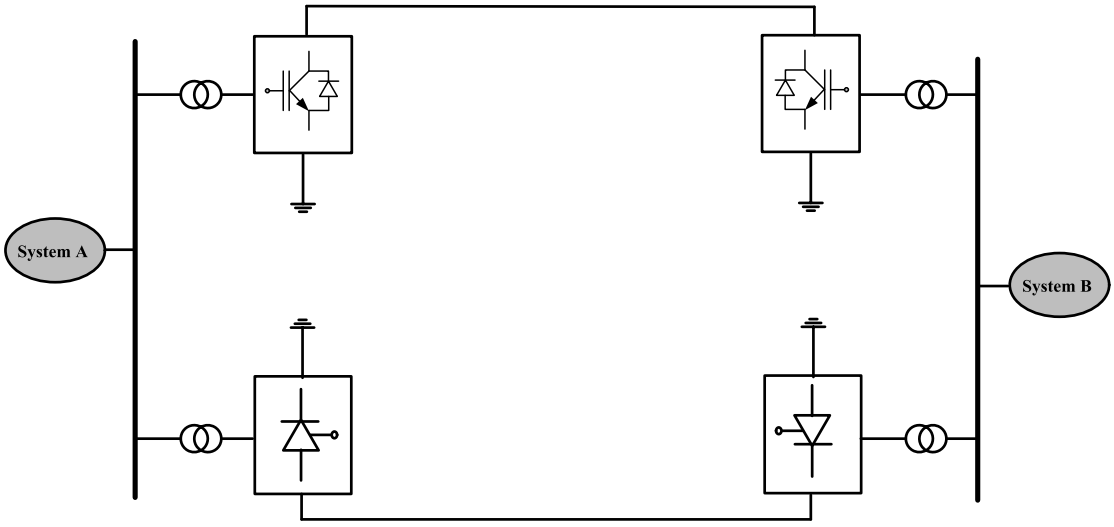

Fig-5.12 The Configuration of the Bipolar Hybrid CSC/VSC HVDC System

5.5.3 Support of the VSC-HVDC Systems to the CSC-HVDC Systems

Considering the two key issues of the CSC-HVDC systems mentioned in Section 5.5.1, the control modes for the rectifier- and inverter-side of the monopolar VSC-HVDC system for the support to the neighbouring monopolar CSC-HVDC system are listed below:

Table-5.1 The Control Modes of VSC-HVDC System in Hybrid CSC-VSC/HVDC System

	Rectifier	**Inverter**
***d*-axis Control Mode**	P	V_{dc}
***q*-axis Control Mode**	Q	Q

For the *d*-axis VSC controllers, the control modes are similar to general VSC-HVDC systems shown in Section Chapter 14.2: ***P*** mode for rectifier-side converter to supervise and control the input active power of the VSC-HVDC system and the $\boldsymbol{V_{dc}}$ mode to supervise and control the DC voltage of inverter-side converter for the balance of AC and DC power transformation of VSC-HVDC systems. The ***Q*** Mode is applied to the *q*-axis VSC controllers on the both sides of this VSC-HVDC system to supervise and control the reactive power for the needs of reactive power compensation for the CSC-HVDC systems during the steady operation. For the large disturbances on the inverter-side, especially the short-circuit faults, the VSC on the inverter-side will provide fast and flexible reactive power support to maintain the AC voltage of the inverter-side converter at the specific levels during the condition of short-circuit faults to avoid severe voltage dips to cause the inverter-side commutation failures [2, 4, 114].

5.6 Case Studies

5.6.1 Simulation Systems

For **Case 1** to **3**, the bipolar ±250 kV 1000 MW rated CSC-HVDC system was firstly built in the DIgSILENT/PowerFactory for power transmission with the length of 200 km. The details of the bipolar CSC-HVDC systems are described in Appendix G. For **Case 4** and **5**, the bipolar hybrid CSC/VSC HVDC system was built in DIgSILENT/PowerFactory as well with

parallel operation of the +250 kV 500 MW rated monopolar VSC-HVDC and the -250 kV 500 MW rated monopolar CSC-HVDC links as the bipolar ±250 kV 1000 MW hybrid system. The details of the bipolar CSC/VSC Hybrid HVDC systems are described in Appendix G. The SCR of the external systems on both sides of HVDC link is 3.

5.6.2 Case 1: Increasing the Power Rating of CSC-HVDC System

In **Case 1**, the power rating of the bipolar CSC-HVDC system increased suddenly from 1.0 p.u. (1000MW) to 1.1 p.u. (1100MW) at 1.0 s as shown in Fig-5.13. According to (5.11), the current order I_{ord} shown in Fig-5.14 changed in response to the changes of power order P_{ord} and the rectifier-side DC Voltage V_{rdc} shown in Fig-5.15.

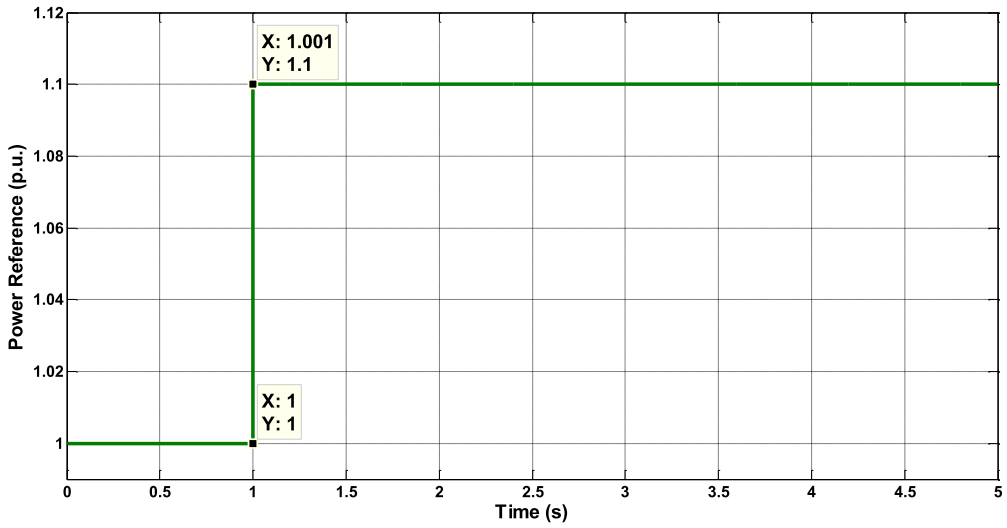

Fig-5.13 The Increase of Power Reference of CSC-HVDC System

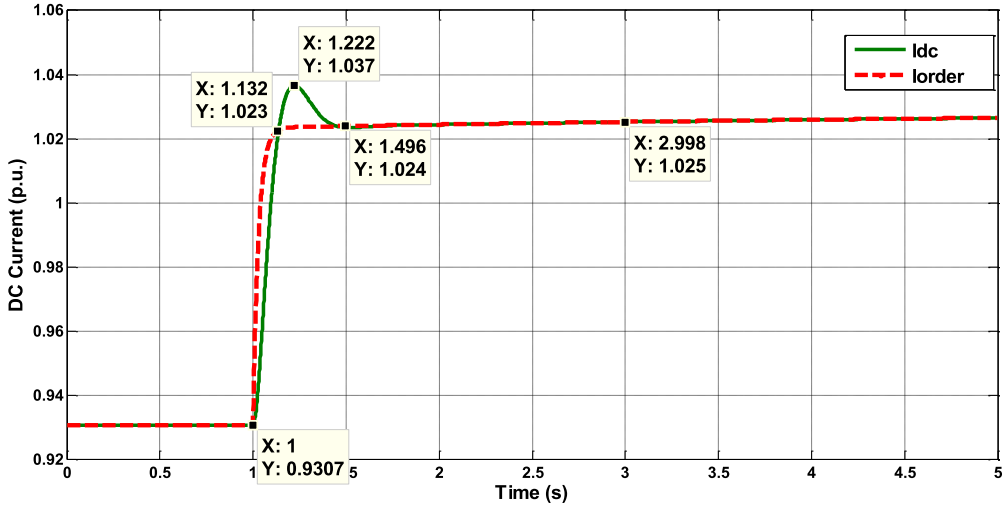

Fig-5.14 The DC Current and Its Current Reference on Rectifier-side

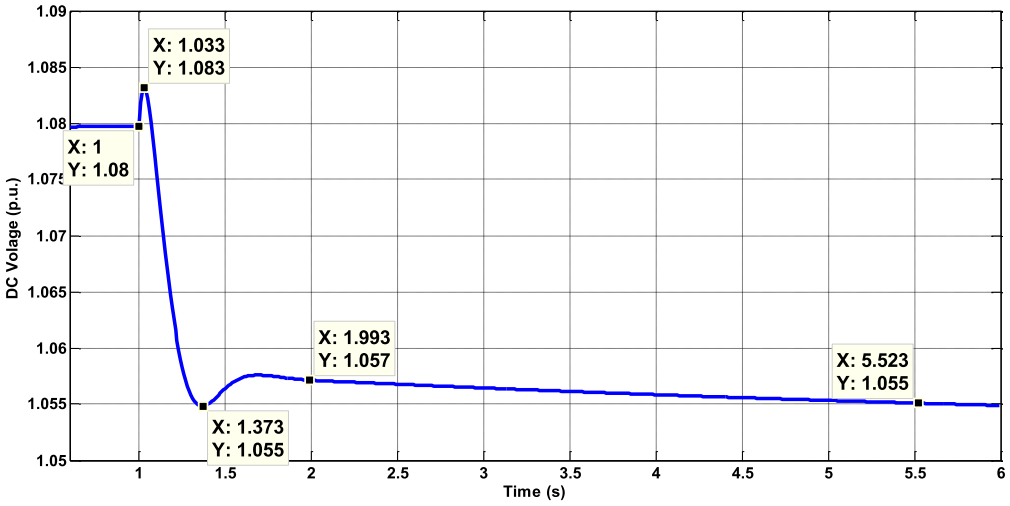

Fig-5.15 The DC Voltage on the Rectifier Side

The increased I_{ord} caused the firing-angle α of the rectifier-side converters to decrease with the purpose of forcing the actual DC current to trace the I_{ord} via the rectifier-side current PI controller. Due to the functions of PI controller and the relatively small SCR of the external system on the rectifier-side, an overshoot of 1.037 (1.26%) at 1.222 s in the curve of the actual DC current I_{dc} shown in Fig-5.14. And the system returned to normal condition of 1.024 p.u. at 1.496 s. For the rectifier-side DC Voltage V_{rdc} in Fig-5.15, the overshoot of 1.083 p.u. (0.2%) appeared at 1.033 s and the system returned to the normal condition at nearly 5.523 s.

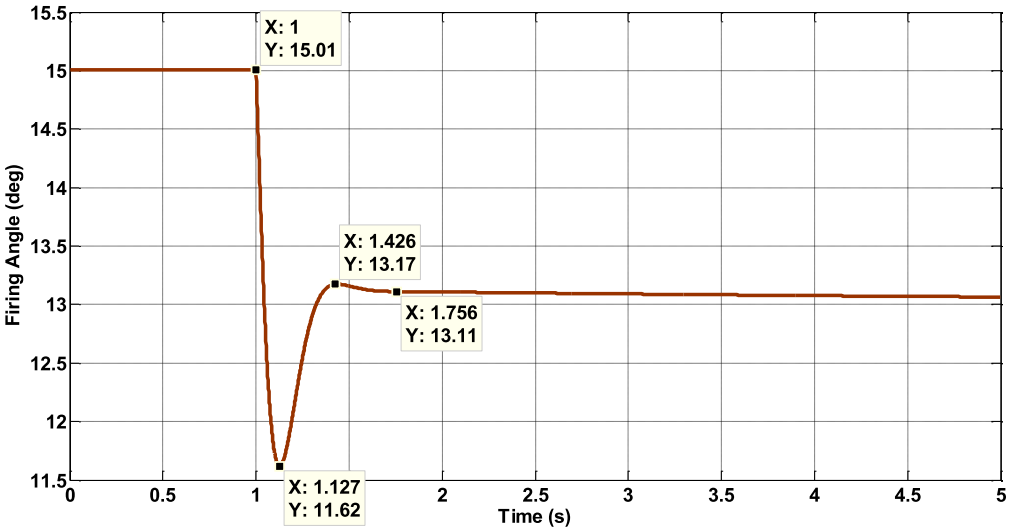

Fig-5.16 The Firing-angle of the Rectifier-side Converters

The changes of α are illustrated in Fig-5.16, the undershoot of 11.62° (22.5%) appeared at 1.127 s and α returned to another operating condition of 13.11° at nearly 1.756 s after the transient process. The extinction angle γ of the inverter-side converters shown in Fig-5.17 changed simultaneously in response to the changes of α to maintain the voltage drops across the two sides at acceptable levels. The undershoot of 24.5° (2.19%) appeared at 1.143 s and the overshoot of 25.09° (0.1%) appeared at 1.503 s. After the transient process, the γ returned to normal operation condition of 25.04° at nearly 1.753 s

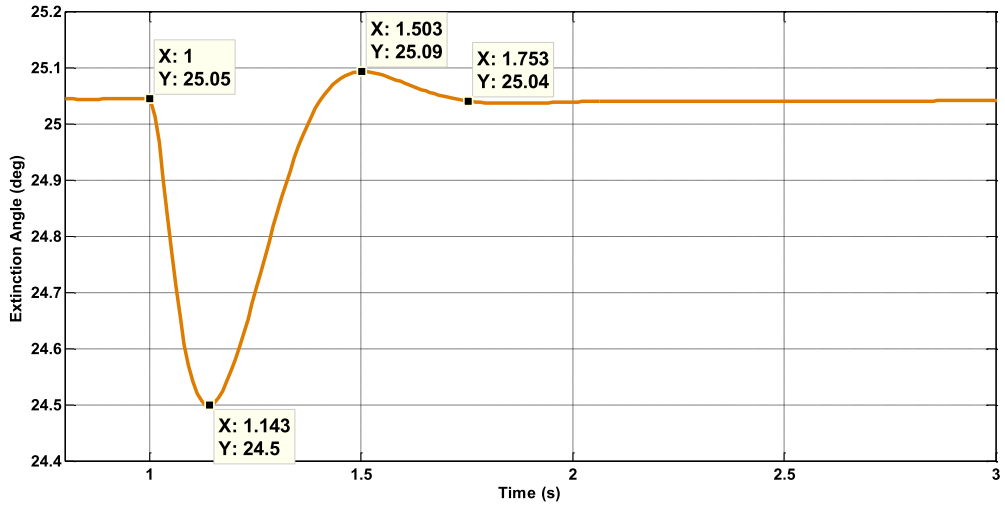

Fig-5.17 The Extinction Angle at the Inverter-Side Converters

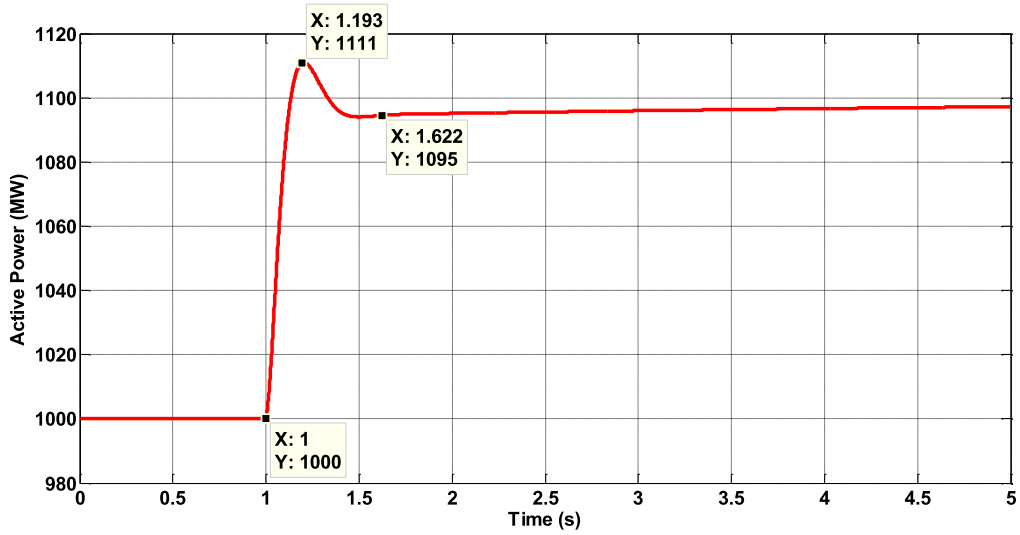

Fig-5.18 The Input active Power to Rectifier-side Converters

As for the active power P_r sent from the rectifier side shown in Fig-5.18, it changed with nearly the same trends as the I_{dc} because the rectifier-side DC voltage V_{rdc} changed slightly compared with the changes of $I_{dc.}$. An overshoot of 1111 MW (1.45%) appeared at 1.193 s and the system returned to normal operation condition of 1095 MW at nearly 1.193 s. For the reactive power Q_r shown in Fig-5.19, a sudden decrease appeared due to the fast-response of firing-angle at the initial stage. After the initial decrease, it increased with the same trends as the P_r according to the power characteristics of thyristor-based converters described in Section 5.5.1.1. An undershoot of 456.4 MVar (1.5%) appeared at 1.033 s and an overshoot of 502.4 (0.4%) at 1.315 s. The system returned to normal condition of 500 MVar at nearly 1.74 s.

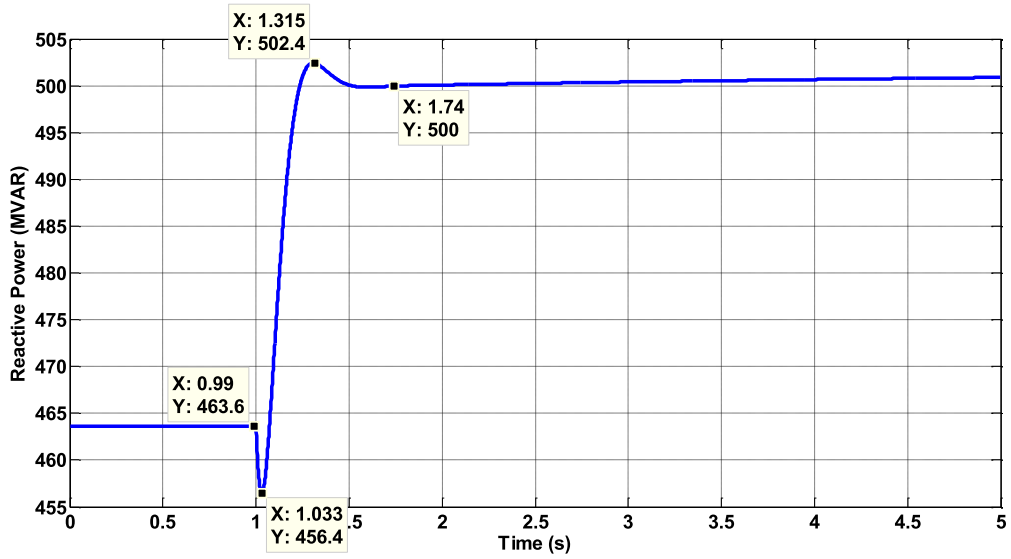

Fig-5.19 The Input Reactive Power to Rectifier-side Converters

Review of all the simulation results, for this scenario, it just brought obvious impacts on the firing angle α during the transient process. For other variables, the dynamic impacts for very small in terms of magnitudes of the over/undershoots. Furthermore the whole system can return to the normal operation with the proper functionalities of converter controllers on both sides of the CSC-HVDC system.

5.6.3 Case 2: Three-phase Short-circuit Fault on Inverter-side

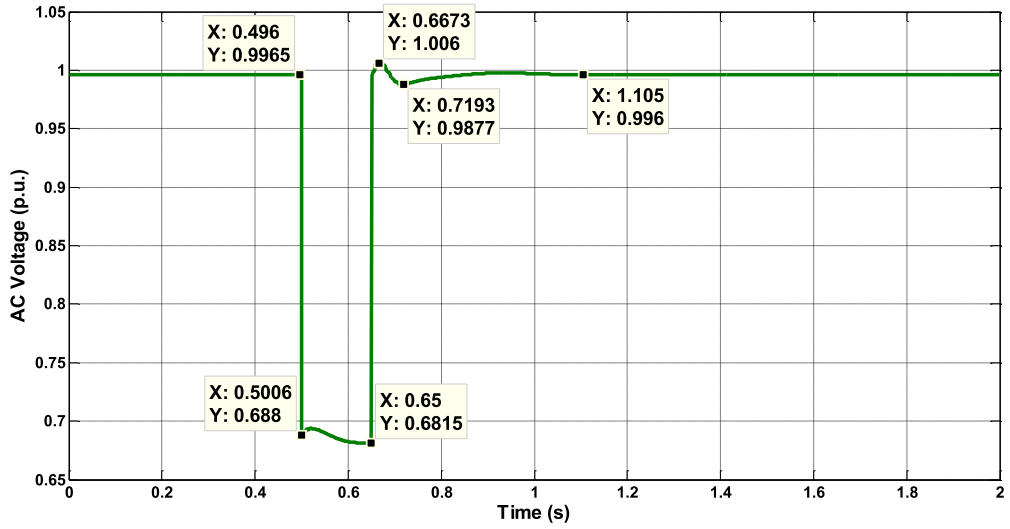

Fig-5.20 The AC Voltage on the Inverter-side

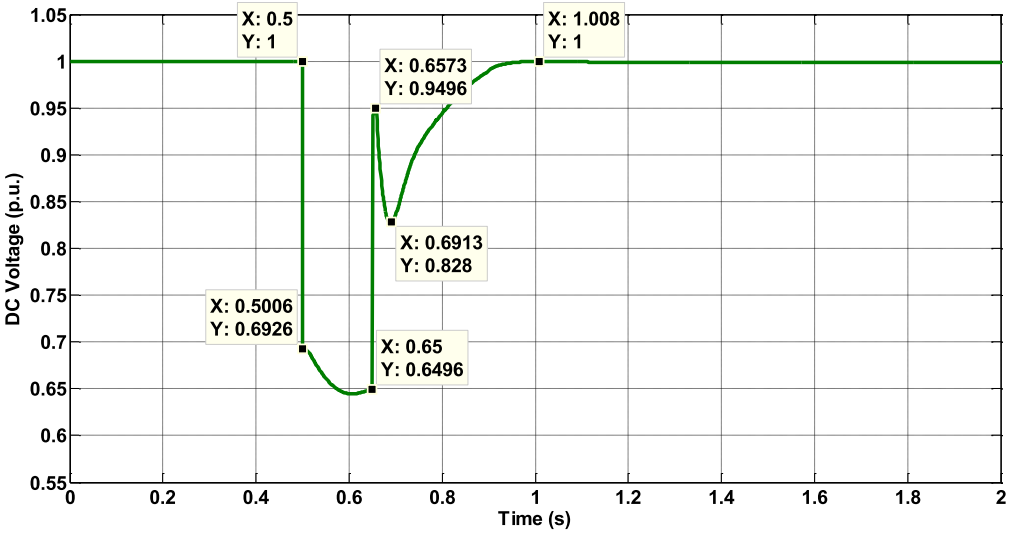

Fig-5.21 The DC Voltage of the Inverter-side DC Bus

In **Case 2**, a three-phase short circuit grounded fault was applied at the AC Bus ***B2*** shown in Fig-5.1 on the inverter–side of CSC-HVDC system at 0.5 s and the time duration of the fault is 0.15 s. The SCR of the external systems on both sides of HVDC was set as 3. The systems on both sides are not so sensitive to the grounded resistance as those with SCR less than 2. As a result, the grounded resistance was set as 10 ohm to make the AC voltage at ***B2*** just drop to 0. 688 p.u. when the fault was applied at 0.5 s shown in Fig-5.20.

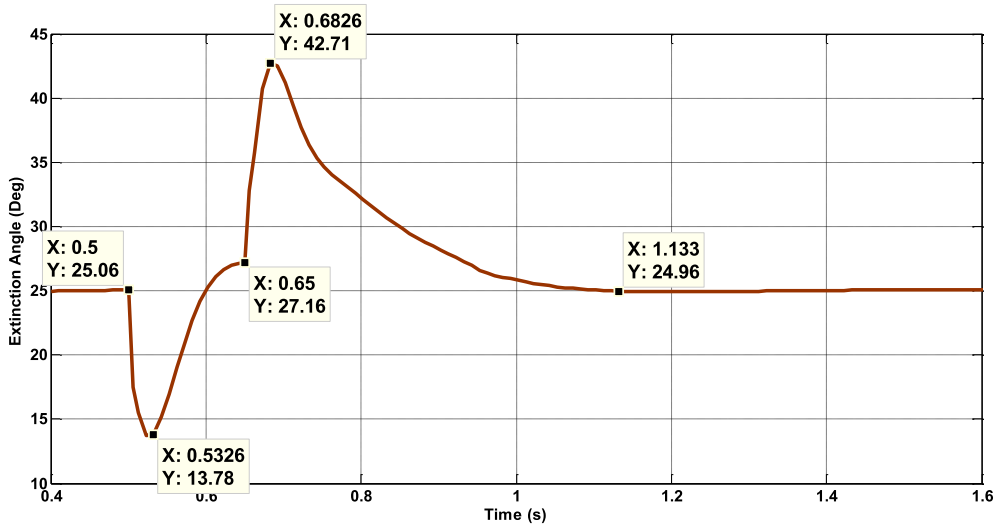

Fig-5.22 The Extinction Angle at the Inverter-Side Converters

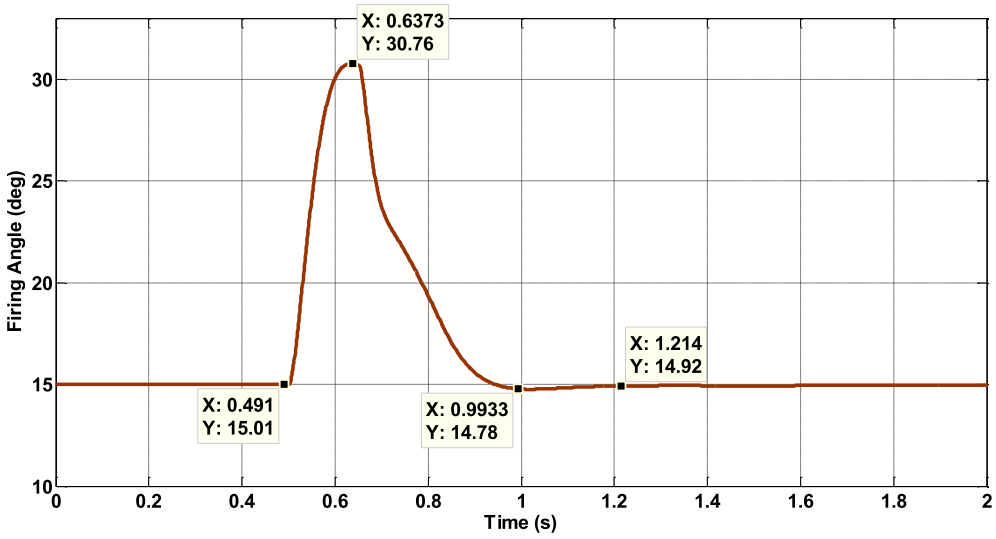

Fig-5.23 The Firing-angle of the Rectifier-side Converters

Following this sudden AC voltage drop, the inverter-side DC voltage V_{idc} was expected to drop in a similar manner shown Fig-5.21. An obvious difference between the AC and DC voltage curves appeared at the time when the fault was removed at 0.65 s. A suddenly overshoot of 0.9496 p.u. appeared at 0.6573 s and it was mainly caused by the reactions of inverter-side voltage controller which led to sudden changes in γ shown in Fig-5.22 in response to the sudden increase of V_{idc} when the fault was removed. The undershoot of 13.78° (45%) appeared at 0.5326 s and the overshoot of 42.71° (71.1%) appeared at 0.6826 s. After

the transient process, the γ returned to normal operation condition of 24.96° at nearly 1.133 s. The changes of α are illustrated in Fig-5.23 in response of the V_{idc} to maintain the voltage drops between the two sides at the acceptable level. The overshoot of 30.76° (104.93%) appeared at 0.6373 s. After the transient process, the α returned to normal operation condition of 14.92° at nearly 1.214 s

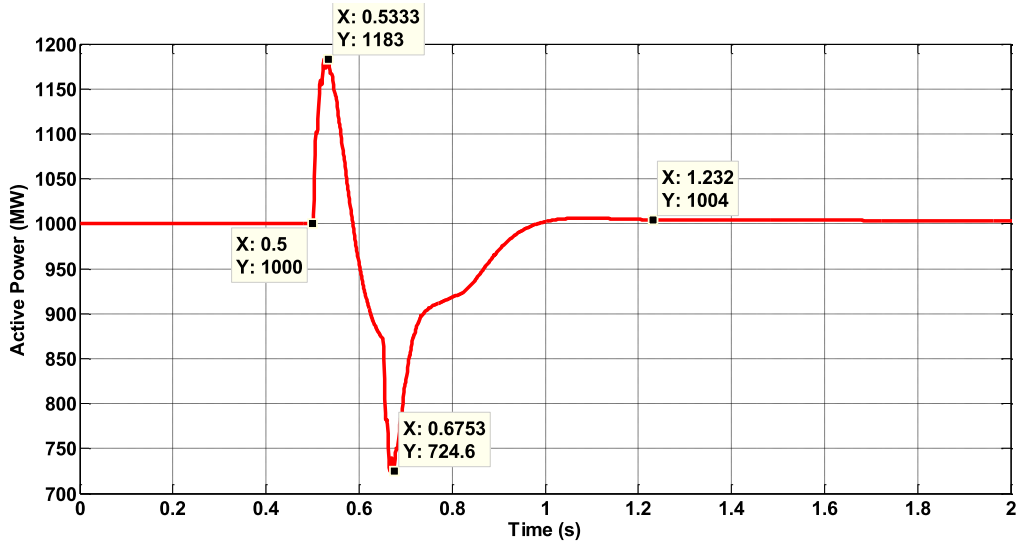

Fig-5.24 The Input Active Power to Rectifier-side Converters

The rectifier-side input power P_r and Q_r, the rectifier-side AC voltage changed in response to the changes of α are illustrated in Fig-5.24 to Fig-5.26. For the P_r, the undershoot of 724.6 MW (27.54%) appeared at 0.6753 s and the overshoot of 1183 MW (18.3%) appeared at 0.5333 s. After the transient process, the P_r returned to normal operation condition o at nearly 1.232 s. For the Q_r, the overshoot of 767.8 MVar (64.97%) appeared at 0.5623 s. After the transient process, the Q_r returned to normal operation condition o at nearly 1.12 s. For the V_{rac}, the undershoot of 0.9143 p.u. (8.57%) appeared at 0.5433 s the overshoot of 1.027 p.u. (2.7%) appeared at 0.6733 s. After the transient process, the V_{rac} returned to normal operation condition o at nearly 1.112 s.

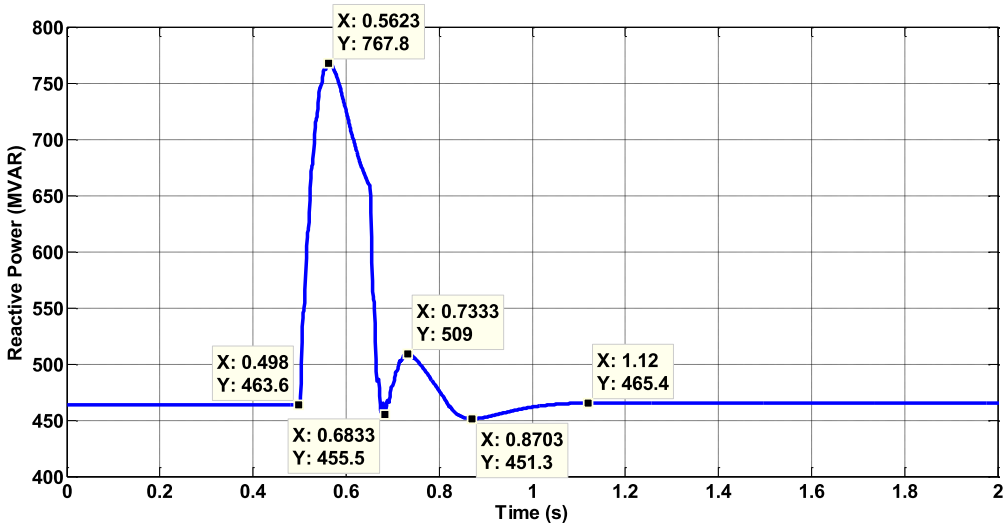

Fig-5.25 The Input Reactive Power to Rectifier-side Converter

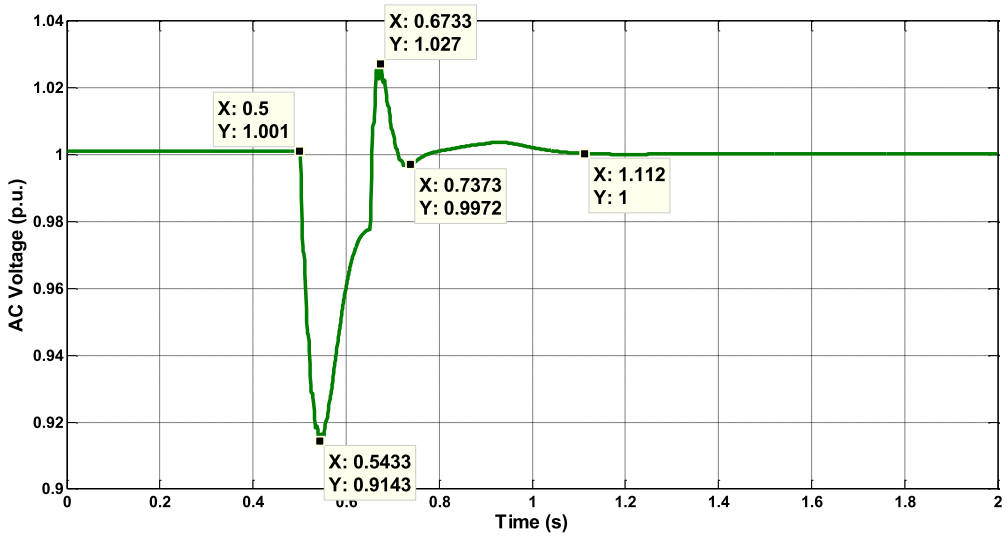

Fig-5.26 The AC Voltage on the Rectifier-side

Review of all the simulation results, for this scenario, it just brought big impacts all the variables during the transient process. However, the whole system can return to the normal operation with the proper functionalities of converter controllers on both sides of the CSC-HVDC system.

5.6.4 Case 3: Three-phase Short-circuit Fault on the Rectifier-side

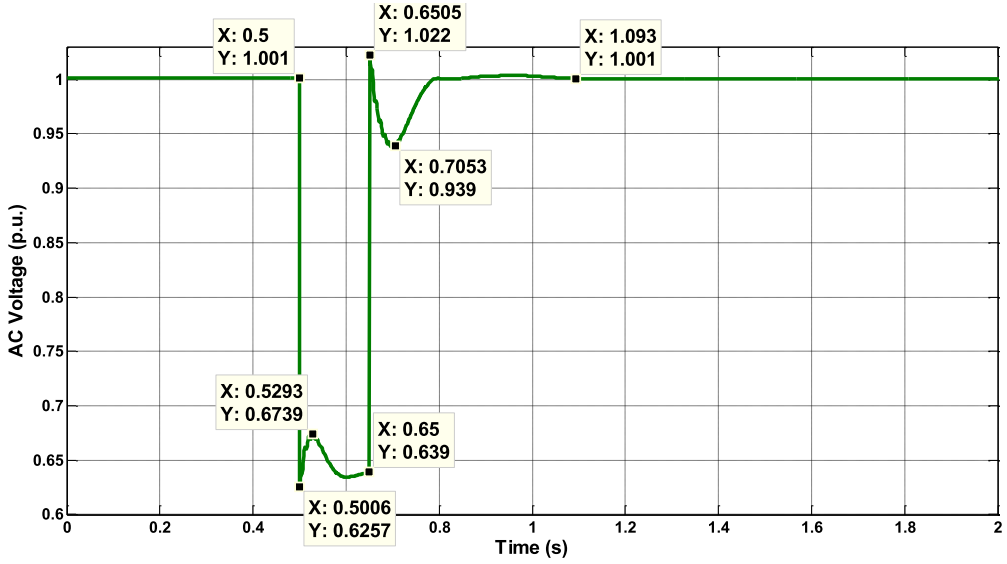

Fig-5.27 The AC Voltage on the Rectifier-side

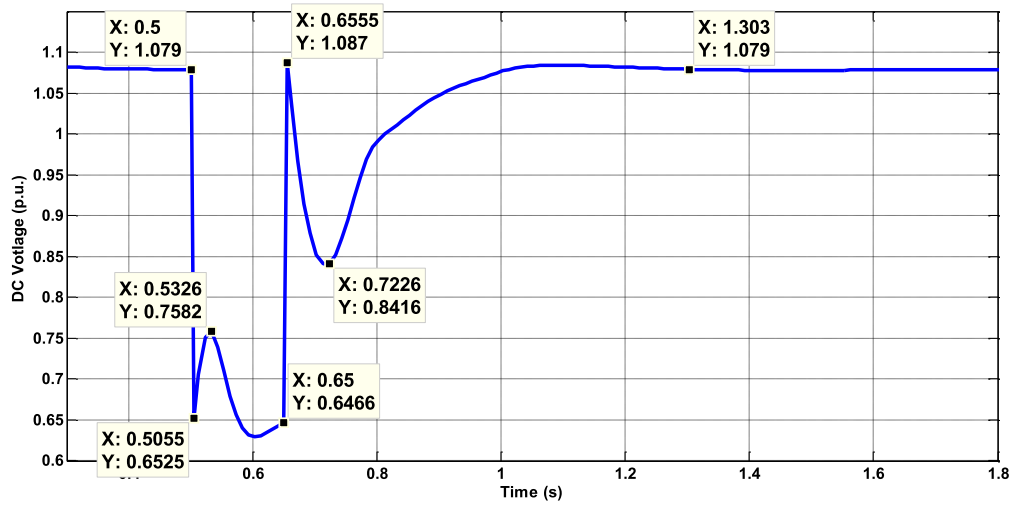

Fig-5.28 The DC Voltage on the Rectifier-side

In **Case 3**, the three-phase short circuit grounded fault was applied at the AC Bus ***B1*** on the rectifier-side of CSC-HVDC system at 0.5s and the time duration of the fault is 0.15s. The grounded resistance of 10 ohm was applied as well similar to Section 5.6.3. So the rectifier-side AC voltage V_{rac} and DC voltage V_{rdc} are shown in Fig-5.27 and Fig-5.28 above. For the V_{rdc}, a suddenly overshoot of 1.087 p.u. appeared at 0.6555 s and the system returned to normal operation at nearly 1.303 s. The V_{rac} suffered from a severe voltage dip so that α suddenly dropped to its minimum value to try to pull up the V_{rdc} shown in Fig-5.29. The

overshoot of 31.29° (108.46%) appeared at 0.7473 s. From the time range between 0.5223 s and 0.6223, α was limited at its minimum value of 3°. At the same time, the inverter-side controller dramatically increased γ to keep the I_{dc} flowing through the DC line from rectifier- to inverter-side shown in Fig-5.30. The overshoot of 61.41° (146.62%) appeared at 0.5626 s and the system returned to normal operation at nearly 1.213 s.

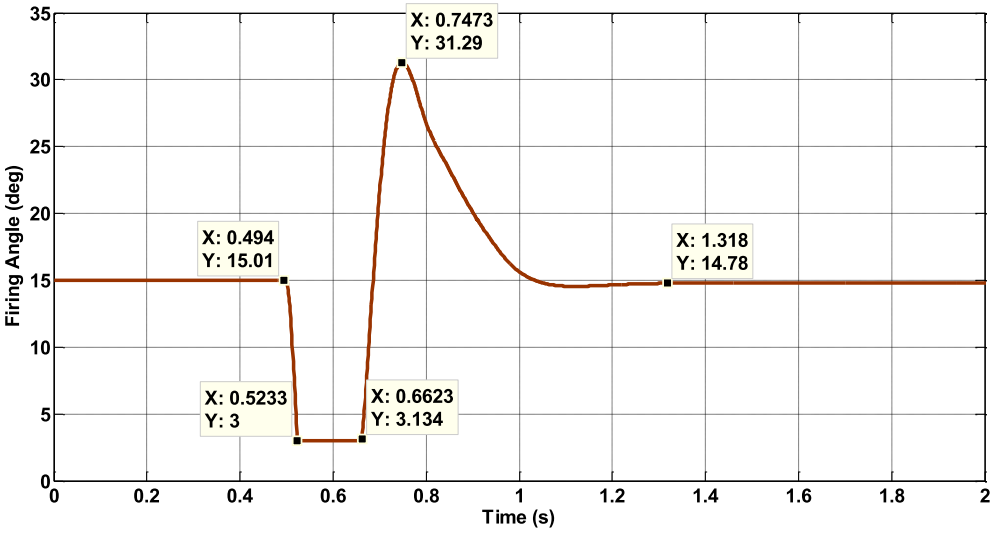

Fig-5.29 The Firing-angle of the Rectifier-side Converters

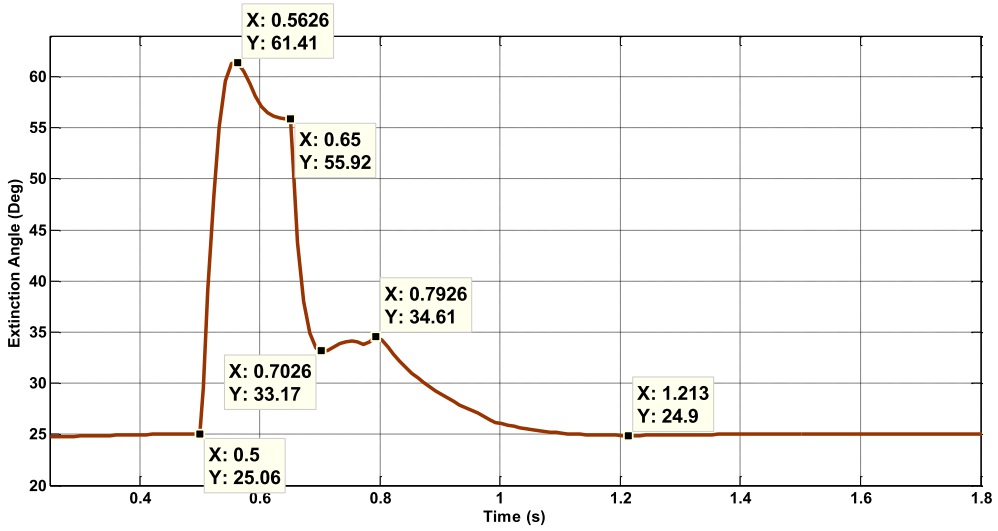

Fig-5.30 The Extinction angle at the Inverter-side Converters

The rectifier-side input power P_r and Q_r changed in response to the changes of α are illustrated in Fig-5.31 to Fig-5.32. For the P_r, the undershoot of 123.7 MW (87.63%) appeared at 0.5293 s and the overshoot of 1512 MW (51.2%) appeared at 0.6793 s. After the

transient process, the P_r returned to normal operation condition o at nearly 1.156 s. For the Q_r, the undershoot of 25.43 MVar (94.51%) appeared at 0.5273 s and the overshoot of 964.8 MVar (108.11%) appeared at 0.7063 s. After the transient process, the Q_r returned to normal operation condition o at nearly 1.192 s.

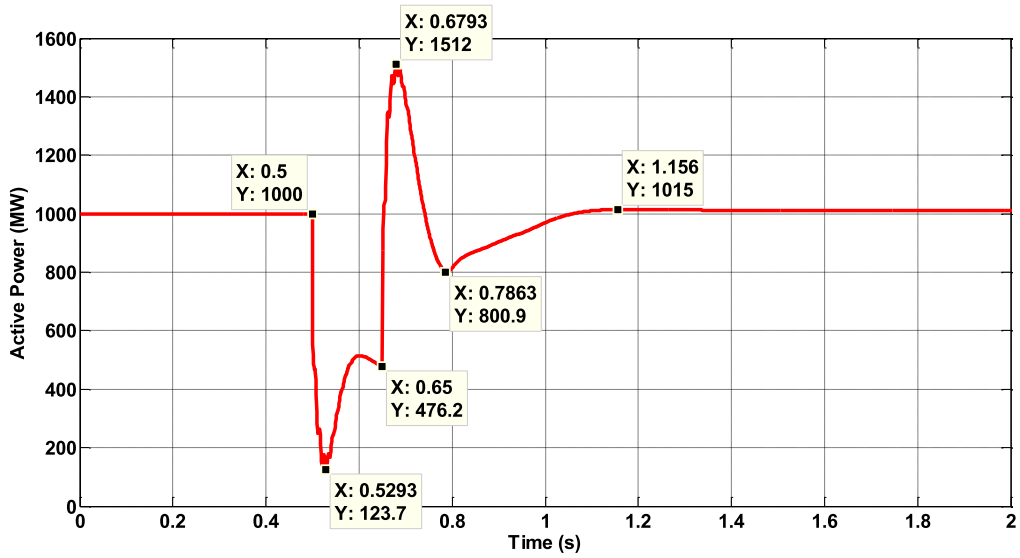

Fig-5.31 The Input Active Power to Rectifier-side Converter

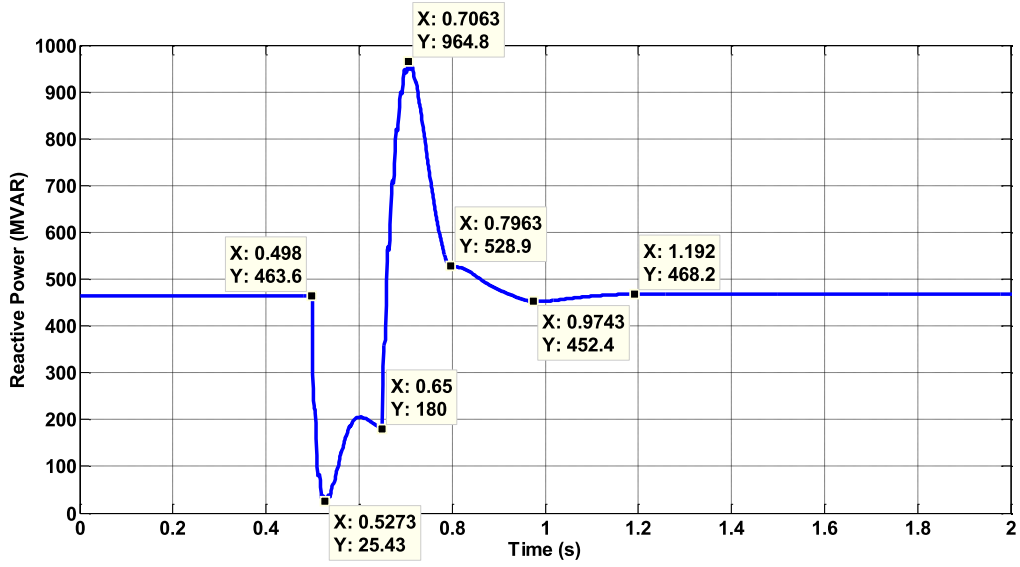

Fig-5.32 The Input Reactive Power to Rectifier-side Converter

Review of all the simulation results, for this scenario, it just brought big impacts all the variables during the transient process. However, the whole system can return to the normal operation with the proper functionalities of converter controllers on both sides of the CSC-HVDC system.

5.6.5 Case 4: Reactive Power Support from VSC-HVDC System

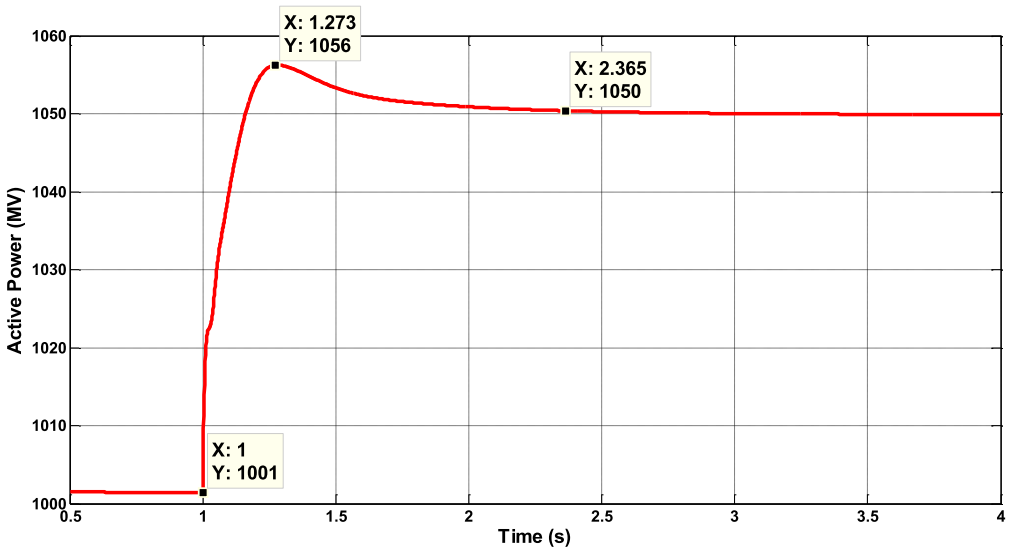

Fig-5.33 The Increases in the Power Rating from 1000 MW to 1050 MW in CSC-HVDC System

In **Case 4**, the power rating of this hybrid-HVDC system increased from 1.0 p.u. (1000 MW) to 1.05 p.u. (1050 MW) at the 1.0 s shown in Fig-5.33. According to the operation characteristics of the CSC-HVDC systems described in Section 5.5.1.1, extra reactive compensations are needed in response to the increases of the power rating. In this way, it should absorb extra 5.5 Mvar reactive power from the external system on the rectifier-side.

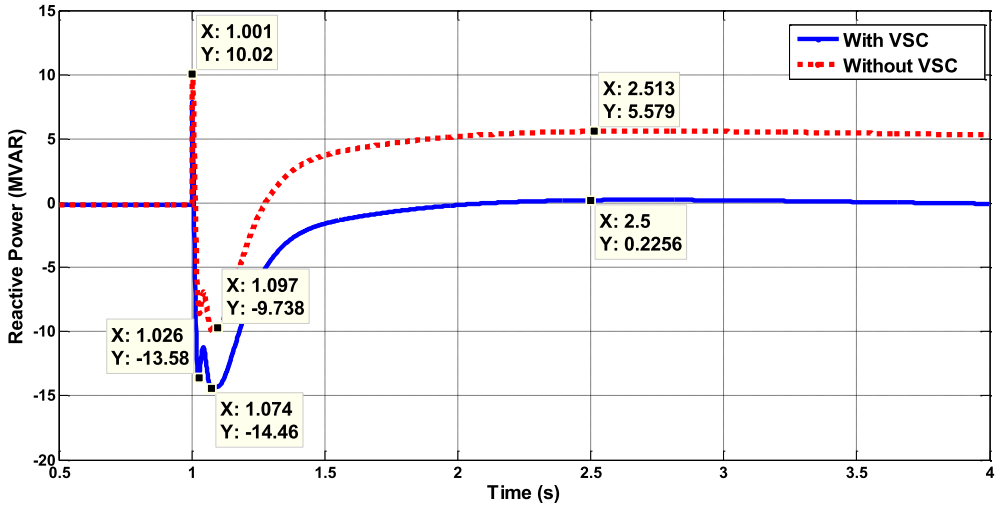

Fig-5.34 The Comparisons of Input Reactive Power for Hybrid and CSC-HVDC Systems

Within the support from the parallel VSC-HVDC system, the extra 5.5 MVar reactive power was provided dynamically from the rectifier-side converter of the VSC-HVDC system to balance the needs of reactive power support from the neighbouring rectifier-side of the CSC-HVDC system shown in Fig-5.34. The overall changes of the two curves are similar with nearly constant differences between 5.0 to 5.5 MVar. Furthermore, the VSC-HVDC system itself did not need extra reactive power due to its operation characteristics [5, 6]. In this way, no extra reactive power from the external power systems is needed for supporting the whole bipolar hybrid CSC/VSC HVDC system.

Review of all the simulation results, for this scenario, with the support of VSC-HVDC link, the extra reactive power can be provide to the neighbouring CSC-HVDC link continuously during the transient process and the whole system can return to normal operation condition after the transient process.

5.6.6 Case 5: Support of VSC-HVDC against Commutation Failure of CSC-HVDC

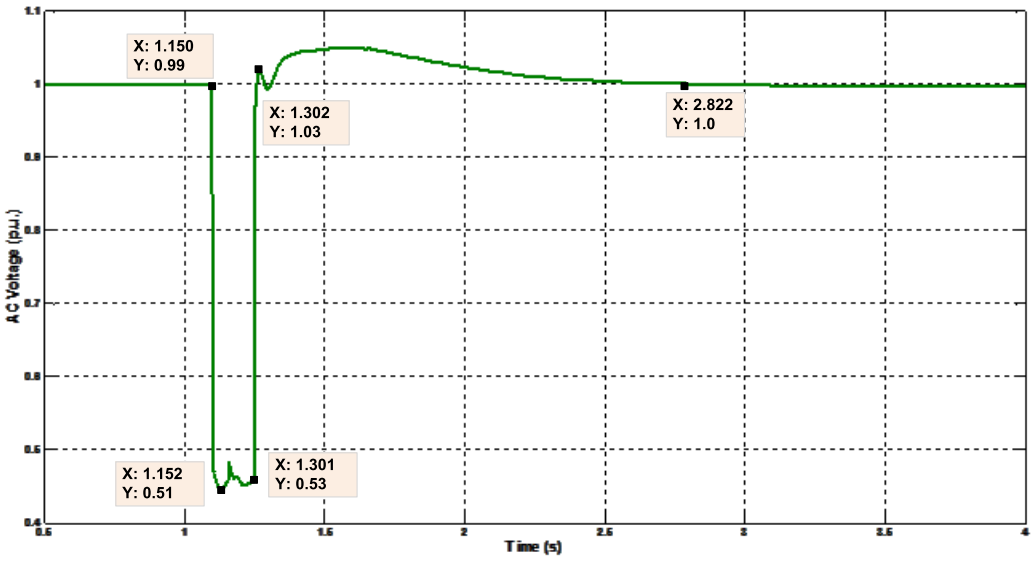

Fig-5.35 The AC Voltage at the AC Bus of Inverter-side of Hybrid HVDC System

In **Case 5**, a three-phase short-circuit grounded fault was applied at the AC Bus of the inverter-side of the bipolar hybrid HVDC system at 1.1s and the time duration is 150 ms. It is easier to trigger the inverter-side commutation failure if the external power system connecting to the inverter is not strong [2]. So the SCR on inverter-side was set as 1.5. In this way, the system on the inverter-side was highly sensitive to the grounded resistance of the fault. As a result, it was set as 15 ohm to avoid final instability cause by the faults with too much strength. So the AC voltage at ***B2*** just droped to 0. 51 p.u. when the fault was applied at 1.1 s shown in Fig-5.35.

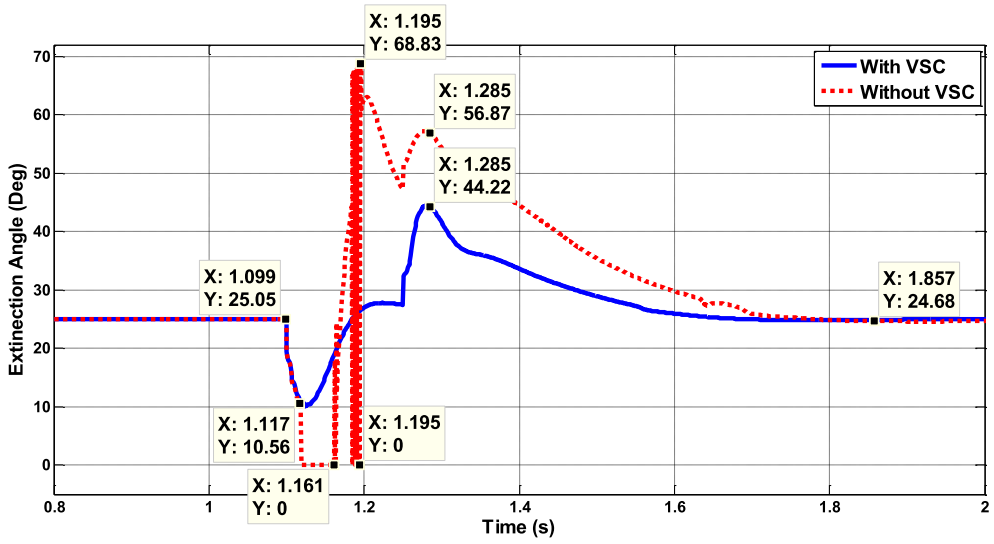

Fig-5.36 The Extinction Angle of the Inverter-side Converters

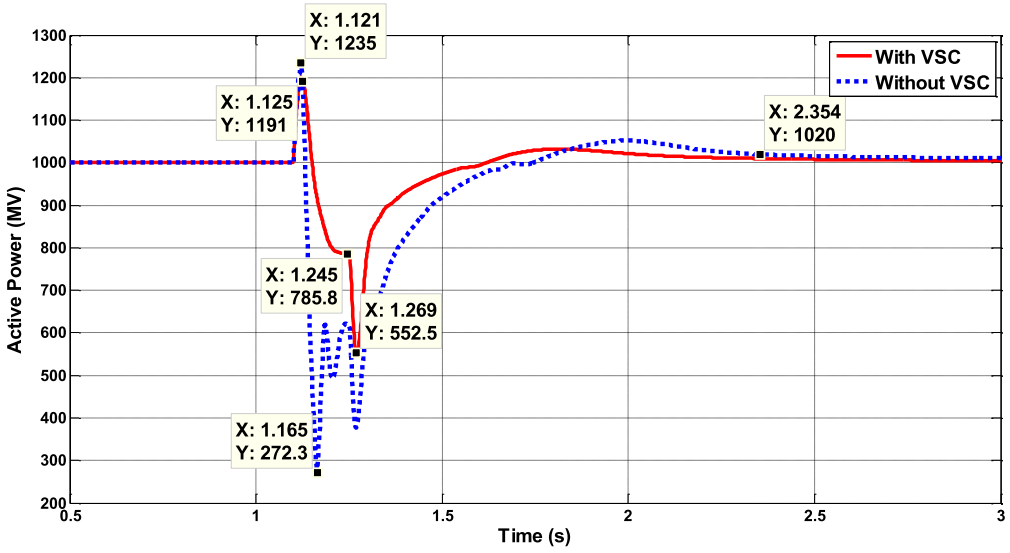

Fig-5.37 The Input Active Power on the Rectifier-side

For the original CSC-HVDC system itself, due to such severe voltage dip, the converters on the inverter-side suffered the commutation failure due to the low-voltage on the inverter-side. And such accidents could bring huge damages to the inverter-side elements of the CSC-HVDC system, so the thyristor-based converters on the inverter-side will be blocked to protect again such severe accidents shown in Fig-5.36. The γ of the inverter-side converters dropped from initial value of 25.05° to zero due to the blocks of the converter controlled by the protection system of the CSC-HVDC system. And the strengths the oscillations for the dynamic response of the input power are very big to cause very significant oscillations during the fault condition shown in Fig-5.37 and Fig-5.38.

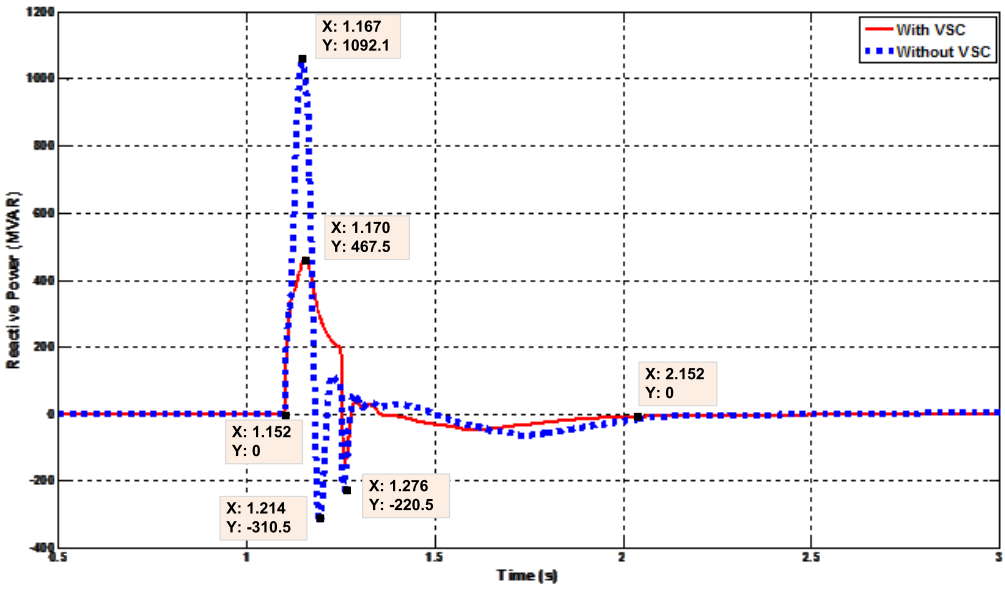

Fig-5.38 The Input Reactive Power on the Rectifier-side

With the support of the parallel VSC-HVDC system, it can monitor the reactive power of the AC bus interconnected with the inverter-side of the CSC-HVDC system. As shown in Fig-5.39, the inverter-side VSC dynamically changed the reactive power for the exchange between the inverter-side CSC and VSC to maintain the V_{iac} at the specific levels to avoid the potential risk of commutation failures due to low voltage during the faults condition. With such support from the parallel VSC-HVDC system, some potential commutation failure can be mitigated with the fast and flexible reactive power compensation to support the AC

voltage for the CSC-converter on the inverter-side. And comparing the simulation results for the extinction-angle of the inverter-side converters and the input power on the rectifier-side without the support of VSC-HVDC system are shown in the Fig-5.36 to Fig-5.38, the dynamic performance of CSC-HVDC system has been obviously improved with the support of parallel VSC-HVDC system. For the two curves of P_r in Fig-5.37, the undershoot of 552.5 MW appeared at 1.269 s for curve with VSC and the undershoot of 272.3 MW appeared at 1.165 s for curve without VSC. The overshoot of 1191.5 MW appeared at 1.125 s for curve with VSC and the undershoot of 1235 MW appeared at 1.121 s for curve without VSC. The system returned to the normal operation at nearly 2.354 s.

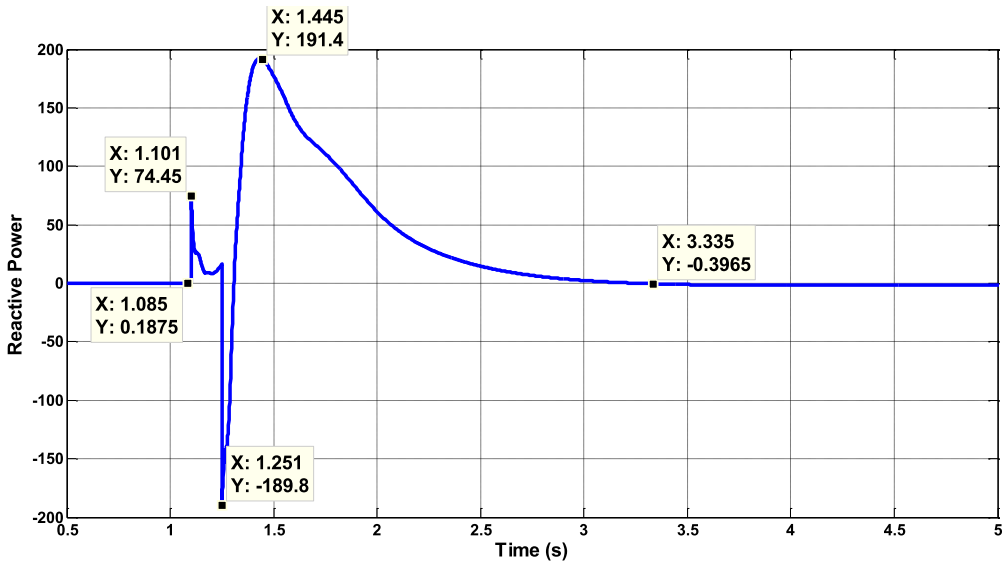

Fig-5.39 The Changes of Reactive Power of Inverter-side VSC

For the two curves of Q_r in Fig-5.38, the undershoot of -220.5 MVar appeared at 1.276 s for curve with VSC and the undershoot of -310.5 MVar appeared at 1.214 s for curve without VSC. The overshoot of 467.5 MVar appeared at 1.170 s for curve with VSC and the undershoot of 1092.1 MVar appeared at 1.167 s for curve without VSC. The system returned to the normal operation at nearly 2.152 s. For the Reactive Power of Inverter-side VSC in Fig-5.39, the undershoot of -189.8 MVar appeared at 1.251 s and the overshoot of 191.4.5 MVar appeared at 1.445 s. The system returned to the normal operation at nearly 3.335 s.

Review of all the simulation results, for this scenario, with the support of VSC-HVDC link, the potential risk of inverter-side commutation failure in the CSC-HVDC system can be mitigated and the dynamic performance of the CSC-HVDC system can be improved as well during the transient process avoiding the big impacts of inverter-side commutation. And the whole Hybrid CSC/HVDC system can return to the normal operation after the short-circuit fault with high severity.

5.7 Summary and Conclusions

In this chapter, the mathematical models and control strategies for rectifier- and inverter-side of CSC-HVDC systems have been investigated for transient stability analysis. Furthermore, the feasibility analysis of the upgrade schemes of the existing monopolar CSC-HVDC link with the support of the neighbouring monopolar VSC-HVDC link working in parallel as the hybrid bipolar CSC/VSC-HVDC system has been carried out to validate the performance of the extra support from the VSC-HVDC link with specified control strategies to the neighbouring CSC-HVDC link for extra reactive power compensation and mitigation of the potential risks of inverter-side commutation failure.

Chapter 6

Small-signal Modelling and Optimal Control of Multi-terminal VSC-based HVDC Grids

6.1 Introduction

For the North Sea Supergrid Scheme (NSSS), the electricity transmission infrastructure is of vital importance for grid integration of large-scale renewable energy systems such as offshore wind farms around North Sea and hydropower power plants in the Nordic countries. With great increases in the total installation capacity of large-scale renewable energy systems, the current transmission systems, especially with the point-to-point structure, have gradually shown their limitations on security and stability for connecting those renewable energy systems. The advent of VSC-HVDC technology has gradually shown some overwhelming advantages over conventional HVAC and CSC-HVDC technologies for the key capabilities described in Section 1.1.2. In this way, the multi-terminal VSC-based HVDC (MTDC) grids have been widely considered having great potentials as the solution to building the backbone of electricity transmission infrastructure for the future NSSS [20-22, 121]. However, due to the absence of MTDC systems in the world, the operation experiences for such systems are limited. So the investigation of the operating characteristics of the MTDC systems and design of the operation mechanisms for system security and stability are of great necessities for the feasibility studies and technical specification establishments just like the grid code to move towards making the NSSS a reality.

For the operation of Supergrid, the operating points of the MTDC grid should be changed frequently due to different scenarios in power exchanges according to the marketing

strategies of regional TSOs. For such MTDC grid, it should maintain the robustness in response to different operating points and it will inevitably bring higher requirements for the power dispatching and control strategies of the MTDC grid. On the one hand, the classical nonlinear robust control methods are widely applied in the power system dynamic stability control and have also been applied into the controller design of VSC-HVDC systems [146-152]. However, the mathematical analysis and processes of the robust controller design are too complex for the practical applications in the electric power systems. As a result, effective methods should be investigated to achieve the balance between the complexity and feasibility for the VSC controllers of MTDC grids.

On the other hand, for the VSC-HVDC systems, the classic linear PI controllers are commonly used. The basic layout of a PI control loop is shown in Fig-6.1 which is expressed by:

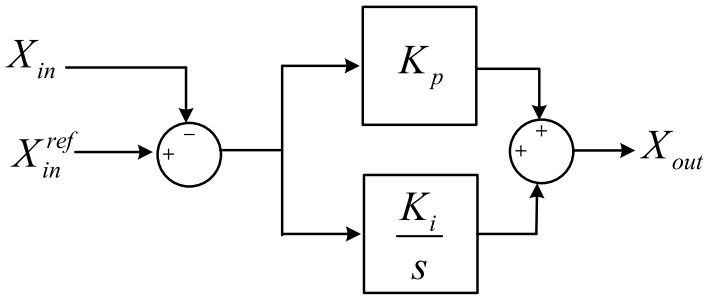

Fig-6.1 The Basic Layout of PI Controller

$$X_{out} = K_p(X_{in}^{ref} - X_{in}) + \frac{K_i}{s}(X_{in}^{ref} - X_{in}) \tag{6.1}$$

There are two blocks in the basic PI control loop, the proportional and integral blocks. The errors between input variable X_{in} and its reference X_{in}^{ref} are sent to the PI controller for tuning as the X_{out}. After tuning two gain parameters K_p for proportional block and K_i for integral block, the expected X_{out} can be obtained. The proportional block contributes to the amplification of input errors. If the K_p is too large, it is easy to make the system unstable. In

contrast, a small K_p makes the controller less sensitive. The integral block contributes to the acceleration of the dynamic process towards the pre-defined setpoint and elimination of steady-state errors. It could cause the overshoot over pre-defined setpoint. As a result, K_p and K_i need to be tuned appropriately so that the system can keep stable with improvement of overshoot and period of oscillation during the transient process [153]. With the development of optimisation techniques, some method such as particle swarm optimisation (PSO) method has been applied in the parameter optimisation of PI controllers of the elements in the electric power systems [57, 136, 137, 154, 155]. However, the parameters of the PI controllers are just optimised for the systems at one specific operating point but could not be applicable for the systems at some other operating points. To obtain a set of optimised parameters of PI controllers suitable for the MTDC grids at multiple operating points, the PSO method is proposed to obtain a set of the optimised parameters of PI controllers for the VSCs in a MTDC grid based on its improved small-signal models for multiple operating points.

In this chapter, the small-signal modelling of the three-terminal VSC-based HVDC grid is carried out according to different control strategies of PI controllers for rectifier- and inverter-side converters. Then the parameter optimisation with the PSO method for the PI controllers of the VSCs in the three-terminal HVDC grid is carried out based on the small-signal models of the system at multiple operating points. And with the small-signal analysis and the comparisons of the dynamic performance of the three-terminal HVDC grid with the sets of original and optimised parameters of the PI controllers, the feasibility of the PSO method for the parameter optimisation of the PI controllers of VSCs in the MTDC grids is validated to improve the dynamic performance of the MTDC grids at multiple operating points under large disturbances.

6.2 Topologies of Multi-terminal VSC-based HVDC Grids

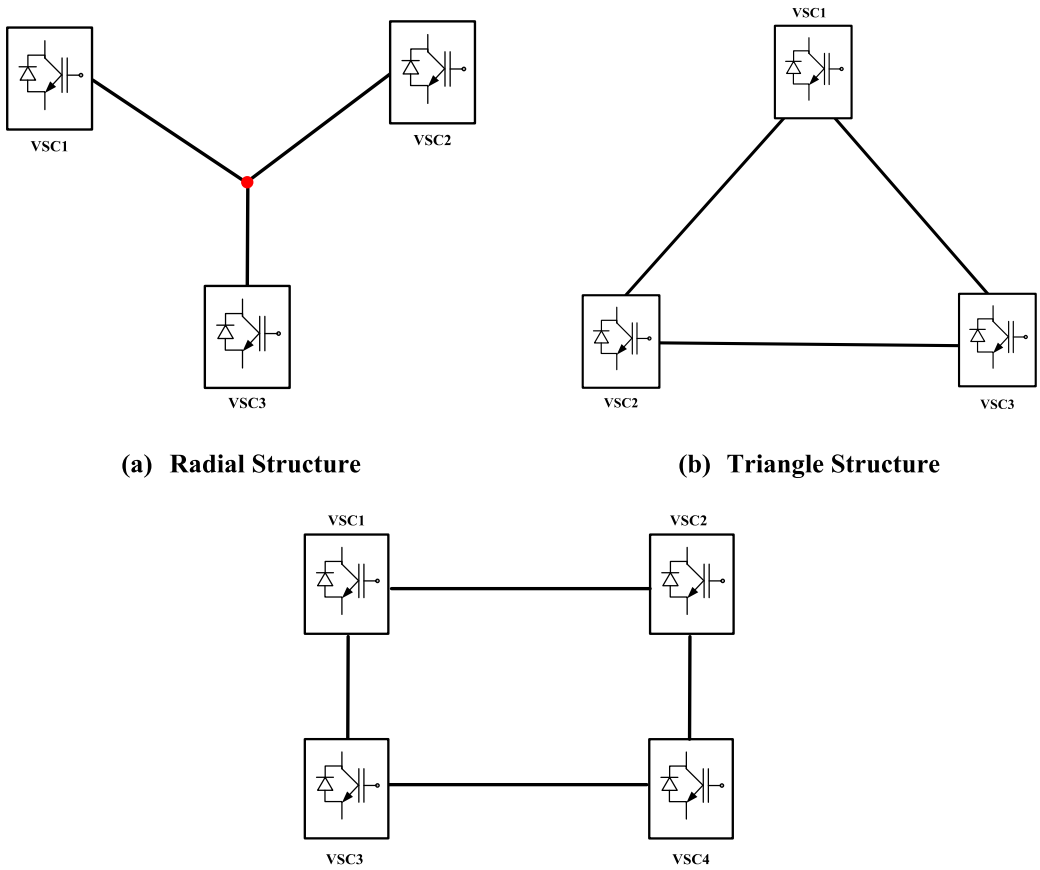

(a) Radial Structure **(b) Triangle Structure**

(c) Meshed Structure

Fig-6.2 The Topologies for Typical MTDC Structures

Different topologies of MTDC grids are described and compared in detail in [156]. In general, the typical layouts of the MTDC grids can be divided into three types of structures shown in the Fig-6.2. In the radial structure shown in Fig-6.2(a), the operation and control are not so complex as those for the interconnected triangle and meshed structures in Fig-6.2(b) and (c). However, in terms of the operation reliability and flexibility, the interconnected structures are better than the radial structures. For the large-scale MTDC grids in the future, their structures can be extended with the combinations among those three basic structures. For the current condition, the initial three-terminal VSC-based MTDC grid with the radial topology is proposed in the Eastern HVDC System Project in the UK for delivering the offshore wind energy in the east coast and the renewable energy in Scotland to the England with UK's

increasing energy demands [9]. And the small-signal modelling and analysis in the next sections are carried out based on this practical scheme of three-terminal VSC-based HVDC grid with radial structure.

6.3 Small-signal Modelling of 3-terminal VSC-based HVDC Grid

6.3.1 Small-signal Modelling of Rectifier-side VSC

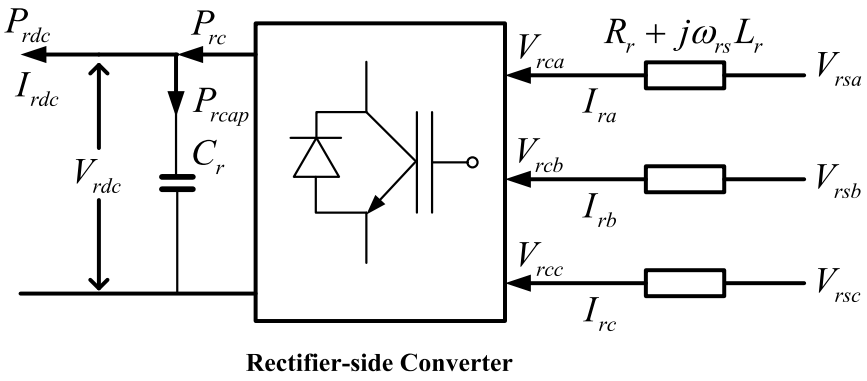

Fig-6.3 The Diagram of Rectifier-side Circuit

For the rectifier-side converter shown in Fig-6.3, the three-phase AC voltages on the converter- and system-side can be express in the (6.2) which is described in Section 4.2.1:

$$\begin{cases} V_{rsa} = V_{rca} + R_r I_{ra} + L_r \dfrac{dI_{ra}}{dt} \\ V_{rsb} = V_{rcb} + R_r I_{rb} + L_r \dfrac{dI_{rb}}{dt} \\ V_{rsc} = V_{rcc} + R_r I_{rc} + L_r \dfrac{dI_{rc}}{dt} \end{cases} \tag{6.2}$$

With park transformation, the three-phase AC voltages in the *a-b-c* coordinate system can be expressed in the (6.3) in the *d-q* coordinate system which is described in Section 4.2.1 [102, 112]:

$$\begin{cases} V_{rcd} = V_{rsd} - R_r I_{rd} - L_r \dfrac{dI_{rd}}{dt} + X_r I_{rq} \\ V_{rcq} = V_{rsq} - R_r I_{rq} - L_r \dfrac{dI_{rq}}{dt} - X_r I_{rd} \end{cases} \tag{6.3}$$

The classic power controller are applied for the rectifier-side VSC controller with the similar principles described in [104-106], the active and reactive power P_r and Q_r on the system-side can be expressed in the (6.4) [102, 112]:

$$\begin{cases} P_r = V_{rsd} I_{rd} + V_{rsq} I_{rq} \\ Q_r = V_{rsq} I_{rd} - V_{rsd} I_{rq} \end{cases} \tag{6.4}$$

Two variables x_{r1} and x_{r2} are defined by the (6.5):

$$\begin{cases} x_{r1} = \int (P_r^{ref} - P_r) \\ x_{r2} = \int (Q_r^{ref} - Q_r) \end{cases} \tag{6.5}$$

So the differential equations of these two variables are expressed in the (6.6):

$$\begin{cases} \dfrac{dx_{r1}}{dt} = P_r^{ref} - P_r \\ \dfrac{dx_{r2}}{dt} = Q_r^{ref} - Q_r \end{cases} \tag{6.6}$$

The references of *d*- and *q*-axis components of rectifier-side AC currents are regulated with the equations expressed in the (6.7):

$$\begin{cases} I_{rd}^{ref} = K_{rp1}(P_r^{ref} - P_r) + K_{ri1}\int (P_r^{ref} - P_r) \\ I_{rq}^{ref} = K_{rp2}(Q_r^{ref} - Q_r) + K_{ri2}\int (Q_r^{ref} - Q_r) \end{cases} \tag{6.7}$$

The other two variables x_{r3} and x_{r4} are defined by the (6.8):

$$\begin{cases} x_{r3} = \int (I_{rd}^{ref} - I_{rd}) \\ x_{r4} = \int (I_{rq}^{ref} - I_{rq}) \end{cases} \tag{6.8}$$

The differential equations of these two variables are expressed in the (6.9):

$$\begin{cases} \dfrac{dx_{r3}}{dt} = I_{rd}^{ref} - I_{rd} = K_{rp1}(P_r^{ref} - P_r) + K_{ri1}x_{r1} - I_{rd} \\ \dfrac{dx_{r4}}{dt} = I_{rq}^{ref} - I_{rq} = K_{rp2}(Q_r^{ref} - Q_r) + K_{ri2}x_{r2} - I_{rq} \end{cases} \tag{6.9}$$

As shown in Fig-6.4 below, the *d*- and *q*-axis components of AC voltages on system- and converter-side, the AC currents and the current PI controllers can be given by the (6.10) which is described in Section 4.2.1:

$$\begin{cases} V_{rcd} = V_{rsd} - K_{rp3}(I_{rd}^{ref} - I_{rd}) - K_{ri3}\int (I_{rd}^{ref} - I_{rd}) + X_r I_{rq} \\ V_{rcq} = V_{rsq} - K_{rp3}(I_{rq}^{ref} - I_{rq}) - K_{ri3}\int (I_{rq}^{ref} - I_{rq}) - X_r I_{rd} \end{cases} \tag{6.10}$$

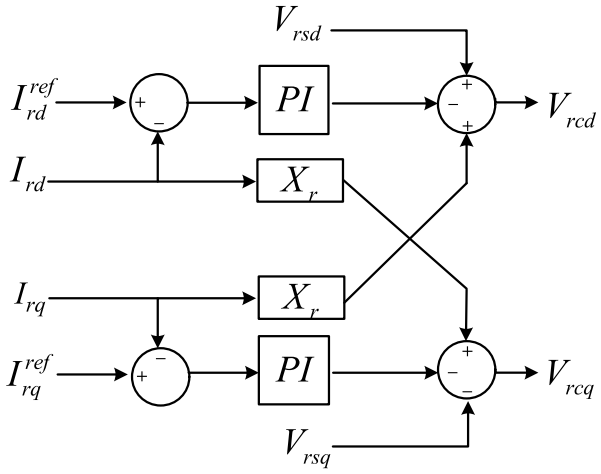

Fig-6.4 The Diagram of Current PI Controller on Rectifier-side

So the small-signal models for the rectifier-side converter are listed below in (6.11) to (6.15):

$$\begin{cases} \dfrac{d\Delta x_{r1}}{dt} = -\Delta P_r = -V_{rsd}\Delta I_{rd} - V_{rsq}\Delta I_{rq} - I_{rd}\Delta V_{rsd} - I_{rq}\Delta V_{rsq} \\ \dfrac{d\Delta x_{r2}}{dt} = -\Delta Q_r = -V_{rsq}\Delta I_{rd} + V_{rsd}\Delta I_{rq} + I_{rq}\Delta V_{rsd} - I_{rd}\Delta V_{rsq} \end{cases} \tag{6.11}$$

$$\begin{aligned} \frac{d\Delta x_{r3}}{dt} &= \Delta I_{rd}^{ref} - \Delta I_{rd} = -K_{rp1}\Delta P_r + K_{ri1}\Delta x_{r1} - \Delta I_{rd} \\ &= K_{ri1}\Delta x_{r1} - K_{rp1}I_{rd}\Delta V_{rsd} - K_{rp1}I_{rq}\Delta V_{rsq} - (K_{rp1}V_{rsd} + 1)\Delta I_{rd} - K_{rp1}V_{rsq}\Delta I_{rq} \end{aligned} \tag{6.12}$$

$$\begin{aligned} \frac{d\Delta x_{r4}}{dt} &= \Delta I_{rq}^{ref} - \Delta I_{rq} = -K_{rp2}\Delta Q_r + K_{ri2}\Delta x_{r2} - \Delta I_{rq} \\ &= K_{ri2}\Delta x_{r2} + K_{rp2}I_{rq}\Delta V_{rsd} - K_{rp2}I_{rd}\Delta V_{rsq} - K_{rp2}V_{rsq}\Delta I_{rd} + (K_{rp2}V_{rsd} - 1)\Delta I_{rq} \end{aligned} \tag{6.13}$$

$$\begin{aligned} \Delta V_{rcd} &= \Delta V_{rsd} - K_{rp3}(\Delta I_{rd}^{ref} - \Delta I_{rd}) - K_{ri3}\Delta x_{r3} + X_r\Delta I_{rq} \\ &= -K_{rp3}K_{ri1}\Delta x_{r1} - K_{ri3}\Delta x_{r3} + (K_{rp1}K_{rp3}I_{rd} + 1)\Delta V_{rsd} + K_{rp1}K_{rp3}I_{rq}\Delta V_{rsq} \\ &+ K_{rp3}(K_{rp1}V_{rsd} + 1)\Delta I_{rd} + (K_{rp1}K_{rp3}V_{rsq} + X_r)\Delta I_{rq} \end{aligned} \tag{6.14}$$

$$\begin{aligned}\Delta V_{rcq} &= \Delta V_{rsq} - K_{rp3}(\Delta I_{rq}^{ref} - \Delta I_{rq}) - K_{ri3}\Delta x_{r4} - X_r \Delta I_{rd} \\ &= -K_{rp3}K_{ri2}\Delta x_{r2} - K_{ri3}\Delta x_{r4} - K_{rp2}K_{rp3}I_{rq}\Delta V_{rsd} + (K_{rp2}K_{rp3}I_{rd} + 1)\Delta V_{rsq} \\ &+ (K_{rp2}K_{rp3}V_{rsq} - X_r)\Delta I_{rd} - K_{rp3}(K_{rp2}V_{rsd} - 1)\Delta I_{rq}\end{aligned} \tag{6.15}$$

6.3.2 Small-signal Modelling of Inverter-side VSC

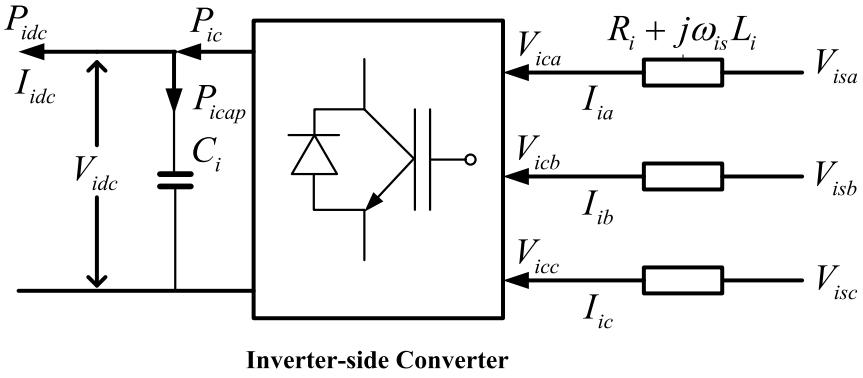

Fig-6.5 The Diagram of Inverter-side Circuit

For the inverter-side converter shown in Fig-6.5, the three-phase AC voltages on the system and converter-side can be expressed in the (6.16) which is described in Section 4.1.2:

$$\begin{cases} V_{isa} = V_{ica} + R_i I_{ia} + L_i \dfrac{dI_{ia}}{dt} \\ V_{isb} = V_{icb} + R_i I_{ib} + L_i \dfrac{dI_{ib}}{dt} \\ V_{isc} = V_{icc} + R_i I_{ic} + L_i \dfrac{dI_{ic}}{dt} \end{cases} \tag{6.16}$$

With park transformation, the three-phase AC voltages in the *a-b-c* coordinate system can be expressed in the (6.17) in the *d-q* coordinate system which is described in Section 4.1.2 [102, 112]:

$$\begin{cases} V_{icd} = V_{isd} - R_i I_{id} - L_i \dfrac{dI_{id}}{dt} + X_i I_{iq} \\ V_{icq} = V_{isq} - R_i I_{iq} - L_i \dfrac{dI_{iq}}{dt} - X_i I_{id} \end{cases} \tag{6.17}$$

The DC voltage V_{idc} of the inverter-side converter and the output reactive power Q_i at the inverter-side PCC are selected as the control targets for inverter-side VSC controller which are described in [105, 110, 111]. And two variables x_{i1} and x_{i2} are defined by the (6.18):

$$\begin{cases} x_{i1} = \int (V_{idc}^{ref} - V_{idc}) \\ x_{i2} = \int (Q_i^{ref} - Q_i) \end{cases} \tag{6.18}$$

The differential equations of these two variables are expressed in the (6.19):

$$\begin{cases} \dfrac{dx_{i1}}{dt} = V_{idc}^{ref} - V_{idc} \\ \dfrac{dx_{i2}}{dt} = Q_i^{ref} - Q_i \end{cases} \tag{6.19}$$

The references of *d*- and *q*-axis components of inverter-side AC currents are regulated with the equations expressed in the (6.20):

$$\begin{cases} I_{id}^{ref} = K_{ip1}(V_{idc}^{ref} - V_{idc}) + K_{ii1}\int (V_{idc}^{ref} - V_{idc}) \\ I_{iq}^{ref} = K_{ip2}(Q_i^{ref} - Q_i) + K_{ii2}\int (Q_i^{ref} - Q_i) \end{cases} \tag{6.20}$$

The other two variables x_{i3} and x_{i4} are defined by the (6.21):

$$\begin{cases} x_{i3} = \int (I_{id}^{ref} - I_{id}) \\ x_{i4} = \int (I_{iq}^{ref} - I_{iq}) \end{cases} \tag{6.21}$$

The differential equations of these two variables are expressed in the (6.22):

$$\begin{cases} \dfrac{dx_{i3}}{dt} = I_{id}^{ref} - I_{id} = K_{ip1}(V_{idc}^{ref} - V_{idc}) + K_{ii1}x_{i1} - I_{id} \\ \dfrac{dx_{i4}}{dt} = I_{iq}^{ref} - I_{iq} = K_{ip2}(Q_i^{ref} - Q_i) + K_{ii2}x_{i2} - I_{iq} \end{cases} \tag{6.22}$$

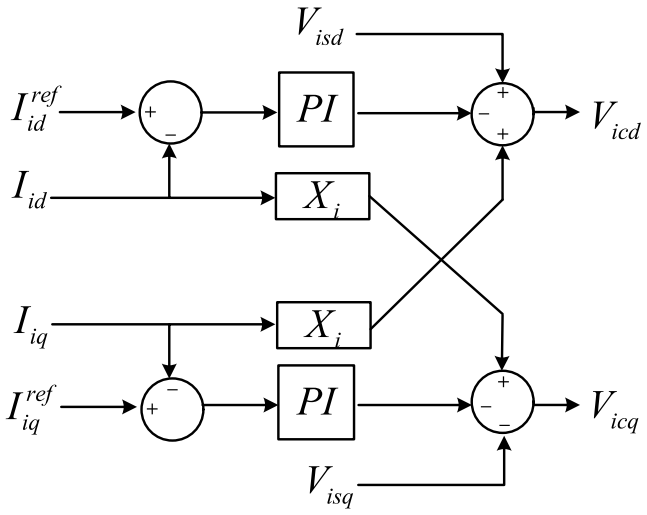

Fig-6.6 The Diagram of Current PI Controller on Inverter-side

As shown in Fig-6.6, the *d*- and *q*-axis components of AC voltages on system- and converter-side, the AC currents and the current PI controllers can be given by the (6.23):

$$\begin{cases} V_{icd} = V_{isd} - K_{ip3}(I_{id}^{ref} - I_{id}) - K_{ii3}\int (I_{id}^{ref} - I_{id}) + X_i I_{iq} \\ V_{icq} = V_{isq} - K_{ip3}(I_{iq}^{ref} - I_{iq}) - K_{ii3}\int (I_{iq}^{ref} - I_{iq}) - X_i I_{id} \end{cases} \tag{6.23}$$

So the small-signal models for the inverter-side converter are listed below in (6.24) to (6.28):

$$\begin{cases} \dfrac{d\Delta x_{i1}}{dt} = -\Delta V_{idc} \\ \dfrac{d\Delta x_{i2}}{dt} = -\Delta Q_i = I_{iq}\Delta V_{isd} - I_{id}\Delta V_{isq} - V_{isq}\Delta I_{id} + V_{isd}\Delta I_{iq} \end{cases} \tag{6.24}$$

$$\frac{d\Delta x_{i3}}{dt} = \Delta I_{id}^{ref} - \Delta I_{id} = -K_{ip1}\Delta V_{idc} + K_{ii1}\Delta x_{i1} - \Delta I_{id} \tag{6.25}$$

$$\begin{aligned} &\frac{d\Delta x_{i4}}{dt} = \Delta I_{iq}^{ref} - \Delta I_{iq} = -K_{ip2}\Delta Q_i + K_{ii2}\Delta x_{i2} - \Delta I_{iq} \\ &= -K_{ip2}V_{isq}\Delta I_{id} + (K_{ip2}V_{isd} - 1)\Delta I_{iq} + K_{ii2}\Delta x_{i2} + K_{ip2}I_{iq}\Delta V_{isd} - K_{ip2}I_{id}\Delta V_{isq} \end{aligned} \tag{6.26}$$

$$\begin{aligned} &\Delta V_{icd} = \Delta V_{isd} - K_{ip3}(\Delta I_{id}^{ref} - \Delta I_{id}) - K_{ii3}\Delta x_{i3} + X_i\Delta I_{iq} \\ &= K_{ip1}K_{ip3}\Delta V_{idc} + K_{ip3}\Delta I_{id} + X_i\Delta I_{iq} - K_{ip3}K_{ii1}\Delta x_{i1} - K_{ii3}\Delta x_{i3} + \Delta V_{isd} \end{aligned} \tag{6.27}$$

$$\begin{aligned} &\Delta V_{icq} = \Delta V_{isq} - K_{ip3}(\Delta I_{iq}^{ref} - \Delta I_{iq}) - K_{ii3}\Delta x_{i4} - X_i\Delta I_{id} \\ &= (K_{ip2}K_{ip3}V_{isq} - X_i)\Delta I_{id} - K_{ip3}(K_{ip2}V_{isd} - 1)\Delta I_{iq} - K_{ip3}K_{ii2}\Delta x_{i2} - K_{ii3}\Delta x_{i4} \\ &-K_{ip2}K_{ip3}I_{iq}\Delta V_{isd} + (K_{ip2}K_{ip3}I_{id} + 1)\Delta V_{isq} \end{aligned} \tag{6.28}$$

6.3.3 Small-signal Modelling of the DC Network

The active power between the AC- and DC-side of the converter is expressed by the (6.29) which is described in Section 4.2.1 and 4.1.2:

$$P_c = V_{cd}I_d + V_{cq}I_q \tag{6.29}$$

The active power in the DC capacitor is given by the (6.30):

$$P_{cap} = V_{dc}C\frac{dV_{dc}}{dt} \tag{6.30}$$

So in the Fig-6.3 and Fig-6.5, the active power on the DC-side is expressed in the (6.31):

$$P_{dc} = P_c - P_{cap} = V_{cd} I_d + V_{cq} I_q - V_{dc} C \frac{dV_{dc}}{dt} = V_{dc} I_{dc} \tag{6.31}$$

So the differential equation of DC voltage can be expressed in the (6.32):

$$\frac{dV_{dc}}{dt} = \frac{V_{cd} I_d + V_{cq} I_q}{CV_{dc}} - I_{dc} \tag{6.32}$$

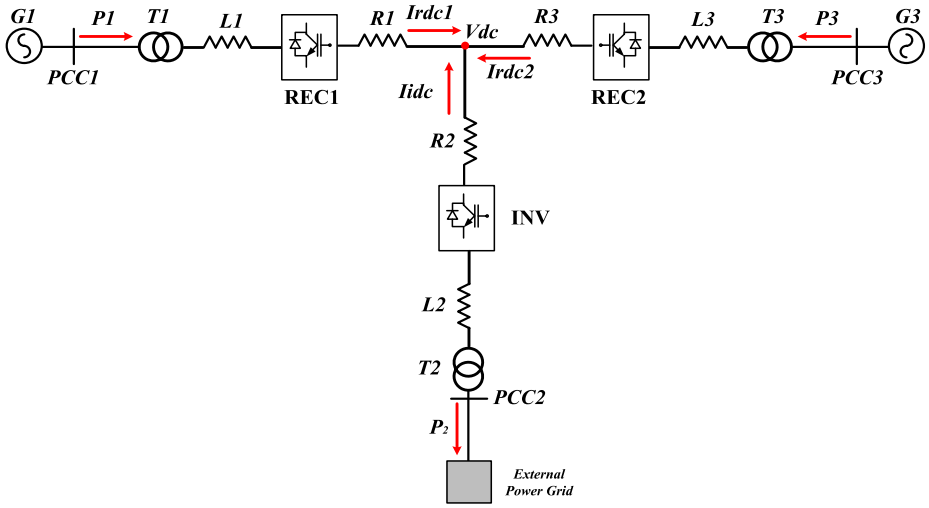

Fig-6.7 The Three-terminal VSC-based HVDC Grid with Radial Topology

Due to the definition of the directions of the DC currents of three VSCs in the Fig-6.7, the DC currents in this HVDC grid can be expressed in the (6.33):

$$I_{rdc1} + I_{rdc2} + I_{idc} = 0 \tag{6.33}$$

And the relationships among the DC voltages V_{rdc1}, V_{rdc2} and V_{idc} at all the three-terminal can be expressed in the (6.34):

$$\frac{(V_{rdc1} - V_{dc})}{R_1} + \frac{(V_{idc} - V_{dc})}{R_2} + \frac{(V_{rdc2} - V_{dc})}{R_3} = 0 \tag{6.34}$$

which the V_{dc} is the DC voltage at the common point of three branches in the DC grid, R_1, R_2 and R_3 are the resistance of the DC cables for each branch. According to the relationship among the three DC voltages, V_{dc} can be expressed in the (6.35):

$$V_{dc} = \frac{R_2 R_3 V_{rdc1} + R_1 R_2 V_{rdc2} + R_1 R_3 V_{idc}}{R_1 R_2 + R_2 R_3 + R_1 R_3} \tag{6.35}$$

So the differential equations for the DC voltages of the three-terminal HVDC grid are expressed by the (6.36):

$$\begin{cases} \dfrac{dV_{rdc1}}{dt} = \dfrac{V_{rcd1}I_{rd1} + V_{rcq1}I_{rq1}}{C_{r1}V_{rdc1}} + \dfrac{R_2V_{rdc2} + R_3V_{idc} - (R_2 + R_3)V_{rdc1}}{R_1R_2 + R_2R_3 + R_1R_3} \\ \dfrac{dV_{rdc2}}{dt} = \dfrac{V_{rcd2}I_{rd2} + V_{rcq2}I_{rq2}}{C_{r2}V_{rdc2}} + \dfrac{R_2V_{rdc1} + R_1V_{idc} - (R_1 + R_2)V_{rdc2}}{R_1R_2 + R_2R_3 + R_1R_3} \\ \dfrac{dV_{idc}}{dt} = \dfrac{V_{icd}I_{id} + V_{icq}I_{iq}}{C_iV_{idc}} + \dfrac{R_3V_{rdc1} + R_1V_{rdc2} - (R_1 + R_3)V_{idc2}}{R_1R_2 + R_2R_3 + R_1R_3} \end{cases} \tag{6.36}$$

And the small-signal models of for the HVDC grid are expressed in the (6.37) to the (6.39):

$$\begin{aligned} \frac{d\Delta V_{rdc1}}{dt} &= -\left(\frac{V_{rcd1}I_{rd1} + V_{rcq1}I_{rq1}}{C_{r1}V_{rdc1}^2} + \frac{R_2 + R_3}{R_1R_2 + R_2R_3 + R_1R_3}\right)\Delta V_{rdc1} \\ &+ \frac{R_2\Delta V_{rdc2} + R_3\Delta V_{idc}}{R_1R_2 + R_2R_3 + R_1R_3} + \frac{I_{rd1}\Delta V_{rcd1} + I_{rq1}\Delta V_{rcq1} + V_{rcd1}\Delta I_{rd1} + V_{rcq1}\Delta I_{rq1}}{C_{r1}V_{rdc1}} \end{aligned} \tag{6.37}$$

$$\begin{aligned} \frac{d\Delta V_{rdc2}}{dt} &= -\left(\frac{V_{rcd2}I_{rd2} + V_{rcq2}I_{rq2}}{C_{r2}V_{rdc2}^2} + \frac{R_1 + R_2}{R_1R_2 + R_2R_3 + R_1R_3}\right)\Delta V_{rdc2} \\ &+ \frac{R_2\Delta V_{rdc1} + R_1\Delta V_{idc}}{R_1R_2 + R_2R_3 + R_1R_3} + \frac{I_{rd2}\Delta V_{rcd2} + I_{rq2}\Delta V_{rcq2} + V_{rcd2}\Delta I_{rd2} + V_{rcq2}\Delta I_{rq2}}{C_{r2}V_{rdc2}} \end{aligned} \tag{6.38}$$

$$\begin{aligned} \frac{d\Delta V_{idc}}{dt} &= -\left(\frac{V_{icd}I_{id} + V_{icq}I_{iq}}{C_iV_{idc}^2} + \frac{R_1 + R_3}{R_1R_2 + R_2R_3 + R_1R_3}\right)\Delta V_{idc} \\ &\frac{R_3\Delta V_{rdc1} + R_1\Delta V_{rdc2}}{R_1R_2 + R_2R_3 + R_1R_3} + \frac{I_{id}\Delta V_{icd} + I_{iq}\Delta V_{icq} + V_{icd}\Delta I_{id} + V_{icq}\Delta I_{iq}}{C_iV_{idc}} \end{aligned} \tag{6.39}$$

6.4 Small-signal Analysis

As shown in Fig-6.7, the three sets state variables for the VSCs **REC1**, **INV** and **REC2** are listed in the (6.40) to the (6.42) as the state variables in (6.43):

$$x_1 = [\Delta V_{rdc1} \quad x_{r1} \quad x_{r2} \quad x_{r3} \quad x_{r4}]^T \tag{6.40}$$

$$x_2 = [\Delta V_{idc1} \quad x_{i1} \quad x_{i2} \quad x_{i3} \quad x_{i4}]^T \tag{6.41}$$

$$x_3 = [\Delta V_{rdc2} \quad x_{r5} \quad x_{r6} \quad x_{r7} \quad x_{r8}]^T \tag{6.42}$$

$$x = \begin{bmatrix} x_1 & x_2 & x_3 \end{bmatrix} \tag{6.43}$$

The *d*- and *q*-axis voltage components at the **PCC1** to **PCC3** are selected as the set of input variables in the (6.44):

$$u = \begin{bmatrix} \Delta V_{rsd1} & \Delta V_{rsq1} & \Delta V_{isd} & \Delta V_{isq} & \Delta V_{rsd2} & \Delta V_{rsq2} \end{bmatrix}^T \tag{6.44}$$

The *d*- and *q*-axis voltage components at the VSCs **REC1**, **INV** and **REC2** are selected as the set of output variables in the (6.45):

$$y = \begin{bmatrix} \Delta V_{rcd1} & \Delta V_{rcq1} & \Delta V_{icd} & \Delta V_{icq} & \Delta V_{rcd2} & \Delta V_{rcq2} \end{bmatrix}^T \tag{6.45}$$

The *d*- and *q*-axis current components of VSCs **REC1**, **INV** and **REC2** are selected as the a set of temporary variables in (6.46)

$$i = \begin{bmatrix} \Delta I_{rd1} & \Delta I_{rq1} & \Delta I_{id} & \Delta I_{iq} & \Delta I_{rd2} & \Delta I_{rq2} \end{bmatrix}^T \tag{6.46}$$

So the state variables of this system can be expressed in the (6.47). And the details for each matrix can be founded in Appendix D.

$$\begin{cases} \dot{x} = Ax + Bu + Cy + Di \\ y = Ex + Fu + Gi \end{cases} \tag{6.47}$$

For the converter, the voltages on the system- and converter-side can be expressed with this relationship in the (6.48):

$$\dot{V}_s = \dot{V}_c + jX\dot{I} \tag{6.48}$$

where $\dot{V}_s$ and $\dot{V}_c$ are the voltage vectors on the system- and converter-side, X is the total reactance of the series AC reactor and transform between the system- and converter-side. So the (6.48) can be expressed in (6.49) in the *d*-*q* coordinate system:

$$\begin{bmatrix} V_{sd} \\ V_{sq} \end{bmatrix} - \begin{bmatrix} V_{cd} \\ V_{cq} \end{bmatrix} = \begin{bmatrix} 0 & -X \\ X & 0 \end{bmatrix} \times \begin{bmatrix} I_d \\ I_q \end{bmatrix} \tag{6.49}$$

So the set of the temporary variables can be replaced by the combination of input and output variables which are expressed in the (6.50):

$$i = H^{-1}u - H^{-1}y \tag{6.50}$$

So the standard representation of the small-signal models of the system is expressed by the (6.51) and (6.52):

$$\begin{aligned}\dot{x} &= \left[A + (C - DH^{-1})(I + GH^{-1})^{-1}E\right]x \\ &+ \left[(B + DH^{-1}) + (C - DH^{-1})(I + GH^{-1})^{-1}(F + GH^{-1})\right]u\end{aligned} \tag{6.51}$$

$$y = (I + GH^{-1})^{-1}Ex + (I + GH^{-1})^{-1}(F + GH^{-1})u \tag{6.52}$$

And the dynamic characteristics of the whole system at the specific operating point can be reflected from the eigen-values in state matrix A' expressed in the (6.53):

$$A' = A + (C - DH^{-1})(I + GH^{-1})^{-1}E \tag{6.53}$$

The $A'_{(j)}$ can be formed according to its steady states at the ***j***th operating point. So for ***N*** units of operating points, the A'_N is the state matrix for the representation of the whole system at all the operating point expressed in the (6.54):

$$A'_N = \begin{bmatrix} A'_{(1)} & 0 & 0 & 0 & 0 \\ 0 & \ddots & 0 & 0 & 0 \\ 0 & 0 & A'_{(j)} & 0 & 0 \\ 0 & 0 & 0 & \ddots & 0 \\ 0 & 0 & 0 & 0 & A'_{(N)} \end{bmatrix} \tag{6.54}$$

6.5 The Particle-swarm Optimisation Method

The PSO method is an evolutionary computation (EC) technique initially proposed and developed by Dr. Russell Eberhart and Dr. James Kennedy, who learnt from the studies of social behaviours in the flocks of birds during their research [132, 133, 157]. In the PSO method, the so-called particle (the candidate solution) moves with its own coordinates in the solution space searching for its personal best solutions (called the personal best fitness $P_{fitness}$). The positions associated with the personal best solutions are named *pbest* (called the personal best position). For all the particles, the best positions obtained by any particles in the solution space for the global best solutions (called the global best fitness $G_{fitness}$) are named *gbest*

(called the global best position). The core concepts of the PSO methods are searching for the $G_{fitness}$ in the solution space by moving the particles with accelerating manners toward their own *pbest* as well as the *gbest*. For each step in the iteration, All the particles try to modify their own positions in the solution space with the random weighting accelerations [157]. The velocity of each particle for each step in the iteration can be expressed with the (6.55) [132, 133, 157]:

$$V_i^{k+1} = w \times V_i^k + c_1 rand_1 \times (pbest_i^k - P_i^k) + c_2 rand_2 \times (gbest - P_i^k) \tag{6.55}$$

where V_i^k is the current velocity of the *i*th particle ($i \in [1, N]$) at the *k*th step of iteration ($k \in [1, M]$); c_1 and c_2 are the weighting factors, $rand_1$ and $rand_2$ are the random numbers distributing uniformly between 0 and 1; P_i^k is the current position of the *i*th particle at the *k*th step of iteration; $pbest_i$ is the personal best of the *i*th particle; *gbest* is the global best of all the particles. *w* is the weighting function which is usually expressed by (6.56) [132, 133, 157] :

$$w = w_{Max} - [(w_{Max} - w_{Min}) \times k] / M \tag{6.56}$$

where w_{Max} is the initial maximum weight; w_{Min} is the final minimum weight; *M* is the total number of the iteration; *k* is the current step in the iteration. So the updated of the P_i^{k+1} can be expressed in the (6.57):

$$P_i^{k+1} = P_i^k + V_i^{k+1} \tag{6.57}$$

Defining the solution of the P_i^k as $f(P_i^k)$. Considering these two condition:

1) If $f(P_i^k) < f(pbest_i)$, $pbest_i$ will be replaced by P_i^k,

2) If $f(P_i^k) < f(gbest)$, *gbest* will be replaced by P_i^k,

In order to improve the searching performance of the general PSO algorithm, many mutation mechanisms have been proposed to strengthen its capabilities for specific problems [137, 157].

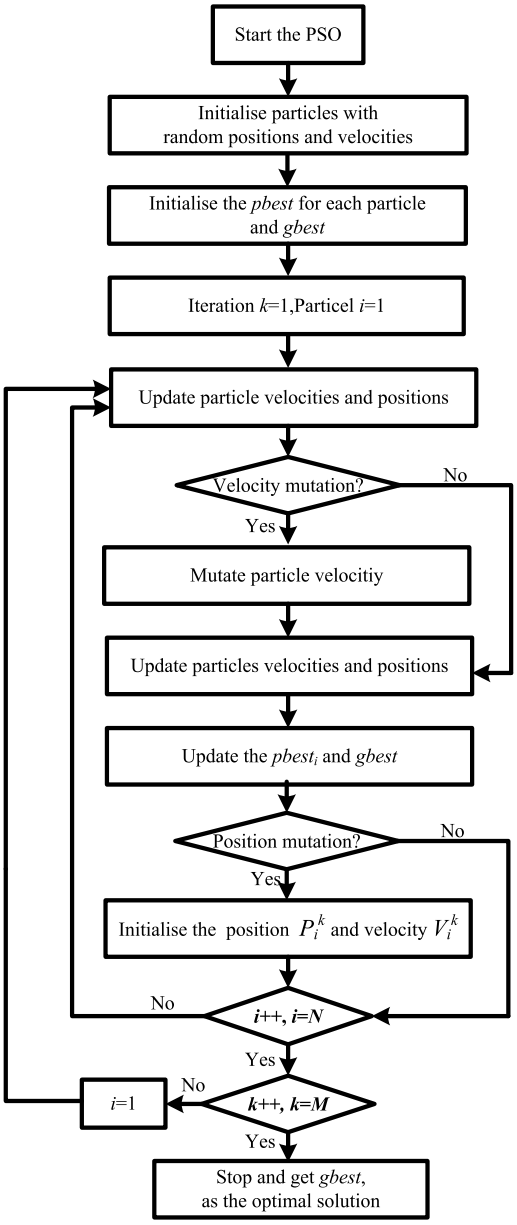

Fig-6.8 The Flow-Chart of Improved PSO Algorithm

The velocity- and position-mutation are considered for the improved PSO algorithm to avoid the solutions being trapped in the local optimum. As seen from the (6.55), the velocities would be very small when P_i^k is very close to the $pbest_i$ at the final stage of the iterations, which might lead to trapping in the local optimum for this particle. So when the $f(pbest_i)$ keeps unchanged for certain number of steps in the iteration, the velocity will be mutated with the absolute value of initial velocity V_i, which is a random value in the uniform distribution $[-V_{maxi}, V_{maxi}]$, which is expressed by the (6.58).

$$V_i^k = \begin{cases} V_i & if \left|V_i^k\right| < \left|V_i\right| \\ V_i^k & if \left|V_i^k\right| \geq \left|V_i\right| \end{cases} \tag{6.58}$$

After the mutation of velocities, if the $f(pbest_i)$ is still unchanged, the mutation of its position P_i^k can be applied, which would reset its initial position and velocity but still keep the current $pbest_i$. In this way, it could decrease the possibilities to trap in the local optimums for the particles. According to the principles mentioned, the flow chart of improved PSO method is shown in Fig-6.8 above [137, 157].

6.6 Case Studies

6.6.1 Parameter Optimisation with PSO Method

In this case, a three-terminal VSC-based HVDC grid with the radial structure shown in Fig-6.7 is connecting to two large-scale energy systems with rated 200 MW respectively. The detailed parameters and the simulation system are described in Appendix H. At the initial stage, the HVDC grid worked at the **Operating Point 1**. After 3 s, the whole system worked at **Operating Point 2**. The details of the operating points are listed in the Table-6.1.

Table-6.1 The Details of Operating Points

	REC1	**REC2**
Operating Point 1	P_1=200 MW	P_2=200 MW
Operating Point 2	$P_{1=}$170 MW	P_2=170 MW

And the PSO program was executed to search for the $G_{fitness}$ with the aim of making the eigen-values of the state matrix with the maximum real-parts on the left-side of the complex plane far from the zero point as far as possible in the range of iteration to maintain the dynamic stability of the whole system [47, 57, 136]. With these principles, the criteria for searching for the $G_{fitness}$ are given by the (6.59) [47]:

$$\begin{cases} G_{fitness} = Max\left(R(\lambda_1), \cdots R(\lambda_j), \cdots R(\lambda_N)\right) \\ G_{fitness} < 0 \end{cases} \tag{6.59}$$

where $R(\lambda_j)$ is the value for the real-part of the jth eigen-value of the state matrix which including N unit of eigen-values ($j \in [1, N]$).

Table-6.2 The Details of Computation Platform

CPU	**Intel Core2 CPU Duo CPU E8400 4.0 GHz**
RAM	**4.00 GB**
Operating System	**Microsoft Windows 7**
Developing Software	**MATLAB 2012a**

Table-6.3 The Initial Configuration of PSO Program

Number of particle	**100**
Number of parameters	**18**
Number of iteration	**200**
c_1	**2**
c_2	**2**
X_{max}	**1.2**
X_{min}	**0.5**
Initial $G_{fitness}$	**10000**

The detailed information of the computation platform and the initial configuration of the PSO program are listed in the Table-6.2 and Table-6.3. The PSO program ran for 8.917 s and the $G_{fitness}$ decreased from 10000 to -14.7408 in the final. After the parameter optimisation with the developed PSO program, the sets of original and optimised parameters of the PI controllers of VSCs are listed in the Table-6.4.

Table-6.4 The Original and Optimised Parameters of VSC Controllers

VSC 1	K_{rp1} **(p.u.)**	K_{ri1} **(s)**	K_{rp2} **(p.u.)**	K_{ri2} **(s)**	K_{rp3} **(p.u.)**	K_{ri3} **(s)**
Original	2.0	20.0	2.0	20.00	0.6	6.0
Optimised	1.0049	29.9986	1.8020	14.3836	0.3222	4.9651
VSC 2	K_{ip1} (p.u.)	K_{ii1} (s)	K_{ip2} (p.u.)	K_{ii2} (s)	K_{ip3} (p.u.)	K_{ii3} (s)
Original	2.0	40.0	2.0	20.0	0.6	6.0
Optimised	1.2633	46.6243	1.9422	16.0032	0.3916	7.4879
VSC 3	K_{rp4} (p.u.)	K_{ri4} (s)	K_{rp5} (p.u.)	K_{ri5} (s)	K_{rp6} (p.u.)	K_{ri6} (s)
Original	2.0	20.0	2.0	20.00	0.6	6.0
Optimised	1.0028	29.8706	1.5581	20.1830	0.4319	7.2214

And the eigen-values of the state matrix for the three-terminal HVDC grid at these two operating points are listed in the Table-6.5. The real-parts of the eigen-values are all located on the left-hand of the zero-point on the complex plane to reflect the dynamic stability of this three-terminal HVDC grid at these two operating points.

Table-6.5 The Eigen-values for the State Matrix

λ_1	-192.4147	λ_{11}	-15.4102	λ_{21}	-14.8194
λ_2	-152.9589	λ_{12}	-14.7408	λ_{22}	-18.3795
λ_3	-37.8378+j50.4096	λ_{13}	-37.7529	λ_{23}	-19.1225
λ_4	-37.8378-j50.4096	λ_{14}	-16.71821	λ_{24}	-19.1225
λ_5	-16.7219	λ_{15}	-16.71821	λ_{25}	-15.4102
λ_6	-14.7904	λ_{16}	-178.1836	λ_{26}	-15.4102
λ_7	-18.4731	λ_{17}	-146.6884	λ_{27}	-14.771
λ_8	-19.1226	λ_{18}	-39.8422+ j43.6888	λ_{28}	-37.4605
λ_9	-19.1226	λ_{19}	-39.8422- j43.6888	λ_{29}	-16.7182
λ_{10}	-15.4102	λ_{20}	-16.7237	λ_{30}	-16.7182

6.6.2 Case 1: Short-circuit Fault at Operating Point 1

With the original and optimised parameters of the PI controllers, the dynamic simulations have been carried out in MATLAB/SIMULINK to compare the dynamic performance of the three-terminal HVDC grid under large-disturbances with the optimised and original parameters. The simulation system in detail is described in Appendix H. In **Case 1**, the dynamic performance of the HVDC grid with original and optimised PI controller parameters has best tested for transient stability analysis. The whole system initially operated at the **Operating Point 1** mentioned in Table-6.1 and The SCR of the external systems on each-side of HVDC grid was set as 3. A three-phase short-circuit grounded fault was applied at the **PCC2** on the inverter-side at the 1.5 s. After 150 ms, the fault was removed. The two AC sources connecting to REC1 and REC2 of this three-terminal HVDC grid are acted as two offshore wind farms, so that their SCR were set as 1.5. The SCR of external power system on the inverter-side was set as 2. Because the three converters are strongly coupled in the DC grid with small electrical distances, the faults on one-side could have obvious impacts on

other two sides of MTDC grid. So the AC source on the inverter-side grounded resistance was set as 20 ohm to avoid final instability. The AC voltage at PCC2 just drop to 0. 6869 p.u. in Fig-6.15 when the fault was applied at 1.5 s.

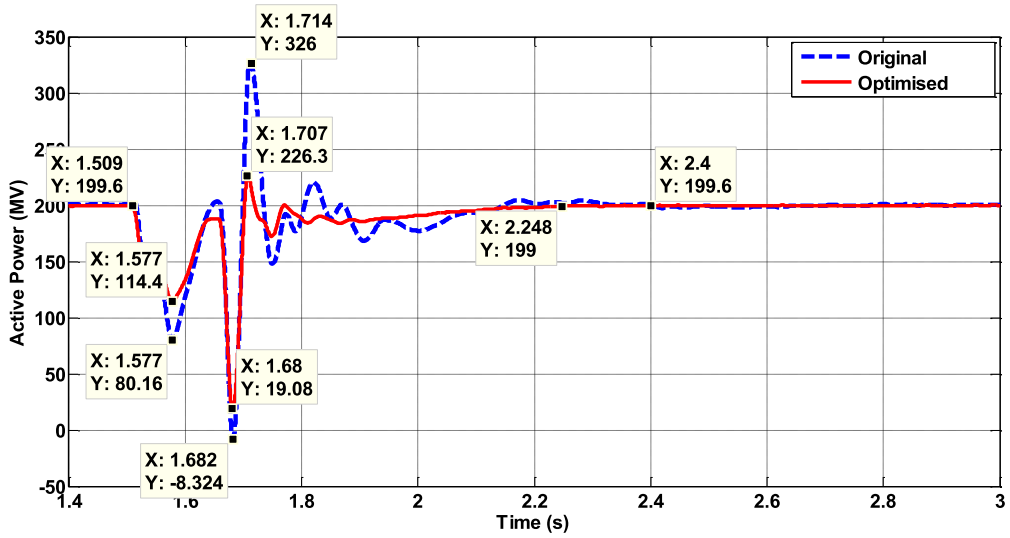

Fig-6.9 The Active Power at PCC1 (Operating Point 1)

The dynamic responses of the power and the AC voltage at each PCC as well as the DC-side voltage of each converter in this HVDC grid at the **Operating Point 1** are shown from Fig-6.9 to Fig-6.20. For the active power at PCC1 in Fig-6.9, the maximum overshoot of the power oscillation with original parameters is 326 MW at 1.714 s and that with optimised parameters is 226.3 MW at 1.707 s. The minimum undershoot of power oscillation with original parameters is -8.324 MW at 1.682 s and that with optimised parameters is 19.08 MW at 1.68 s. And the active power with optimised parameters returned to normal condition at nearly 2.248 s after the third swing but that with original parameters returned to the normal condition at nearly 2.4 s after nearly seven swings.

For the reactive power at PCC1 in Fig-6.10, the maximum overshoot of the power oscillation with original parameters is 63.06 MVar at 1.689 s and that with optimised parameters is 23.03 MVar at 1.685 s. The minimum undershoot of power oscillation with original

parameters is -77.95 MVar at 1.716 s and that with optimised parameters is -28.05 MVar at 1.709 s. And the reactive power with optimised parameters returned to normal condition at nearly 2.009 s after the fourth swing after the removal of fault but that with original parameters returned to the normal condition at nearly 2.429 s after nearly seventh swings.

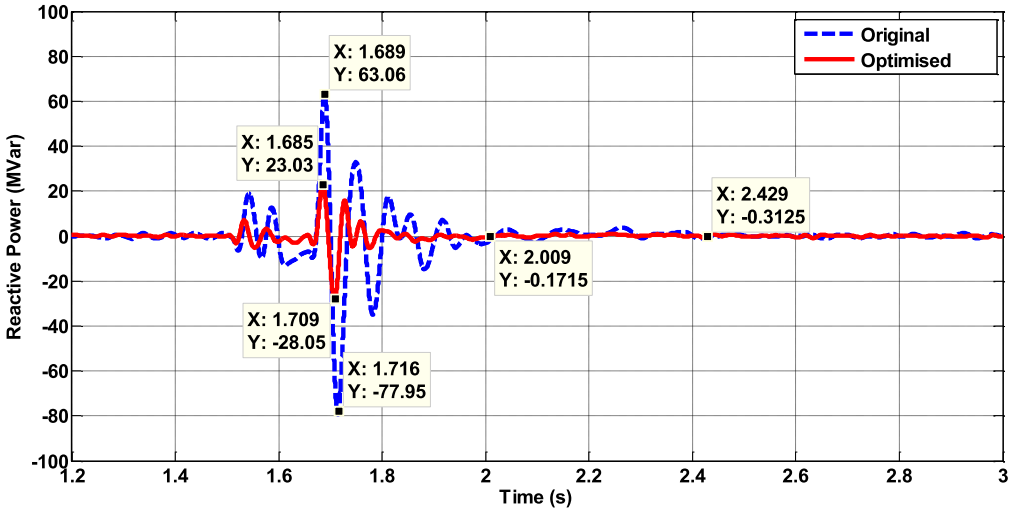

Fig-6.10 The Reactive Power at PCC1 (Operating Point 1)

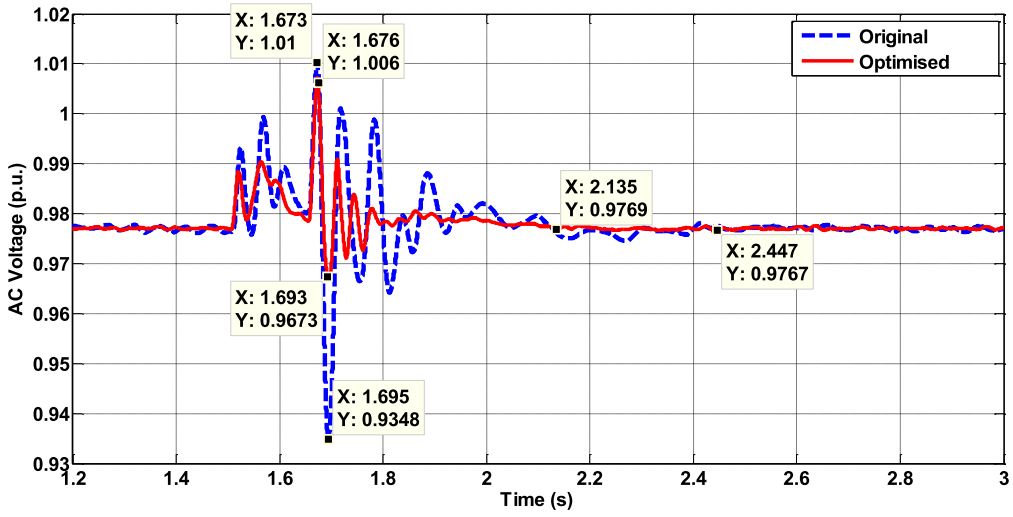

Fig-6.11 The AC Voltage at PCC1 (Operating Point 1)

For the AC voltage at PCC1 in Fig-6.11, the maximum overshoot of the voltage oscillation with original parameters is 1.01 p.u. at 1.673 s and that with optimised parameters is 1.006 p.u. at 1.676 s. The minimum undershoot of voltage oscillation with original parameters is 0.9348 p.u. at 1.695 s and that with optimised parameters is 0.9673 p.u. at 1.693 s. And the

AC voltage with optimised parameters returned to normal condition at nearly 2.135 s after the fifth swing after the removal of fault but that with original parameters returned to the normal condition at nearly 2.447 s after several swings.

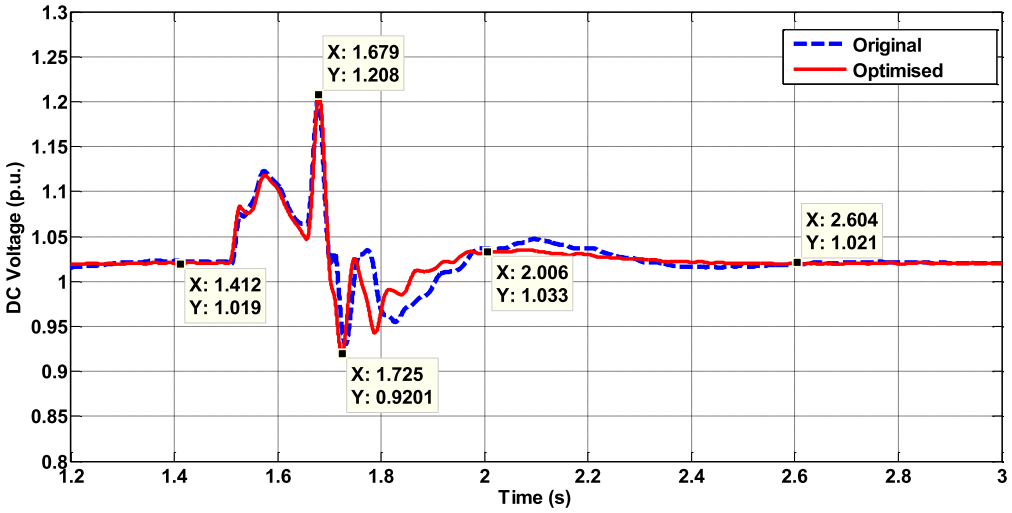

Fig-6.12 The DC Voltage of REC1 (Operating Point 1)

For the DC voltage of **REC1** in Fig-6.12, the differences of maximum overshoots and minimum undershoots of the voltage oscillation with original and optimised parameters are very small. However, the DC voltage with optimised parameters returned to normal condition at nearly 2.006 s after several swings after the removal of fault but that with original parameters returned to the normal condition at nearly 2.604 s after several swings.

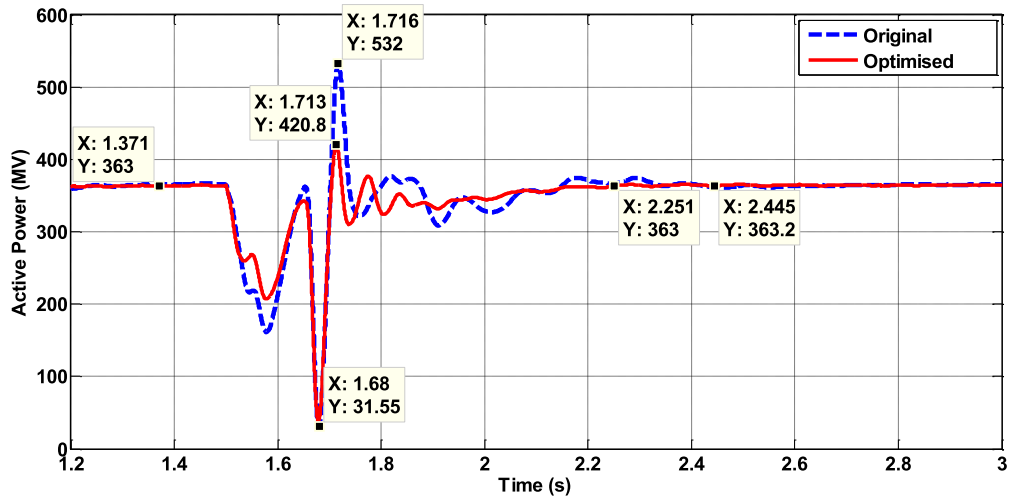

Fig-6.13 The Active Power at PCC2 (Operating Point 1)

For the active power at PCC2 in Fig-6.13, the maximum overshoots of the power oscillation with original and optimised parameters are nearly same at 31.55 MW at 1.68 s. The minimum undershoot of power oscillation with original parameters is 532 MW at 1.716 s and that with optimised parameters is 420.8 MW at 1.713 s. And the active power with optimised parameters returned to normal condition at nearly 2.251 s after nearly four swings but that with original parameters returned to the normal condition at nearly 2.445 s after several swings.

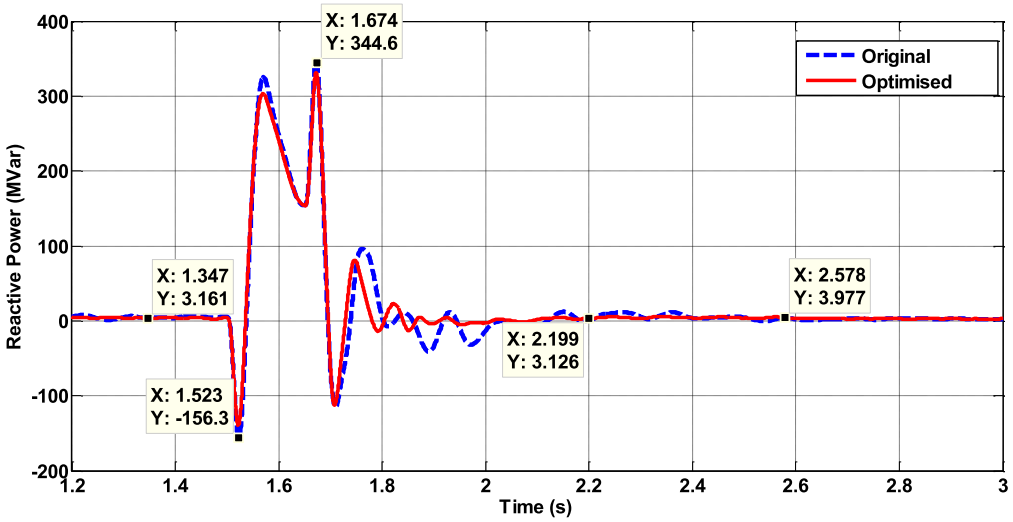

Fig-6.14 The Reactive Power at PCC2 (Operating Point 1)

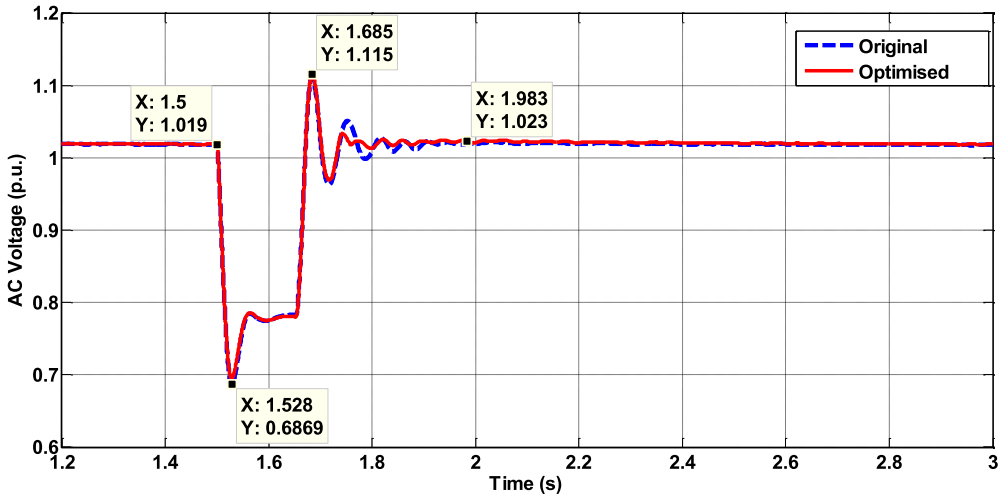

Fig-6.15 The AC Voltage at PCC2 (Operating Point 1)

For the reactive power at PCC2 in Fig-6.14, the maximum overshoots and minimum undershoots of the power oscillation with original and optimised parameters are nearly same as 344.6 MVar at 1.674 s and -156.3 MVar at 1.523 s respectively. And the reactive power with optimised parameters returned to normal condition at nearly 2.199 s after the fourth swing after the removal of fault but that with original parameters returned to the normal condition at nearly 2.578 s after several swings. For the AC voltage at PCC2 in Fig-6.15, the maximum overshoots and minimum undershoots of the voltage oscillation with original and optimised parameters are nearly same as 1.115 p.u. at 1.685 s and 0.6869 p.u. at 1.528 s respectively. And the differences of two curves are nearly similar with small differences.

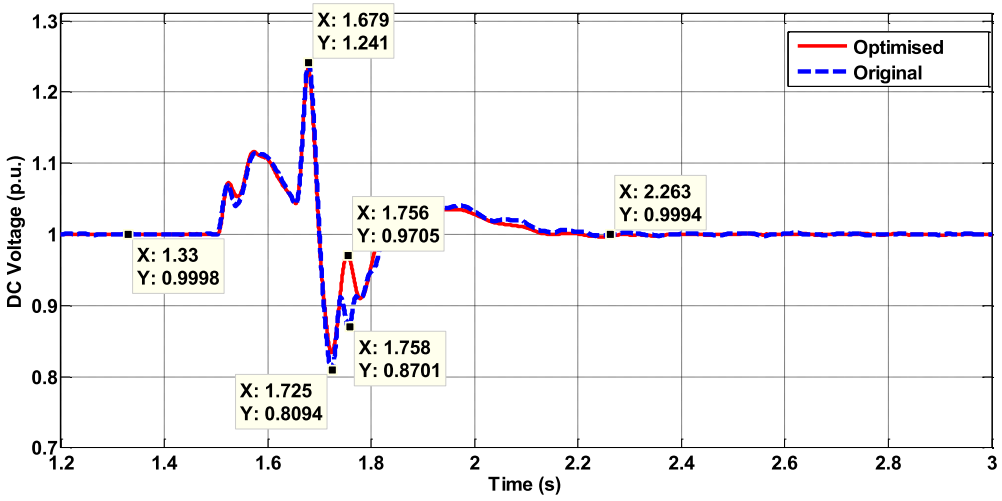

Fig-6.16 The DC Voltage of INV (Operating Point 1)

For the DC voltage of **INV** in Fig-6.16, the differences of two curves for the voltage oscillation with original and optimised parameters are very small except the time range when the overshoot of 0.9705 p.u. appeared at 1.756 s for the DC voltage with optimised parameters and the undershoot of 0.8701 p.u. appeared at 1.758 s for the DC voltage with original parameters.

For the active power at PCC3 in Fig-6.17, the maximum overshoot of the power oscillation with original parameters is 267.6 MW at 1.71 s and that with optimised parameters is 227.2

MW at 1.708 s. The minimum undershoots of power oscillations with original and optimised parameters are nearly same as 14.41 MW at 1.683 s. And the active power with optimised parameters returned to normal condition at nearly 2.251 s after the third swing but that with original parameters returned to the normal condition at nearly 2.396 s after several swings.

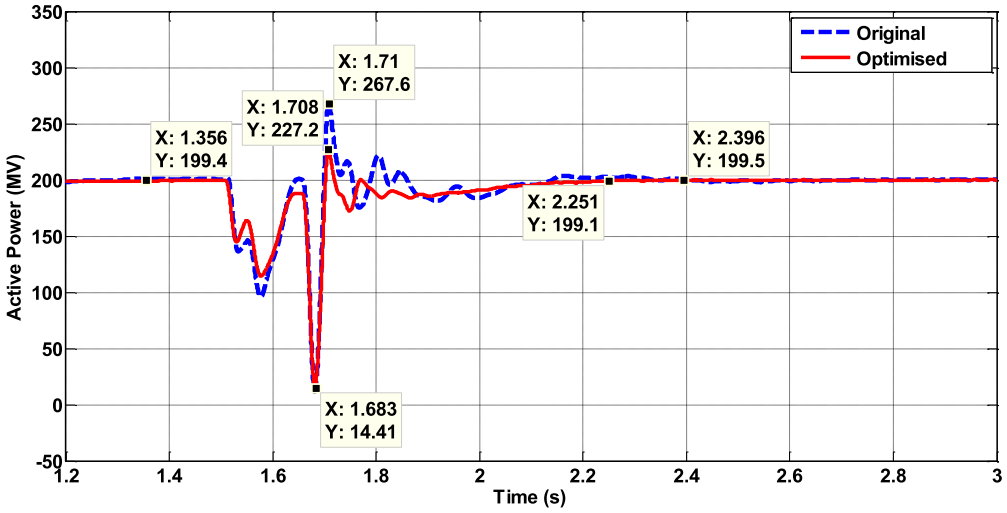

Fig-6.17 The Active Power at PCC3 (Operating Point 1)

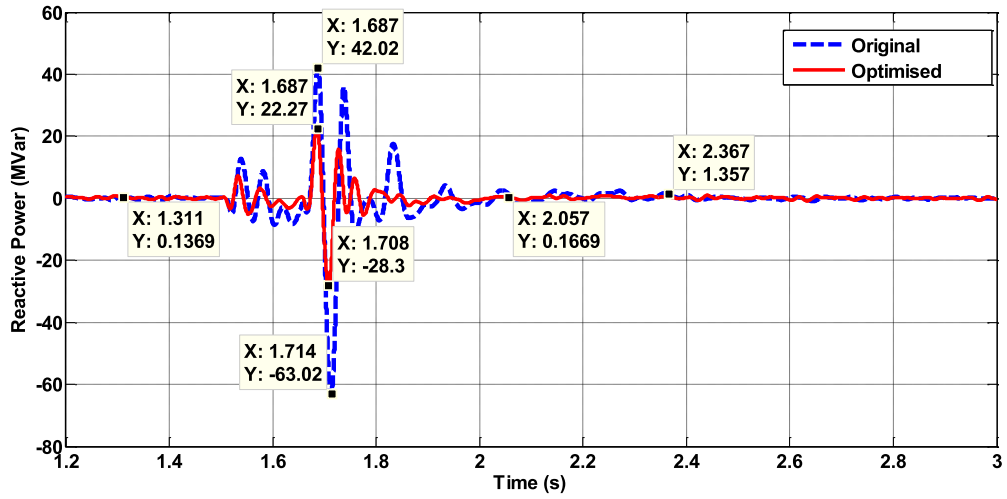

Fig-6.18 The Reactive Power at PCC3 (Operating Point 1)

For the reactive power at PCC3 in Fig-6.18, the maximum overshoot of the power oscillation with original parameters is 42.02 MVar at 1.687 s and that with optimised parameters is 22.27 MVar at 1.687 s. The minimum undershoot of power oscillation with original parameters is -63.02 MVar at 1.714 s and that with optimised parameters is -28.3 MVar at

1.708 s. And the reactive power with optimised parameters returned to normal condition at nearly 2.057 s after several swings after the removal of fault but that with original parameters returned to the normal condition at nearly 2.367 s after several swings.

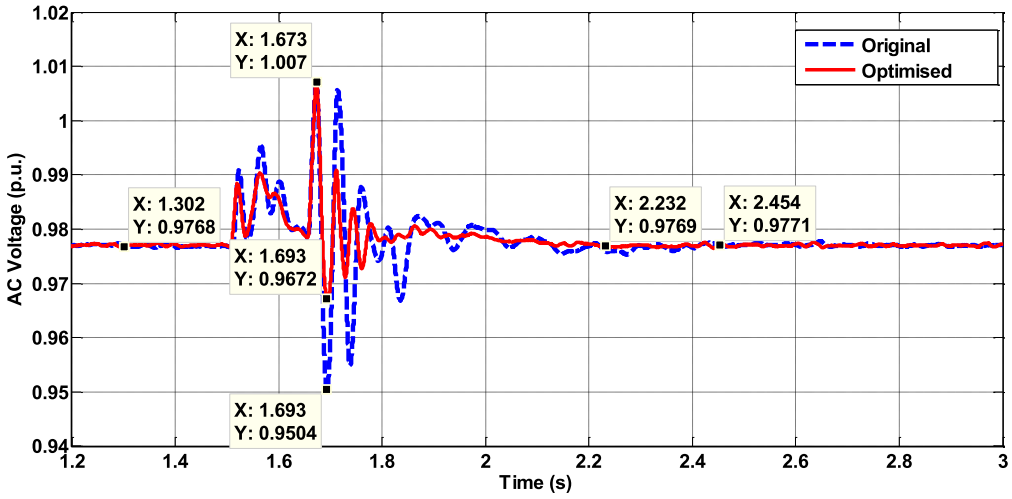

Fig-6.19 The AC Voltage at PCC3 (Operating Point 1)

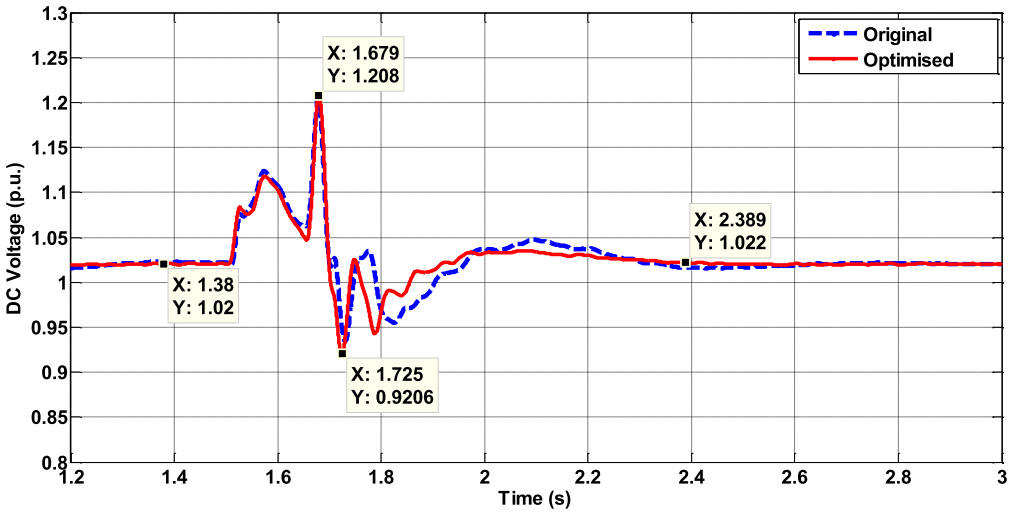

Fig-6.20 The DC Voltage of REC3 (Operating Point 1)

For the AC voltage at PCC1 in Fig-6.19, the maximum overshoots of the voltage oscillations with original and optimised parameters are as same as 1.007 p.u. at 1.673 s. The minimum undershoot of voltage oscillation with original parameters is 0.9504 p.u. at 1.693 s and that with optimised parameters is 0.9672 p.u. at 1.693 s. And the AC voltage with optimised parameters returned to normal condition at nearly 2.232 s after several swings after the

removal of fault but that with original parameters returned to the normal condition at nearly 2.454 s after several swings. For the DC voltage of **REC3** in Fig-6.20, the differences of maximum overshoots and minimum undershoots of the voltage oscillation with original and optimised parameters are very small. The DC voltage with original and optimised parameters returned to normal condition at nearly 2.389 s after several swings.

Comparing the simulation results for the system at the **Operating Point 1** shown above, the active and reactive power, the AC voltage at PCC1 for the **REC1** and PCC3 for the **REC2** have been obviously improved in terms of the magnitudes of over/undershoot, the period of oscillations and number of oscillation swings. For the DC voltages of **REC1** and **REC2,** the dynamic responses have been improved in the period of oscillations and number of oscillation swings. But the improvements are not as obvious as those for other three variables. For the **INV**, the active and reactive power at PCC2 have been obviously improved in terms of the magnitudes of over/undershoot, the period of oscillations and number of oscillation swings. But for AC voltage at PCC3 and the DC voltage of **INV**, the dynamic responses have just improved slightly. Overall, the dynamic performance of the whole HVDC grid has been improved with the set of optimised parameters for the **Operating Point 1.**

6.6.3 Case 2: Short-circuit Fault at Operating Point 2

In **Case 2,** the system changed its operating points at the 3 s to the **Operating Point 2**, the same fault was applied again at 3.5 s and the fault duration was 150 ms as well. The dynamic responses of the same variables of each converter in this HVDC grid at the **Operating Point 2** are shown from Fig-6.21 to Fig-6.32.

For the active power at PCC1 in Fig-6.21, the maximum overshoot of the power oscillation with original parameters is 270.3 MW at 3.71 s and that with optimised parameters is 225.8

MW at 3.709 s. The minimum undershoots of power oscillations with original and optimised parameters are nearly same as 1.405 MW at 3.682 s. And the active power with optimised parameters returned to normal condition at nearly 4.13 s after the fourth swing but that with original parameters returned to the normal condition at nearly 4.360 s after nearly six swings.

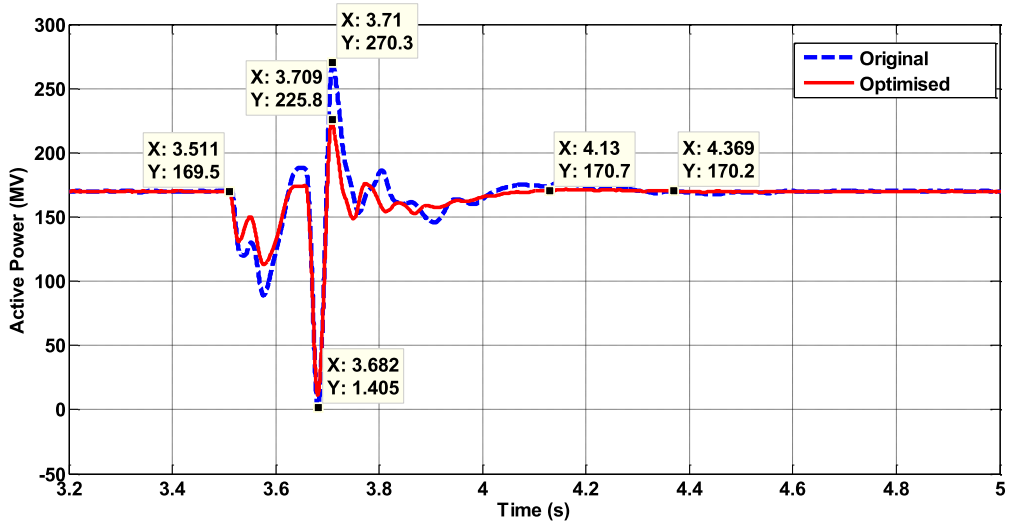

Fig-6.21 The Active Power at PCC1 (Operating Point 2)

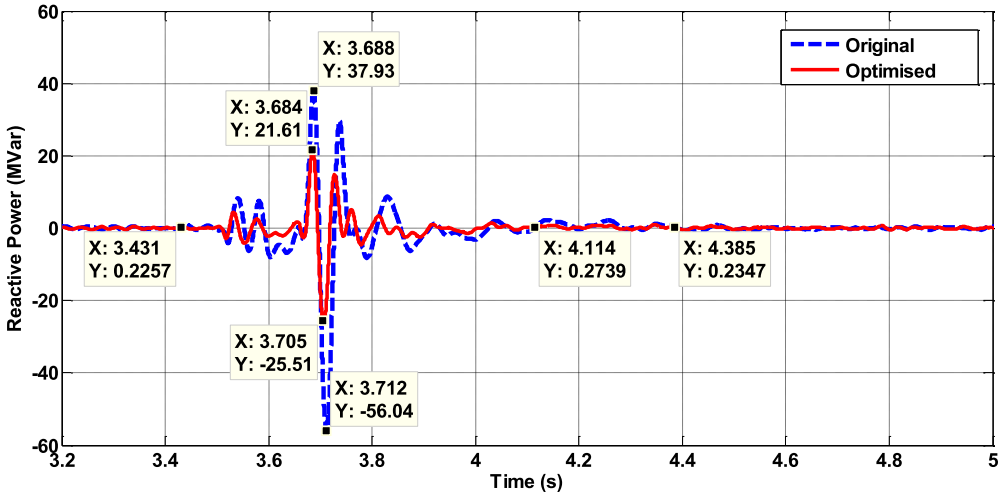

Fig-6.22 The Reactive Power at PCC1 (Operating Point 2)

For the reactive power at PCC1 in Fig-6.22, the maximum overshoot of the power oscillation with original parameters is 37.93 MVar at 3.688 s and that with optimised parameters is 21.61 MVar at 3.684 s. The minimum undershoot of power oscillation with original parameters is -56.04 MVar at 3.712 s and that with optimised parameters is -25.51 MVar at

3.705 s. And the reactive power with optimised parameters returned to normal condition at nearly 4.114 s after several swings after the removal of fault but that with original parameters returned to the normal condition at nearly 4.385 s after several swings. For the AC voltage at PCC1 in Fig-6.23, the maximum overshoots of the voltage oscillations with original and optimised parameters are nearly as same as 1.007 p.u. at 3.673 s. The minimum undershoot of voltage oscillation with original parameters is 0.9553 p.u. at 3.694 s and that with optimised parameters is 0.9693 p.u. at 3.692 s. And the AC voltage with optimised parameters returned to normal condition at nearly 4.158 s after several swings after the removal of fault but that with original parameters returned to the normal condition at nearly 4.5 s after several swings.

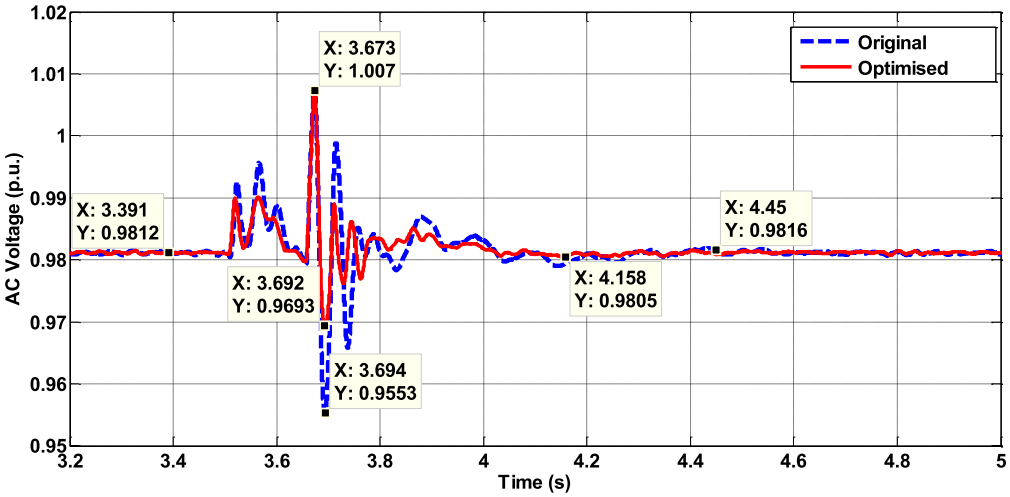

Fig-6.23 The AC Voltage at PCC1 (Operating Point 2)

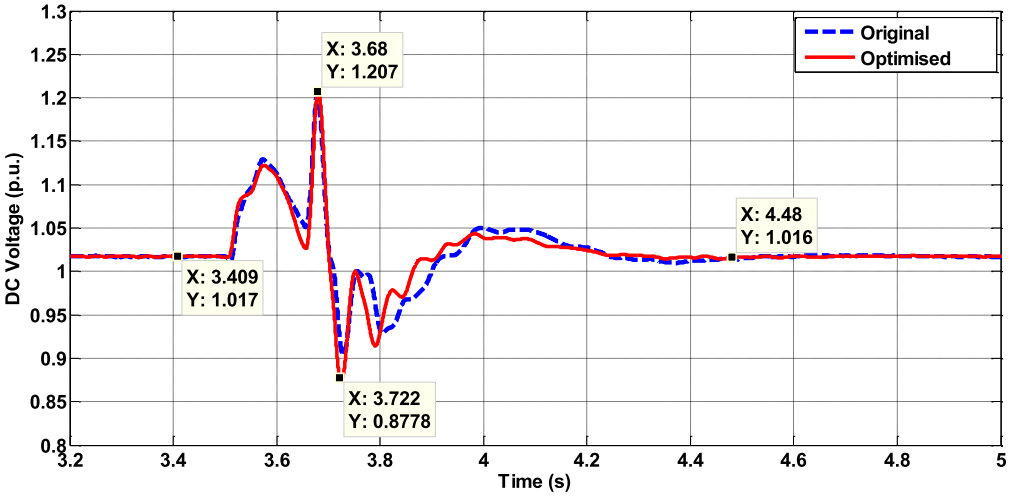

Fig-6.24 The DC Voltage of REC1 (Operating Point 2)

For the DC voltage of **REC1** in Fig-6.24, the differences of maximum overshoots and minimum undershoots of the voltage oscillation with original and optimised parameters are very small. However, the DC voltage with original and optimised parameters returned to normal condition at nearly 4.48 s after several swings after the removal of fault.

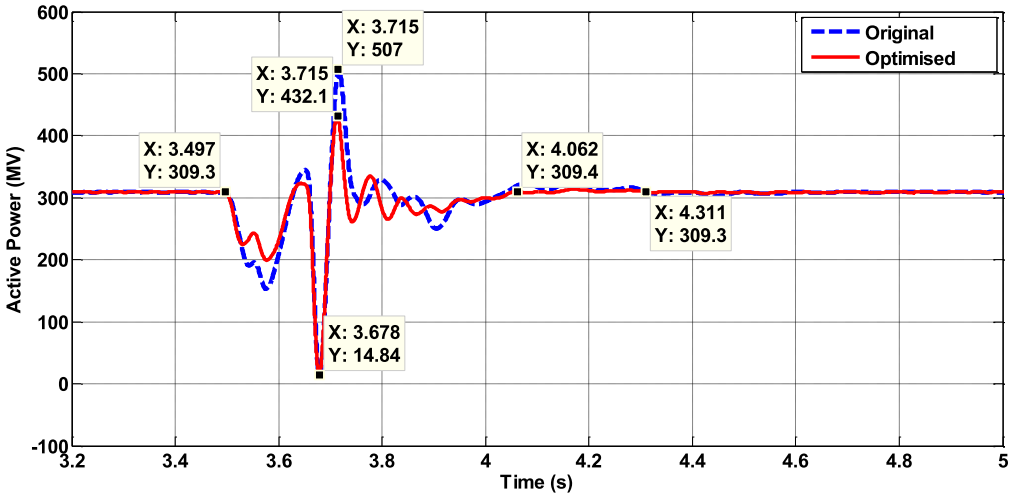

Fig-6.25 The Active Power at PCC2 (Operating Point 2)

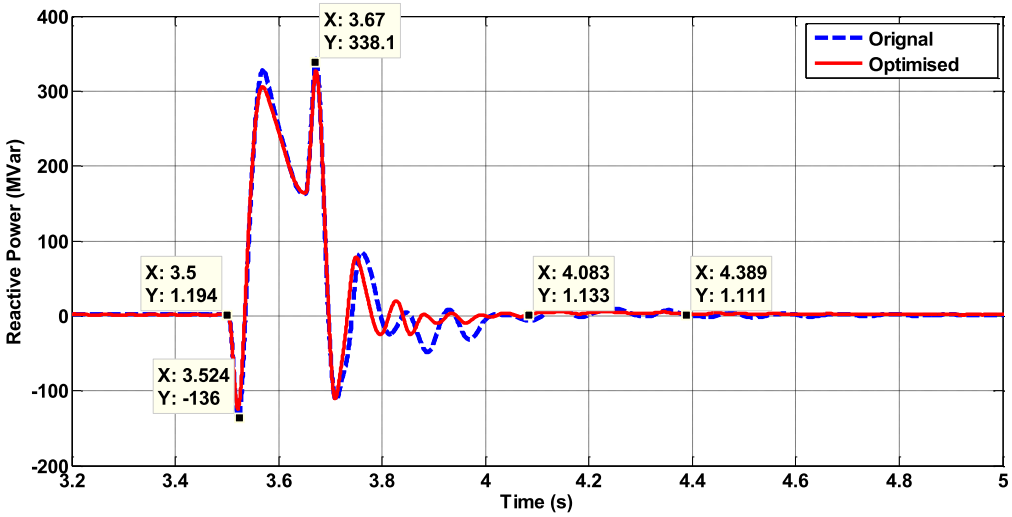

Fig-6.26 The Reactive Power at PCC2 (Operating Point 2)

For the active power at PCC2 in Fig-6.25, the minimum undershoot of power oscillation with original parameters is 532 MW at 1.716 s and that with optimised parameters is 420.8 MW at 1.713 s. The maximum undershoots of the power oscillation with original and optimised parameters are nearly same at 14.84 MW at 3.678 s. And the active power with optimised

parameters returned to normal condition at nearly 4.062 s after several swings but that with original parameters returned to the normal condition at nearly 4.311 s after several swings.

For the reactive power at PCC2 in Fig-6.26, the maximum overshoots and minimum undershoots of the power oscillation with original and optimised parameters are nearly same as 338.1 MVar at 3.67 s and -136 MVar at 3.524 s respectively. And the reactive power with optimised parameters returned to normal condition at nearly 4.083 s after several swings after the removal of fault but that with original parameters returned to the normal condition at nearly 4.389 s after several swings. For the AC voltage at PCC2 in Fig-6.27, the maximum overshoots and minimum undershoots of the voltage oscillation with original and optimised parameters are nearly same as 1.105 p.u. at 3.686 s and 0.6664 p.u. at 3.532 s respectively. And the differences of two curves are nearly similar with small differences. For the DC voltage of **INV** in Fig-6.28, the differences of two curves for the voltage oscillation with original and optimised parameters are very small except the time range when the overshoot of 0.9705 p.u. appeared at 1.756 s for the DC voltage with optimised parameters and the undershoot of 0.8701 p.u. appeared at 1.758 s for the DC voltage with original parameters

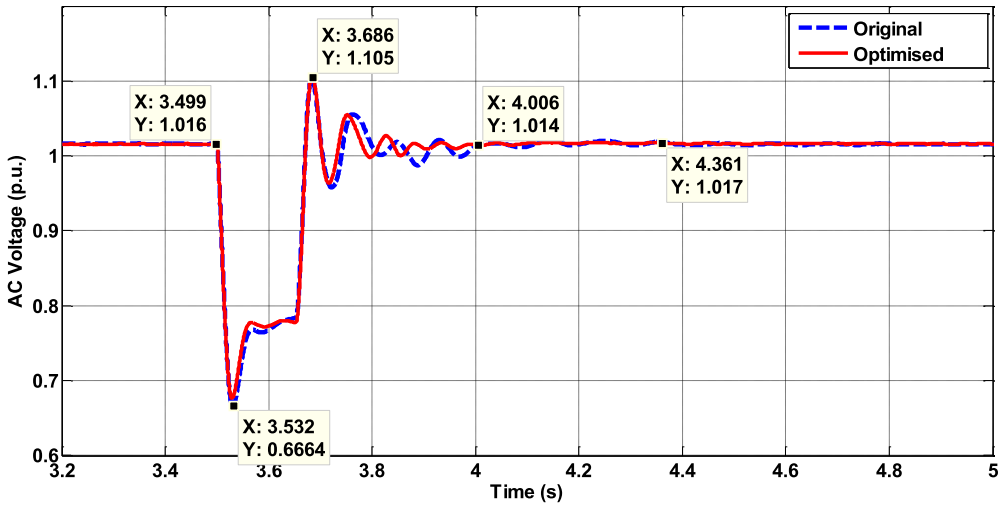

Fig-6.27 The AC Voltage at PCC2 (Operating Point 2)

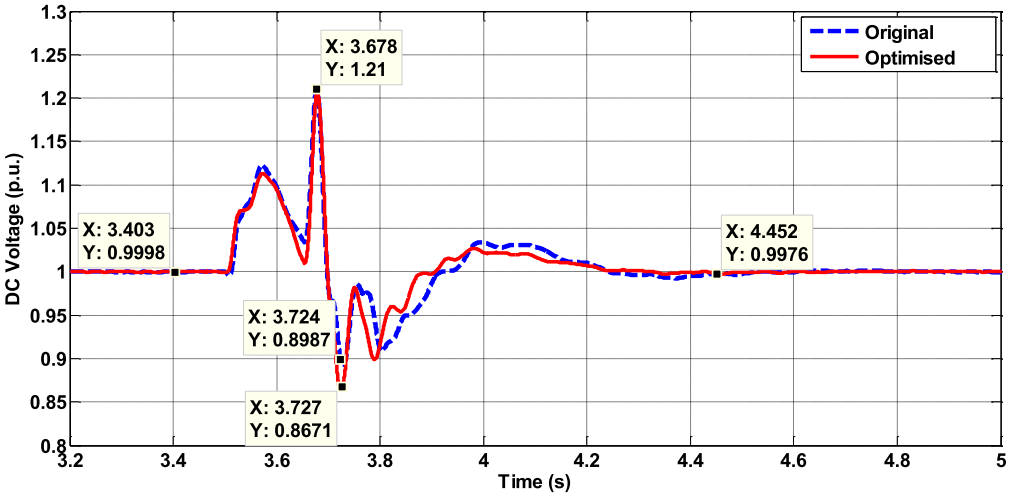

Fig-6.28 The DC Voltage of INV (Operating Point 2)

For the active power at PCC3 in Fig-6.29, the maximum overshoot of the power oscillation with original parameters is 282.1 MW at 3.712 s and that with optimised parameters is 227.6 MW at 3.709 s. The minimum undershoot of the power oscillation with original parameters is -2.077 MW at 3.683 s and that with optimised parameters is 12.25 MW at 3.681 s. And the active power with optimised parameters returned to normal condition at nearly 4.113 s after several but that with original parameters returned to the normal condition at nearly 4.521 s after several swings.

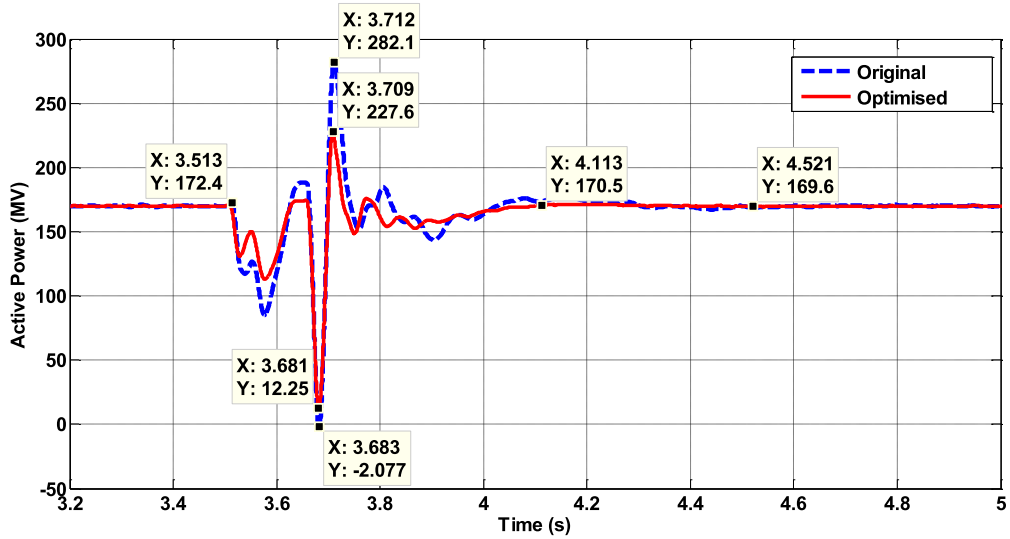

Fig-6.29 The Active Power at PCC3 (Operating Point 2)

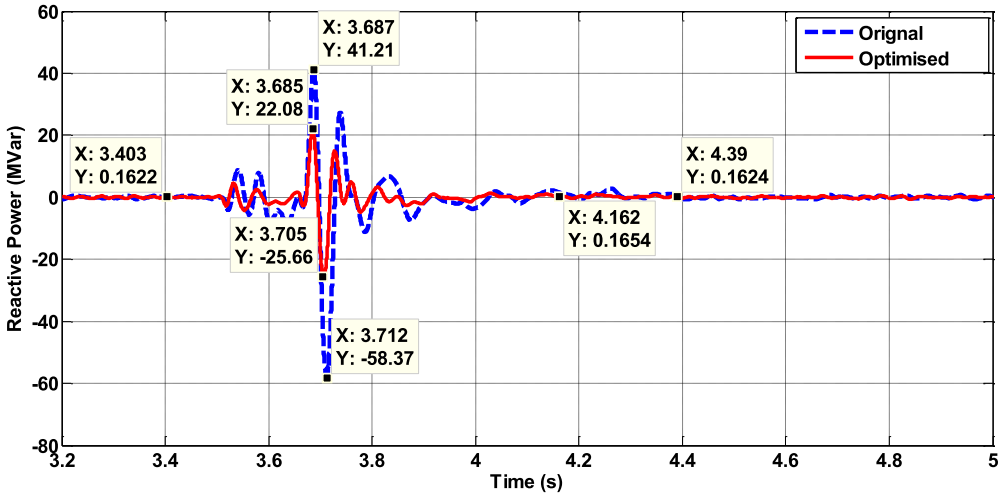

Fig-6.30 The Reactive Power at PCC3 (Operating Point 2)

For the reactive power at PCC3 in Fig-6.30, the maximum overshoot of the power oscillation with original parameters is 41.21 MVar at 3.687 s and that with optimised parameters is 22.08 MVar at 3.685 s. The minimum undershoot of the power oscillation with original parameters is -58.37 MW at 3.712 s and that with optimised parameters is -25.66 MVar at 3.705 s. And the active power with optimised parameters returned to normal condition at nearly 4.162 s after several but that with original parameters returned to the normal condition at nearly 4.39 s after several swings.

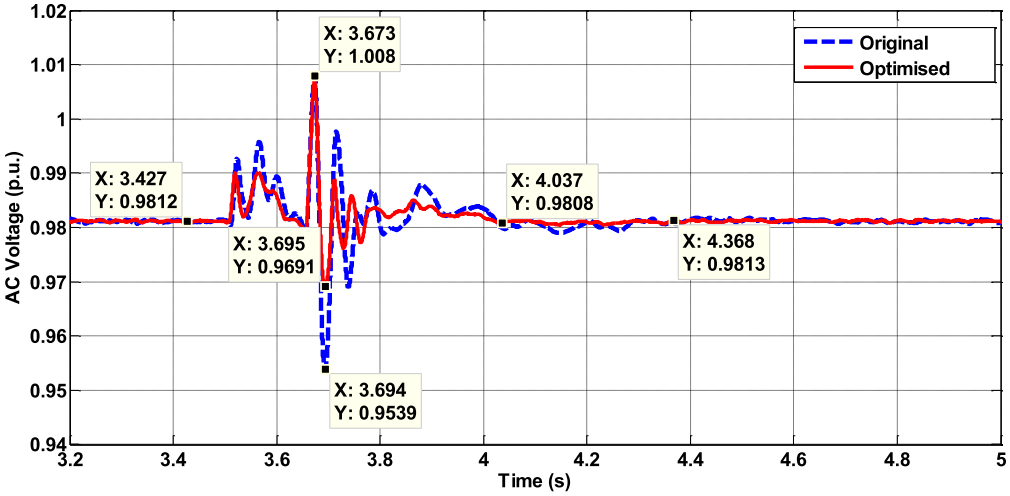

Fig-6.31 The AC Voltage at PCC3 (Operating Point 2)

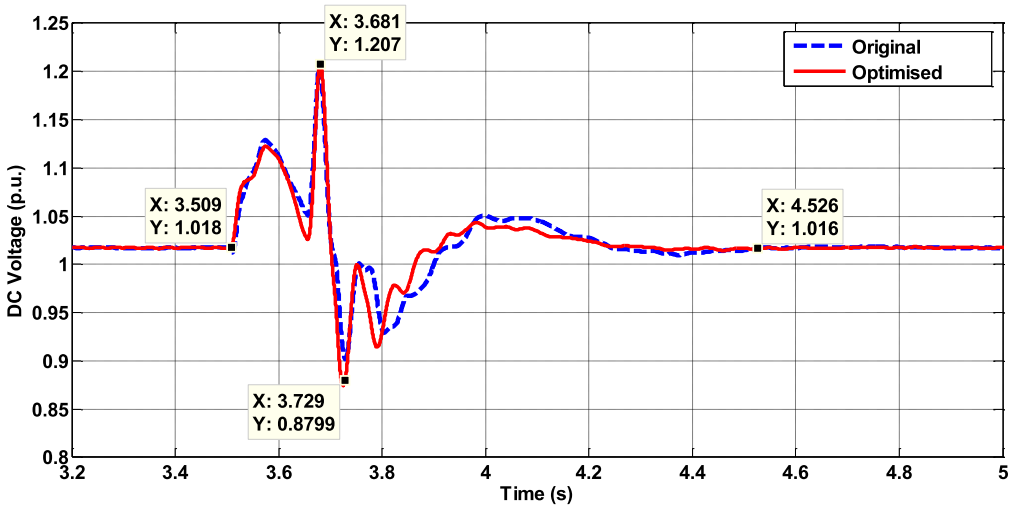

Fig-6.32 The DC Voltage of REC2 (Operating Point 2)

For the AC voltage at PCC3 in Fig-6.31, the maximum overshoots of the voltage oscillations with original and optimised parameters are as same as 1.008 p.u. at 3.673 s. The minimum undershoot of voltage oscillation with original parameters is 0.9539 p.u. at 3.694 s and that with optimised parameters is 0.9691 p.u. at 3.695 s. And the AC voltage with optimised parameters returned to normal condition at nearly 4.037 s after several swings after the removal of fault but that with original parameters returned to the normal condition at nearly 4.368 s after several swings. For the DC voltage of **REC3** in Fig-6.32, the differences of maximum overshoots and minimum undershoots of the voltage oscillation with original and optimised parameters are very small. The DC voltage with original and optimised parameters returned to normal condition at nearly 2.389 s after several swings.

Comparing the simulation results for the system at the **Operating Point 2** shown above, the active and reactive power, the AC voltage at PCC1 for the **REC1** and PCC3 for the **REC2** have been obviously improved in terms of the magnitudes of over/undershoot, the period of oscillations and number of oscillation swings. For the DC voltages of **REC1** and **REC2,** the dynamic responses have been improved in the period of oscillations and number of oscillation swings. But the improvements are not as obvious as those for other three variables.

For the **INV**, the active and reactive power at PCC2 have been obviously improved in terms of the magnitudes of over/undershoot, the period of oscillations and number of oscillation swings. But for AC voltage at PCC3 and the DC voltage of **INV**, the dynamic responses have just improved slightly. Overall, the dynamic performance of the whole HVDC grid has been improved with the set of optimised parameters for the **Operating Point 2.**

6.6.4 Case 3: Transfer from Operating Point 1 to 2

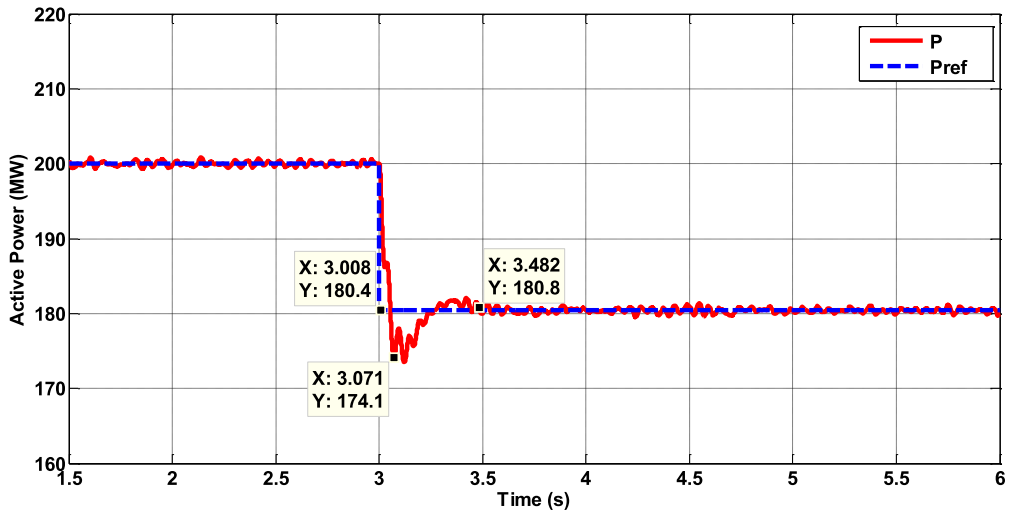

Fig-6.33 The Changes of Active Power at PCC1 from Operating Point 1 to 2

In **Case 3,** the operation condition from **Operating Point 1** to **Operation Point 2** at 3 s for the three-terminal HVDC Grid with optimised parameters. And the simulation results are illustrated from Fig-6.33 to Fig-6.36. In Fig-6.33 and Fig-6.34, the output power references for *d*-axis active power controllers in **REC1** and **REC2** suddenly changed from 200 MW to 180 MW. As a result, the output reactive power in **REC1** and **REC2** tracked the changes of output power references due to the functionality of the PI-based *d*-axis power controllers in **REC1** and **REC2**. In Fig-6.33, an undershoot of 174.1 MW appeared at 3.071 s. The difference between the undershoot and the normal values are 5.9 MW which is a small dynamic impact on the **REC1**. And the system returned to normal condition at 3.482 s. The time duration is nearly 0.411 s for the transient process. In Fig-6.34, an undershoot of 173.5

MW appeared at 3.071 s. The difference between the undershoot and the normal values are 6.5 MW which is a small dynamic impact on the **REC3**. And the system returned to normal condition at 3.482 s. The time duration is nearly 0.411 s for the transient process.

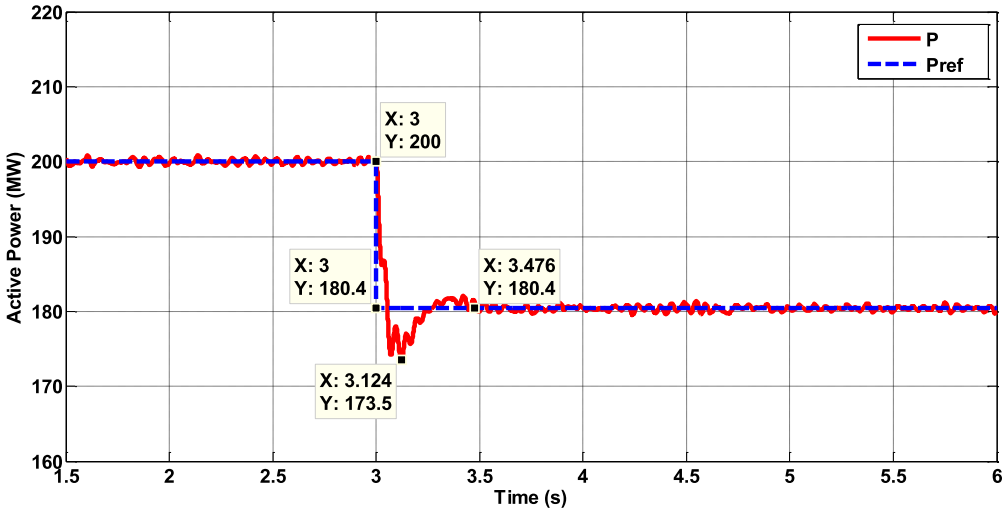

Fig-6.34 The Changes of Active Power at PCC3 from Operating Point 1 to 2

The input active power at PCC2 of **INV** changed in response of output power changes in PCC1 and PCC3 for **REC1** and **REC2** illustrated in Fig-6.35. The undershoot of 315.2 MW appeared at 3.13 s and the system returned to normal operation of 326.4 MW at 3.502 s. The difference between the normal condition and undershoot is 11.2 MW and the time duration is 0.502 s for transient process. Furthermore, the DC voltage of **INV** was controlled by the *d*-axis voltage controller. With the changes of output active power of **REC 1** and **REC 2**, there was the imbalance between the AC and DC power during the transient process shown in Fig-6.36. An undershoot of 0.9704 p.u. appeared at 3.032 s and the difference between the normal condition and undershoot is 0.0296 p.u.. Furthermore, the time duration for the transient process is 0.454 s.

During the transient process from **Operating Point 1** to **Operating Point 2**, the impacts of the undershoots on the active power and DC voltage are acceptable with the ratio below than 5%. Furthermore, the time duration of the transient process for each variable is nearly 0.5 s

which are acceptable for time range of steady-state operation (Minute-level). So the set of optimised parameters are applicable for this three-terminal HVDC grid for transfer of operating points without obvious impacts on the system in terms of transient stability.

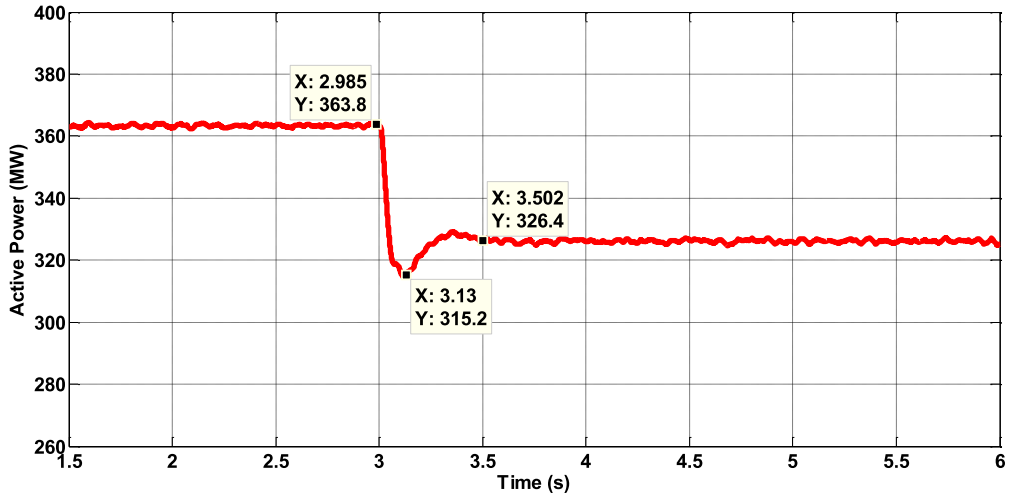

Fig-6.35 The Changes of Active Power at PCC2 from Operating Point 1 to 2

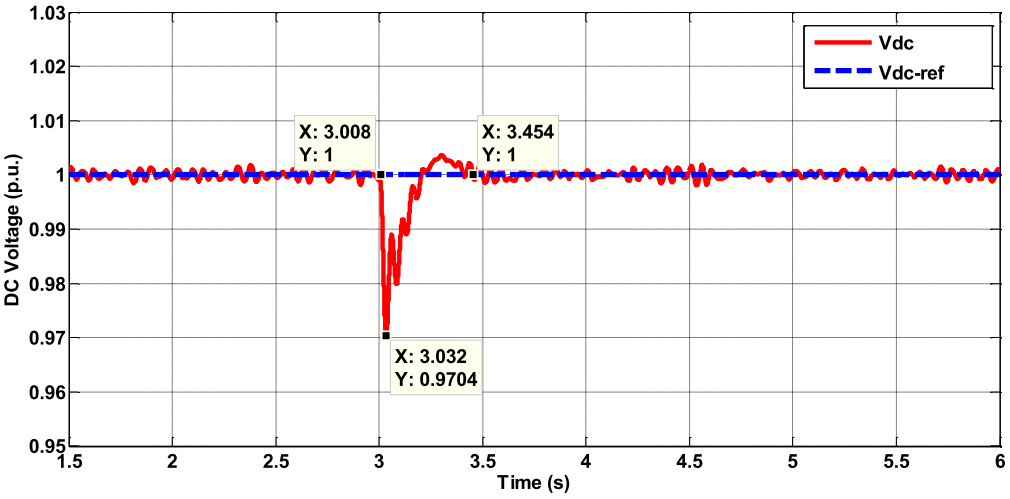

Fig-6.36 The Changes of DC Voltage of INV from Operating Point 1 to 2

6.7 Summary and Conclusions

In this chapter, the small-signal models of the three-terminal VSC-based HVDC grid with radial structure have been firstly derived. Based on the small-signal models, the parameters of the PI controllers have been optimised with the PSO method for this HVDC grid at two operating points. The simulation system for the this three-terminal HVDC grid has been

tested in the MATLAB/SIMULINK with comparison of the dynamic performance of the whole system with the two sets of original and optimised parameters. According to the simulation results, the dynamic performance of the whole system have been improved with the set of optimised parameters of the PI controllers at two specified operating points and the proposed method has been validated for the parameter optimisation of the PI controllers of voltage-sourced converters in order to improve the dynamic performance of the whole MTDC grid at multiple operating points in terms of transient stability.

Chapter 7

Conclusions and Future Research Plans

7.1 Conclusions

In this PhD thesis, the main work is listed as follows:

1) The dynamic aggregated modelling method has been proposed for large-scale offshore wind farms consisting of the WT-DFIGs and WT-PMSGs respectively to simplify the system in detail to some extent by dividing the wind turbines with similar dynamic characteristics into several so-called coherency groups and representing each coherency group using an equivalent machine to achieve the balance between the computational time and requirement of simulation accuracy for the transient stability analysis. With the validation of the proposed method via the simulation systems with different aggregated models in the DIgSILENT/PowerFactory, the effective representations of large-scale offshore wind farms including 32 units of WT-DFIGs and WT-PMSGs have been proposed for the requirements of transient stability analysis in terms of computational time and requirement of simulation accuracy which are hard to achieve simultaneously which is hard to achieve by conventional methods using either detailed models over-simplified single equivalent machine.
2) Two control schemes for the rectifier-side converter of point-to-point VSC-HVDC link have been investigated for grid integration of large-scale offshore wind farms including WT-DFIGs and WT-PMSGs respectively. The comparisons of these two control schemes have been carried out based on the simulation in DIgSILENT/PowerFactory to validate that the emerging control scheme with control of the AC voltage at the rectifier-side PCC is more suitable for grid integration of those large-scale offshore wind farms than the

classical scheme with control of the output power at the rectifier-side PCC in terms of transient stability.

3) The CSC-HVDC system has been investigated for its dynamic characteristics. The emerging bipolar hybrid CSC/VSC-HVDC system has been proposed for the updated scheme of a monopolar CSC-HVDC link using a monopolar CSC-HVDC link operating in parallel. The performance of the support from the VSC-HVDC link has been validated in DIgSILENT/PowerFactory for helping the neighbouring CSC-HVDC link to deal with its two key issues: reactive power compensation and inverter-side commutation failure.

4) The PSO-based parameter optimisation method for PI controllers of voltage-sourced converters in the emerging multi-terminal HVDC (MTDC) grid with multiple system operation points based on the small-signal models of the whole system has been proposed. Compared with conventional PSO-based parameter optimisation methods for single operating point, the set of parameters of PI controllers optimised by the proposed method is validated by simulation in MATLAB/SIMULINK for improving the dynamic performance of the MTDC grid at multiple operating points in terms of transient stability.

7.2 Future Research Plans

7.2.1 Further Validation of Proposed Method in Chapter 6

In the Chapter 6, the proposed PSO-based method has been validated for three-terminal VSC-HVDC grid with radial structure. However, this method should be further validated considering three aspects: Firstly, with the extension of HVDC grids in the future such as the North Sea Supergrid, more and more voltage-sourced converters will be interconnected via DC interlinks with higher complexity of topologies such as meshed or combination of the meshed and radial. As a result, the proposed method should be further validated in the HVDC grids including more VSCs with higher complexity of topologies.

Secondly, the detailed representations of the external systems connected to the VSCs, especially the dynamic models of generators should be further considered. For the offshore HVDC grids such as North Sea Supergrid, are considered the optimal solution for grid integration of offshore wind farms described in Chapter 1 and Chapter 6. These wind turbines such as WT-DFIGs and WT-PMSGs have their own dynamic characteristics mentioned in Chapter 3 and Chapter 4. So the proposed method in Chapter 6 should be further validated for the small-signal models of the whole power systems including the wind turbines to consider the interactions between the offshore wind turbines and HVDC grids such as power exchanges at the PCCs.

Thirdly, the set of parameters of the PI controller of converters in the MTDC grids optimised by proposed method has been validated for two operation points which are not far from each other in one region. However, the changes of operating points of the practical power systems can be very large (such as power reversal). As a result, two operating points can be located far from each other in different regions. This method is based on the classic linear PI controller and the set of optimised parameters by the proposed method for operating points in the same region could not applicable in some potential condition that the two operating points are very far from each other in different regions. As a result, the proposed method should be further validated with the extension of the desired operational performance over a region to cover several regions by applying soft switching of the regional PI controllers with different sets of optimised parameters in response to operating points in different regions and the fuzzy logic control with the aim of monitoring the changes of operating points can be applied for the improvement of the proposed method to realise the soft switching of the regional PI controllers [158].

7.2.2 Design and Control of Modular-Multilevel Converters in VSC-HVDC Systems

Currently, the VSCs with two- and three-level topologies have dominated the markets. However, due to their high switching frequencies, the switching losses and harmonic distortions are obvious for such converters [6]. For the state-of-the-art next generation VSC-HVDC technology based on the modular multilevel converters (MMCs) [6], In each bridge arm, a large number of basic IGBT modules coordinate with each other in small voltage steps to achieve the desired waveform. With this principle, the switching frequencies can be reduced greatly and bring big benefits as follows [6, 159]:

1) Low switching losses;
2) Low generation of high frequency (HF) harmonics;
3) Compact layouts with scalable design.

With these benefits, the power losses of the converters, the costs of the high frequency filters (HFFs) and installation spaces can be reduced greatly. Furthermore, the current two-or three-level VSCs in the VSC-HVDC systems are vulnerable to DC-side faults [160] and it has become a bottleneck on the further development of MTDC grids. However, for the MMC technology, it has the capabilities of suppressing the DC-side faults [161-163]. In this way, this technology has gradually shown its advantage over the conventional two- or three-level VSC-HVDC technology for grid integration of offshore wind farms and solution to building the backbone of MTDC grids [20, 21, 23, 164, 165]. As a result, great attention has been paid to the research and development of MMC technology for the further HVDC transmission systems [166-172] and the first MMC-based VSC-HVDC transmission project has been put into commercial operation in 2010 [6]. So the further research plans for the design and their control of the MMC-based VSC-HVC systems are listed as follows:

1) Investigating the current studies of the MMC technology and understanding the capabilities and limitations of the current MMC-based VSC-HVDC systems;
2) Building and testing the detailed MMCs in the VSC-HVDC systems using the state-of-the-art real time digital simulator (RTDS) [173]. And design of the coordinated control strategies for the basic modules to achieve the required waveforms.
3) Comparing the simulation results of detailed, average [169], and equivalent models of MMCs [174] in the VSC-HVDC systems to evaluate their capabilities and limitations for different research purposes using RTDS;
4) Building the MMC-based MTDC grids and testing their performance for power flow and dynamic stability analysis using RTDS.

7.2.3 Fault Management of MTDC Grids using AC and DC Circuit Breakers

Although the proposed concepts of MTDC grids such as the so-called North Sea Supergrid Scheme (NSSS) will bring big opportunities for the EU's pan-European electricity markets, making it from concepts to reality is still a long road considering the technique challenges and obstacles to be solved as follows [20, 21]:

1) Grid code of MTDC grids;
2) DC power flow analysis;
3) Control and protection against DC-side faults;
4) Interfaces for offshore DC loads;
5) Offshore platforms for installation of converter stations.

The control and protection mechanisms against DC-side faults in the MTDC grids are of great important for the operation reliability and security of the whole system. Due to the technical limitations and high costs [160, 175, 176], the high voltage DC circuit breakers have not currently put into commercial operation. And the protection schemes against the DC

faults using the mature AC circuit breakers have been investigated in [160, 177-181]. For such protection schemes, all the AC circuit breakers are triggered to open and converters are blocked when a DC fault is detected. Although the schemes have been well proven for small-scale MTDC grids, for large-scale systems, all the converters should quit operation due to just a DC fault within some transmission line and it will reduce the reliability and security of the whole system significantly. So the technical limitations of DC circuit breakers become bottleneck on the further development of MTDC grids. In this way, the research on the DC circuit breakers and the fault-management systems based on them are of great importance to move towards the practical commercial operation of MTDC grids. So the further research plans are listed as follows:

1) Investigating the basics and principles of HVDC circuit breakers;
2) Building the DC circuit breakers and testing their performance for evaluating their capabilities and limitations in simple DC testing systems using RTDS;
3) Optimising their performance with improved or new design schemes and testing them using RTDS for verification and validation;
4) Applying the design schemes of DC circuit breakers in the MMC-based MTDC grids for testing the protection mechanisms against different types of DC-side faults;
5) Developing the fault management systems for protection against different types of AC- and DC-side faults with coordination among the AC, DC circuit breakers and converters in the MMC-based MTDC grids.

7.2.4 Design of Models and Control Strategies for High-gain MW-level DC/DC Converter

The VSC-HVDC technology provides the optimal solutions to integration of large offshore DC loads just like the offshore oil/gas rig platforms. Currently, the power is delivered to such offshore platforms via the point-to-point HVDC Systems from the onshore converter stations

such as the ValHall Project which can delivery 78 MW power for the offshore rig platforms via the 292 km subsea cable [182] and Troll-A Project which can delivery total 188 MW power for offshore rig platforms via the 70 km subsea cables [183]. For powering such offshore loads, the investments in the onshore converter stations should be considered. Furthermore, the costs and reliability of the long-distance point-to-point subsea cables limit the possibilities to explore the oil/gas resources far from the onshore converter stations. The MTDC grids can provide the optimal solution to providing the interfaces for the offshore oil/gas rig platforms directly without the extra investment in onshore converter stations. The offshore platforms will connect to the nearest offshore power resources such as the offshore wind farms. As a result, the investments in the subsea cables can be greatly reduced as well and it can maximise the exploration of oil/gas resources. However, due to different technical specifications, the offshore DC loads will operate at different DC voltage levels such as 150 kV for Valhall Project [182] and ±60 kV for Troll A Project [183]. In this way, the DC/DC interfaces hould be investigated for providing the compatible DC voltage-levels for the different offshore DC loads directly to meet their technical specifications.

In the AC power systems, the AC voltages can be easily tuned for different voltage-levels just with designed turns ratios between the windings on primary- and secondary-side of AC transformers. However, it is not easy to achieve directly in DC power systems, especially for megawatt-level high-gain DC/DC converters. The development of such DC/DC converters are still at the initial stage for academic studies [184-188] and there is still a long road to realise the commercial application of those DC/DC converters with great potentials. In this way, the further research plans for the high-gain MW-level DC/DC converters in MTDC grids are listed as follows:

1) Investigation of the basics and principles of IGBT-based DC/DC converters and understanding the key issues of such technology for further development;
2) Design of the IGBT-based DC/DC converters and building the simulation system using RTDS for testing their performance and evaluating their capabilities and limitations for different types of DC loads;
3) Design of the MMC-based DC/DC converters and the control strategies for the basic modules to coordinate with each other to achieve the high-gain turns ratio of DC voltages and testing the performance of such DC/DC converters using RTDS for different technical specifications of offshore DC loads;
4) Integrating the offshore DC loads via such DC/DC converters into the MTDC offshore grids to verify and validate the feasibilities and performance of those high-gain MW-level DC/DC converters for power flow and dynamic stability analysis.
5) Improvement of the fault-management systems to set up proper protection and control mechanisms against different types of faults within the demanding-side of MTDC grids including the DC/DC converters and DC loads to enhance the operation reliability and security of the offshore DC loads in the MTDC grids.

Appendix A

Modelling of WT-DFIG in Detail for Chapter 3

The three-phase voltages equations on the rotor-side of induction generator are given by:

$$\begin{cases} V_{ra} = R_r \times I_{ra} + \dfrac{d\psi_{ra}}{dt} \\ V_{rb} = R_r \times I_{rb} + \dfrac{d\psi_{rb}}{dt} \\ V_{rc} = R_r \times I_{rc} + \dfrac{d\psi_{rc}}{dt} \end{cases} \tag{A.1}$$

where V_{ra}, V_{rb} and V_{rc} are the rotor-side three-phase voltages; I_{ra}, I_{rb} and I_{rc} are the rotor-side three-phase currents; ψ_{ra}, ψ_{rb} and ψ_{rc} are the rotor-side three-phase flux linkage; R_r is the rotor-side resistance. Transformation of (A.1) from *a-b-c* to rotating *d-q* coordinates with the Park transformation matrix expressed in (A.2).:

$$P_r = \frac{2}{3}\begin{bmatrix} \cos(s\omega_s t) & \cos(s\omega_s t - \frac{2}{3}\pi) & \cos(s\omega_s t + \frac{2}{3}\pi) \\ -\sin(s\omega_s t) & -\sin(s\omega_s t - \frac{2}{3}\pi) & -\sin(s\omega_s t + \frac{2}{3}\pi) \end{bmatrix} \tag{A.2}$$

where P_r is the rotor-side Park transformation matrix; s is rotor slip of induction generator given by:

$$s = \frac{(\omega_s - \omega_r)}{\omega_s} \tag{A.3}$$

where ω_s is the synchronous rotational speed and ω_r is the rotor rotational speed.

$$P_r \times \begin{bmatrix} V_{ra} \\ V_{rb} \\ V_{rc} \end{bmatrix} = R_r \times P_r \times \begin{bmatrix} I_{ra} \\ I_{rb} \\ I_{rc} \end{bmatrix} + P_r \times \frac{d}{dt}\left(P_r^{-1} \times P_r \begin{bmatrix} \psi_{ra} \\ \psi_{rb} \\ \psi_{rc} \end{bmatrix} \right) \tag{A.4}$$

$$\begin{bmatrix} V_{rd} \\ V_{rq} \end{bmatrix} = R_r \times \begin{bmatrix} I_{rd} \\ I_{rq} \end{bmatrix} + P_r \times P_r^{-1} \times \begin{bmatrix} \dfrac{d\psi_{rd}}{dt} \\ \dfrac{d\psi_{rq}}{dt} \end{bmatrix} + P_r \times \frac{dP_r^{-1}}{dt} \times \begin{bmatrix} \psi_{rd} \\ \psi_{rq} \end{bmatrix} \tag{A.5}$$

$$P_r \times \frac{dP_r^{-1}}{dt} = \begin{bmatrix} 0 & -s\omega_s \\ s\omega_s & 0 \end{bmatrix} \tag{A.6}$$

$$\begin{cases} V_{rd} = R_r \times I_{rd} + \dfrac{d\psi_{rd}}{dt} - s\omega_s \times \psi_{rq} \\ V_{rq} = R_r \times I_{rq} + \dfrac{d\psi_{rq}}{dt} + s\omega_s \times \psi_{rd} \end{cases} \tag{A.7}$$

where V_{rd} and V_{rq} are the rotor-side d- and q-axis voltages; I_{rd} and I_{rq} are the rotor-side d- and q-axis currents; ψ_{rd} and ψ_{rq} are the rotor-side d- and q-axis flux linkage which are expressed in (A.8):

$$\begin{cases} \psi_{rd} = L_r \times I_{rd} + L_m \times I_{sd} \\ \psi_{rq} = L_r \times I_{rq} + L_m \times I_{sq} \end{cases} \tag{A.8}$$

where I_{sd} and I_{sq} are the stator-side d- and q-axis currents; L_r is the rotor self-inductance; L_m is the mutual inductance. And I_{rd} and I_{rq} can be substituted from (A.8) into(A.9):

$$\begin{cases} V_{rd} = R_r \times \dfrac{\left(\psi_{rd} - L_m \times I_{sd}\right)}{L_r} + \dfrac{d\psi_{rd}}{dt} - s\omega_s \times \psi_{rq} \\ V_{rq} = R_r \times \dfrac{\left(\psi_{rq} - L_m \times I_{sq}\right)}{L_r} + \dfrac{d\psi_{rq}}{dt} + s\omega_s \times \psi_{rd} \end{cases} \tag{A.9}$$

Both sides of (A.9) are multiplied by $\frac{\omega_s L_m}{L_r}$ and some variables are defined in (A.10) to (A.12):

$$\begin{cases} E'_d = -\dfrac{\omega_s L_m}{L_r}\psi_{rq} \\ E'_q = \dfrac{\omega_s L_m}{L_r}\psi_{rd} \end{cases} \tag{A.10}$$

$$\begin{cases} X_s = \omega_s L_s \\ X'_s = \omega_s (L_s - \dfrac{L_m{}^2}{L_r}) \end{cases} \tag{A.11}$$

$$T'_0 = \frac{L_r}{R_r} \tag{A.12}$$

where E'_d and E'_q are the *d*- and *q*- axis voltages behind the transient reactance; X_s is the stator reactance; X'_s is the stator transient reactance; T'_0 is the rotor circuit time constant. So the (A.9) can be expressed in (A.13) as the second-order dynamic models on the rotor-side:

$$\begin{cases} \dfrac{dE'_d}{dt} = s\omega_s E'_q - \dfrac{\omega_s L_m}{L_r} V_{rq} - \dfrac{1}{T'_0}[E'_d + (X_s - X'_s) I_{sq}] \\ \dfrac{dE'_q}{dt} = -s\omega_s E'_d + \dfrac{\omega_s L_m}{L_r} V_{rd} - \dfrac{1}{T'_0}[E'_q - (X_s - X'_s) I_{sd}] \end{cases} \tag{A.13}$$

The three-phase voltages equations on the stator-side of generator are given by:

$$\begin{cases} V_{sa} = R_s \times I_{sa} + \dfrac{d\psi_{sa}}{dt} \\ V_{sb} = R_s \times I_{sb} + \dfrac{d\psi_{sb}}{dt} \\ V_{sc} = R_s \times I_{sc} + \dfrac{d\psi_{sc}}{dt} \end{cases} \tag{A.14}$$

where V_{sa}, V_{sb} and V_{sc} are the stator-side three-phase voltages; I_{sa}, I_{sb} and I_{sc} are the stator-side three-phase currents; ψ_{sa}, ψ_{sb} and ψ_{sc} are the stator-side three-phase flux linkage; R_s is the stator-side resistance. Transformation of (A.14) from *a-b-c* to rotating *d-q* coordinates with the Park Transformation Matrix expressed with (A.15):

$$P_s = \frac{2}{3}\begin{bmatrix} \cos\omega_s t & \cos(\omega_s t - \frac{2}{3}\pi) & \cos(\omega_s t + \frac{2}{3}\pi) \\ -\sin\omega_s t & -\sin(\omega_s t - \frac{2}{3}\pi) & -\sin(\omega_s t + \frac{2}{3}\pi) \end{bmatrix} \tag{A.15}$$

$$\begin{bmatrix} V_{sd} \\ V_{sq} \end{bmatrix} = R_s \times \begin{bmatrix} I_{sd} \\ I_{sq} \end{bmatrix} + P_s \times P_s^{-1} \times \begin{bmatrix} \dfrac{d\psi_{sd}}{dt} \\ \dfrac{d\psi_{sq}}{dt} \end{bmatrix} + P_s \times \frac{dP_s^{-1}}{dt} \times \begin{bmatrix} \psi_{sd} \\ \psi_{sq} \end{bmatrix} \tag{A.16}$$

$$P_s \times \frac{dP_s^{-1}}{dt} = \begin{bmatrix} 0 & -\omega_s \\ \omega_s & 0 \end{bmatrix} \tag{A.17}$$

After the transformation processes expressed from (A.16) to (A.17), the stator-side voltages in the rotating d-q coordinates is expressed in (A.18):

$$\begin{cases} V_{sd} = R_s \times I_{sd} + \dfrac{d\psi_{sd}}{dt} - \omega_s \times \psi_{sq} \\ V_{sq} = R_s \times I_{sq} + \dfrac{d\psi_{sq}}{dt} + \omega_s \times \psi_{sd} \end{cases} \tag{A.18}$$

where V_{sd} and V_{sq} are the stator-side d- and q-axis voltages; ψ_{sd} and ψ_{sq} are the stator-side d- and q-axis flux linkage expressed in (A.19):

$$\begin{cases} \psi_{sd} = L_s \times I_{sd} + L_m \times I_{rd} \\ \psi_{sq} = L_s \times I_{sq} + L_m \times I_{rq} \end{cases} \tag{A.19}$$

The differential equations for ψ_{sd} and ψ_{sq} are given by:

$$\begin{cases} \dfrac{d\psi_{sd}}{dt} = V_{sd} + \omega_s \times \psi_{sq} - R_s \times I_{sd} \\ \dfrac{d\psi_{sq}}{dt} = V_{sq} - \omega_s \times \psi_{sd} - R_s \times I_{sq} \end{cases} \tag{A.20}$$

And I_{rd} and I_{rq} is substituted from (A.8) into (A.19). And ψ_{sd} and ψ_{sq} are express by:

$$\begin{cases} \psi_{sd} = L_{ss} I_{sd} + L_m \dfrac{\psi_{rd} - L_m I_{sd}}{L_{rr}} \\ \psi_{sq} = L_{ss} I_{sq} + L_m \dfrac{\psi_{rq} - L_m I_{sq}}{L_{rr}} \end{cases} \tag{A.21}$$

(A.21) is substituted into (A.20) and the differential equations of I_{sd} and I_{sq} can be expressed in (A.22):

$$\begin{cases} \dfrac{X'_s}{\omega_s} \dfrac{dI_{sd}}{dt} = V_{sd} - R_s \times I_{sd} - E'_d - \dfrac{1}{\omega_s} \dfrac{dE'_q}{dt} + X'_s I_{sq} \\ \dfrac{X'_s}{\omega_s} \dfrac{dI_{qs}}{dt} = V_{sq} - R_s \times I_{sq} - E'_q + \dfrac{1}{\omega_s} \dfrac{dE'_d}{dt} - X'_s I_{sd} \end{cases} \tag{A.22}$$

And (A.13) is substituted into (A.22), so the 2nd-order dynamic models for the stator-side of generator are expressed:

$$\begin{cases} \dfrac{X'_s}{\omega_s} \dfrac{dI_{sd}}{dt} = V_{sd} - [R_s + \dfrac{1}{\omega_s T'_0}(X_s - X'_s)] I_{sd} - (1-s) E'_d - V'_{rd} + \dfrac{1}{\omega_s T'_0} E'_q + X'_s I_{sq} \\ \dfrac{X'_s}{\omega_s} \dfrac{dI_{sq}}{dt} = V_{sq} - [R_s + \dfrac{1}{\omega_s T'_0}(X_s - X'_s)] I_{sq} - (1-s) E'_q - V'_{rq} - \dfrac{1}{\omega_s T'_0} E'_d - X'_s I_{sd} \end{cases} \tag{A.23}$$

So the detailed dynamic models of the induction generator in the WT-DFIG system can be represented by the 4th-order differential equations of E'_d, E'_q, I_{sd} and I_{sq},. In some situations, the detailed models can be simplified with neglecting the transients on the stator-side for reducing the computational efforts in the transient stability simulation. So the detailed 4th-order dynamic models can be reduced to the simplified 2nd-order models and the comparisons of the simulation results between the detailed and simplified models and their applications for different analysis purposes are discussed in [38].

For the grid-side converter in Fig-3.6, the three-phase voltage equations are expressed by (A2.24):

$$\begin{cases} V_{ga} = V_{sa} + R_g I_{ga} + L_g \dfrac{dI_{ga}}{dt} \\ V_{gb} = V_{sb} + R_g I_{gb} + L_g \dfrac{dI_{gb}}{dt} \\ V_{gc} = V_{sc} + R_g I_{gc} + L_g \dfrac{dI_{gc}}{dt} \end{cases} \tag{A.24}$$

where V_{ga}, V_{gb} and V_{gc} are the three-phase voltages of grid-side converter; I_{sa}, I_{sb} and I_{sc} are the three-phase currents of grid-side converter; R_g is the grid-side converter resistance ; L_g is the grid-side converter reactance. Transformation of (A.24) from *a-b-c* to rotating *d-q* coordinates with the Park Transformation Matrix expressed with (A.25):

$$P_g = \frac{2}{3}\begin{bmatrix} \cos\omega_g t & \cos(\omega_g t - \frac{2}{3}\pi) & \cos(\omega_g t + \frac{2}{3}\pi) \\ -\sin\omega_g t & -\sin(\omega_g t - \frac{2}{3}\pi) & -\sin(\omega_g t + \frac{2}{3}\pi) \end{bmatrix} \tag{A.25}$$

where $\omega_g = 2\pi f_g$ (f_g is the system frequency on grid-side converter).

$$P_g \times \begin{bmatrix} V_{ga} \\ V_{gb} \\ V_{gc} \end{bmatrix} = P_g \times \begin{bmatrix} V_{sa} \\ V_{sb} \\ V_{sc} \end{bmatrix} + R_g \times P_g \times \begin{bmatrix} I_{ga} \\ I_{gb} \\ I_{gc} \end{bmatrix} + L_g \times P_g \times \frac{d}{dt}\left(P_g^{-1} \times P_g \begin{bmatrix} I_{ga} \\ I_{gb} \\ I_{gc} \end{bmatrix} \right) \tag{A.26}$$

$$\begin{bmatrix} V_{gd} \\ V_{gq} \end{bmatrix} = \begin{bmatrix} V_{sd} \\ V_{sq} \end{bmatrix} + R_g \times \begin{bmatrix} I_{gd} \\ I_{gq} \end{bmatrix} + L_g \times P_g \times P_g^{-1} \times \begin{bmatrix} \frac{dI_{gd}}{dt} \\ \frac{dI_{gq}}{dt} \end{bmatrix} + P_g \times \frac{dP_g^{-1}}{dt} \times \begin{bmatrix} I_{gd} \\ I_{gq} \end{bmatrix} \tag{A.27}$$

$$P_g \times \frac{dP_g^{-1}}{dt} = \begin{bmatrix} 0 & -\omega_g \\ \omega_g & 0 \end{bmatrix} \tag{A.28}$$

After the transformation processes expressed from (A.26) to (A.28), the grid-side voltages in the rotating *d*-*q* coordinates are expressed in (A.29):

$$\begin{cases} V_{gd} = V_{sd} + R_g \times I_{gd} + L_g \times \frac{dI_{gd}}{dt} - \omega_g \times I_{gq} \\ V_{gq} = V_{sq} + R_g \times I_{gq} + L_g \times \frac{dI_{gq}}{dt} + \omega_g \times I_{gd} \end{cases} \tag{A.29}$$

where V_{gd} and V_{gq} are the *d*- and *q*-axis voltage on converter-side of grid-side converter; V_{sd} and V_{sq} are the *d*- and *q*-axis voltage on system-side of grid-side converter; I_{gd} and I_{gq} are the *d* and *q*-axis current of grid-side converter.

Appendix B

Modelling of PMSG in Detail for Chapter 3

The three-phase voltages equations on the stator-side of synchronous generator are given by:

$$\begin{cases} V_{sa} = R_s \times I_{sa} + \dfrac{d\psi_{sa}}{dt} \\ V_{sb} = R_s \times I_{sb} + \dfrac{d\psi_{sb}}{dt} \\ V_{sc} = R_s \times I_{sc} + \dfrac{d\psi_{sc}}{dt} \end{cases} \tag{B.1}$$

where V_{sa}, V_{sb} and V_{sc} are the stator-side three-phase voltages; I_{sa}, I_{sb} and I_{sc} are the stator-side three-phase currents; ψ_{sa} , ψ_{sb} and ψ_{sc} are the stator-side three-phase flux linkage; R_s is the stator-side resistance. Transformation of (B.1) from *a-b-c* to rotating *d-q* coordinates with the Park transformation matrix expressed in (B.2).

$$P = \frac{2}{3}\begin{bmatrix} \cos\omega_p t & \cos(\omega_p t - \frac{2}{3}\pi) & \cos(\omega_p t + \frac{2}{3}\pi) \\ -\sin\omega_p t & -\sin(\omega_p t - \frac{2}{3}\pi) & -\sin(\omega_p t + \frac{2}{3}\pi) \end{bmatrix} \tag{B.2}$$

$$\omega_p = \frac{\omega_s}{P} \tag{B.3}$$

where ω_s is the synchronous rotational speed and the P is the number of poles in the synchronous generator.

$$P \times \begin{bmatrix} V_{sa} \\ V_{sb} \\ V_{sc} \end{bmatrix} = R_s \times P \times \begin{bmatrix} I_{sa} \\ I_{sb} \\ I_{sc} \end{bmatrix} + P \times \frac{d}{dt}\left(P^{-1} \times P \times \begin{bmatrix} \psi_{sa} \\ \psi_{sb} \\ \psi_{sc} \end{bmatrix} \right) \tag{B.4}$$

$$\begin{bmatrix} V_{sd} \\ V_{sq} \end{bmatrix} = R_s \times \begin{bmatrix} I_{sd} \\ I_{sq} \end{bmatrix} + P \times P^{-1} \times \begin{bmatrix} \dfrac{d\psi_{sd}}{dt} \\ \dfrac{d\psi_{sq}}{dt} \end{bmatrix} + P \times \frac{dP^{-1}}{dt} \times \begin{bmatrix} \psi_{sd} \\ \psi_{sq} \end{bmatrix} \tag{B.5}$$

$$P \times \frac{dP^{-1}}{dt} = \begin{bmatrix} 0 & -\omega_p \\ \omega_p & 0 \end{bmatrix} \tag{B.6}$$

the stator voltages in the *d*-*q* coordinates are given by:

$$\begin{cases} V_{sd} = R_s \times I_{sd} + \dfrac{d\psi_{sd}}{dt} - \omega_p \times \psi_{sq} \\ V_{sq} = R_s \times I_{sq} + \dfrac{d\psi_{sq}}{dt} + \omega_p \times \psi_{sd} \end{cases} \tag{B.7}$$

where V_{sd} and V_{sq} are the stator-side *d*- and *q*-axis voltages; I_{sd} and I_{sq} are the stator-side *d*- and *q*-axis currents; ψ_{sd} and ψ_{sq} are the stator-side *d*- and *q*-axis flux linkage which are expressed in [47]:

$$\begin{cases} \psi_{sd} = L_s \times I_{sd} + \psi \\ \psi_{sq} = L_s \times I_{sq} \end{cases} \tag{B.8}$$

where L_s is the stator self-inductance, ψ is the constant flux linkage of PMSG. Substituting (B.8) to (B.7), the 2nd-order dynamic models of the multi-pole permanent magnetic synchronous generator are given by [47, 57]:

$$\begin{cases} V_{sd} = R_s \times I_{sd} + L_s \dfrac{dI_{sd}}{dt} - \omega_p L_s \times I_{sq} \\ V_{sq} = R_s \times I_{sq} + L_s \dfrac{dI_{sq}}{dt} + \omega_p L_s \times I_s + \omega_p \psi \end{cases} \tag{B.9}$$

where V_{sd} and V_{sq} are the *d*- and *q*-axis stator voltages of synchronous generator; I_{sd} and I_{sq} are the *d* and *q*-axis stator currents of synchronous generator; ω_p is the rotational speed of the turbine.

Appendix C

Modelling of P2P VSC System in Detail for Chapter 4

For the AC circuit on the rectifier-side shown in Fig-4.2, the relationship of three-phase voltages on the system- and converter-side can be expressed by (C.1):

$$\begin{cases} V_{rsa} = V_{rca} + R_r I_{ra} + L_r \dfrac{dI_{ra}}{dt} \\ V_{rsb} = V_{rcb} + R_r I_{rb} + L_r \dfrac{dI_{rb}}{dt} \\ V_{rsc} = V_{rcc} + R_r I_{rc} + L_r \dfrac{dI_{rc}}{dt} \end{cases} \tag{C.1}$$

where V_{rsa}, V_{rsb} and V_{rsc} are the three-phase AC voltages at the PCC for external power system; V_{rca}, V_{rcb} and V_{rcc} are the three-phase AC voltages on the AC-side of rectifier; I_{ra}, I_{rb} and I_{rc} are the three-phase AC currents on the rectifier-side; L_r and R_r are the total inductance and resistance of the AC transformer and series AC reactor on the rectifier-side.

The (C.1) is converted from *a-b-c* to *d-q* coordinate system with the Park transformation matrix expressed in (C.2):

$$P_{rs} = \frac{2}{3}\begin{bmatrix} \cos(\omega_{rs}t) & \cos(\omega_{rs}t - \frac{2}{3}\pi) & \cos(\omega_{rs}t + \frac{2}{3}\pi) \\ -\sin(\omega_{rs}t) & -\sin(\omega_{rs}t - \frac{2}{3}\pi) & -\sin(\omega_{rs}t + \frac{2}{3}\pi) \end{bmatrix} \tag{C.2}$$

where P_r is the rectifier-side Park transformation matrix; ω_{rs} the synchronous rotational speed of the AC system on the rectifier-side and $\omega_{rs} = 2\pi f_{rs}$ (f_{rs} is the system frequency on rectifier-side).

$$P_{rs} \times \begin{bmatrix} V_{rsa} \\ V_{rsb} \\ V_{rsc} \end{bmatrix} = P_{rs} \times \begin{bmatrix} V_{rca} \\ V_{rcb} \\ V_{rcc} \end{bmatrix} + R_r \times P_{rs} \times \begin{bmatrix} I_{ra} \\ I_{rb} \\ I_{rc} \end{bmatrix} + L_r \times P_{rs} \times \frac{d}{dt}\left(P_{rs}^{-1} \times P_{rs} \begin{bmatrix} I_{ra} \\ I_{rb} \\ I_{rc} \end{bmatrix} \right) \tag{C.3}$$

$$\begin{bmatrix} V_{rsd} \\ V_{rsq} \end{bmatrix} = \begin{bmatrix} V_{rcd} \\ V_{rcq} \end{bmatrix} + R_r \times \begin{bmatrix} I_{rd} \\ I_{rq} \end{bmatrix} + L_r \times P_{rs} \times P_{rs}^{-1} \times \begin{bmatrix} \frac{dI_{rd}}{dt} \\ \frac{dI_{rq}}{dt} \end{bmatrix} + P_{rs} \times \frac{dP_{rs}^{-1}}{dt} \times \begin{bmatrix} I_{rd} \\ I_{rq} \end{bmatrix} \tag{C.4}$$

$$P_{rs} \times \frac{dP_{rs}^{-1}}{dt} = \begin{bmatrix} 0 & -\omega_{rs} \\ \omega_{rs} & 0 \end{bmatrix} \tag{C.5}$$

After the transformation processes expressed from (C.3) to (C.5), the rectifier-side voltages in the rotating *d*-*q* coordinates are expressed in (C.6):

$$\begin{cases} V_{rsd} = V_{rcd} + R_r \times I_{rd} + L_r \times \dfrac{dI_{rd}}{dt} - \omega_{rs} \times I_{rq} \\ V_{rsq} = V_{rcq} + R_r \times I_{rq} + L_r \times \dfrac{dI_{rq}}{dt} + \omega_{rs} \times I_{rd} \end{cases} \tag{C.6}$$

where V_{rsd} and V_{rsq} are the *d*- and *q*-axis voltage on system-side of rectifier-side converter; V_{rcd} and V_{rcq} are the *d*- and *q*-axis voltage on converter-side of rectifier-side converter; I_{rd} and I_{rq} are the *d* and *q*-axis current of rectifier-side converter.

For the AC circuit on the inverter-side shown in Fig-4.3, the relationship of three-phase voltages on the system-side and inverter-side are defined as same as those on the rectifier-side by (C.7):

$$\begin{cases} V_{isa} = V_{ica} + R_i I_{ia} + L_i \dfrac{dI_{ia}}{dt} \\ V_{isb} = V_{icb} + R_i I_{ib} + L_i \dfrac{dI_{ib}}{dt} \\ V_{isc} = V_{icc} + R_i I_{ic} + L_i \dfrac{dI_{ic}}{dt} \end{cases} \tag{C.7}$$

where V_{isa}, V_{isb} and V_{isc} are the three-phase AC voltages at the PCC for external power system on the inverter-side; V_{ica}, V_{icb} and V_{icc} are the three-phase AC voltages on the AC-side of inverter; I_{ia}, I_{ib} and I_{ic} are the three-phase AC currents; L_i and R_i and are the total resistance and inductance of AC transformer and series AC reactor on the inverter-side. The (C.7) is

converted from *a-b-c* to *d-q* coordinate system with the Park transformation expressed in (C.8):

$$P_{is}=\frac{2}{3}\begin{bmatrix}\cos(\omega_{is}t) & \cos(\omega_{is}t-\frac{2}{3}\pi) & \cos(\omega_{is}t+\frac{2}{3}\pi)\\ -\sin(\omega_{is}t) & -\sin(\omega_{is}t-\frac{2}{3}\pi) & -\sin(\omega_{is}t+\frac{2}{3}\pi)\end{bmatrix} \tag{C.8}$$

where P_{is} is the inverter-side Park transformation matrix; ω_{is} the synchronous rotational speed of the AC system on the inverter-side and $\omega_{is}=2\pi f_{is}$ (f_{is} is the system frequency on inverter-side).

$$P_{is}\times\begin{bmatrix}V_{isa}\\V_{isb}\\V_{isc}\end{bmatrix}=P_{is}\times\begin{bmatrix}V_{ica}\\V_{icb}\\V_{icc}\end{bmatrix}+R_i\times P_{is}\times\begin{bmatrix}I_{ia}\\I_{ib}\\I_{ic}\end{bmatrix}+L_i\times P_{is}\times\frac{d}{dt}\left(P_{is}^{-1}\times P_{is}\begin{bmatrix}I_{ia}\\I_{ib}\\I_{ic}\end{bmatrix}\right) \tag{C.9}$$

$$\begin{bmatrix}V_{isd}\\V_{isq}\end{bmatrix}=\begin{bmatrix}V_{icd}\\V_{icq}\end{bmatrix}+R_i\times\begin{bmatrix}I_{id}\\I_{iq}\end{bmatrix}+L_i\times P_{is}\times P_{is}^{-1}\times\begin{bmatrix}\frac{dI_{id}}{dt}\\\frac{dI_{iq}}{dt}\end{bmatrix}+P_{is}\times\frac{dP_{is}^{-1}}{dt}\times\begin{bmatrix}I_{id}\\I_{iq}\end{bmatrix} \tag{C.10}$$

$$P_{is}\times\frac{dP_{is}^{-1}}{dt}=\begin{bmatrix}0 & -\omega_{is}\\ \omega_{is} & 0\end{bmatrix} \tag{C.11}$$

After the transformation processes expressed from (C.9) to (C.11), the inverter-side voltages in the rotating *d-q* coordinates are expressed in (C.12):

$$\begin{cases}V_{isd}=V_{icd}+R_iI_{id}+L_i\dfrac{dI_{id}}{dt}-\omega_{is}L_iI_{iq}\\ V_{isq}=V_{icq}+R_iI_{iq}+L_i\dfrac{dI_{iq}}{dt}+\omega_{is}L_iI_{id}\end{cases} \tag{C.12}$$

where V_{isd} and V_{isq} are the *d*- and *q*-axis voltage on system-side of inverter-side converter; V_{icd} and V_{icq} are the *d*- and *q*-axis voltage on converter-side of inverter-side converter; I_{id} and I_{iq} are the *d*- and *q*-axis current of inverter-side converter.

Appendix D

Derivation of the Small-signal Models for Chapter 6

$$A_1 = \begin{bmatrix} -\left(\frac{V_{rcd1}I_{rd1} + V_{rcq1}I_{rq1}}{C_{r1}V_{rdc1}^2} + \frac{R_2 + R_3}{R_1R_2 + R_2R_3 + R_1R_3}\right) & 0 & 0 & 0 & 0 \\ 0 & 0 & 0 & 0 & 0 \\ 0 & 0 & 0 & 0 & 0 \\ 0 & K_{ri1} & 0 & 0 & 0 \\ 0 & 0 & K_{ri2} & 0 & 0 \end{bmatrix} \quad \text{(D.1)}$$

$$A_2 = \begin{bmatrix} -\left(\frac{V_{icd}I_{id} + V_{icq}I_{iq}}{C_iV_{idc}^2} + \frac{R_1 + R_3}{R_1R_2 + R_2R_3 + R_1R_3}\right) & 0 & 0 & 0 & 0 \\ -1 & 0 & 0 & 0 & 0 \\ 0 & 0 & 0 & 0 & 0 \\ -K_{ip1} & K_{ii1} & 0 & 0 & 0 \\ 0 & 0 & K_{ii2} & 0 & 0 \end{bmatrix} \quad \text{(D.2)}$$

$$A_3 = \begin{bmatrix} -\left(\frac{V_{rcd2}I_{rd2} + V_{rcq2}I_{rq2}}{C_{r2}V_{rdc2}^2} + \frac{R_2 + R_3}{R_1R_2 + R_2R_3 + R_1R_3}\right) & 0 & 0 & 0 & 0 \\ 0 & 0 & 0 & 0 & 0 \\ 0 & 0 & 0 & 0 & 0 \\ 0 & K_{ri4} & 0 & 0 & 0 \\ 0 & 0 & K_{ri4} & 0 & 0 \end{bmatrix} \quad \text{(D.3)}$$

$$A_4 = \begin{bmatrix} \frac{R_1}{R_1R_2 + R_2R_3 + R_1R_3} & 0 & 0 & 0 & 0 \\ 0 & 0 & 0 & 0 & 0 \\ 0 & 0 & 0 & 0 & 0 \\ 0 & 0 & 0 & 0 & 0 \\ 0 & 0 & 0 & 0 & 0 \end{bmatrix} \quad \text{(D.4)}$$

$$A_5 = \begin{bmatrix} \frac{R_2}{R_1R_2 + R_2R_3 + R_1R_3} & 0 & 0 & 0 & 0 \\ 0 & 0 & 0 & 0 & 0 \\ 0 & 0 & 0 & 0 & 0 \\ 0 & 0 & 0 & 0 & 0 \\ 0 & 0 & 0 & 0 & 0 \end{bmatrix} \quad \text{(D.5)}$$

$$A_6 = \begin{bmatrix} \frac{R_3}{R_1R_2 + R_2R_3 + R_1R_3} & 0 & 0 & 0 & 0 \\ 0 & 0 & 0 & 0 & 0 \\ 0 & 0 & 0 & 0 & 0 \\ 0 & 0 & 0 & 0 & 0 \\ 0 & 0 & 0 & 0 & 0 \end{bmatrix} \tag{D.6}$$

$$A = \begin{bmatrix} A_1 & A_6 & A_5 \\ A_6 & A_2 & A_4 \\ A_5 & A_4 & A_3 \end{bmatrix} \tag{D.7}$$

$$B_1 = \begin{bmatrix} 0 & 0 \\ -I_{rd1} & -I_{rq1} \\ I_{rq1} & -I_{rd1} \\ -K_{rp1}I_{rd1} & -K_{rp1}I_{rq1} \\ K_{rp2}I_{rq1} & -K_{rp2}I_{rd1} \end{bmatrix} \tag{D.8}$$

$$B_2 = \begin{bmatrix} 0 & 0 \\ 0 & 0 \\ I_{iq} & -I_{id} \\ 0 & 0 \\ K_{ip2}I_{iq} & -K_{ip2}I_{id} \end{bmatrix} \tag{D.9}$$

$$B_3 = \begin{bmatrix} 0 & 0 \\ -I_{rd2} & -I_{rq2} \\ I_{rq2} & -I_{rd2} \\ -K_{rp4}I_{rd2} & -K_{rp4}I_{rq2} \\ K_{rp5}I_{rq2} & -K_{rp5}I_{rd2} \end{bmatrix} \tag{D.10}$$

$$B = \begin{bmatrix} B_1 & 0 & 0 \\ 0 & B_2 & 0 \\ 0 & 0 & B_3 \end{bmatrix} \tag{D.11}$$

$$C_1 = \begin{bmatrix} \frac{I_{rd1}}{C_{r1}V_{rdc1}} & \frac{I_{rq1}}{C_{r1}V_{rdc1}} \\ 0 & 0 \\ 0 & 0 \\ 0 & 0 \\ 0 & 0 \end{bmatrix} \tag{D.12}$$

$$C_2 = \begin{bmatrix} \frac{I_{id}}{C_i V_{idc}} & \frac{I_{iq}}{C_i V_{idc}} \\ 0 & 0 \\ 0 & 0 \\ 0 & 0 \\ 0 & 0 \end{bmatrix} \tag{D.13}$$

$$C_3 = \begin{bmatrix} \frac{I_{rd2}}{C_{r2} V_{rdc2}} & \frac{I_{rq2}}{C_{r2} V_{rdc2}} \\ 0 & 0 \\ 0 & 0 \\ 0 & 0 \\ 0 & 0 \end{bmatrix} \tag{D.1}$$

$$C = \begin{bmatrix} C_1 & 0 & 0 \\ 0 & C_2 & 0 \\ 0 & 0 & C_3 \end{bmatrix} \tag{D.14}$$

$$D_1 = \begin{bmatrix} \frac{V_{rcd1}}{C_{r1} V_{rdc1}} & \frac{V_{rcq1}}{C_{r1} V_{rdc1}} \\ -V_{rsd1} & -V_{rsq1} \\ -V_{rsq1} & V_{rsd1} \\ -(K_{rp1} V_{rsd1} + 1) & -K_{rp1} V_{rsq1} \\ -K_{rp2} V_{rsq1} & K_{rp2} V_{rsd1} - 1 \end{bmatrix} \tag{D.15}$$

$$D_2 = \begin{bmatrix} \frac{V_{icd}}{C_i V_{idc}} & \frac{V_{icq}}{C_i V_{idc}} \\ 0 & 0 \\ -V_{isq} & V_{isd} \\ -1 & 0 \\ -K_{ip2} V_{isq} & K_{ip2} V_{isd} - 1 \end{bmatrix} \tag{D.16}$$

$$D_3 = \begin{bmatrix} \frac{V_{rcd2}}{C_{r2} V_{rdc2}} & \frac{V_{rcq2}}{C_{r2} V_{rdc2}} \\ -V_{rsd2} & -V_{rsq2} \\ -V_{rsq2} & V_{rsd2} \\ -(K_{rp4} V_{rsd2} + 1) & -K_{rp4} V_{rsq2} \\ -K_{rp5} V_{rsq2} & K_{rp5} V_{rsd2} - 1 \end{bmatrix} \tag{D.17}$$

$$D = \begin{bmatrix} D_1 & 0 & 0 \\ 0 & D_2 & 0 \\ 0 & 0 & D_3 \end{bmatrix} \tag{D.18}$$

$$E_1 = \begin{bmatrix} 0 & -K_{rp3}K_{ri1} & 0 & -K_{ri3} & 0 \\ 0 & 0 & -K_{rp3}K_{ri2} & 0 & -K_{ri3} \end{bmatrix} \tag{D.19}$$

$$E_2 = \begin{bmatrix} K_{ip1}K_{ip3} & -K_{ip3}K_{ii1} & 0 & -K_{ii3} & 0 \\ 0 & 0 & -K_{ip3}K_{ii2} & 0 & -K_{ii3} \end{bmatrix} \tag{D.20}$$

$$E_3 = \begin{bmatrix} 0 & -K_{rp6}K_{ri4} & 0 & -K_{ri6} & 0 \\ 0 & 0 & -K_{rp6}K_{ri5} & 0 & -K_{ri6} \end{bmatrix} \tag{D.21}$$

$$E = \begin{bmatrix} E_1 & 0 & 0 \\ 0 & E_2 & 0 \\ 0 & 0 & E_3 \end{bmatrix} \tag{D.22}$$

$$F_1 = \begin{bmatrix} K_{rp1}K_{rp3}I_{rd1} + 1 & K_{rp1}K_{rp3}I_{rq1} \\ -K_{rp2}K_{rp3}I_{rq1} & K_{rp2}K_{rp3}I_{rd1} + 1 \end{bmatrix} \tag{D.23}$$

$$F_2 = \begin{bmatrix} 1 & 0 \\ -K_{ip2}K_{ip3}I_{iq} & K_{ip2}K_{ip3}I_{id} + 1 \end{bmatrix} \tag{D.24}$$

$$F_3 = \begin{bmatrix} K_{rp4}K_{rp6}I_{rd2} + 1 & K_{rp4}K_{rp6}I_{rq2} \\ -K_{rp5}K_{rp6}I_{rq2} & K_{rp5}K_{rp6}I_{rd2} + 1 \end{bmatrix} \tag{D.25}$$

$$F = \begin{bmatrix} F_1 & 0 & 0 \\ 0 & F_2 & 0 \\ 0 & 0 & F_3 \end{bmatrix} \tag{D.26}$$

$$G_1 = \begin{bmatrix} K_{rp3}(K_{rp1}V_{rsd1} + 1) & K_{rp1}K_{rp3}V_{rsq1} + X_{r1} \\ K_{rp2}K_{rp3}V_{rsq1} - X_{r1} & -K_{rp3}(K_{rp2}V_{rsd1} - 1) \end{bmatrix} \tag{D.27}$$

$$G_2 = \begin{bmatrix} K_{ip3} & X_i \\ K_{ip2}K_{ip3}V_{isq} - X_i & -K_{ip3}(K_{ip2}V_{isd} - 1) \end{bmatrix} \tag{D.28}$$

$$G_3 = \begin{bmatrix} K_{rp6}(K_{rp4}V_{rsd2} + 1) & K_{rp4}K_{rp6}V_{rsq2} + X_{r2} \\ K_{rp5}K_{rp6}V_{rsq2} - X_{r2} & -K_{rp6}(K_{rp5}V_{rsd2} - 1) \end{bmatrix} \tag{D.29}$$

$$G = \begin{bmatrix} G_1 & 0 & 0 \\ 0 & G_2 & 0 \\ 0 & 0 & G_3 \end{bmatrix} \tag{D.30}$$

$$H = \begin{bmatrix} 0 & -X_{r1} & 0 & 0 & 0 & 0 \\ X_{r1} & 0 & 0 & 0 & 0 & 0 \\ 0 & 0 & 0 & -X_i & 0 & 0 \\ 0 & 0 & X_i & 0 & 0 & 0 \\ 0 & 0 & 0 & 0 & 0 & -X_{r2} \\ 0 & 0 & 0 & 0 & X_{r2} & 0 \end{bmatrix} \tag{D.31}$$

Appendix E

Simulation System and the Parameters for Chapter 3

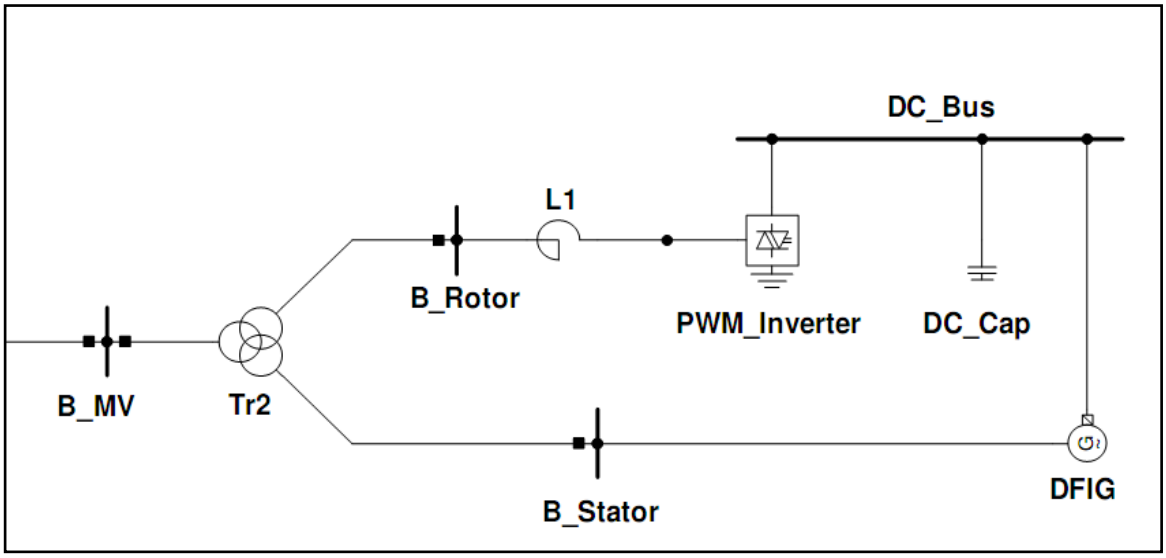

Fig-E.1 The Detailed Layout of the WT-DFIG System in DIgSILENT/PowerFactory

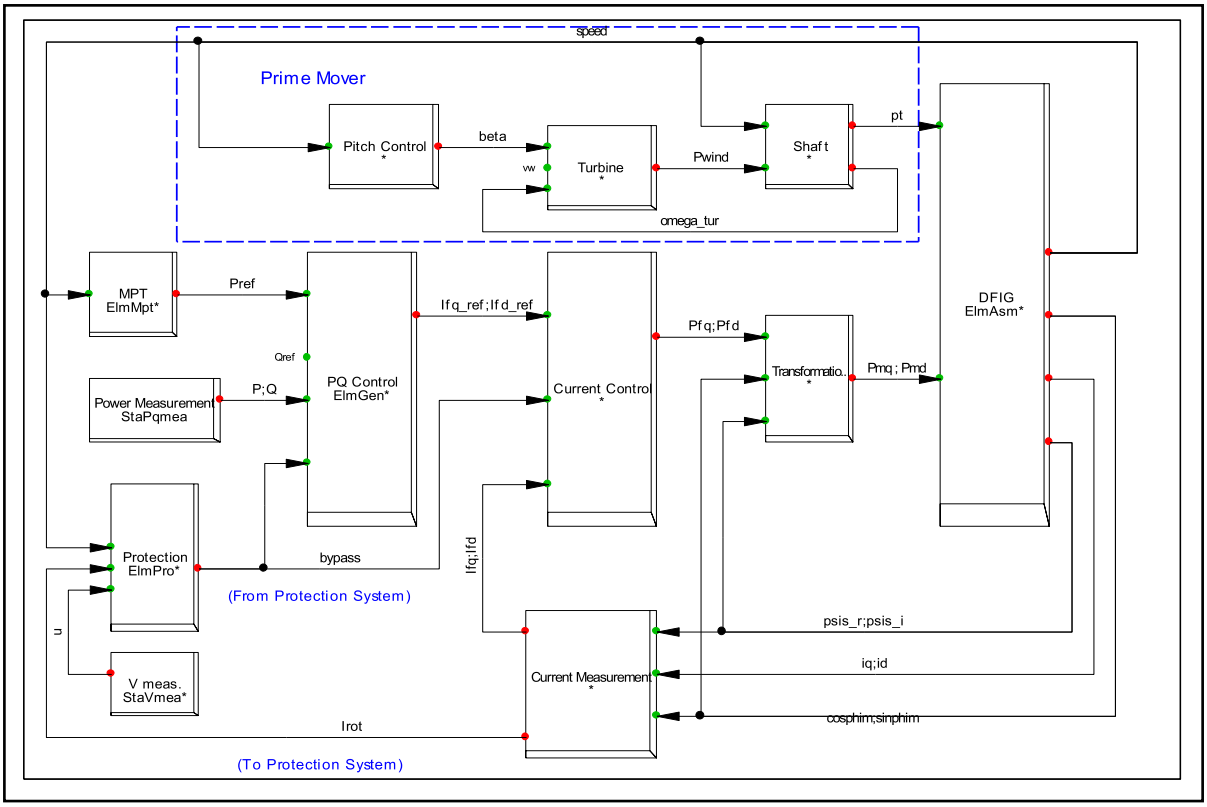

Fig-E.2 The Control Scheme of Rotor-side Converter in the WT-DFIG System

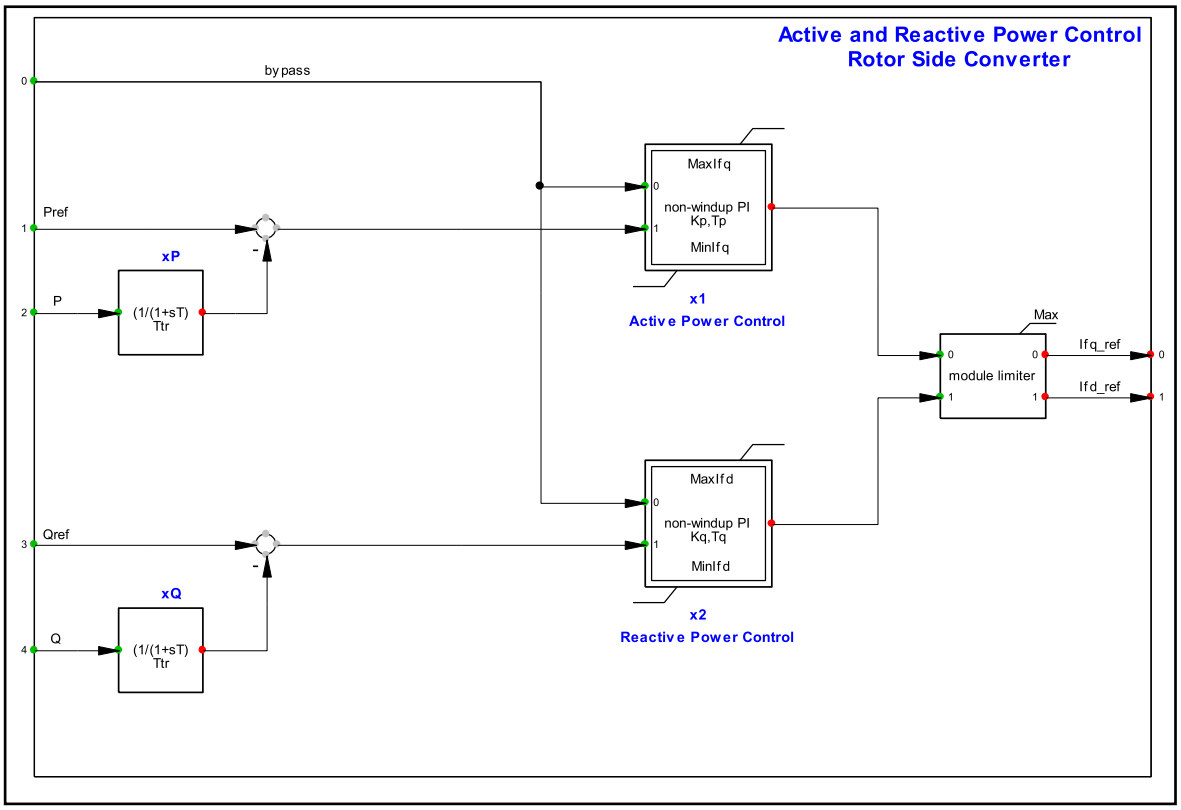

Fig-E.3 The Power Controller of Rotor-side Converter in the WT-DFIG System

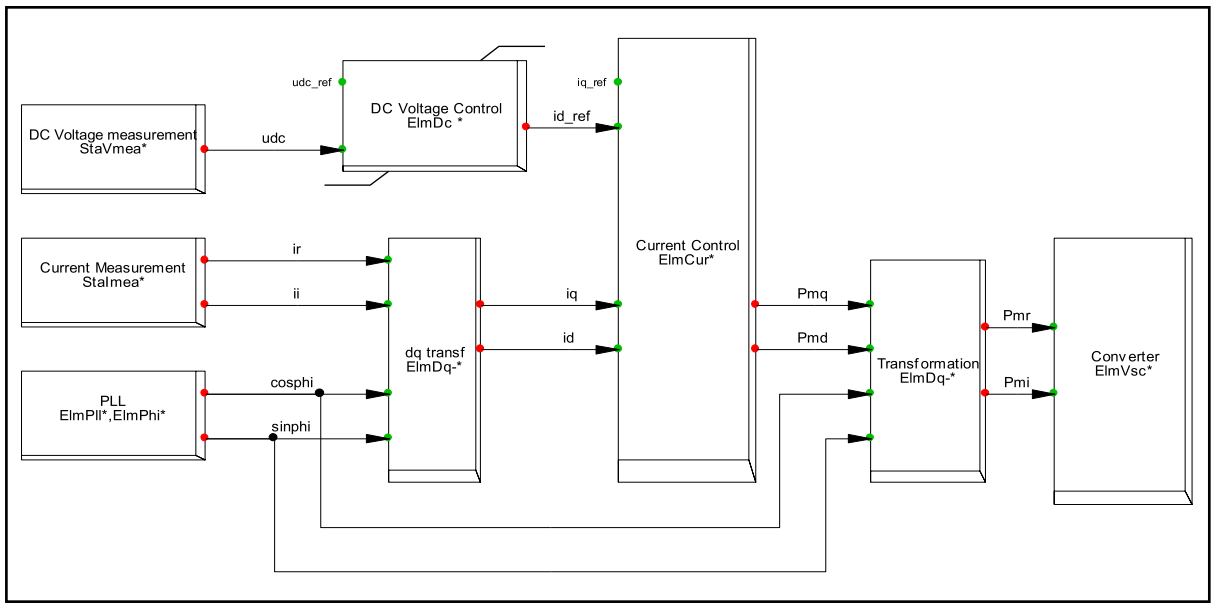

Fig-E.4 The Control Scheme of Grid-side Converter in the WT-DFIG System

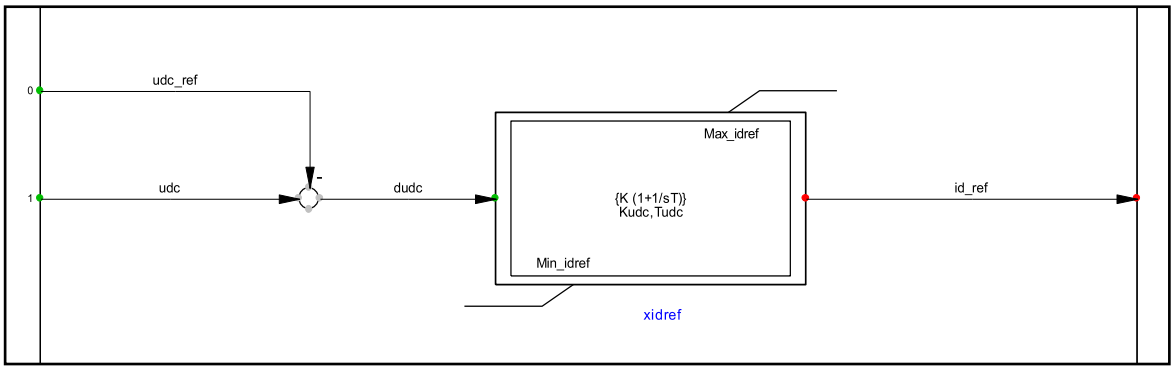

Fig-E.5 The DC Voltage Controller of Grid-side Converter in the WT-DFIG System

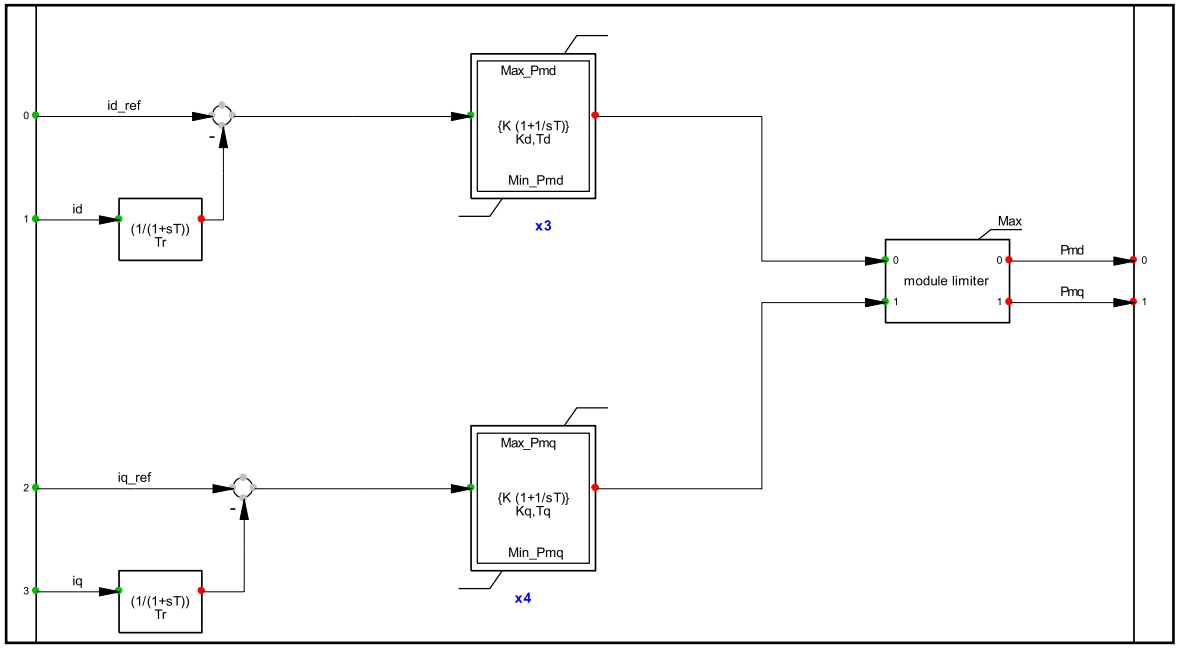

Fig-E.6 The General Current Controller of Rotor- and Grid-side Converters in WT-DFIG System

Table-E.1 The System Parameter of the Single WT-DFIG System

Per-unit Rated Capacity	5.0 MW
Output AC Voltage	20 kV
Voltage of DC Link	1.15 kV
System Frequency	50 Hz
Inductance of AC Reactor	0.2408289 mH
Resistance of AC Reactor	0.00249952 ohm
Capacitance of the DC Capacitor	4813.76 μF
Stator Resistance of DFIG	0.00298989 p.u.
Stator Reactance of DFIG	0.125 p.u.
Mutual Reactance of DFIG	2.5 p.u.
Acceleration Time Constant	0.5 s

Table-E.2 The Parameter of the Three-Winding Transformer

Turns Ratio of 3-Winding Transformer	0.69 kV/3.3 kV/20 kV
Reactance of Transformer (HV-MV)	0.0535068 p.u.
Reactance of Transformer (HV-LV)	0.00428516 p.u.
Reactance of Transformer (MV-LV)	0.00428153 p.u.
Resistance of Transformer (HV-MV)	0.00263074 p.u.
Resistance of Transformer (HV-LV)	0.00018941 p.u.
Resistance of Transformer (MV-LV)	0.00006888 p.u.

Table-E.3 The Parameter of the Rotor-side Control System

Time Constant of the First-stage Low-Pass Filter	0.001s
Proportional Gain of the *d*-axis *P* Controller	1.0 p.u.
Time Constant of the *d*-axis *P* Controller	0.1 s
Proportional Gain of the *q*-axis *Q* Controller	1.0 p.u.
Time Constant of the *q*-axis *Q* Controller	0.1 s
Time Constant of the Second-stage Low-Pass Filter	0.0001s
Proportional Gain of the *d*-axis Current Controller	0.2 p.u.
Time Constant of the *d*-axis Current Controller	0.01 s
Proportional Gain of the *q*-axis Current Controller	0.2 p.u.
Time Constant of the *q*-axis Current Controller	0.01 s

Table-E.4 The Parameter of the Grid-side Control System

Proportional Gain of the *d*-axis V_{dc} Controller	5.0 p.u.
Time Constant of the *d*-axis V_{dc} Controller	0.1 s
Time Constant of the Second-stage Low-Pass Filter	0.0001s
Proportional Gain of the *d*-axis Current Controller	1.0 p.u.
Time Constant of the *d*-axis Current Controller	0.015 s
Proportional Gain of the *q*-axis Current Controller	3.0 p.u.
Time Constant of the *q*-axis Current Controller	0.015 s

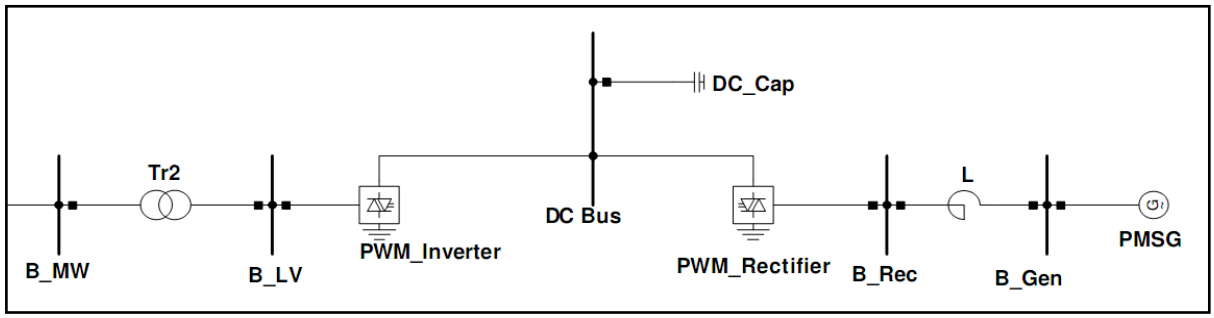

Fig-E.7 The Detailed Layout of the WT-PMSG System in DIgSILENT/PowerFactory

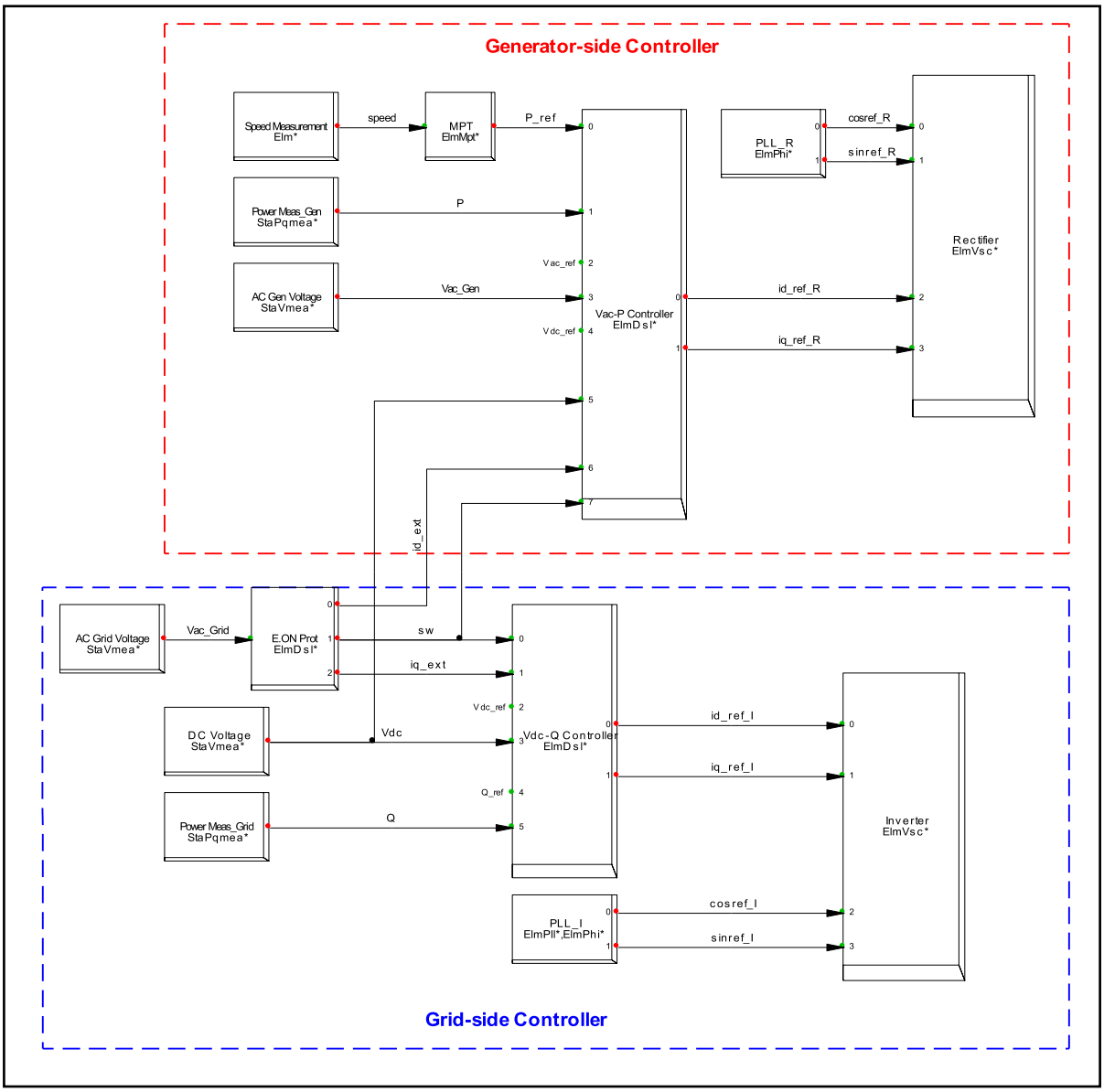

Fig-E.8 The Layout of Control System of WT-PMSG System in DIgSILENT/PowerFactory

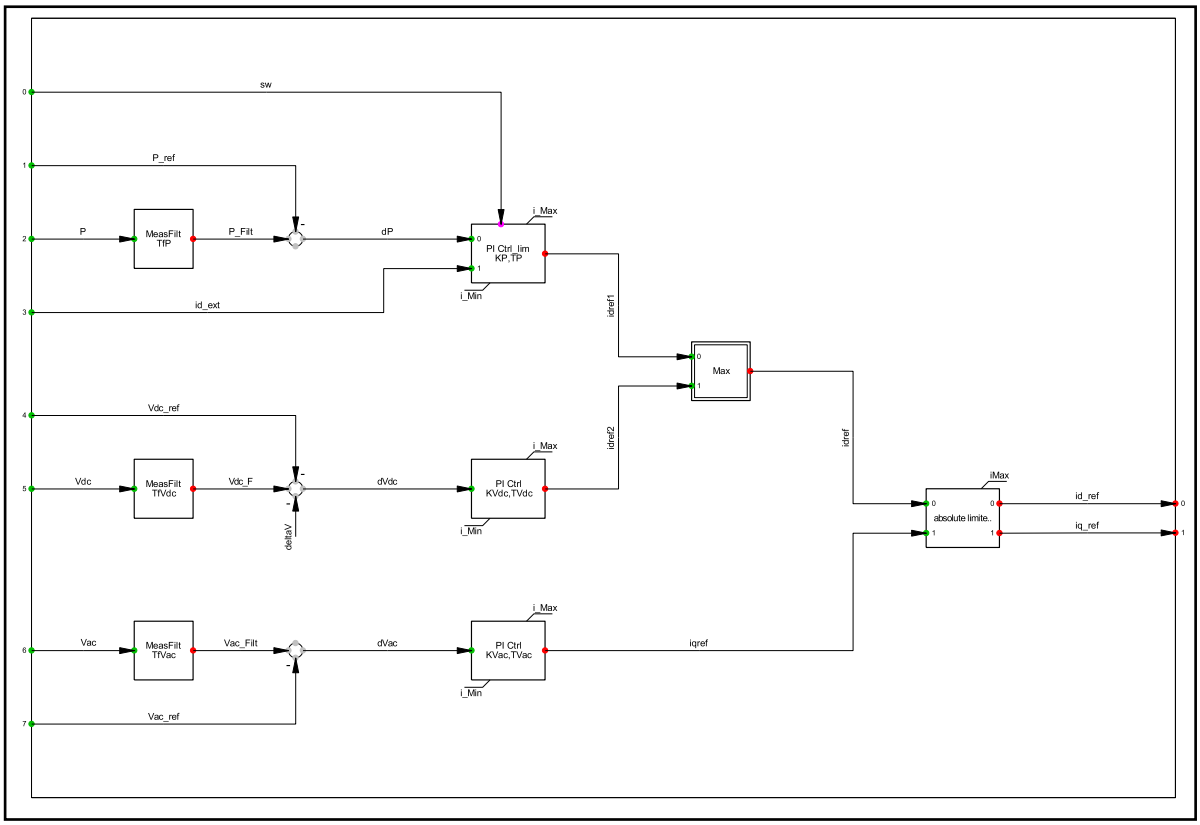

Fig-E.9 The First-stage Controller for the Generator-side Converter of WT-PMSG System

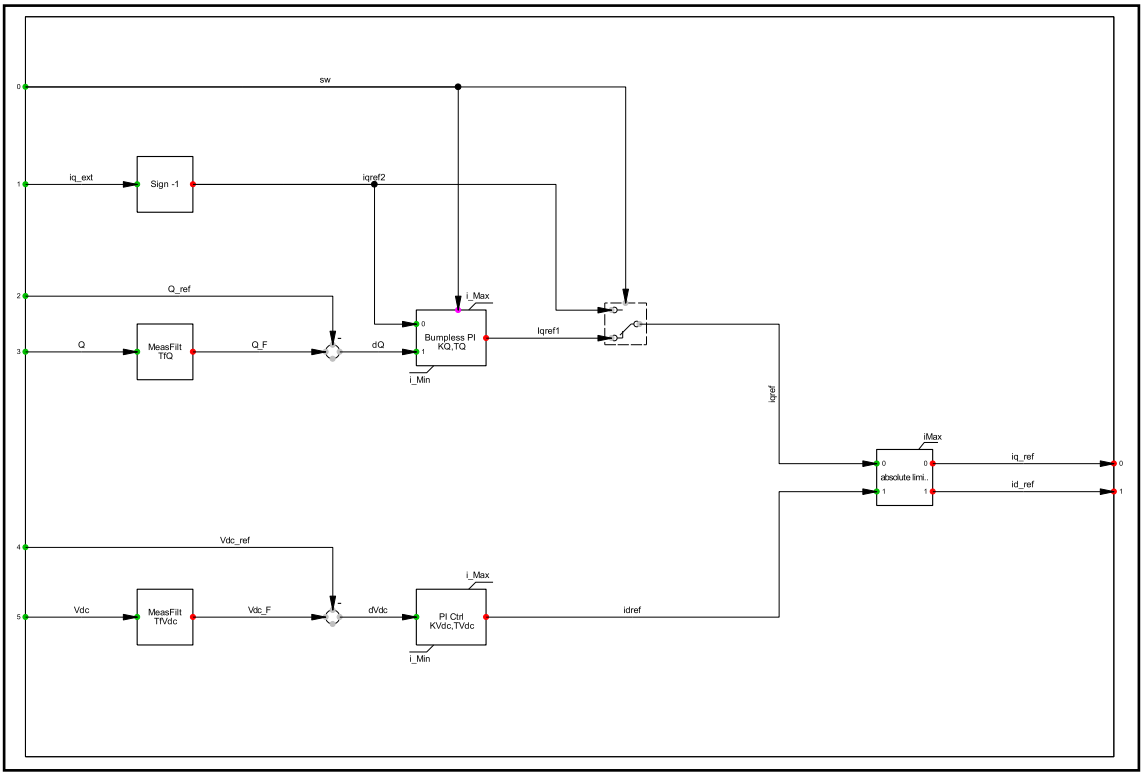

Fig-E.10 The First-stage Controller for the Grid-side Converter of WT-PMSG System

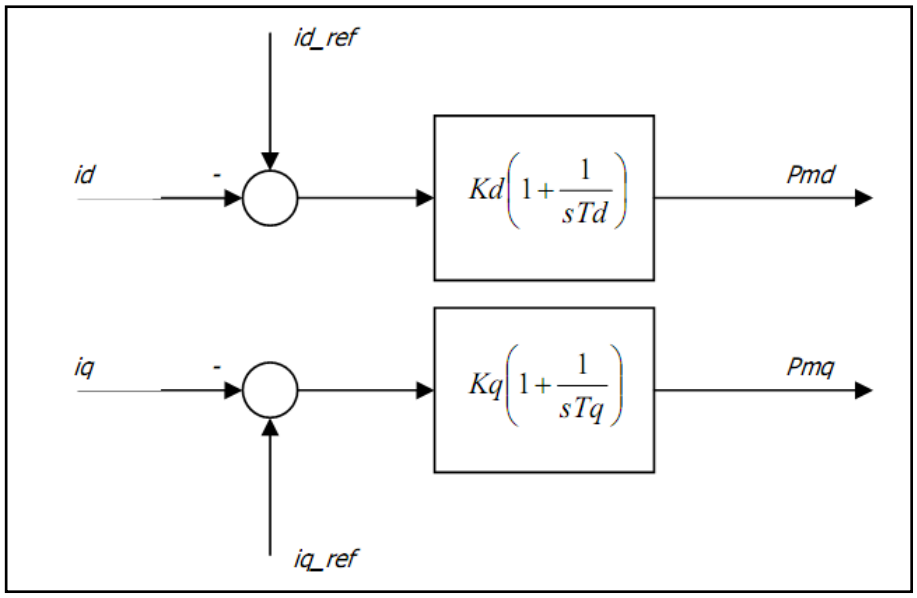

Fig-E.11 The General Built-in Second-stage Current Controller in Generator and Grid-side Converter

Table-E.5 The System Parameter of the Single WT-PMSG System

Per-unit Rated Capacity	5.0 MW
Short Circuit Ratio for External Grid	5
Output AC Voltage	20 kV
Voltage of DC Link	6.6 kV
System Frequency	50 Hz
Inductance of AC Reactor	0.5546231 mH
Capacitance of the DC Capacitor	1370.136 μF
Stator Reactance of DFIG	1.5 p.u.
Acceleration Time Constant	2.0 s
Turns Ratio of 3-Winding Transformer	3.3 kV/20 kV
Reactance of Transformer	0.06 p.u.

Table-E.6 The Parameter of the Generator-side Control System

Time Constant of the First-stage Low-Pass Filter	0.01s
Proportional Gain of the *d*-axis *P* Controller	0.5 p.u.
Time Constant of the *d*-axis *P* Controller	0.005 s
Proportional Gain of the *q*-axis V_{ac} Controller	5.0 p.u.
Time Constant of the *q*-axis V_{ac} Controller	0.01 s
Proportional Gain of the *d*-axis Current Controller	1.0 p.u.
Time Constant of the *d*-axis Current Controller	0.01 s
Proportional Gain of the *q*-axis Current Controller	1.0 p.u.
Time Constant of the *q*-axis Current Controller	0.01 s

Table-E.7 The Parameter of the Grid-side Control System

Time Constant of the *d*-axis First-stage Low-Pass Filter	0.001s
Time Constant of the *q*-axis First-stage Low-Pass Filter	0.01 s
Proportional Gain of the *q*-axis V_{dc} Controller	5.0 p.u.
Time Constant of the *q*-axis V_{dc} Controller	0.008 s
Proportional Gain of the *q*-axis Q Controller	1.0 p.u.
Time Constant of the *q*-axis Q Controller	0.05 s
Proportional Gain of the *d*-axis Current Controller	2.0 p.u.
Time Constant of the *d*-axis Current Controller	0.01 s
Proportional Gain of the *q*-axis Current Controller	2.0 p.u.
Time Constant of the *q*-axis Current Controller	0.01 s

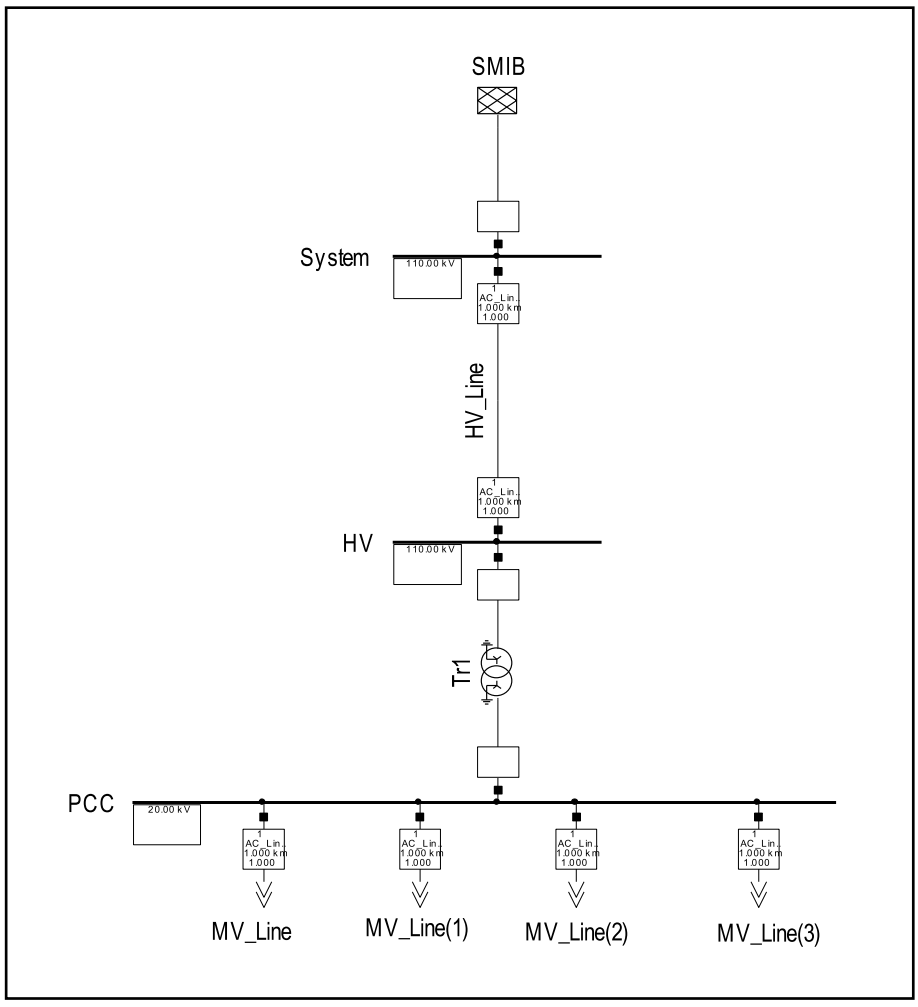

Fig-E.12 The Layout of the External power system in DIgSILENT/PowerFactory

Table-E.8 The Parameter of the External power system

The Rated Capacity of the Step-up Transformer	300.0 MVA
Turns Ratio of Transformer	110 kV/ 20 kV
System Frequency	50 Hz
Per-unit Resistance of AC Cable	0.02 ohm/m
Per-unit Susceptance of AC Cable	0.26 μs/m
Transmission Length	50 km

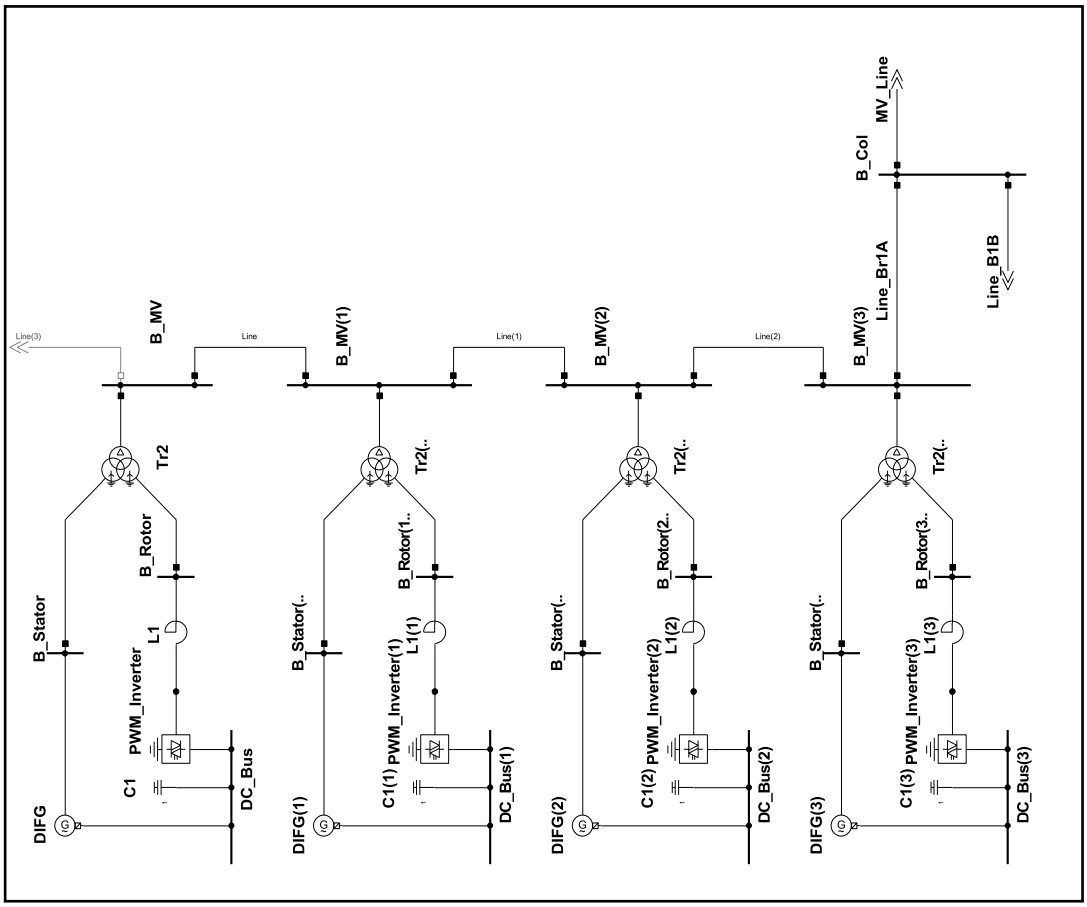

Fig-E.13 The Layout of Four WT-PMSGs Connecting in the Same Chain

Table-E.9 The Parameter of the WT-DFIG Based Offshore Wind Farm

The Rated Capacity of the Wind Farm	160 MVA
Units of WT-DFIGs	32
Number of Chains	8
Per-unit Resistance of AC Cable	0.02 ohm/m

Per-unit Susceptance of AC Cable	0.26 μs/m
Length of Cable for Machine Interconnection	0.2 km

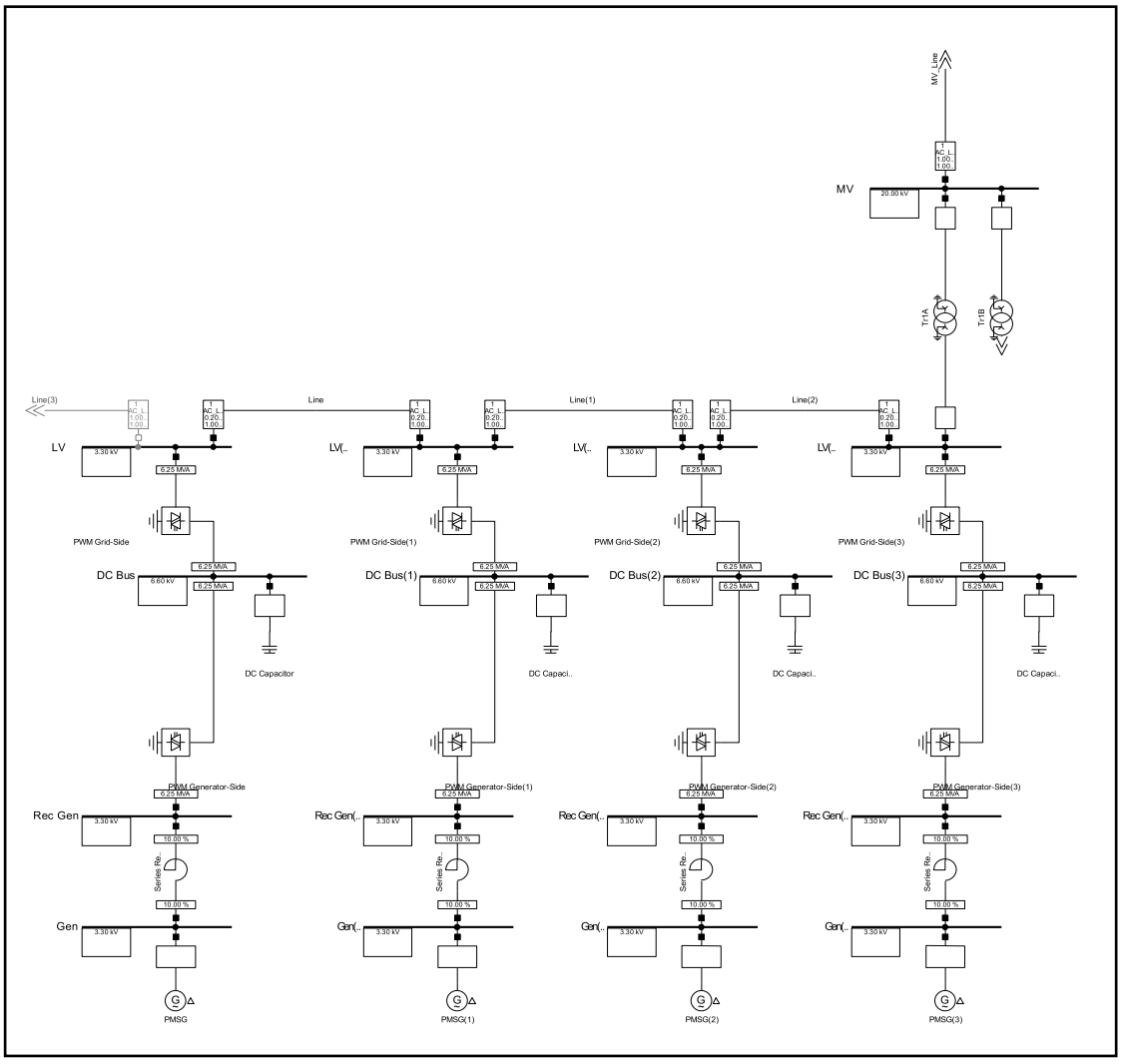

Fig-E.14 The Layout of Four WT-PMSGs Connecting in the Same Chain

Table-E.10 The Parameter of the WT-PMSG Based Offshore Wind Farm

The Rated Capacity of the Wind Farm	160 MVA
Units of WT-DFIGs	32
Number of Chains	8
Per-unit Resistance of AC Cable	0.02 ohm/m
Per-unit Susceptance of AC Cable	0.26 μs/m
Length of Cable for Machine Interconnection	0.2 km

Appendix F

Simulation System and the Parameters for Chapter 4

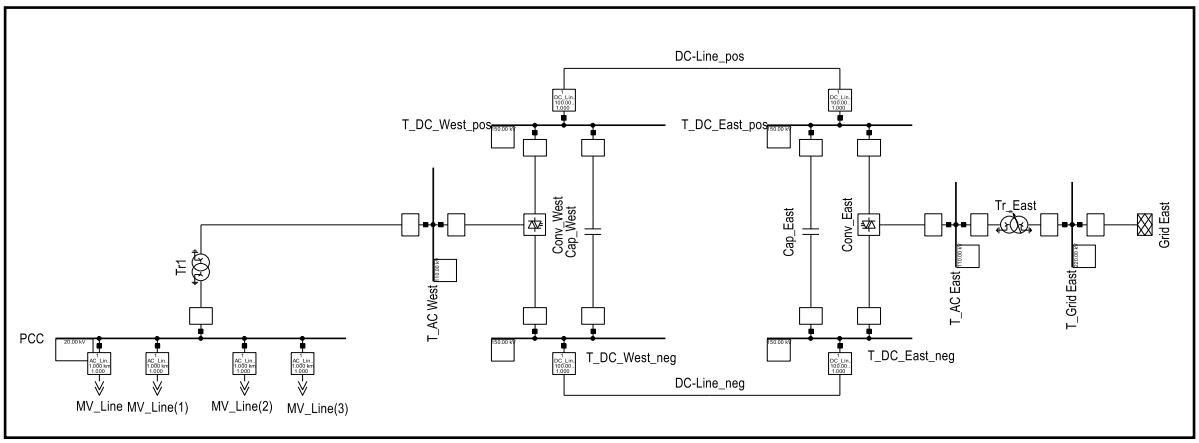

Fig-F.1 The Layout of Point-to-point VSC-HVDC System Connecting with Offshore Wind Farms in DIgSILENT/PowerFactory

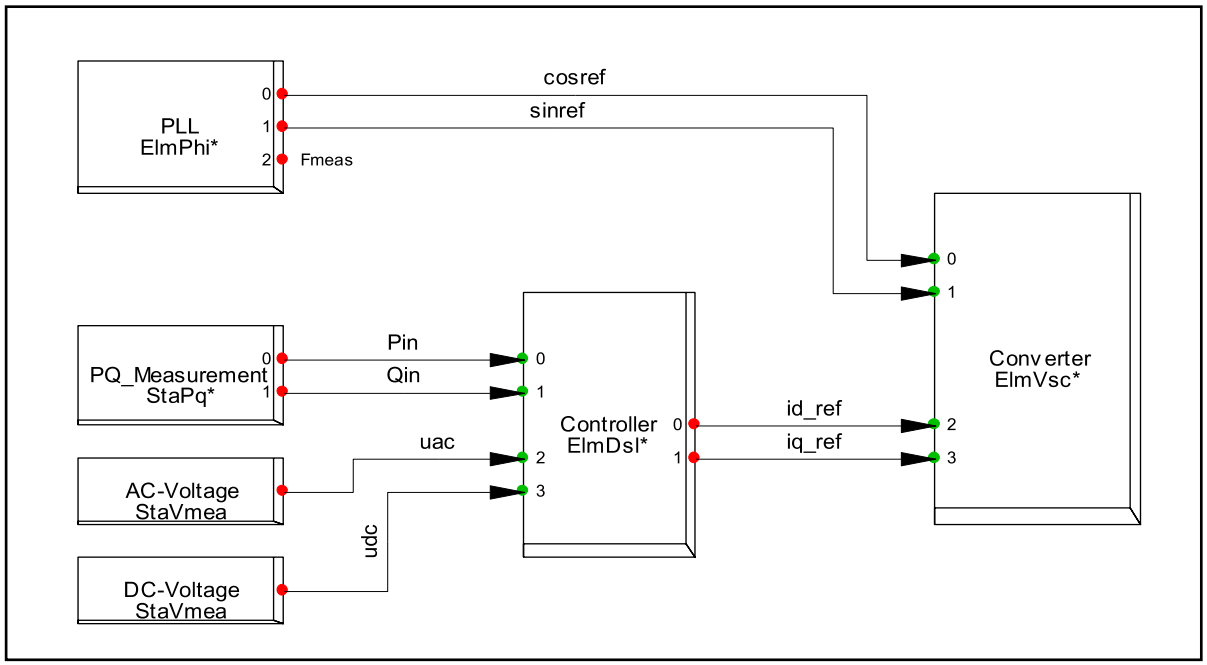

Fig-F.2 The General Control Scheme for Both Sides of Point-to point VSC-HVDC System

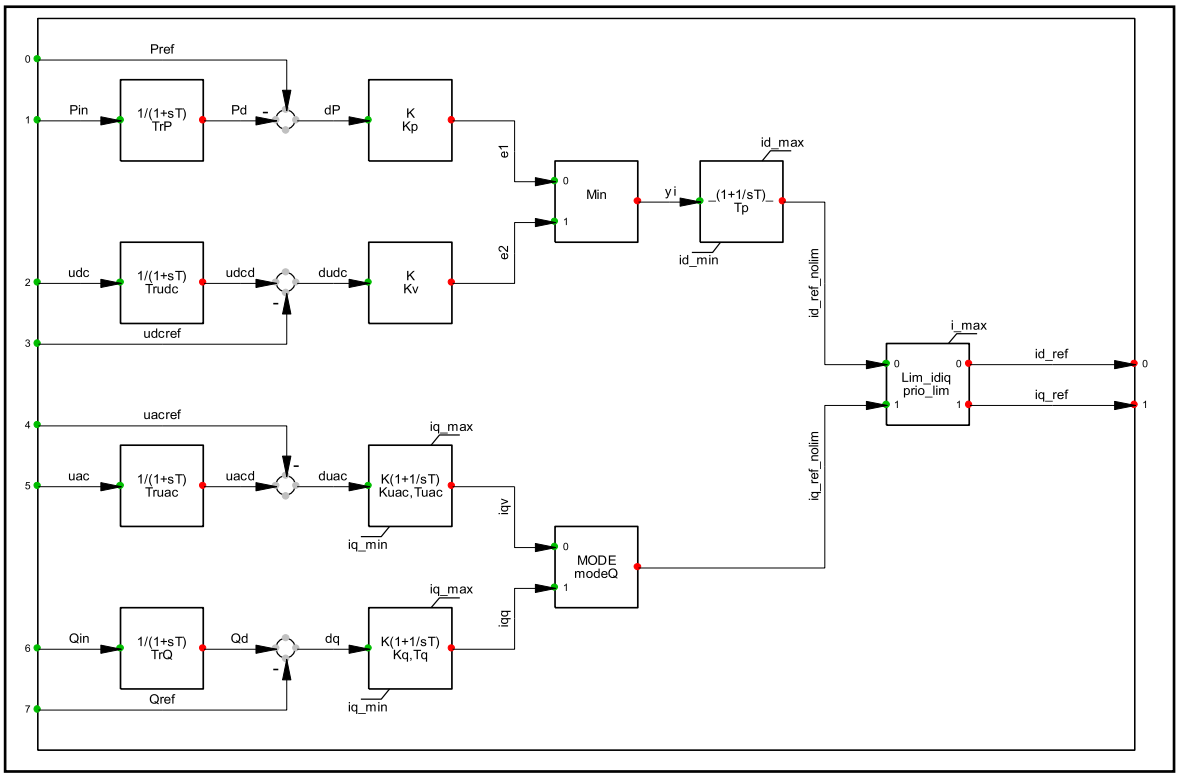

Fig-F.3 The Detailed Control Scheme for Both Sides of Point-to point VSC-HVDC System

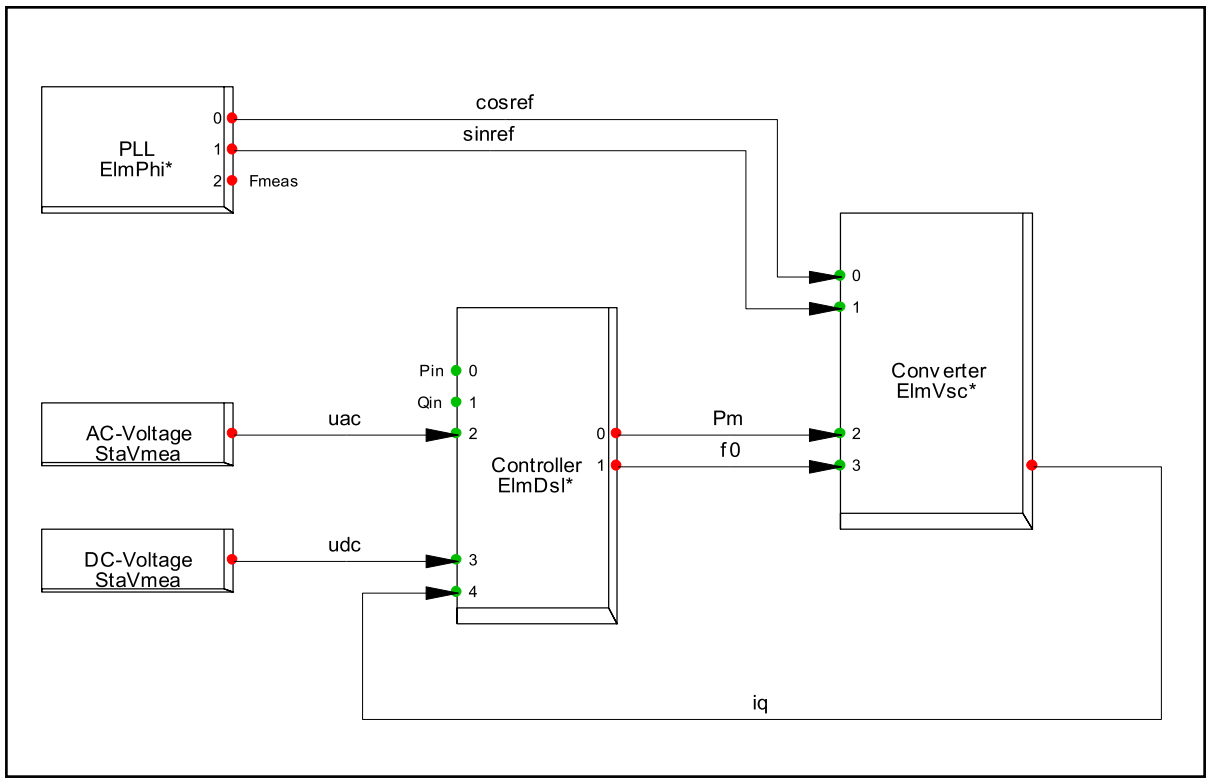

Fig-F.4 The Control Scheme 2 for Rectifier-side Converter of Point-to point VSC-HVDC System

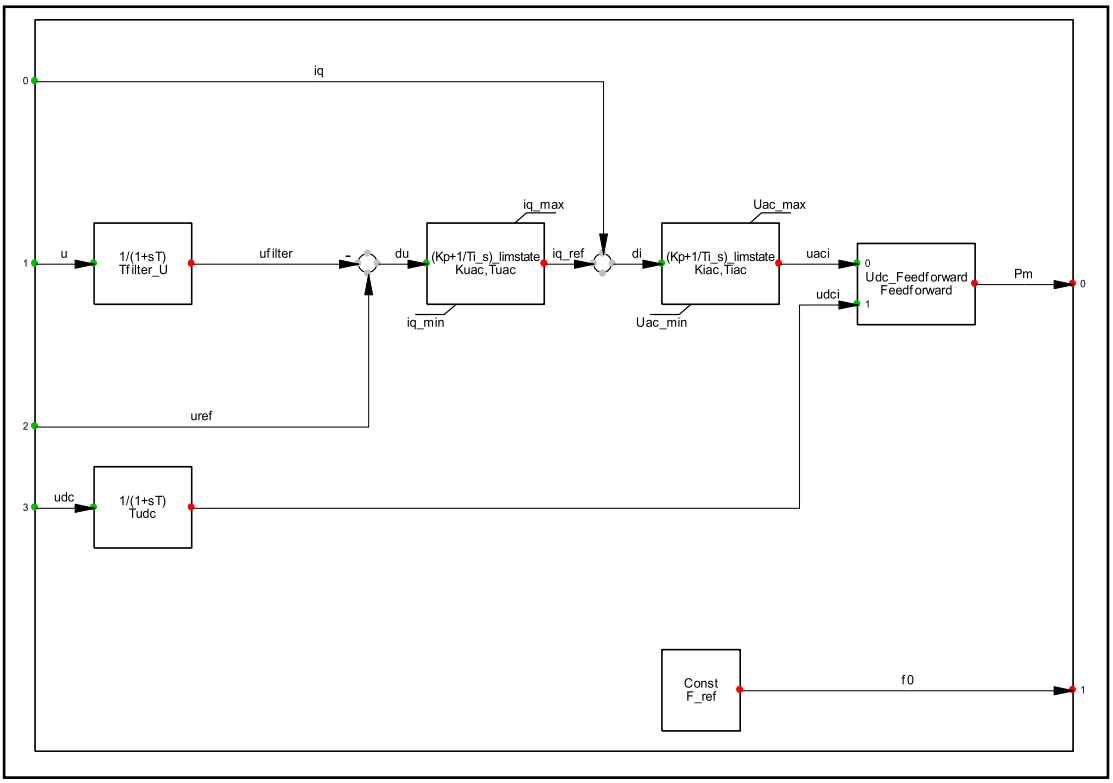

Fig-F.5 The Detailed Control Scheme 2 for Rectifier-side Converter of Point-to point VSC-HVDC System

Table-F.1 The System Parameter of VSC-HVDC System

Rated Capacity	250.0 MVA
System AC Voltage	110 kV
DC-side Voltage of Converters	± 150 kV
System Frequency	50 Hz
Short-circuit Impedance of AC Reactor	15%
Capacitance of the DC Capacitor	100.00 μF
Per-unit Resistance of AC Cable	0.05 ohm/m
Transmission Length	100 km

Table-F.2 The Parameter of the Rectifier-side Control System with Control Scheme 1

Time Constant of the First-stage Low-Pass Filter	0.005s
Proportional Gain of the *d*-axis *P* Controller	1.0 p.u.
Time Constant of the *d*-axis *P* Controller	0.01 s
Proportional Gain of the *q*-axis *Q* Controller	1.0 p.u.
Time Constant of the *q*-axis *Q* Controller	0.03 s
Proportional Gain of the *d*-axis Current Controller	2.0 p.u.
Time Constant of the *d*-axis Current Controller	0.01 s
Proportional Gain of the *q*-axis Current Controller	2.0 p.u.
Time Constant of the *q*-axis Current Controller	0.01 s

Table-F.3 The Parameter of the Rectifier-side Control System with Control Scheme 2

Time Constant of the First-stage Low-Pass Filter	0.005s
Proportional Gain of the q-axis V_{ac} Controller	2.0 p.u.
Time Constant of the q-axis V_{ac} Controller	0. 1 s
Proportional Gain of the q-axis Current Controller	3.0 p.u.
Time Constant of the q-axis Current Controller	0.005 s

Table-F.4 The Parameter of the Inverter-side Control System

Time Constant of the First-stage Low-Pass Filter	0.005s
Proportional Gain of the d-axis V_{dc} Controller	10.0 p.u.
Time Constant of the d-axis V_{dc} Controller	0.01 s
Proportional Gain of the q-axis Q Controller	1.0 p.u.
Time Constant of the q-axis Q Controller	0.03 s
Proportional Gain of the d-axis Current Controller	0.5 p.u.
Time Constant of the d-axis Current Controller	0.01 s
Proportional Gain of the q-axis Current Controller	0.5 p.u.
Time Constant of the q-axis Current Controller	0.01 s

Appendix G

Simulation System and the Parameters for Chapter 5

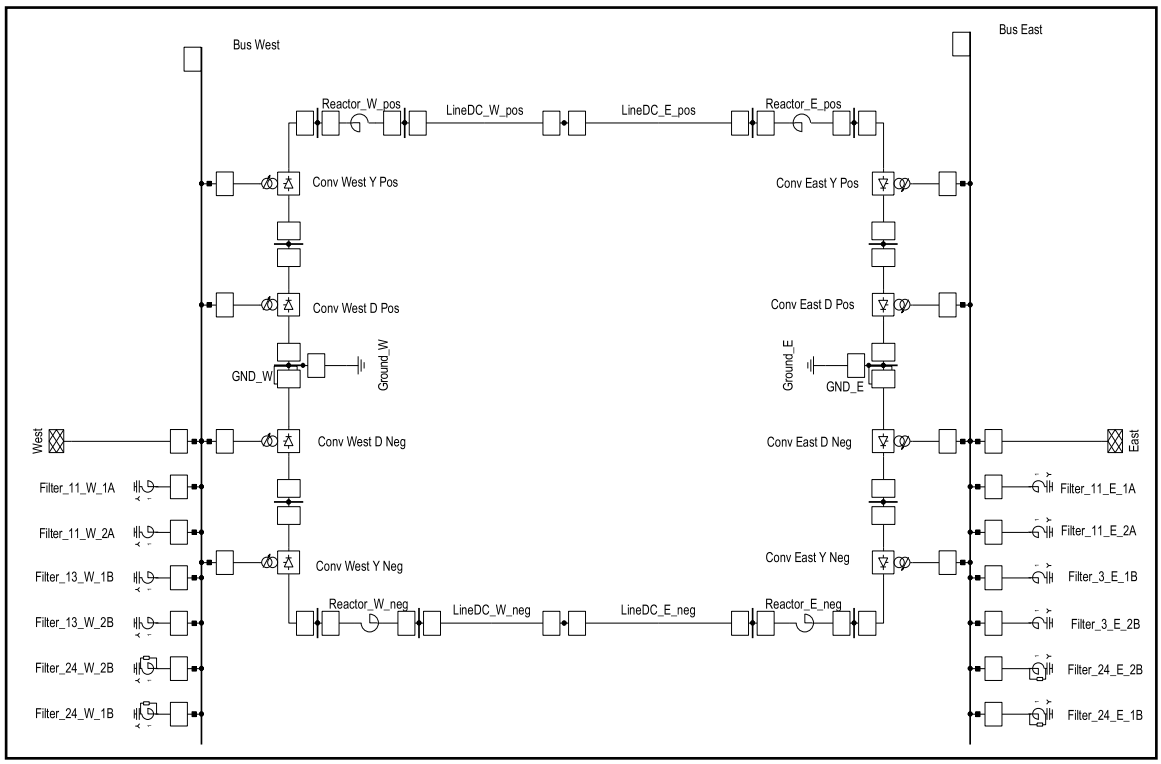

Fig-G.1 The Layout of the Bipolar CSC-HVDC System in DIgSILENT/PowerFactory

Table-C.1 The System Parameter of the Three-terminal VSC-Based HVDC Grid

System Rated Capacity per Pole	500 MW
Magnitude of System AC Voltage	400 kV
Magnitude of System DC Voltage	± 250 kV
System Frequency	50 Hz
Turns Ratio of Transformer	400 kV/96 kV
Commutation Reactance	5.25 ohm
Reactance of DC Reactor	0.15 p.u.
DC Resistance Per Meter	0.01 ohm/m
Length of Each DC Cable	200 km

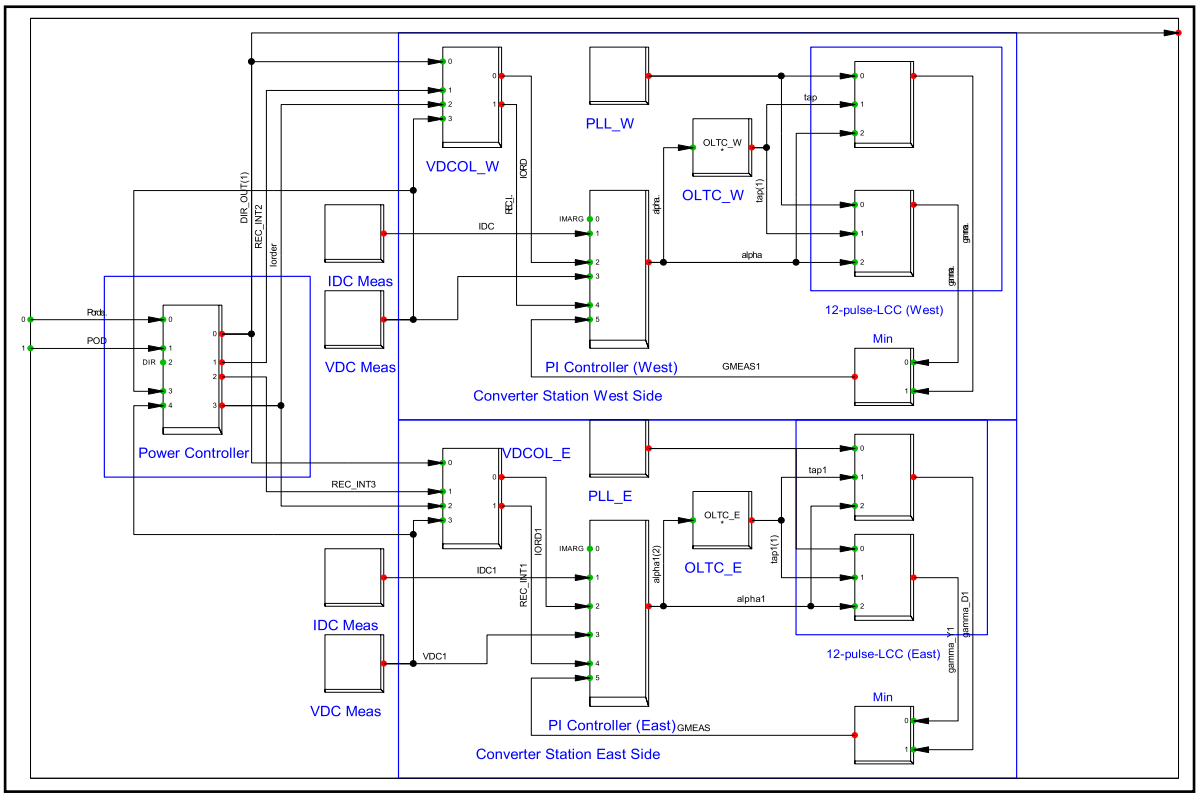

Fig-G.2 The Layout of the Control System for One Pole of Bipolar CSC-HVDC System

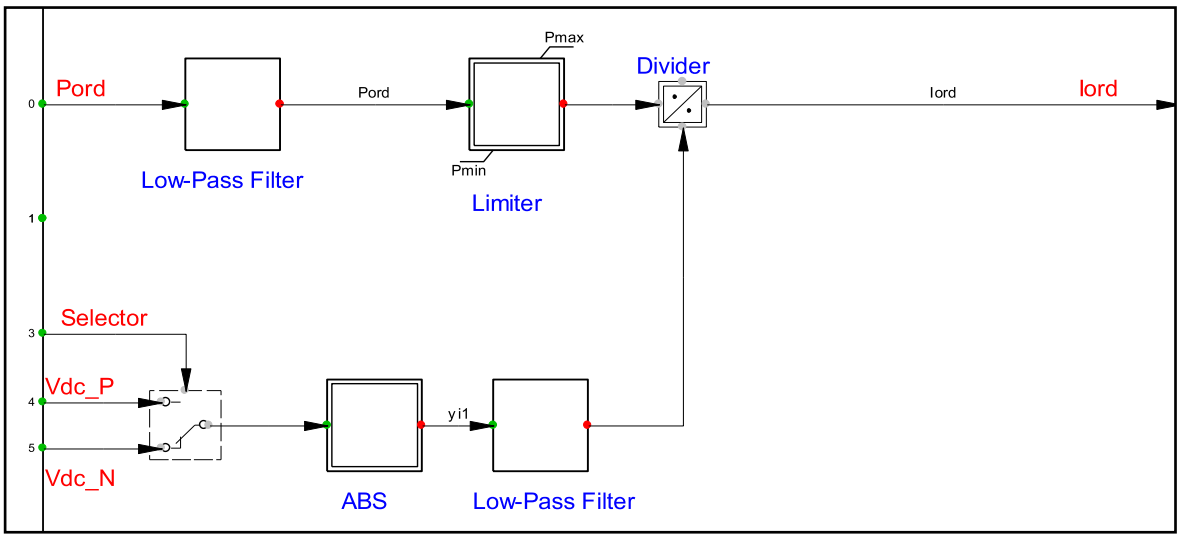

Fig-G.3 The Layout of the Power Controller for One Pole of Bipolar CSC-HVDC System

Table-G.2 The Parameter of the Power Controller on Rectifier-side of CSC-HVDC System

Power Reference	1.0
Maximum Limit of Power	1.2 p.u.
Minimum Limit of Power	-1.2 p.u.
Time Constant of Low-pass Filter for P_{ref}	0.03 p.u.
Time Constant of Low-pass Filter for V_{dc}	5 p.u.

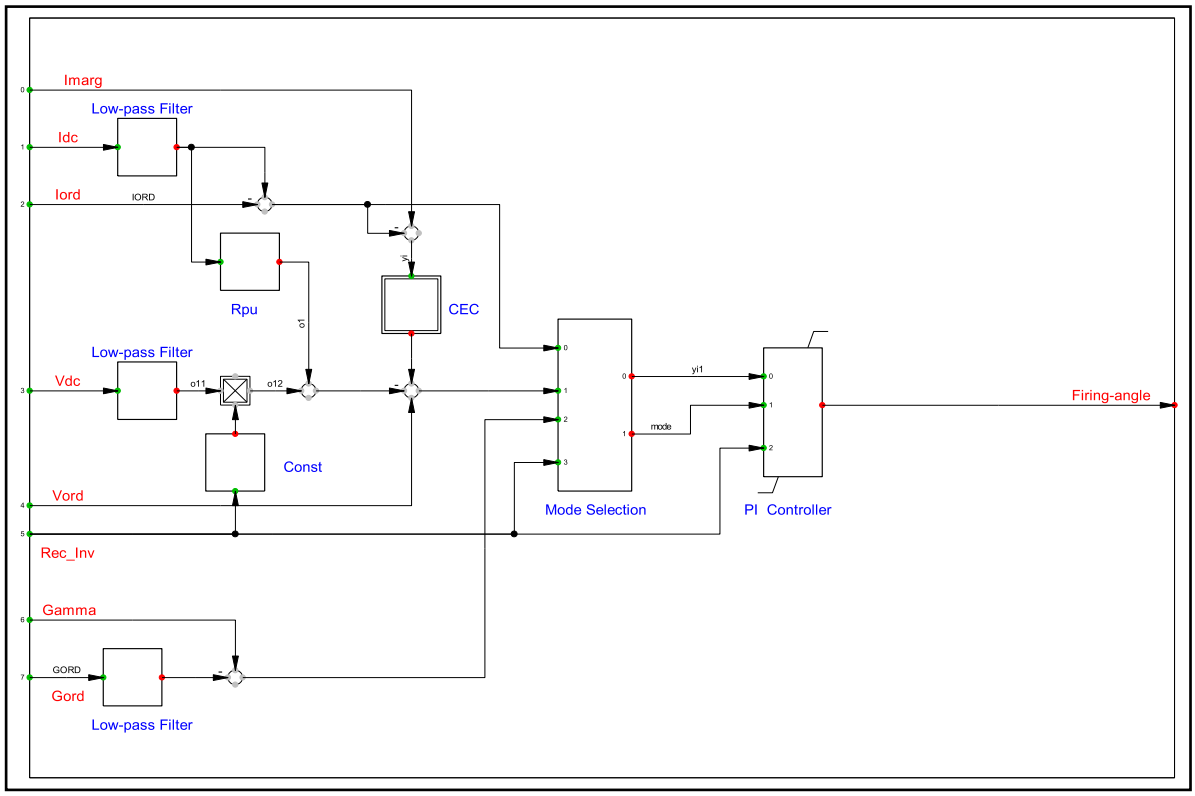

FigG.4 The Detailed Control System for One Pole of Bipolar CSC-HVDC System

Table-G.3 The Parameter of the Current Controller on Rectifier-side of CSC-HVDC System

Time Constant of Low-pass Filter for Firing Angle	0.01
Maximum Limit of Firing-angle	120 Deg
Minimum Limit of Firing-angle	3 Deg
Proportional Gain of the PI-Controller	0.25 p.u.
Time Constant of of the PI-Controller	0.02 p.u.
Current Margin	0.1 p.u.

Table-G.4 The Parameter of the Voltage Controller on Inverter-side of CSC-HVDC System

Time Constant of Low-pass Filter for Firing Angle	0.01
Proportional Gain of the PI-Controller	1.0 p.u.
Time Constant of of the PI-Controller	0.02 p.u.

Table-G.5 The Parameter of the Extinction-angle Controller on Inverter-side of CSC-HVDC System

Proportional Gain of the PI-Controller	0.5 p.u.
Time Constant of of the PI-Controller	0.04 p.u.
Maximum Limit of Firing-angle	90 Deg
Minimum Limit of Firing-angle	165 Deg

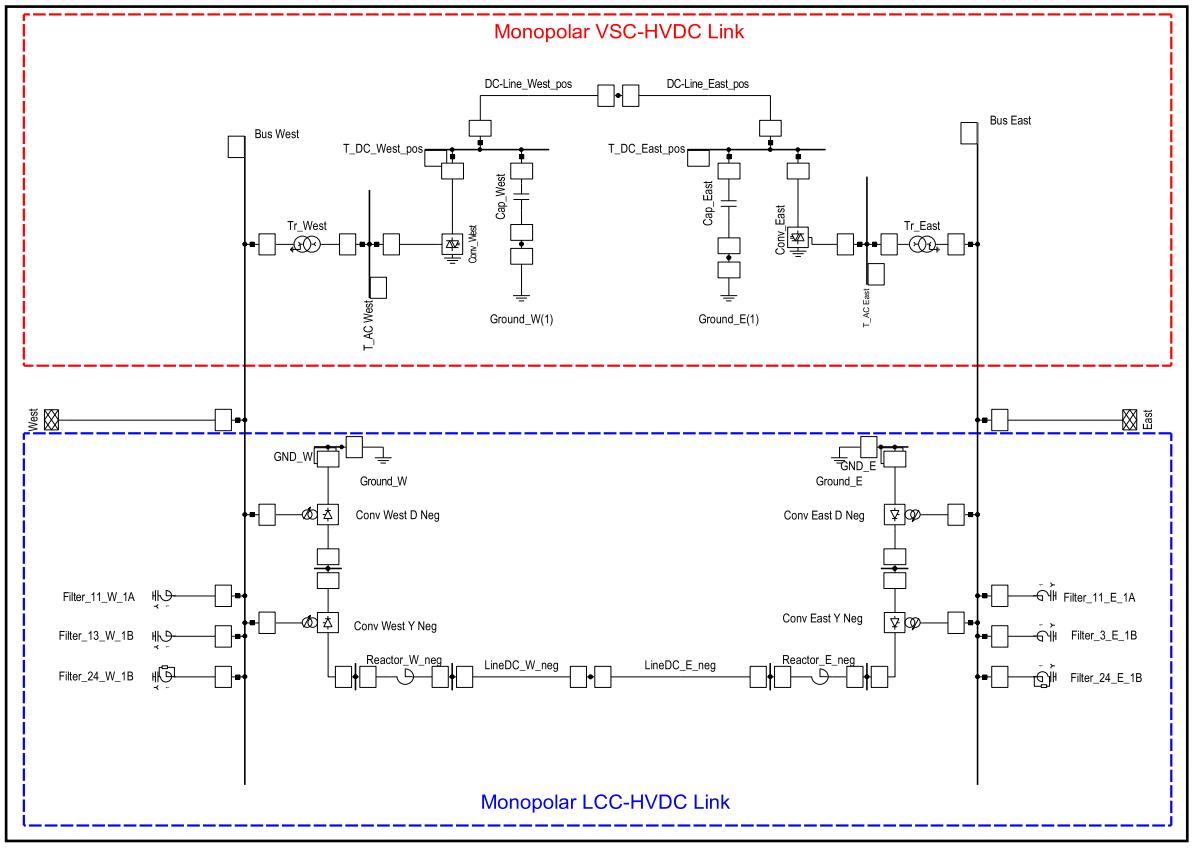

Fig-G.5 The Configuration of Hybrid CSC/VSC HDC System in DIgSILENT/PowerFactory

Table-G.6 The System Parameter of the Bipolar Hybrid HVDC System

System Rated Capacity of Each Link	500 MW
AC System Voltage	400 kV
DC Voltage of VSC-HVDC System	+250 kV
DC Voltage of CSC-HVDC System	-250 kV
System Frequency	50 Hz
Turns Ratio of Transformer of CSC-HVDC System	400 kV/110 kV
Turns Ratio of Transformer of CSC-HVDC System	400 kV/96 kV

Table-G.7 The Parameter of the Rectifier-side Control System of VSC-HVDC System

Time Constant of the First-stage Low-Pass Filter	0.005s
Proportional Gain of the *d*-axis *P* Controller	1.0 p.u.
Time Constant of the *d*-axis *P* Controller	0.01 s
Proportional Gain of the *q*-axis *Q* Controller	1.0 p.u.
Time Constant of the *q*-axis *Q* Controller	0.03 s
Proportional Gain of the *d*-axis Current Controller	2.0 p.u.
Time Constant of the *d*-axis Current Controller	0.01 s
Proportional Gain of the *q*-axis Current Controller	2.0 p.u.
Time Constant of the *q*-axis Current Controller	0.01 s

Table-G.8 The Parameter of the Inverter-side Control System of VSC-HVDC System

Time Constant of the First-stage Low-Pass Filter	0.005s
Proportional Gain of the *d*-axis V_{dc} Controller	10.0 p.u.
Time Constant of the *d*-axis V_{dc} Controller	0.01 s
Proportional Gain of the *q*-axis *Q* Controller	1.0 p.u.
Time Constant of the *q*-axis *Q* Controller	0.03 s
Proportional Gain of the *d*-axis Current Controller	0.5 p.u.
Time Constant of the *d*-axis Current Controller	0.01 s
Proportional Gain of the *q*-axis Current Controller	0.5 p.u.
Time Constant of the *q*-axis Current Controller	0.01 s

Appendix H

1. Details of Simulation System for Chapter 6

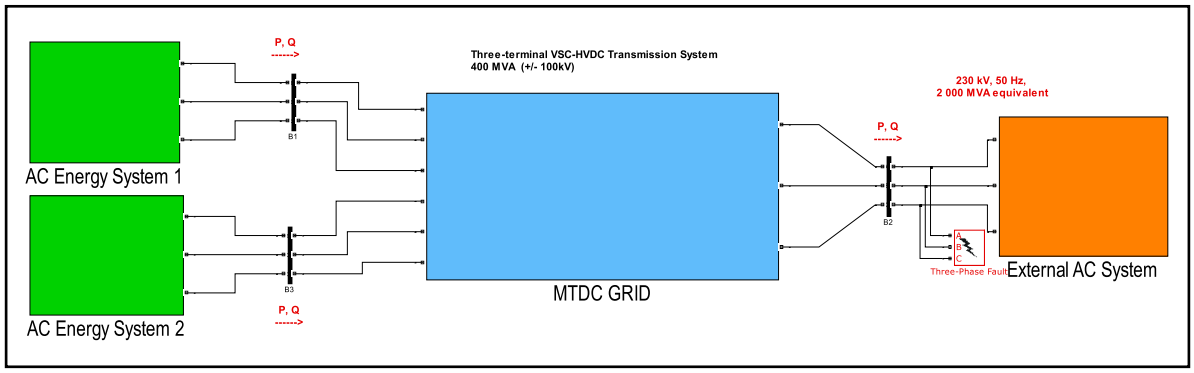

Fig-H.1 The Layout of the Three-terminal VSC-based HVDC Grid in MATLAB/SIMULINK

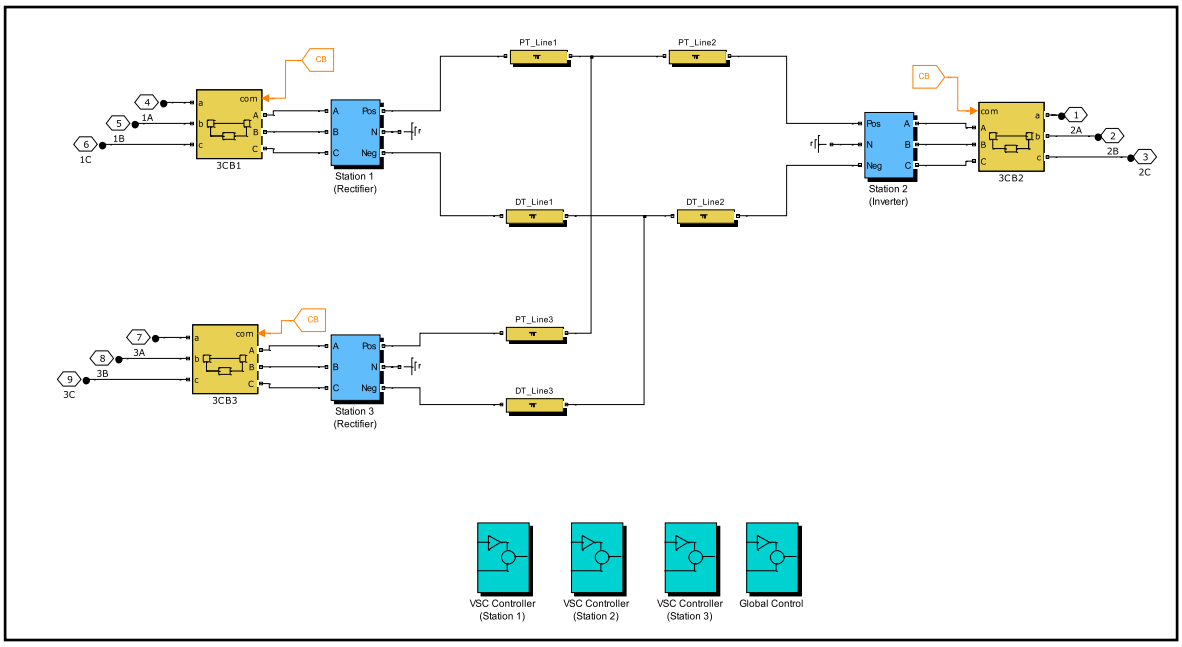

Fig-H.2 The Detailed Configuration of the Three-terminal HVDC Grid in MATLAB/SIMULINK

Table-H.1 The System Parameter of the Three-terminal VSC-Based HVDC Grid

System Rated Capacity	400 MVA
Magnitude of System AC Voltage	230 kV
Magnitude of System DC Voltage	± 100 kV
System Frequency	50 Hz
Turns Ratio of Transformer	230 kV/100 kV
Reactance of Transformer	0.15 p.u.
Reactance of AC Reactor	0.15 p.u.
Capacitance of the DC Capacitor	70 μF
DC Resistance Per Meter	1.3900e-002 ohm/m
Length of Each DC Cable	50 km

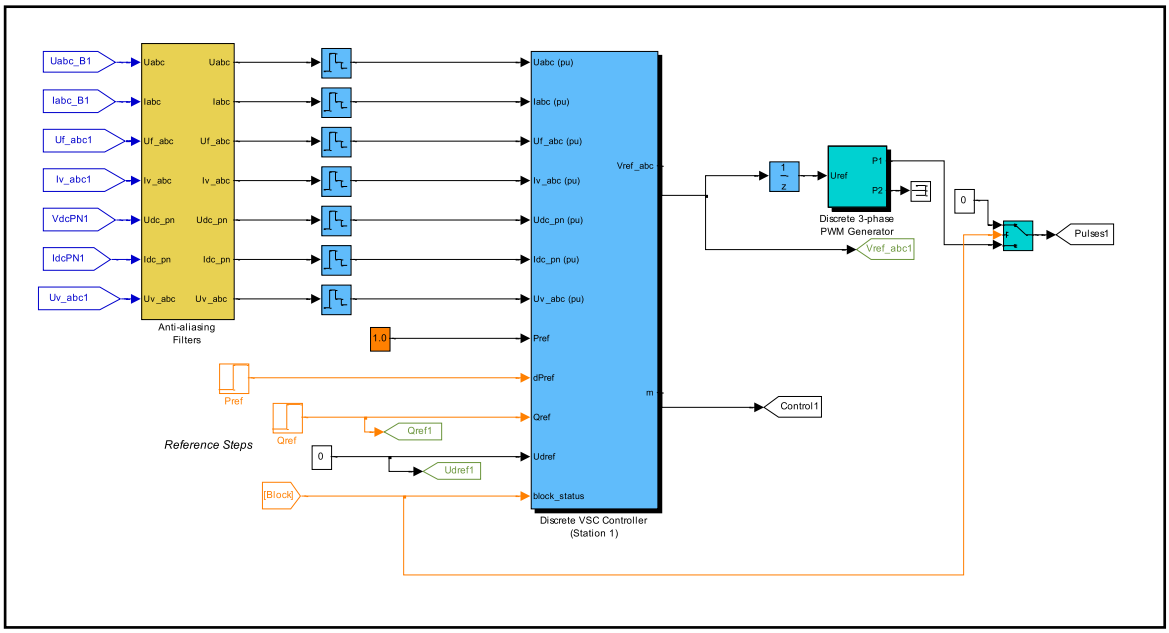

Fig-H.3 The General Structure of VSC Controller

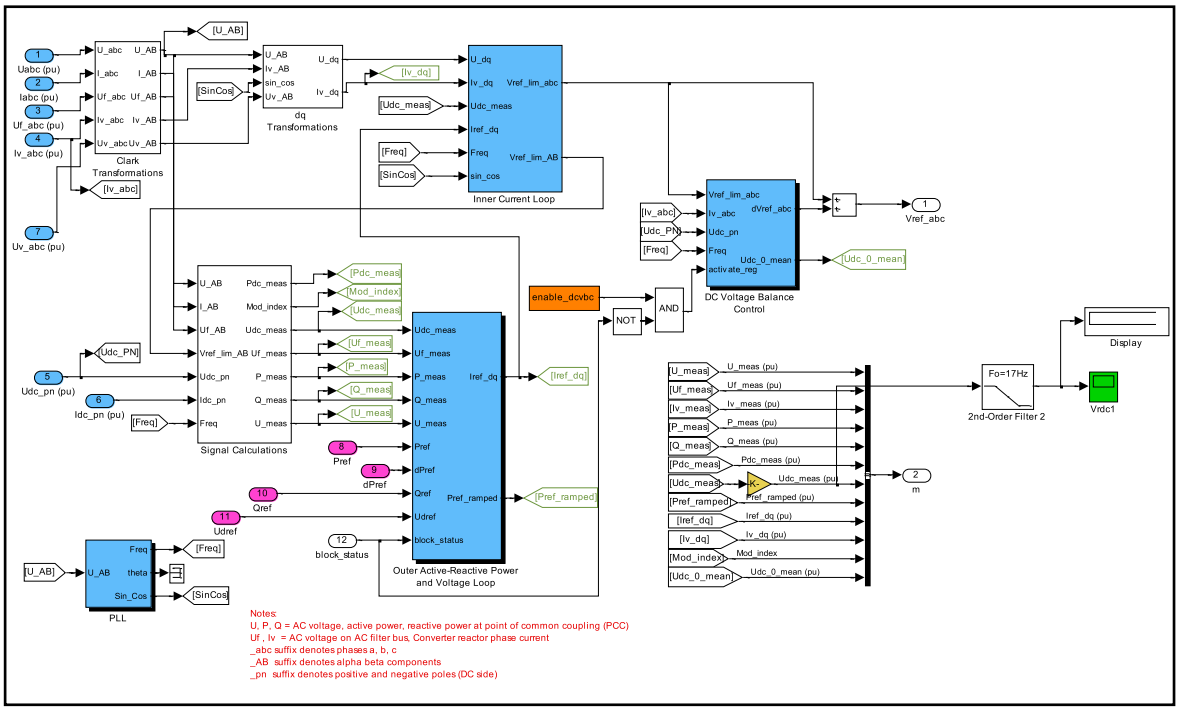

Fig-H.4 The Detailed Layout of VSC Controller

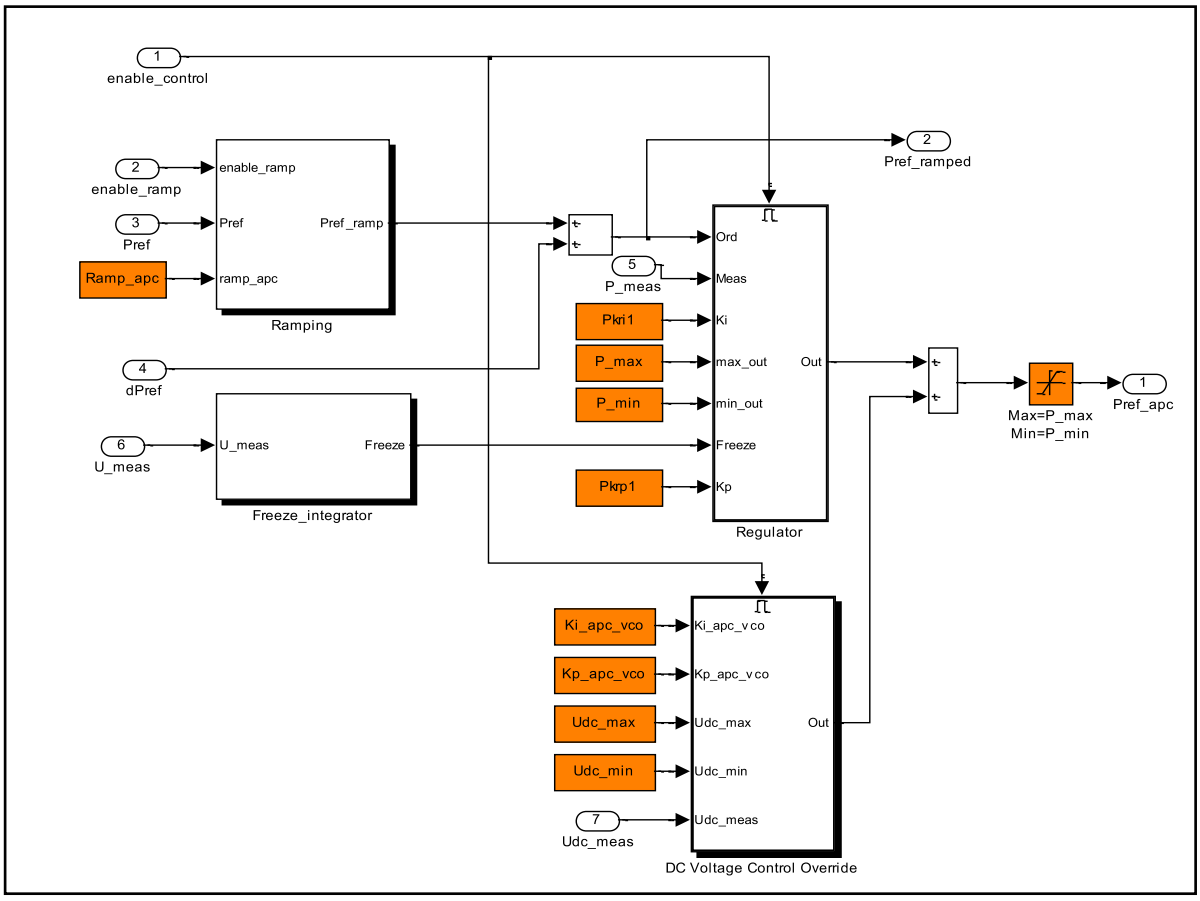

Fig-H.5 The Detailed Configuration of the *d*-axis Active Power Controller and DC Voltage Controller

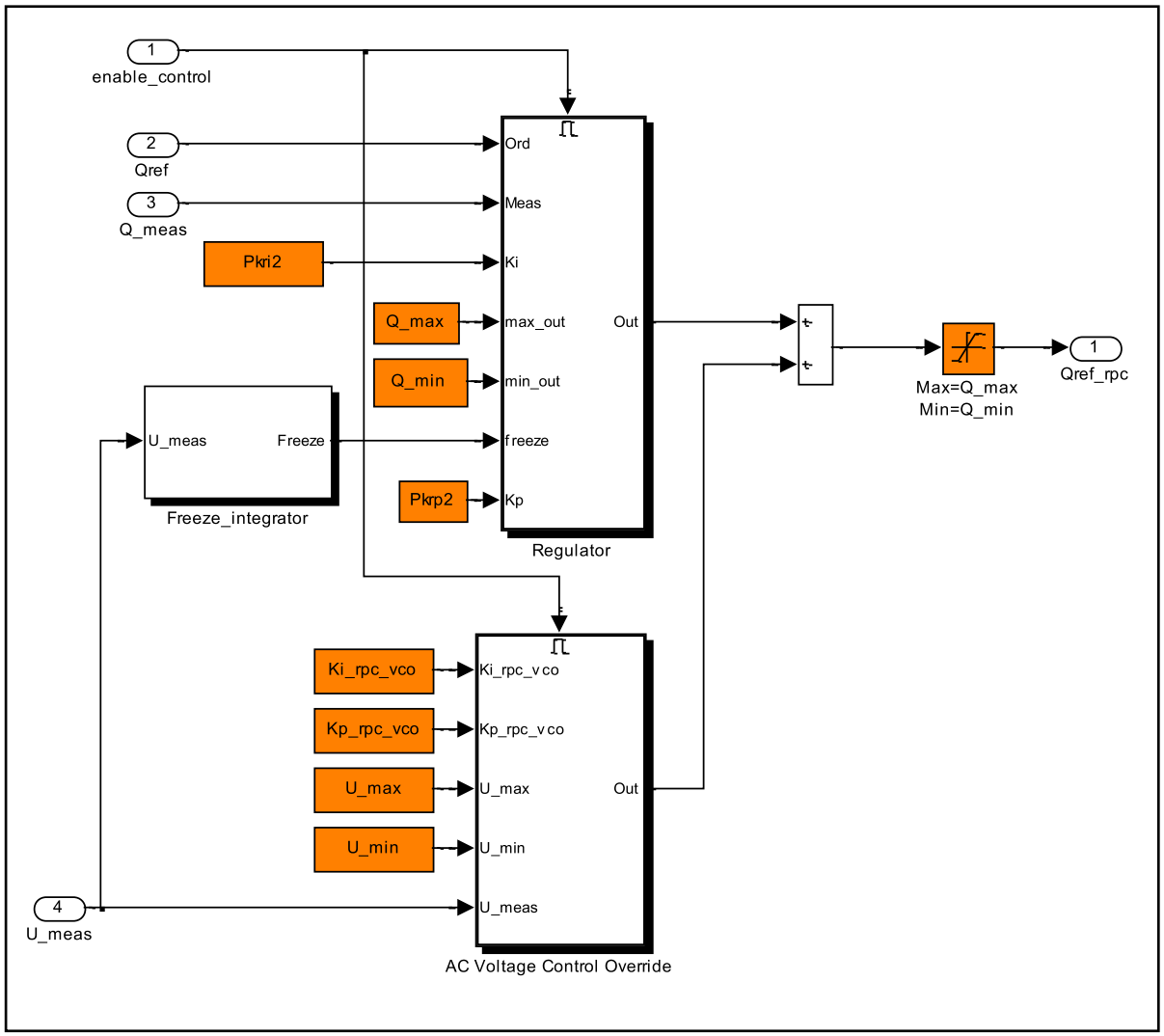

Fig-H.6 The Detailed Configuration of the *q*-axis Reactive Power Controller

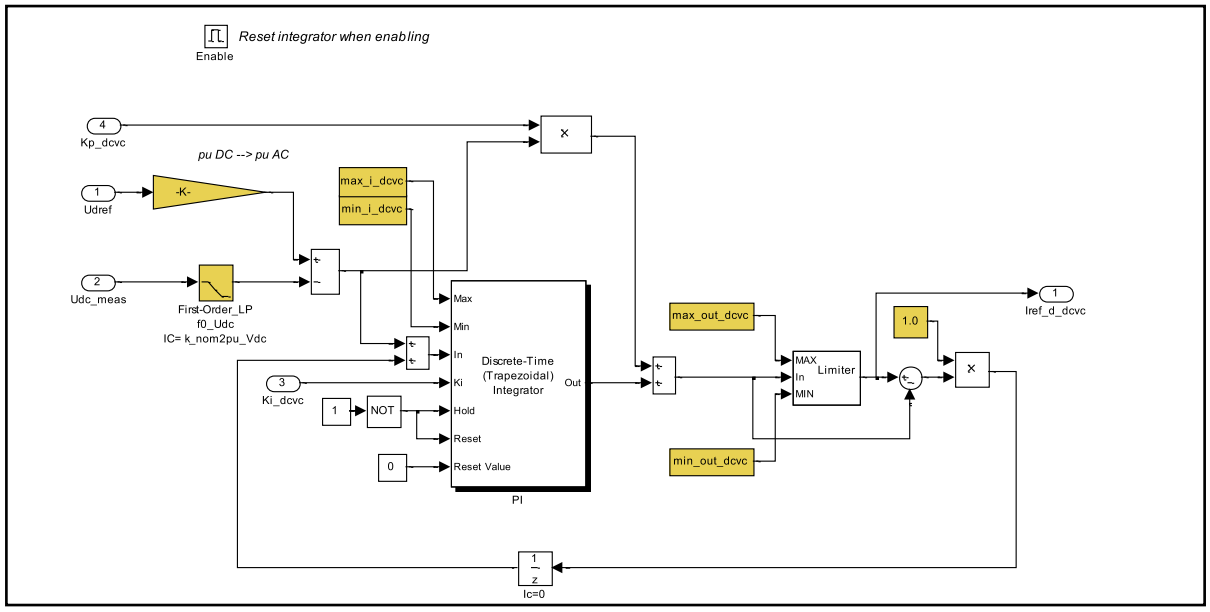

Fig-H.7 The Inner Current Cont roller with Decoupled Structure on Rectifier- and Inverter-side

List of References

[1] P. Kundur, *et al.*, "Definition and classification of power system stability IEEE/CIGRE joint task force on stability terms and definitions," *Power Systems, IEEE Transactions on,* vol. 19, pp. 1387-1401, 2004.

[2] P. Kundur, "Power System Stability and Control," ed New York: McGraw-Hill, 1994, pp. 473-580.

[3] G. Andersson, *et al.*, "Causes of the 2003 major grid blackouts in North America and Europe, and recommended means to improve system dynamic performance," *Power Systems, IEEE Transactions on,* vol. 20, pp. 1922-1928, 2005.

[4] "HVDC: Connecting to the Future," ed: Alston Grid, 2010, pp. 15-53.

[5] M. P. Bahrman and B. K. Johnson, "The ABCs of HVDC Transmission Technologies," *IEEE Power and Energy Mag,* vol. 5, pp. 32-44, 2007.

[6] M. Davies, *et al.*, "HVDC PLUS - Basics and Principle of Operation," Siemens Energy Sector,, Technical article,August, 2008.

[7] "HVDC–High Voltage Direct Current Power Transmission Unrivaled Practical Experience," Siemens AG Energy Sector,2011.

[8] "HVDC Classic - Reference list Thyristor valve projects and upgrades," ABB,Apr, 2012.

[9] "Our Electricity Transmission Network: A Vision for 2020," Electricity Networks Strategy GroupMar, 2009.

[10] ABB. *Gotland: the first commercial HVDC Light project*. Available: http://www.abb.com/industries/ap/db0003db004333/a34c41e0fe23b18cc125774a0033abbe.aspx

[11] F. A. R. A. Jowder and O. Boon-Teck, "Series compensation of radial power system by a combination of SSSC and dielectric capacitors," *Power Delivery, IEEE Transactions on,* vol. 20, pp. 458-465, 2005.

[12] H. Barati, *et al.*, "Application of Static Synchronous Series Compensator to Damp Sub-Synchronous Resonance," in *Power Electronics, Drives and Energy Systems, 2006. PEDES '06. International Conference on*, 2006, pp. 1-6.

[13] "The EU's Target for Renewable Energy: 20% by 2020," European Union Committee,Oct, 2008.

[14] "'Gone Green' a Scenario for 2020," National Grid,Jun, 2008.

[15] "UK Future Energy Scenarios: UK gas and electricity transmission," National Grid,Nov, 2011.

[16] L. Qianjin, *et al.*, "A novel active damping control of TCSC for SSR suppression in a radial corridor," in *Electric Utility Deregulation and Restructuring and Power Technologies, 2008. DRPT 2008. Third International Conference on*, 2008, pp. 136-142.

[17] "UK Offshore Wind Report 2012," The Crown Estate,May, 2012.

[18] "Round 3 offshore wind site selection at national and project levels," The Crown Estate,May, 2012.

[19] N. Fichaux, *et al.*, "Upwind Design limits and solutions for very large wind turbines," European Wind Energy Association, Technical Report,Mar, 2011.

[20] S. Cole, *et al.*, "A European Supergrid: Present State and Future Challenges," in *17th Power Systems Computatio Conference (PSCC)*, 2011, pp. 1-7.

[21] V. H. Dirk and G. Mehrdad, "Multi-terminal VSC HVDC for the European supergrid: Obstacles," *Renewable and Sustainable Energy Reviews,* vol. 14, pp. 3156-3163, 2010.

[22] A. L'Abbate, *et al.*, "The Role of Facts and HVDC in the Future Paneuropean Transmission System Development," in *2010 9th IET International Conference on AC and DC Power Transmission*, 2010, pp. 1-8.
[23] "Roadmap to the Supergrid Technologies," Friends of the Supergrid (FOSG),, Final Report,Mar, 2012.
[24] Y. X. Ni, *et al.*, "Dynamic Power System Theory and Analysis," ed Beijing: Tsinghua University Publishing House, 2002.
[25] "The Grid Code," National Grid 2013.
[26] "Grid Code - High and extra high voltage," Tennet TSO GmbH2012
[27] S. Gsänger and J.-D. Pitteloud, "The World Wind Energy Association 2011 Report," World Wind Energy Association,May, 2012.
[28] "List of Operational Offshore Wind Farms end 2007," European Wind Energy Association,2007.
[29] H. Li and Z. Chen, "Overview of Different Wind Generator Systems and Their Comparisons," *IET Renewable Power Generation,* vol. 2, pp. 123-138, 2008.
[30] "Siemens 6.0 MW Offshore Wind Turbine," Siemens AG Energy Sector,2011.
[31] H. Sugimoto, *et al.*, "Comparative studies of subsynchronous resonance damping schemes," in *Power System Technology, 2002. Proceedings. PowerCon 2002. International Conference on*, 2002, pp. 1472-1476 vol.3.
[32] J. M. Jonkman, "Dynamics Modeling and Loads Analysis of an Offshore Floating Wind Turbine," US National Renewable Energy Laboratory, Technical Report,Nov 2007.
[33] "The world's most remote offshore wind farm BorWin1 HVDC Light® offshore wind farm link," ABB,Feb, 2011.
[34] "WindFloat Project,," Principle PowerFeb. 2010.
[35] "Dynamic Modelling of Doubly-Fed Induction Machines Wind Generators," DIgSILENT GmbH,, Germany, Technical Documentation,August, 2003.
[36] V. Akhmatov, *et al.*, "Modelling and Tansient Stability of Large Wind Farms," *International Journal of Electrical Power & Energy Systems.,* vol. 25, pp. 123-144, Feb. 2003.
[37] Y. Coughlan, *et al.*, "Wind Turbine Modelling for Power System Stability Analysis - A System Operator Perspective," *IEEE Trans. Energy Convers.,* vol. 22, pp. 929-936, Aug. 2007.
[38] J. B. Ekanayake, *et al.*, "Comparison of 5th Order and 3rd Order Machine Models for Doubly Fed Induction Generator (DFIG) Wind Turbines," *Elect. Power Syst. Res.,* vol. 67, pp. 207-215, Dec. 2003.
[39] J. B. Ekanayake, *et al.*, "Dynamic Modeling of Doubly Fed Induction Generator Wind Turbines," *IEEE Trans. Power Syst.,* vol. 18, pp. 803-809, May. 2003.
[40] I. Erlich, *et al.*, "Modeling of Wind Turbines Based on Doubly-Fed Induction Generators for Power System Stability Studies," *iEEE Trans. Power Syst.,* vol. 22, pp. 909-919, Aug. 2007.
[41] P. Ledesma and J. Usaola, "Doubly Fed Induction Generator Model for Transient Stability Analysis," *IEEE Trans. Energy Convers.,* vol. 20, pp. 388-397, Jun. 2005.
[42] Y. Lei, *et al.*, "Modeling of the Wind Turbine with A Doubly Fed Induction Generator for Grid Integration Studies," *IEEE Trans. Energy Convers.,* vol. 21, pp. 257-264, Mar. 2006.
[43] F. Mei and B. C. Pal, "Modelling and Small-signal Analysis of a Grid Connected Doubly-fed Induction Generator," in *2005 IEEE Power Engineering Society General Meeting*, 2005, pp. 2101-2108.

[44] J. G. Slootweg, *et al.*, "General Model for Representing Variable Speed Wind Turbines in Power System Dynamics Simulations," *IEEE Trans. Power Syst.,* vol. 18, pp. 144-151, Feb. 2003.
[45] A. Tapia, *et al.*, "Modeling and Control of a Wind Turbine Driven Doubly Fed Induction Generator," *IEEE Trans. Energy Convers.,* vol. 18, pp. 194-204, Jun. 2003.
[46] L. Xu and Y. Wang, "Dynamic Modeling and Control of DFIG-Based Wind Turbines under Unbalanced Network Conditions," *IEEE Trans. Power Syst.,* vol. 22, pp. 314-323, Feb. 2007.
[47] F. Wu, "Modelling and Control of Wind and Wave Energy Conversion Systems," Doctor of Philosophy, School of Electronic, Electrical and Computer Engineering, University of Birmingham, Birmingham, 2009.
[48] G. Abad, *et al.*, "Direct Power Control of Doubly-Fed-Induction-Generator-Based Wind Turbines Under Unbalanced Grid Voltage," *IEEE Trans. Power Electron.,* vol. 25, pp. 442-452, Feb. 2010.
[49] F. M. Hughes, *et al.*, "Control of DFIG-based Wind Generation for Power Network Support," *IEEE Trans. Power Syst.,* vol. 20, pp. 1958-1966, Nov. 2005.
[50] F. Wu, *et al.*, "Decentralized Nonlinear Control of Wind Turbine With Doubly Fed Induction Generator," *iEEE Trans. Power Syst.,* vol. 23, pp. 613-621, May. 2008.
[51] M. Yamamoto and O. Motoyoshi, "Active and Reactive Power Control for Doubly-Fed Wound Rotor Induction Generator," *IEEE Trans. Power Electron. ,* vol. 6, pp. 624-629, Oct. 1991.
[52] L. Yang, *et al.*, "Optimal Controller Design of a Doubly-Fed Induction Generator Wind Turbine System for Small Signal Stability Enhancement," *Proc. Inst. Elect. Eng., Gen., Transm., Distrib.,* vol. 4, pp. 579-597, May. 2010.
[53] O. Anaya-Lara, *et al.*, "Contribution of DFIG-based wind farms to power system short-term frequency regulation," *Proc. Inst. Elect. Eng., Gen., Transm., Distrib.,* vol. 153, pp. 164-170, Mar. 2006.
[54] S. Engelhardt, *et al.*, "Reactive Power Capability of Wind Turbines Based on Doubly Fed Induction Generators," *IEEE Trans. Energy Convers.,* vol. 26, pp. 364-372, Mar. 2011.
[55] J. Morren and S. W. H. de Haan, "Short-Circuit Current of Wind Turbines with Doubly Fed Induction Generator," *IEEE Trans. Energy Convers.,* vol. 22, pp. 174-180, Mar. 2007.
[56] H. Huang, *et al.*, "Small-signal modelling and analysis of wind turbine with direct drive permanent magnet synchronous generator connected to power grid," *Renewable Power Generation, IET,* vol. 6, pp. 48-58, 2012.
[57] F. Wu, *et al.*, "Small Signal Stability Analysis and Control of the Wind Turbine With the Direct-Drive Permanent Magnet Generator Integrated to the Grid," *Electric Power Systems Research,* vol. 79, pp. 1661-1667, 2009.
[58] Y. Errami, *et al.*, "Modelling and control strategy of PMSG based variable speed wind energy conversion system," in *Multimedia Computing and Systems (ICMCS), 2011 International Conference on*, 2011, pp. 1-6.
[59] E. N. Lopez-Ortiz, *et al.*, "Modelling of a wind turbine with permanent magnet synchronous generator," in *North American Power Symposium (NAPS), 2012*, 2012, pp. 1-6.
[60] Y. Ming, *et al.*, "Modeling of the Wind Turbine with a Permanent Magnet Synchronous Generator for Integration," in *Power Engineering Society General Meeting, 2007. IEEE*, 2007, pp. 1-6.

[61] M. G. Molina, *et al.*, "Dynamic modeling of wind farms with variable-speed direct-driven PMSG wind turbines," in *Transmission and Distribution Conference and Exposition: Latin America (T&D-LA), 2010 IEEE/PES*, 2010, pp. 816-823.

[62] Y. Xiao, *et al.*, "Dynamic modeling and equivalent description of directly driven wind power system," in *Advanced Power System Automation and Protection (APAP), 2011 International Conference on*, 2011, pp. 906-910.

[63] Q. Zhipeng, *et al.*, "Modeling and control of diode rectifier fed PMSG based wind turbine," in *Electric Utility Deregulation and Restructuring and Power Technologies (DRPT), 2011 4th International Conference on*, 2011, pp. 1384-1388.

[64] M. Chinchilla, *et al.*, "Control of permanent-magnet generators applied to variable-speed wind-energy systems connected to the grid," *Energy Conversion, IEEE Transactions on,* vol. 21, pp. 130-135, 2006.

[65] M. E. Haque, *et al.*, "A Novel Control Strategy for a Variable-Speed Wind Turbine With a Permanent-Magnet Synchronous Generator," *Industry Applications, IEEE Transactions on,* vol. 46, pp. 331-339, 2010.

[66] S. M. Muyeen, *et al.*, "A Variable Speed Wind Turbine Control Strategy to Meet Wind Farm Grid Code Requirements," *Power Systems, IEEE Transactions on,* vol. 25, pp. 331-340, 2010.

[67] S. M. Muyeen, *et al.*, "Operation and Control of HVDC-Connected Offshore Wind Farm," *Sustainable Energy, IEEE Transactions on,* vol. 1, pp. 30-37, 2010.

[68] A. A. Daoud, *et al.*, "Control scheme of PMSG based wind turbine for utility network connection," in *Environment and Electrical Engineering (EEEIC), 2011 10th International Conference on*, 2011, pp. 1-5.

[69] K. Tan and S. Islam, "Optimum control strategies in energy conversion of PMSG wind turbine system without mechanical sensors," *Energy Conversion, IEEE Transactions on,* vol. 19, pp. 392-399, 2004.

[70] L. Shuhui, *et al.*, "Optimal and Direct-Current Vector Control of Direct-Driven PMSG Wind Turbines," *Power Electronics, IEEE Transactions on,* vol. 27, pp. 2325-2337, 2012.

[71] Q. Chen, *et al.*, "Robust control based on quantitative feedback theory for PMSG wind power generation system," in *Control and Decision Conference, 2009. CCDC '09. Chinese*, 2009, pp. 2122-2127.

[72] Z. Shao, *et al.*, "Design of a Robust Grid Interface System for PMSG-Based Wind Turbine Generators," *Industrial Electronics, IEEE Transactions on,* vol. 58, pp. 316-328, 2011.

[73] W. Mian, *et al.*, "A hybrid LVRT control scheme for PMSG wind power system," in *Power Electronics and Motion Control Conference (IPEMC), 2012 7th International*, 2012, pp. 1173-1177.

[74] A. Abedini and A. Nasiri, "PMSG Wind Turbine Performance Analysis During Short Circuit Faults," in *Electrical Power Conference, 2007. EPC 2007. IEEE Canada*, 2007, pp. 160-165.

[75] A. D. Hansen and G. Michalke, "Multi-Pole Permanent Magnet Synchronous Generator Wind Turbines' Grid Support Capability in Uninterrupted Operation During Grid Faults," *IET Renewable Power Generation,* vol. 3, pp. 333-348, 2009.

[76] J. F. Conroy and R. Watson, "Low-voltage ride-through of a full converter wind turbine with permanent magnet generator," *Renewable Power Generation, IET,* vol. 1, pp. 182-189, 2007.

[77] K. Ki-Hong, *et al.*, "LVRT Scheme of PMSG Wind Power Systems Based on Feedback Linearization," *Power Electronics, IEEE Transactions on,* vol. 27, pp. 2376-2384, 2012.

[78] G. Ramtharan, *et al.*, "Fault ride through of fully rated converter wind turbines with AC and DC transmission," *Renewable Power Generation, IET,* vol. 3, pp. 426-438, 2009.
[79] N. P. W. Strachan and D. Jovcic, "Stability of a Variable-Speed Permanent Magnet Wind Generator With Weak AC Grids," *Power Delivery, IEEE Transactions on,* vol. 25, pp. 2779-2788, 2010.
[80] W. W. Price, *et al.*, "Large-scale System Testing of a Power System Dynamic Equivalencing Program," *IEEE Trans. Power Syst,* vol. 13, pp. 768-774, 1998.
[81] L. Wang, *et al.*, "Dynamic Reduction of Large Power Systems for Stability Studies," *IEEE Trans. Power Syst,* vol. 12, pp. 889-895, 1997.
[82] S. E. M. de Oliveira and J. F. de Queiroz, "Modal dynamic equivalent for electric power systems. I. Theory," *Power Systems, IEEE Transactions on,* vol. 3, pp. 1723-1730, 1988.
[83] S. E. M. de Oliveira and A. G. Massaud, "Modal dynamic equivalent for electric power systems. II. Stability simulation tests," *Power Systems, IEEE Transactions on,* vol. 3, pp. 1731-1737, 1988.
[84] J. C. Cepeda, *et al.*, "Identification of dynamic equivalents based on heuristic optimization for smart grid applications," in *Evolutionary Computation (CEC), 2012 IEEE Congress on*, 2012, pp. 1-8.
[85] T. Singhavilai, *et al.*, "Identification of the dynamic equivalent of a power system," in *Universities Power Engineering Conference (UPEC), 2009 Proceedings of the 44th International*, 2009, pp. 1-5.
[86] Y. Q. Jin and P. Ju, "Dynamic equivalent modeling of FSIG based wind farm according to slip coherency," in *Sustainable Power Generation and Supply, 2009. SUPERGEN '09. International Conference on*, 2009, pp. 1-7.
[87] Z. J. Meng, "An improved equivalent wind method for the aggregation of DFIG wind turbines," in *Power System Technology (POWERCON), 2010 International Conference on*, 2010, pp. 1-6.
[88] Z. J. Meng and F. Xue, "An Investigation of the Equivalent Wind Method for the Aggregation of DFIG Wind Turbines," in *Power and Energy Engineering Conference (APPEEC), 2010 Asia-Pacific*, 2010, pp. 1-6.
[89] Z. J. Meng and F. Xue, "Improving the performance of the equivalent wind method for the aggregation of DFIG wind turbines," in *Power and Energy Society General Meeting, 2011 IEEE*, 2011, pp. 1-6.
[90] Z. J. Meng, *et al.*, "Applications of an improved equivalent wind method for the aggregation of DFIG wind turbines," in *Electric Utility Deregulation and Restructuring and Power Technologies (DRPT), 2011 4th International Conference on*, 2011, pp. 151-155.
[91] L. M. Fernandez, *et al.*, "Aggregation of doubly fed induction generators wind turbines under different incoming wind speeds," in *Power Tech, 2005 IEEE Russia*, 2005, pp. 1-6.
[92] L. M. Fernandez, *et al.*, "Reduced model of DFIGs wind farms using aggregation of wind turbines and equivalent wind," in *Electrotechnical Conference, 2006. MELECON 2006. IEEE Mediterranean*, 2006, pp. 881-884.
[93] Z. Xu, *et al.*, "Aggregation of doubly-fed induction generator based wind farm considering storage device and coordinated control strategy," in *Advanced Power System Automation and Protection (APAP), 2011 International Conference on*, 2011, pp. 1013-1018.
[94] Z. Sizhen, *et al.*, "Coherency-based equivalencing method for large wind farms," in *Power & Energy Society General Meeting, 2009. PES '09. IEEE*, 2009, pp. 1-8.

[95] Y. Yang, *et al.*, "Aggregating DFIGS in power system online analysis," in *Power Engineering and Automation Conference (PEAM), 2011 IEEE*, 2011, pp. 63-67.
[96] J. Conroy and R. Watson, "Aggregate modelling of wind farms containing full-converter wind turbine generators with permanent magnet synchronous machines: transient stability studies," *Renewable Power Generation, IET,* vol. 3, pp. 39-52, 2009.
[97] A. M. Alsseid, *et al.*, "Small signal modelling and stability analysis of multiterminal VSC-HVDC," in *Power Electronics and Applications (EPE 2011), Proceedings of the 2011-14th European Conference on*, 2011, pp. 1-10.
[98] Z. Lidong, *et al.*, "Modeling and Control of VSC-HVDC Links Connected to Island Systems," *Power Systems, IEEE Transactions on,* vol. 26, pp. 783-793, 2011.
[99] K. R. Padiyar and N. Prabhu, "Modelling, control design and analysis of VSC based HVDC transmission systems," in *Power System Technology, 2004. PowerCon 2004. 2004 International Conference on*, 2004, pp. 774-779 Vol.1.
[100] Y. Wei, *et al.*, "Modeling and simulation of VSC-HVDC with dynamic phasors," in *Electric Utility Deregulation and Restructuring and Power Technologies, 2008. DRPT 2008. Third International Conference on*, 2008, pp. 1416-1421.
[101] C. Zheng, *et al.*, "Dynamic Modeling and Transient Simulation for VSC based HVDC in Multi-Machine System," in *Power System Technology, 2006. PowerCon 2006. International Conference on*, 2006, pp. 1-7.
[102] G. O. Kalcon, *et al.*, "Small-Signal Stability Analysis of Multi-Terminal VSC-Based DC Transmission Systems," *Power Systems, IEEE Transactions on,* vol. 27, pp. 1818-1830, 2012.
[103] P. Rault, *et al.*, "Method for small signal stability analysis of VSC-MTDC grids," in *Power and Energy Society General Meeting, 2012 IEEE*, 2012, pp. 1-7.
[104] L. Gengyin, *et al.*, "Decoupling Control for Multiterminal VSC-HVDC Based Wind Farm Interconnection," in *Power Engineering Society General Meeting, 2007. IEEE*, 2007, pp. 1-6.
[105] R. Song, *et al.*, "VSCs based HVDC and its control strategy," in *Transmission and Distribution Conference and Exhibition: Asia and Pacific, 2005 IEEE/PES*, 2005, pp. 1-6.
[106] H. F. Latorre, *et al.*, "Active and reactive power control of a VSC-HVdc," *Electric Power Systems Research,* vol. 78, pp. 1756-1763, 2008.
[107] J. Pan, *et al.*, "VSC-HVDC Control and Application in Meshed AC Networks," in *IEEE Power and Energy Society (PES) General Meeting*, 2006.
[108] D. Jovcic, "Interconnecting offshore wind farms using multiterminal VSC-based HVDC," in *Power Engineering Society General Meeting, 2006. IEEE*, 2006, p. 7 pp.
[109] X. Lie, *et al.*, "Multi-terminal DC transmission systems for connecting large offshore wind farms," in *Power and Energy Society General Meeting - Conversion and Delivery of Electrical Energy in the 21st Century, 2008 IEEE*, 2008, pp. 1-7.
[110] C. Du, *et al.*, "Comparison of Different Frequency Controllers for a VSC-HVDC Supplied System," *Power Delivery, IEEE Transactions on,* vol. 23, pp. 2224-2232, 2008.
[111] D. Tao, *et al.*, "Coordinated control strategy for multi-terminal VSC-HVDC based wind farm interconnection," in *Sustainable Power Generation and Supply, 2009. SUPERGEN '09. International Conference on*, 2009, pp. 1-6.
[112] X. Lie, *et al.*, "Grid Integration of Large DFIG-Based Wind Farms Using VSC Transmission," *Power Systems, IEEE Transactions on,* vol. 22, pp. 976-984, 2007.
[113] C. Feltes, *et al.*, "Enhanced Fault Ride-Through Method for Wind Farms Connected to the Grid Through VSC-Based HVDC Transmission," *Power Systems, IEEE Transactions on,* vol. 24, pp. 1537-1546, 2009.

[114] B. R. Andersen and X. Lie, "Hybrid HVDC system for power transmission to island networks," *Power Delivery, IEEE Transactions on,* vol. 19, pp. 1884-1890, 2004.
[115] Z. Honglin*, et al.*, "Modeling, Analysis, and Control for the Rectifier of Hybrid HVdc Systems for DFIG-Based Wind Farms," *Energy Conversion, IEEE Transactions on,* vol. 26, pp. 340-353, 2011.
[116] H. Zhou*, et al.*, "Control of a hybrid high-voltage DC connection for large doubly fed induction generator-based wind farms," *Renewable Power Generation, IET,* vol. 5, pp. 36-47, 2011.
[117] C. Xia*, et al.*, "Integrating Wind Farm to the Grid Using Hybrid Multiterminal HVDC Technology," *Industry Applications, IEEE Transactions on,* vol. 47, pp. 965-972, 2011.
[118] J. P. Kjærgaard*, et al.*, "Bipolar Operation of an HVDC VSC Converter with an LCC Converter," in *CIGRÉ 2012 San Francisco Colloquium: HVDC and Power Electronic Systems for Overhead Line and Insulated Cable Applications*, San Francisco, 2012, pp. 1-7.
[119] Z. Lidong*, et al.*, "Interconnection of Two Very Weak AC Systems by VSC-HVDC Links Using Power-Synchronization Control," *Power Systems, IEEE Transactions on,* vol. 26, pp. 344-355, 2011.
[120] B. Parkhideh and S. Bhattacharya, "Vector-Controlled Voltage-Source-Converter-Based Transmission Under Grid Disturbances," *Power Electronics, IEEE Transactions on,* vol. 28, pp. 661-672, 2013.
[121] S. Gordon, "Supergrid to the rescue," *Power Engineer,* vol. 20, pp. 30-33, 2006.
[122] A. H. Ahmad and A. A. Abdelqader, "Power system stabilizer design using real-coded genetic algorithm," in *Control, Instrumentation and Automation (ICCIA), 2011 2nd International Conference on*, 2011, pp. 25-31.
[123] A. Al-Hinai, "Dynamic stability enhancement using Genetic Algorithm Power System Stabilizer," in *Power System Technology (POWERCON), 2010 International Conference on*, 2010, pp. 1-7.
[124] P. Bera*, et al.*, "Design of P-I-D power system stabilizer for multimachine system," in *India Annual Conference, 2004. Proceedings of the IEEE INDICON 2004. First*, 2004, pp. 446-450.
[125] D. Devaraj and B. Selvabala, "Real-coded genetic algorithm and fuzzy logic approach for real-time tuning of proportional-integral - derivative controller in automatic voltage regulator system," *Generation, Transmission & Distribution, IET,* vol. 3, pp. 641-649, 2009.
[126] A. Jalilvand and M. R. S. Tirtashi, "Design of output feedback controller for PSS and TCSC by GA to improve the damping of power system oscillations," in *Power and Energy (PECon), 2010 IEEE International Conference on*, 2010, pp. 178-182.
[127] A. Phiri and K. A. Folly, "Application of Breeder GA to power system controller design," in *Swarm Intelligence Symposium, 2008. SIS 2008. IEEE*, 2008, pp. 1-5.
[128] B. Selvabala and D. Devaraj, "Co-ordinated tuning of AVR-PSS using differential evolution algorithm," in *IPEC, 2010 Conference Proceedings*, 2010, pp. 439-444.
[129] S. Shajari*, et al.*, "Coordinate control of TCSC based GA controller with PSS for stability improving in single machine system," in *Environment and Electrical Engineering (EEEIC), 2011 10th International Conference on*, 2011, pp. 1-4.
[130] S. Sheetekela and K. A. Folly, "Breeder Genetic Algorithm for Power System Stabilizer design," in *Evolutionary Computation (CEC), 2010 IEEE Congress on*, 2010, pp. 1-7.

[131] L. Zhijian, *et al.*, "Coordination control between PSS and SVC based on improved genatic - tabu hybrid algorithm," in *Sustainable Power Generation and Supply, 2009. SUPERGEN '09. International Conference on*, 2009, pp. 1-5.
[132] R. Eberhart and J. Kennedy, "A new optimizer using particle swarm theory," in *Micro Machine and Human Science, 1995. MHS '95., Proceedings of the Sixth International Symposium on*, 1995, pp. 39-43.
[133] J. Kennedy and R. Eberhart, "Particle swarm optimization," in *Neural Networks, 1995. Proceedings., IEEE International Conference on*, 1995, pp. 1942-1948 vol.4.
[134] M. A. Abido, "Optimal design of power-system stabilizers using particle swarm optimization," *Energy Conversion, IEEE Transactions on,* vol. 17, pp. 406-413, 2002.
[135] S. Panda and N. P. Padhy, "Comparison of particle swarm optimization and genetic algorithm for FACTS-based controller design," *Applied Soft Computing,* vol. 8, pp. 1418-1427, 2008.
[136] F. Wu, *et al.*, "Small signal stability analysis and optimal control of a wind turbine with doubly fed induction generator," *Proc. Inst. Elect. Eng., Gen., Transm., Distrib.,* vol. 1, pp. 751-760, Sep. 2007.
[137] Z. Yu and L. Chongru, "Parameters Optimal Design of HVDC PI Controller Based on APSO Algorithm," in *Power and Energy Engineering Conference (APPEEC), 2012 Asia-Pacific*, 2012, pp. 1-4.
[138] Z. Chengyong, *et al.*, "Parameters Optimization of VSC-HVDC Control System Based on Simplex Algorithm," in *Power Engineering Society General Meeting, 2007. IEEE*, 2007, pp. 1-7.
[139] J. Zhuo and Z. Chengyong, "Parameters optimization of HVDC control system based on Simplex Algorithm in RTDS," in *Critical Infrastructure (CRIS), 2010 5th International Conference on*, 2010, pp. 1-6.
[140] "GE 4.1-113 Offshore Wind Turbine," GE Energy2011.
[141] "PWM Converter " DIgSILENT GmbH,, Germany, Technical Documentation,August, 2008.
[142] L. Xu and S. Islam, "Reliability Issues of Offshore Wind Farm Topology," in *Proceedings of the 2008 10th International Conference on Probabilistic Methods Applied to Power Systems (PMAPS)*, 2008, pp. 1-5.
[143] E. Muljadi, *et al.*, "Equivalencing the Collector System of a Large Wind Power Plant," in *2006 IEEE PES General Meeting*, 2006, pp. 1-9.
[144] M. Marques, *et al.*, "Connection of offshore wind parks: HVAC and HVDC-LCC links with STATCOM," in *Electrical Power Quality and Utilisation (EPQU), 2011 11th International Conference on*, 2011, pp. 1-6.
[145] J.-H. Ying, *et al.*, "Improvement of subsynchronous torsional damping using VSC HVDC," in *Power System Technology, 2002. Proceedings. PowerCon 2002. International Conference on*, 2002, pp. 998-1003 vol.2.
[146] M. Durrant, *et al.*, "A Comparison of LMI and GA Based Robust Controller Designs for VSC HVDC," in *Decision and Control, 2006 45th IEEE Conference on*, 2006, pp. 3990-3995.
[147] A. Farag, *et al.*, "Robust control of a VSC HVDC terminal attached to a weak AC system," in *Control Applications, 2003. CCA 2003. Proceedings of 2003 IEEE Conference on*, 2003, pp. 173-177 vol.1.
[148] A. Moharana and P. K. Dash, "Input-Output Linearization and Robust Sliding-Mode Controller for the VSC-HVDC Transmission Link," *Power Delivery, IEEE Transactions on,* vol. 25, pp. 1952-1961, 2010.

[149] N. Nayak, *et al.*, "A robust control strategies to improve transient stability in VSC-HVDC based interconnected power systems," in *Energy, Automation, and Signal (ICEAS), 2011 International Conference on*, 2011, pp. 1-8.
[150] H. S. Ramadan, *et al.*, "On the robustness of VSC-HVDC systems controllers under parameters uncertainties," in *Power Symposium, 2008. NAPS '08. 40th North American*, 2008, pp. 1-8.
[151] H. S. Ramadan, *et al.*, "A robust stabilizing nonlinear control design for VSC-HVDC systems: A comparative study," in *Industrial Technology, 2009. ICIT 2009. IEEE International Conference on*, 2009, pp. 1-6.
[152] L. Wenze and C. Zexiang, "Model analysis and robust control design of VSC-HVDC converter with dq0 axis," in *Electric Utility Deregulation and Restructuring and Power Technologies, 2008. DRPT 2008. Third International Conference on*, 2008, pp. 1792-1796.
[153] Wikipedia. *PID controller*. Available: http://en.wikipedia.org/wiki/PID_controller
[154] D. C. Kong and X. P. Zhang, "Transient stability analysis and optimal coordinated control of multi-terminal VSC-HVDC based offshore wind farms," in *Renewable Power Generation (RPG 2011), IET Conference on*, 2011, pp. 1-6.
[155] P. Mc Namara and G. Lightbody, "PSO optimized PID parameters for coupled HVDC control," in *Signals and Systems Conference (ISSC 2010), IET Irish*, 2010, pp. 30-35.
[156] O. Gomis-Bellmunt, *et al.*, "Topologies of multiterminal HVDC-VSC transmission for large offshore wind farms," *Electric Power Systems Research,* vol. 81, pp. 271-281, 2011.
[157] H. Lu, *et al.*, "Experimental study of a new hybrid PSO with mutation for economic dispatch with non-smooth cost function," *International Journal of Electrical Power & Energy Systems,* vol. 32, pp. 921-935, 2010.
[158] M. A. Mannan, *et al.*, "Fuzzy-logic-based self-tuning PI controller for speed control of indirect field-oriented induction motor drive," in *SICE 2004 Annual Conference*, 2004, pp. 466-470 vol. 1.
[159] L. G. Franquelo, *et al.*, "The Age of Multilevel Converters Arrives," *IEEE Industrial Electronics Mag.,* vol. 2, pp. 28-39, Jul. 2008.
[160] J. Candelaria and J.-D. Park, "VSC-HVDC System Protection: A Review of Current Methods," in *Power Systems Conference and Exposition (PSCE), 2011 IEEE/PES*, 2011, pp. 1-7.
[161] T. Qingrui, *et al.*, "Suppressing DC Voltage Ripples of MMC-HVDC Under Unbalanced Grid Conditions," *IEEE Trans. Power Del.,* vol. 27, pp. 1332-1338, Jul. 2012.
[162] M. M. C. Merlin, *et al.*, "A New Hybrid Multi-level Voltage-Source Converter with DC Fault Blocking Capability," in *2010 9th IET International Conference on AC and DC Power Transmission*, 2010, pp. 1-5.
[163] C. C. Davidson and D. R. Trainer, "Innovative Concepts for Hybrid Multi-level Converters for HVDC Power Transmission," in *2010 9th IET International Conference on AC and DC Power Transmission*, 2010, pp. 1-5.
[164] "Clean Power from Deserts," DESERTEC Foundation,, White Book,Feb, 2009.
[165] P. Adam, *et al.*, "Medgrid, a Co-development Project for the Exchanges of Electricity in the Mediterranean Basin," in *17th Power Systems Computatio Conference (PSCC)*, 2011, pp. 1-6.
[166] G. Minyuan and X. Zheng, "Modeling and Control of a Modular Multilevel Converter-Based HVDC System Under Unbalanced Grid Conditions," *IEEE Trans. Power Electron.,* vol. 27, pp. 4858-4867, Dec. 2012.

[167] M. Saeedifard and R. Iravani, "Dynamic Performance of a Modular Multilevel Back-to-Back HVDC System," *IEEE Trans. Power Del.,* vol. 25, pp. 2903-2912, Oct. 2010.
[168] T. Qingrui and X. Zheng, "Impact of Sampling Frequency on Harmonic Distortion for Modular Multilevel Converter," *IEEE Trans. Power Del.,* vol. 26, pp. 298-306, Jan. 2011.
[169] J. Peralta*, et al.*, "Detailed and Averaged Models for a 401-Level MMC-HVDC System," *IEEE Trans. Power Del.,* vol. 27, pp. 1501-1508, Jul. 2012.
[170] Q. Jiangchao and M. Saeedifard, "Predictive Control of a Modular Multilevel Converter for a Back-to-Back HVDC System," *IEEE Trans. Power Del.,* vol. 27, pp. 1538-1547, Jul 2012.
[171] S. Gum Tae*, et al.*, "Design and Control of a Modular Multilevel HVDC Converter With Redundant Power Modules for Noninterruptible Energy Transfer," *IEEE Trans. Power Del.,* vol. 27, pp. 1611-1619, Jul. 2012.
[172] U. N. Gnanarathna*, et al.*, "Modular Multi-level Converter Based HVDC System for Grid Connection of Offshore Wind Power Plant," in *2010 9th IET International Conference on AC and DC Power Transmission*, 2010, pp. 1-5.
[173] R. P. Wierckx and N. Dhaliwal, "Detailed Modeling of Large Interconnected AC/DC Systems Using a Real-time Digital Simulator," in *2010 9th IET International Conference on AC and DC Power Transmission*, 2010, pp. 1-6.
[174] U. N. Gnanarathna*, et al.*, "Efficient Modeling of Modular Multilevel HVDC Converters (MMC) on Electromagnetic Transient Simulation Programs," *IEEE Trans. Power Del.,* vol. 26, pp. 316-324, Oct. 2011.
[175] C. M. Franck, "HVDC Circuit Breakers: A Review Identifying Future Research Needs," *IEEE Trans. Power Del.,* vol. 26, pp. 998-1007, Apr. 2011.
[176] J. Häfner and B. Jacobson, "Proactive Hybrid HVDC Breakers - A Key Innovation for Reliable HVDC Grids," in *The Electric Power System of the Future - Integrating Supergrids and Microgrids International Symposium*, Bologna, 2011, pp. 1-8.
[177] L. Tang and B.-T. Ooi, "Locating and Isolating DC Faults in Multi-Terminal DC Systems," *IEEE Trans. Power Del.,* vol. 22, pp. 1877-1884, Jul. 2007.
[178] W. Lu and B.-T. Ooi, "DC Overvoltage Control During Loss of Converter in Multiterminal Voltage-source Converter-based HVDC (M-VSC-HVDC)," *IEEE Trans. Power Del.,* vol. 18, pp. 915-920, Jul. 2003.
[179] L. Tang, "Control and Protection of Multi-terminal DC Transmission Systems based on Voltage-source Converters," PhD Thesis, Department of Electrical and Computer Engineering, McGill University, Montreal, Canada, 2003.
[180] H. Liu*, et al.*, "Study of Protection Strategy for VSC based HVDC System," in *2003 IEEE PES Transmission and Distribution Conference and Exposition*, 2003, pp. 49-54 Vol.1.
[181] L. Tang and B.-T. Ooi, "Protection of VSC-multi-terminal HVDC against DC faults," in *2002 IEEE 33rd Annual Power Electronics Specialists Conference (PESC)*, 2002, pp. 719-724.
[182] ABB. *Valhall HVDC Light*. Available: http://www.abb.co.uk/industries/ap/db0003db004333/57f0293bd4a9d8ccc125774a004ba547.aspx
[183] ABB. *Power from shore: ABB technologies at Troll A platform*. Available: http://www.abb.co.uk/industries/ap/db0003db004333/8c3aa401373d6f9cc125774a0049a015.aspx
[184] D. Jovcic, "Step-up DC-DC Converter for Megawatt Size Applications," *IET Power Electron,* vol. 2, pp. 675-685, Nov. 2009.

[185] Z. Qun and F. C. Lee, "High-efficiency, High step-up DC-DC converters," *IEEE Trans. Power Electron.,* vol. 18, pp. 65-73, Jan. 2003.
[186] D. Jovcic and B. T. Ooi, "Developing DC Transmission Networks Using DC Transformers," *IEEE Trans. Power Del.,* vol. 25, pp. 2535-2543, Oct. 2010.
[187] D. Jovcic, "Bidirectional, High-Power DC Transformer," *IEEE Trans. Power Del.,* vol. 24, pp. 2276-2283, Oct. 2009.
[188] N. Denniston*, et al.*, "Multiple-Module High-Gain High-Voltage DC-DC Transformers for Offshore Wind Energy Systems," *IEEE Trans. Industrial Electron.,* vol. 58, pp. 1877-1886, May. 2011.

List of Publications

1) **D. Kong**, X.-P. Zhang. “Transient Stability Analysis and Optimal Coordinated Control of Multi-terminal VSC-HVDC based Offshore Wind Farms”. *Proceedings of IET Renewable Power Generation Conference 2011*, 6-8, Sept., 2011, Edinburgh, UK.
2) **D. Kong**, X.-P. Zhang. “Modelling and Control of Offshore Wind Farm with VSC-HVDC Transmission System”. *Proceedings of the IET 9th International Conference on AC/DC Power Transmission*, 20-21 Oct., 2010, London, UK.
3) **D. Kong**, X.-P. Zhang. “The Dynamic Equivalent Modeling of Large-scale Offshore Wind Farms for Power System Transient Stability Study”. *Proceeding of the 4th International Conference on Liberalization and Modernization of Power Systems - Coordinated Monitoring and Control towards Smart Grids*, 13-17 Jul., 2009, Irkutsk, Russia.
4) R. Shi, X.-P. Zhang, **D. Kong**, N. Deng and P. Wang. “Dynamic Impacts of Fast-charging Stations for Electric Vehicles on Active Distribution Networks”. *Proceedings of IEEE PES Innovative Smart Grid Technology (ISGT) -Asia Conference*, 21-24, May 2012, Tianjin, China.